University of Bath

UNIVERSITY OF BATH

PHD

Molecular and Atomic Confinement in Large Core Photonic Microcells for Slow Light and Laser Metrology Applications

Wheeler, Natalie

Award date:
2010

Awarding institution:
University of Bath

[Link to publication](#)

Molecular and Atomic Confinement in Large Core Photonic Microcells for Slow Light and Laser Metrology Applications

Natalie Violet Wheeler

A thesis submitted for the degree of Doctor of Philosophy

University of Bath

Department of Physics

November 2010

Abstract

This thesis describes developments in the fabrication and applications of photonic microcells (PMCs). A PMC is a length of gas-filled hollow core-photonic crystal fibre (HC-PCF) that is hermetically sealed by splicing both ends to standard single mode fibre. A PMC enables integration of gas-filled HC-PCF into all-fibre systems with low insertion loss.

PMCs have applications in coherent optics and metrology, where specific HC-PCF designs are advantageous. Two types of state-of-the-art HC-PCF, double bandgap HC-PCF and large-pitch Kagome fibre, are fabricated. The double bandgap HC-PCF extends the usable bandwidth of the fibre by providing low loss guidance across two transmission bands. The large-pitch Kagome HC-PCF has a record low attenuation of 0.3 dB/m at 800 nm, while maintaining broadband guidance, which is partially attributed to the core shape.

Three distinct developments in the field of PMCs are described. Firstly, a record length 20 metre acetylene-filled PMC is fabricated which is the key component in the first demonstration of an all-fibre slow and fast light system based on electromagnetically induced transparency. Secondly, a technique based on fibre tapering is presented which enables low loss integration of large core Kagome HC-PCFs into PMC form. Thirdly, micromirrors are developed and integrated with HC-PCF to confine light in the longitudinal dimension, providing a means to fabricate multi-pass PMCs. Two uncoated micromirrors are used to form a low finesse microcavity in Kagome HC-PCF, with record high fringe visibility using reflections from a silica/air junction.

In collaboration with Kansas State University, an acetylene optical reference with sub-10 KHz accuracy and the first acetylene laser based on population inversion are demonstrated using Kagome HC-PCF.

Finally, this thesis reports on rubidium vapour loading in HC-PCF with the ultimate aim being the production of a rubidium-filled PMC for applications in metrology. Preliminary results highlight the limited loading distance of the current technique and modified loading schemes are outlined accordingly.

Preface

In 1999, the first hollow core photonic crystal fibre (HC-PCF) was fabricated, realising a long standing goal of achieving low loss optical guidance in a micron-scale hollow core. This form of optical fibre does not guide via total internal reflection. Instead, the fibre cladding, typically a periodic transverse arrangement of air holes defined by a silica matrix, is designed to exhibit a photonic bandgap (PBG). A PBG is a range of frequencies for which modes with specific propagation constant β cannot propagate. If a core defect is introduced into this periodic background, which does support modes within the PBG, then light guided in these optical modes will be effectively trapped in this core.

In parallel to the development of PBG HC-PCF, a second guidance mechanism has been demonstrated which enables low loss, broadband guidance in a hollow core. HC-PCFs of this design are referred to as large-pitch HC-PCFs; the most notable example is Kagome lattice HC-PCF. This class of fibre guides by a mechanism akin to Von-Neumann Wigner bounds states within a continuum as it accommodates both core and cladding modes with the same propagation constant β without significant coupling between the two types of mode.

Importantly, low loss guidance in a hollow core has opened up a new paradigm for gas-laser interactions since the hollow defect can be filled with gas-phase material. The key advantage of this interaction scheme is the tight modal confinement in the hollow core combined with low loss guidance. This provides the means to create high intensity beams at low power, enabling the observation of extremely weak interactions between light and matter. In recent years, this advantage has enabled great advances in a variety of fields including: stimulated Raman scattering, multi-octave frequency comb generation, electromagnetically induced transparency (EIT), saturated absorption spectroscopy (SAS) and high power soliton delivery. Exciting potential applications include attosecond pulse generation, frequency metrology, laser stabilisation and other applications in quantum optics.

In parallel to these advances, fabrication techniques have been developed to transform gas-filled HC-PCF into a compact and stand-alone photonic component, called a photonic microcell (PMC). A PMC is a length of gas-filled HC-PCF which is spliced at both ends to standard all-solid single mode fibre (SMF) in order to trap the gas in the core and provide low loss input and output coupling to the HC-PCF. PMCs are compact and portable and easily integrated into all fibre systems.

The development of photonic devices and components based on this technology is a current and exciting trend in this field. This trend is driven by the ability of a PMC to

exquisitely control and confine both gas and light in micron-scale mode areas on one hand, and by the increasing need for high performance electro-optical functionalities to be delivered in compact physical packages on the other hand. An important example of such a pressing need is the demand for compact alternatives to current state-of-the-art atomic clocks and frequency standards. Indeed, because of the ubiquitous use of frequency-referenced devices in science and technology, the advent of such electro-optical devices would radically transform fields as different and diverse as quantum optics, optical processing and precision measurement to mention a few. Within this context, the demonstrated PMC attributes such as compactness, integrability and extremely long interaction length make this photonic technology a promising candidate to take on the aforementioned challenges.

The work undertaken and reported in this thesis is part of a broader effort to find and develop photonic solutions based on HC-PCF for coherent optics, quantum optics and laser frequency metrology. In particular, this thesis tackles some of the limitations encountered in the early PMCs and embodies work that spans from advances in fibre design and fabrication to the development of new techniques in PMC assembly and experimental demonstrations of several coherent optics and laser metrology related applications using PMCs.

This thesis comprises 8 chapters. In chapter 1 the relevant background material in the field of quantum and coherent optics is introduced. In chapter 2, two main classes of HC-PCF are identified and their guidance mechanisms described. The two most recent developments in the fabrication of these fibres are presented, in which the author has performed a significant role. In chapters 3 to 7, work of the author in the development of the application of PMCs for EIT, slow and fast light and SAS is described along with advances in the PMC assembly technique which enable large core fibres to be integrated as well as novel micromirrors.

Chapter 1 is an introduction to the coherent techniques used throughout this thesis to create spectrally narrow, sub-Doppler features in gas-filled HC-PCF. The means for quantitative analysis of such spectral features is discussed. The linewidth of these features is essential in defining their potential applications, for example in the aforementioned fields of frequency stabilisation or slow light. The advantages and potential disadvantages of using gas-filled HC-PCF for coherent optical interactions are described. In particular, the confinement of the gas in the micron-scale hollow core is discussed with respect to its contribution to collisional broadening, which limits the minimum linewidth of spectral features observed in this gas-laser interaction scheme. The use of larger core fibres, such as large-pitch Kagome fibre is identified as a means for reducing this spectral linewidth.

In chapter 2, two classes of HC-PCF, PBG and large-pitch, are discussed in detail and the relevant guidance mechanisms are described. Two examples of recent fabrication

advances in which the author played a significant role in the fabrication process are presented. Firstly, double bandgap HC-PCF is introduced; this enables low loss guidance in two transmission windows by designing a cladding structure with optimal apex and strut size. Secondly, large-pitch Kagome fibres are described which have significantly reduced attenuation while still maintaining the broadband optical guidance and large core diameters offered by this class of fibre.

In chapter 3, the first all-fibre slow and superluminal light scheme based on EIT is presented. The key to this scheme is a record length, 20 metre acetylene-filled PMC. Experimental pulse delays and advances of 5 ns and 1 ns respectively were recorded. A simple analytical model is described which provides intuitive insight into how to improve the experimental parameters in order to optimise pulse delay. Specifically, the use of a larger core HC-PCF is highlighted as a means to increase the maximum achievable delay using this slow light scheme.

In chapter 4, the advantages of Kagome fibre are presented for gas-phase spectroscopy. These advantages are highlighted by three experiments in which the author has been involved. Firstly, the spectral linewidths of EIT features in acetylene-filled Kagome and PBG HC-PCF are compared. Secondly, a sub-10 kHz accuracy optical reference is described which is based on SAS in an acetylene-filled 19-cell Kagome fibre. Finally, the first demonstration of an optically pumped acetylene laser in HC-PCF is presented. These experiments clearly define regimes in which the Kagome fibre has a superior performance to PBG HC-PCF. From this conclusion, it is clear that a means for integrating large dimension HC-PCF into PMC form is required. A technique which achieves this goal by fibre tapering is described in chapter 5.

In chapter 6, micromirrors formed from tapered SMFs are introduced. These can be inserted into the core of a HC-PCF to provide confinement in the longitudinal dimension and therefore can be used to create multi-pass PMCs. Using two micromirrors, a microcavity is formed in Kagome HC-PCF which exhibits record fringe extinction. Furthermore, SAS is demonstrated using the compact reflected probe scheme and a silver-coated micromirror.

Chapter 7 presents preliminary work towards the fabrication of rubidium-filled PMC. Specifically, rubidium vapour loading into HC-PCF is studied and the results highlight the limited lengths of HC-PCF which can be loaded using the existing experimental scheme. A siloxane-coated glass cylinder in the rubidium release chamber is shown to extend the lifetime of the rubidium vapour in the chamber and is also demonstrated as a source of rubidium vapour using light-induced atomic desorption. Modified loading schemes are presented based on the conclusions from the preliminary work.

Chapter 8 summarises the work presented in this thesis and outlines future work.

Acknowledgements

Table of Contents

Journal Publications

1. **Wheeler, N. V.,** Grogan, M. D. W., Bradley, T. D., Couny, F., Birks, T. A. and Benabid, F. Multi-Pass Hollow Core PCF Microcell using a Tapered Micro-Mirror. Manuscript accepted for publication in *JLT* (2010)

2. Wang, Y. Y., **Wheeler, N. V.,** Couny, F., Roberts, P. J. and Benabid, F., 2011. Low Loss Broadband Transmission in Optimized Core-Shape Kagome Hollow-Core PCF. *Optics Letters*, 36(5), pp. 669-771.

3. Jones, A. M., Nampoothiri, V., Ratanavis, A., Fiedler, T., **Wheeler, N. V.,** Couny, F., Kadel, R., Benabid, F., Washburn, B. R., Corwin, K. L. and Rudolph, W., 2011. Mid-infrared gas filled photonic crystal fiber laser based on population inversion. *Optics Express,* 19(3), pp. 2309-2316.

4. **Wheeler, N. V.,** Grogan, M. D. W., Light, P. S., Couny, F., Birks, T. A., Benabid, F., 2010. Large-core acetylene-filled photonic microcells made by tapering a hollow-core photonic crystal fiber. *Optics Letters,* 35 (11), pp. 1875-1877.

5. **Wheeler, N. V.,** Light, P. S., Couny, F., Benabid, F., 2010. Slow and superluminal light pulses via EIT in a 20-m acetylene-filled photonic microcell. *Journal of Lightwave Technology,* 28 (6), pp. 870-875.

6. Beaudou, B., Couny, F., Wang, Y. Y., Light, P. S., **Wheeler, N. V.,** Gerome, F., Benabid, F., 2010. Matched cascade of bandgap-shift and frequency-conversion using stimulated Raman scattering in a tapered hollow-core photonic crystal fibre. *Optics Express,* 18 (12), pp. 12381-12390.

7. Light, P.S., Couny, F., Wang, Y., **Wheeler, N.V.,** Roberts, P.J., Benabid, F., 2009. Double photonic bandgap hollow-core photonic crystal fiber. *Optics Express,* 17 (18), pp. 16238-16243.

8. Knabe, K., Wu, S., Lim, J. K., Tillman, K. A., Light, P. S., Couny, F., **Wheeler, N. V.,** Thapa, R., Jones, A. M., Nicholson, J. W., Washburn, B. R., Benabid, F., Corwin, K. L., 2009. 10 kHz accuracy of an optical frequency reference based on (C_2H_2)-filled large-core kagome photonic crystal fibers. *Optics Express,* 17 (18), pp. 16017-16026.

Conference Papers

1. Rudolph, W., Nampoothiri, A. V.V., Ratanavis, A., Jones, A., Kadel, R., Washburn, B.R., Corwin, K. L., **Wheeler, N.V.,** Couny, F. and Benabid, F. Mid-IR Laser Emission from a C_2H_2 Gas Filled Hollow Core Fiber [Invited]. *ICTON* (Munich 2010).

2. Corwin, K. L., Wang, C., Knabe, K., Wu, S., Lim, J., Washburn, B. R., **Wheeler, N.V.,** Couny, F. and Benabid, F. 10 kHz Accuracy Spectroscopy in Acetylene-filled Hollow Core Kagome Fiber and Improved Linewidths [Invited]. *Frontiers in Optics* (Rochester 2010).

3. **Wheeler, N. V.,** Grogan, M. D. W., Light, P. S., Couny, F., Birks, T. A. and Benabid, F. Developments in the Fabrication and Applications of Photonic Microcells. *Photon10* (Southampton 2010).

4. Jones, A. M., Nampoothiri, A. V. V., Ratanavis, A., Kadel, R., **Wheeler, N. V.,** Couny, F., Benabid, F., Rudolph, W., Washburn, B. R. and Corwin, K. L., C_2H_2 Gas Laser Inside Hollow-Core Photonic Crystal Fiber Based on Population Inversion. *Conference on Lasers and Electro-Optics* (CLEO), CTuU1, (2010).

5. **Wheeler, N. V.,** Grogan, M. D. W., Light, P. S., Couny, F., Birks, T. A. and Benabid, F. Large Core Acetylene-Filled Photonic Microcells Made by Tapering the Hollow-Core Fiber. *Conference on Lasers and Electro-Optics* (CLEO), CTuS5, (2010).

6. **Wheeler, N. V.,** Grogan, M. D. W., Bradley, T. D., Couny, F., Birks, T. A. and Benabid, F. Ultra-High Reflectivity Hollow Core PCF Microcell using a Tapered Micro-Mirror. *Conference on Lasers and Electro-Optics* (CLEO), CThB3 (2010).

7. Nampoothiri, V., Jones, A. M., Ratanavis, A., Kadel, R., **Wheeler, N. V.,** Couny, F., Benabid, F., Washburn, B. R., Corwin, K. L. and Rudolph, W. Mid-IR laser emission from a C_2H_2 gas filled hollow core photonic crystal fiber [Postdeadline]. *Proceedings of the SPIE - The International Society for Optical Engineering*, 7580, 758001 (2010).

8. **Wheeler, N. V.,** Light, P. S., Couny, F. and Benabid, F. EIT-based slow and fast light in an all-fiber system [Invited]. *Proceedings of SPIE - The International Society for Optical Engineering*, 7612, 761202 (2010).

9. **Wheeler, N. V.,** Light, P. S., Couny, F., Benabid, F., 2010. Slow and superluminal light pulses via EIT in a 20-m acetylene-filled photonic microcell. *Conference on Lasers and Electro-Optics* (CLEO), JTuD61 (2009).

10. Couny, F., Beaudou, B., Light, P. S., Wang, Y. Y., **Wheeler, N. V.,** Gerome, F., Benabid, F. Modal and Spectral Evolution of Raman Lines in a H_2-Filled Hollow Core PCF Taper. *Conference on Lasers and Electro-Optics* (CLEO), JTuB4 (2009).

11. Light, P.S., Couny, F., Wang, Y., **Wheeler, N.V.,** Roberts, P.J., Benabid, F., Double Photonic Bandgap Hollow-Core PCF [Postdeadline]. *Conference on Lasers and Electro-Optics* (CLEO), CPDA7 (2009).

12. **Wilding, N. V.,** Light, P.S., Couny, F. and Benabid, F. Experimental Comparison of Electromagnetically Induced Transparency in Acetylene-Filled Kagome and Triangular Lattice Hollow Core Photonic Crystal Fiber. *Conference on Lasers and Electro-Optics* IEEE, pp. 1953-1954 (2008).

Definitions of Symbols

α	Absorption coefficient
β	Axial component of wavevector
c	Speed of light in a vacuum
h	Planck constant
$\hbar$	Reduced Planck constant
k	wavevector
k_B	Boltzmann constant
Λ	Fibre cladding pitch
λ	Vacuum wavelength
λ_{fp}	Mean free path
μ	Transition dipole moment
n_g	Group refractive index
R_c	Fibre core radius

Definitions of Abbreviations

AM	Amplitude Modulation
CNFL	Carbon Nanotube Fibre Laser
CQED	Cavity Quantum Electrodynamics
CW	Continuous Wave
DOPS	Density of Photonic States
ECDL	External Cavity Diode Laser
EDFA	Erbium Doped Fibre Amplifier
EIT	Electromagnetically Induced Transparency
FM	Frequency Modulation
HC-PCF	Hollow Core-Photonic Crystal Fibre
IR	Infra Red
OSA	Optical Spectrum Analyser
PBG	Photonic Bandgap
PCF	Photonic Crystal Fibre
PMC	Photonic Microcell
SAS	Saturated Absorption Spectroscopy
SBS	Stimulated Brillouin Scattering
SMF	Single Mode Fibre (in particular, SMF-28e for all experimental work)
SRS	Stimulated Raman Scattering
UHV	Ultra High Vacuum

Chapter 1

Quantum and Coherent Optics in Gas-phase Media

This chapter reviews the main coherent optical techniques used throughout this thesis for the generation of narrow spectral features in acetylene gas. Additionally, applications which require such features are described.

The advantages and challenges of using gas-filled hollow core-photonic crystal fibre for coherent optics are discussed and benchmark results using this gas-laser interaction scheme are presented.

1.1.   Introduction

Narrow and stable spectral features are required for applications such as laser frequency stabilisation, frequency metrology and slow light. For example, in the field of frequency stabilisation, the frequency stability of a laser, locked to a resonance, is defined by the resonance spectral linewidth. The long term frequency stability will be affected by shifts in the resonant frequency which can occur due to temperature and pressure changes in the local environment.

Gas-phase media are often chosen for the aforementioned applications. Spectroscopic features in gas-phase materials are generally narrower than those in solid or liquid systems due to their rarefied nature and subsequently lower dephasing rates. A further advantage of a gaseous medium is that it is relatively simple to establish the relevant spectral broadening mechanisms and therefore one can tackle the challenge of reducing or eliminating these effects by different techniques.

Atomic and molecular resonators are often described as Lorentzian oscillators. The essential resonance characteristics derived from this assumption, including the resonance quality factor (Q-factor) and signal-to-noise ratio (SNR), are introduced in the first part of this chapter (section 1.2), along with spectral broadening mechanisms relevant to gas-phase media. These mechanisms set a limit, ultimately due to Doppler broadening, on the minimum linewidth of a spectral feature. For example, for acetylene gas at room temperature, the Doppler-limited linewidth is ~470 MHz. Fortunately, this limit can be overcome by a judicious choice of experimental conditions and a technique which creates a sub-Doppler feature within an absorption line. Three of these techniques are outlined

in the second part of this chapter (sections 1.3 and 1.4): electromagnetically induced transparency (EIT), coherent population trapping (CPT) and saturated absorption spectroscopy (SAS).

Until recently the gas medium for these experiments was typically confined in a macroscopic glass cell; confining the gas in this manner enables the temperature and pressure of the gas to be carefully controlled and provides a means to transport the gas. Current applications of gas cells are described in section 1.6. In these cells the interaction length between the light and gas is severely restricted, which in turn limits the linewidth of the spectral features observed. Furthermore, the limited interaction length restricts the observation of coherent effects, such as EIT, to atomic vapours which have relatively large dipole moments. A gas host which provides long interaction length and tight light confinement, without providing additional contributions to the spectral linewidth, can remove these limitations.

In the work presented in this thesis, hollow core-photonic crystal fibre (HC-PCF) is used to confine the chosen gas; HC-PCF provides low loss optical guidance, extremely long gas-laser interaction length and is compact and easily integrated with existing fibre-based optical components. The advantages and potential disadvantages of using such a gas-laser interaction scheme are presented in the final part of this chapter (section 1.7). Additionally, benchmark results using this scheme are described.

1.2.   Quantitative Analysis of Spectral Features

Before describing techniques to generate a narrow, sub-Doppler feature within an absorption line, it is useful to first consider the means for quantitative characterisation of spectral features. To this end, the signal-to-noise ratio (SNR) and line quality factor (Q-factor) are introduced in this section. Moreover, key line broadening mechanisms which limit the spectral linewidth of an absorption feature are described. It is crucial to understand the origin of these mechanisms in order to reduce their magnitude effectively.

1.2.1.   Resonance Characteristics of a Lorentzian Oscillator

To quantitatively define the characteristics of a spectral feature, the light-atom interaction can be considered classically. Starting from Maxwell's equations, solutions to the wave equation define the dispersion and absorption of a resonance using the real and imaginary parts of the complex form of the refractive index respectively. The complex refractive index is expressed, using the linear susceptibility $\chi = \chi' + i\chi''$, as

$$\tilde{n}(\omega) = \sqrt{1 + \chi(\omega)} \cong 1 + \frac{\chi' + i\chi''}{2} \quad . \tag{1-1}$$

Within this derivation the Beer-Lambert law,

$$I = I_0 \, e^{-\alpha L} \, ,$$

(1-2)

is introduced, which describes the resultant intensity I of a light beam with an input intensity I_0 after travelling through a medium of interaction length L and absorption co-efficient α. From the Beer-Lambert law, it is clear that the absorption co-efficient of a spectral resonance is crucial in defining the SNR of a resonant feature and it is expressed as,

$$\alpha = \frac{\omega^2 \chi''}{c^2 k} = \, k\chi'' \, ,$$

(1-3)

where ω is the frequency of the incident light, c is the speed of light in a vacuum and k is the vacuum wavenumber. Also from the Beer-Lambert law, it is apparent that a means to increase the SNR of a resonance with a small absorption co-efficient is to increase the interaction length between the light and the absorbing medium.

Furthermore, using the classical dipole moment model of a Lorentzian oscillator, which considers a hypothetical atom consisting of a single proton and electron joined by a spring with restoring constant, the real and imaginary parts of the susceptibility are expressed as,

$$\chi' = \frac{Nq^2}{m\varepsilon_0} \left[\frac{\omega_0{}^2 - \omega^2}{(\omega_0{}^2 - \omega^2)^2 + \omega^2 \gamma^2} \right]$$

(1-4)

and

$$\chi'' = \frac{Nq^2}{m\varepsilon_0} \left[\frac{\omega \gamma}{(\omega_0{}^2 - \omega^2)^2 + \omega^2 \gamma^2} \right] ,$$

(1-5)

where N is the atomic density, q is the electronic charge, γ is the damping constant, m is the mass of an electron, ω_0 is the resonant frequency and ε_0 is the permittivity of free space.

Expressions (1-4) and (1-5) can be approximated using the near resonance approximation [1],

$$\omega_0{}^2 - \omega^2 = (\omega_0 + \omega)(\omega_0 - \omega) \approx 2\omega_0(\omega_0 - \omega) \approx 2\omega(\omega_0 - \omega),$$

(1-6)

which is valid in the limit of small frequency detuning from the resonant frequency. Using this approximation, equations (1-4) and (1-5) can be simplified and expressed respectively as,
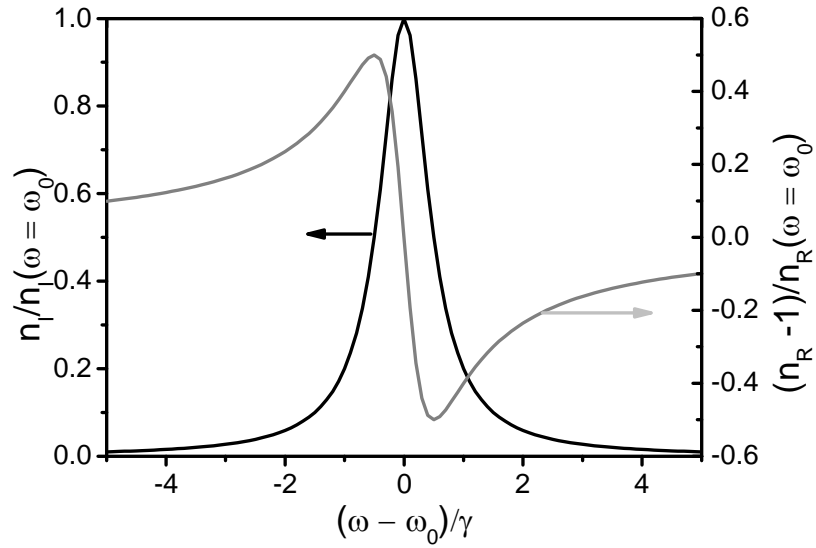
Figure 1-1: *Real (n_R) (grey line) and imaginary (n_I) (black line) parts of the complex refractive index define the dispersion and absorption characteristics of a Lorentzian oscillator respectively (calculated using equations (1-1), (1-7) and (1-8).)*

$$\chi' = -\frac{Nq^2}{m\varepsilon_0\gamma\omega_0}\frac{\dfrac{2(\omega-\omega_0)}{\gamma}}{\left(\dfrac{2(\omega-\omega_0)}{\gamma}\right)^2+1} \qquad (1\text{-}7)$$

$$\chi'' = \frac{Nq^2}{m\varepsilon_0\gamma\omega_0}\frac{1}{\left(\dfrac{2(\omega-\omega_0)}{\gamma}\right)^2+1}. \qquad (1\text{-}8)$$

Using equations (1-1), (1-7) and (1-8) the real and imaginary parts of the complex index of refraction are plotted in Figure 1-1. These describe the dispersive and absorptive properties of an ideal Lorentzian oscillator respectively. Figure 1-1 shows that these properties are centred on the resonance frequency.

The full-width at half maximum (FWHM) is used to define the spectral linewidth of an absorption feature. From equation (1-8) the FWHM ($\Delta\omega$) of a Lorentzian absorption feature is γ. Using this, we can introduce a characteristic time, $\tau = \frac{1}{\gamma}$ which represents the time after which energy in the oscillator has been reduced by a factor of $1/e$. In the context of an atomic oscillator τ describes the lifetime of an excited state [2]. This finite lifetime demonstrates that an atomic line always has a finite linewidth that cannot be reduced to zero. A damped oscillation can be further characterised using the resonance Q-factor, which describes the ratio between average energy stored in the resonant

system, *W*, and the rate at which the energy is dissipated. Mathematically, the Q-factor is defined as [2]

$$Q = \frac{\omega_0 W}{-dW/dt} \,.$$

(1-9)

A high Q-factor, therefore, describes a system from which energy is lost slowly, corresponding to a small damping constant. Equation (1-9) can be rewritten in the form [2]

$$Q = \frac{\omega_0}{\Delta \omega} \,.$$

(1-10)

The Q-factor is used extensively to characterise resonators employed in frequency standards and metrology; for example, the fractional frequency deviations of an atomic clock are described by,

$$\frac{\delta \omega}{\omega_0} \propto \frac{1}{(SNR) * Q} \,.$$

(1-11)

To minimise these deviations, it is clear that a high Q-factor and SNR are simultaneously required. A high SNR can be obtained by optimising the light-matter interaction and by employing a suitable detection scheme. This will be further discussed in section 1.7.1. Equation (1-10) shows that, in order to obtain a high Q-factor, the linewidth of the resonance needs to be minimised; the following section describes the main mechanisms which act to broaden resonance features.

1.2.2. Spectral Lineshapes

A spectral line, corresponding to a specific atomic transition, is typically broadened by four main mechanisms which combine to produce the experimentally observed spectral lineshape, namely natural, Doppler, collisional and power broadening. In this section the origins of these linewidth broadening mechanisms and the means to reduce them are reviewed.

Natural Broadening

Natural broadening is a fundamental result of quantum uncertainty in energy level spacing, ΔE, as defined by the Heisenberg uncertainty principle in the form,

$$\tau \Delta E \geq \hbar \,,$$

(1-12)

where $\hbar$ is the reduced Planck constant. As discussed in the previous section, the lifetime of an excited state is always finite and therefore equation (1-12) shows that there is always some uncertainty in the energy level spacing. Natural broadening is a homogeneous effect in the sense that it affects all of the atoms or molecules in the gas in the same manner; this leads to a Lorentzian lineshape distribution. The magnitude of this

broadening mechanism is much smaller than the other contributions which are discussed in this section and ultimately signifies the quantum limit to which the linewidth of an atomic transition can be reduced to.

Doppler Broadening

Doppler broadening arises from the spread in the atomic velocities in an ensemble of gas molecules according to the Maxwell-Boltzmann velocity distribution. In one dimension this is given by [3],

$$P(v_x)dN_x = \left(\frac{m}{2\pi k_B T}\right)^{\frac{1}{2}} e^{-mv_x^2/2k_B T} dN_x \, , \tag{1-13}$$

where m is the mass of the atom, T is the temperature and k_B is the Boltzmann constant. v_x is the velocity of the atom in the x-direction, which in the case here is defined by the direction of laser beam propagation. Atoms moving perpendicular to the laser beam are unaffected by Doppler broadening; all other atoms will absorb at a frequency v which is shifted from the resonant frequency v_0 ($v_0 = \frac{\omega_0}{2\pi}$) by,

$$v = v_0 \left(1 - \frac{v_x}{c}\right). \tag{1-14}$$

Doppler broadening is an inhomogeneous process and thus results in a Gaussian lineshape whose FWHM, Δv_g, is [2]

$$\Delta v_g = v_0 \sqrt{2\ln 2 \frac{k_B T}{mc^2}} \, . \tag{1-15}$$

The temperature dependence of this FWHM can be used to decrease the spectral linewidth induced by Doppler broadening using techniques such as laser cooling.

Collisional Broadening

Collisional broadening is a pressure dependent mechanism and originates from the shortening of the lifetime of an atom in an excited state that is induced by collisions, either between the gas atoms or between the atoms and the container walls [3]. In this context, a collision refers to an event where the two or more particles can exchange energy and momentum (magnitude or direction) [2]. During a collision, the energy levels of an atom or molecule can be modified, depending on the distance between the two colliding particles. For example, the FWHM of an absorption line from the $v_1 + v_3$ overtone band of acetylene is broadened by ~10 MHz/mbar [4], indicating that this contribution will only surpass the effects of Doppler broadening for acetylene pressures

above 50 mbar. This contribution to spectral broadening is also a homogeneous effect and has, therefore, a Lorentzian lineshape distribution.

In addition to collisional broadening, collisional shifts can also occur, where the centre of the resonance is shifted in frequency. However, the magnitude of collisional shift is usually at least an order of magnitude lower than the collisional broadening for optical frequency standards [2].

In order to observe sharply defined spectral features, atomic and molecular spectral lines are observed at low pressures, which effectively eliminate contributions to the spectral lineshape from collisions between gas atoms or molecules. At these low pressures the mean free path of the gaseous species can become greater than the dimensions of the gas confinement and therefore collisions between the confined atoms or molecules and the inner walls of the container can become the limiting factor in defining the resonance linewidth.

Power Broadening

The final broadening effect considered here is power or saturation broadening which describes the dependence of the observed spectral lineshape on the intensity of the incident light. To describe saturation effects, a dimensionless saturation parameter, S, is defined as

$$S = \frac{2B_{12}\rho(v)}{A_{21}},\tag{1-16}$$

where B_{12} and A_{21} are the Einstein rate coefficients for stimulated absorption and spontaneous emission respectively, and $\rho(v)$ describes the spectral energy density of the incident field [2]. Near a resonance, S is described by a Lorentzian distribution as it follows the frequency dependence of the absorption rate. It can be expressed as,

$$S = S_0 \frac{\left(\frac{\gamma}{2}\right)^2}{\left(\frac{\gamma}{2}\right)^2 + (v - v_0)^2},\tag{1-17}$$

where S_0 is the on resonance saturation parameter given by,

$$S_0 = \frac{I}{I_{sat}}.\tag{1-18}$$

Here, I is the incident field intensity and I_{sat} is saturation intensity [2]. By including the effects of saturation broadening, the resonance linewidth is increased by a factor of $(1 + S_0)^{1/2}$. Saturation effects are particularly important for long-lived states with small

damping constants. This is considered further in chapter 7, in the context of rubidium vapour which has a very small saturation intensity of 1.6 mW/cm^2 [5].

One of the main focuses of the work presented in thesis is the minimisation of the linewidth of absorption features in a gas-filled HC-PCF. By considering the broadening mechanisms above in this context, potential means to achieve this goal include low gas pressure (< 1 mbar), low incident laser power and low temperatures. Cryogenic systems are large and would inhibit the portability that a gas-filled HC-PCF can provide. A low temperature is required to reduce Doppler broadening but fortunately there are several alternative velocity selective techniques available which can be used to create sub-Doppler features within an absorption line and therefore enable generation of narrow spectral features without a cooling system; three examples of these techniques are described in the next section.

1.3.   Coherent Optical Techniques

1.3.1.   Coherence

Techniques based on atomic or molecular coherence are often used to generate narrow spectroscopic signatures in atomic or molecular ensembles thanks to their velocity selectivity. The coherence is driven by coupling one or more lasers to energy transitions between atomic states. The oscillating electromagnetic wave stimulates electric dipole oscillations which are strongly enhanced if the laser frequency is tuned close to a resonant frequency of the ensemble. The term coherence refers to the active role of the phase relationship between these oscillations. In this section, a semiclassical approach is used to explore coherent effects within an atomic ensemble; the light field is treated as a classical electromagnetic wave while the atomic structure is fully quantised. Using this
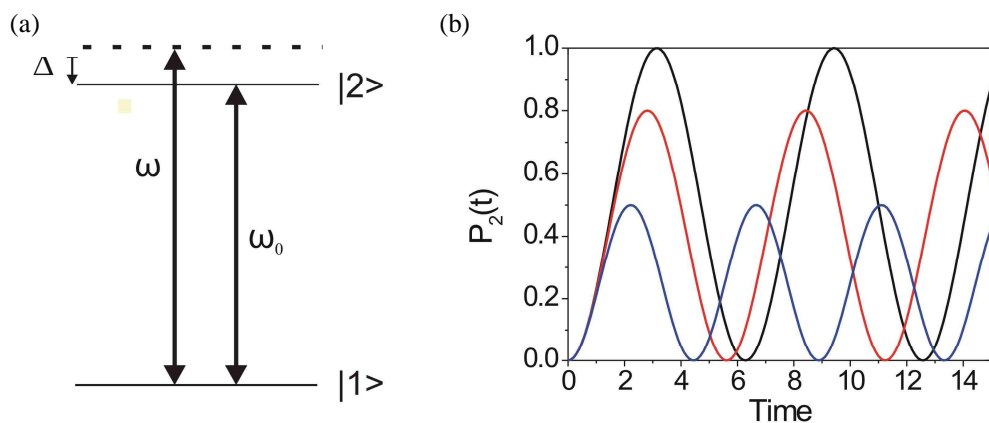
Figure 1-2: *(a) 2-level system resonant at frequency ω_0 is irradiated by a laser field at frequency ω. Coherence effects are manifested in this system in the form of Rabi oscillations.(b) Equation (1-19) is plotted for resonant detuning, Δ, of 0 (black line), $0.5\Omega_0$ (red line) and Ω_0 (blue line), where Ω_0 is the Rabi frequency for zero detuning.*
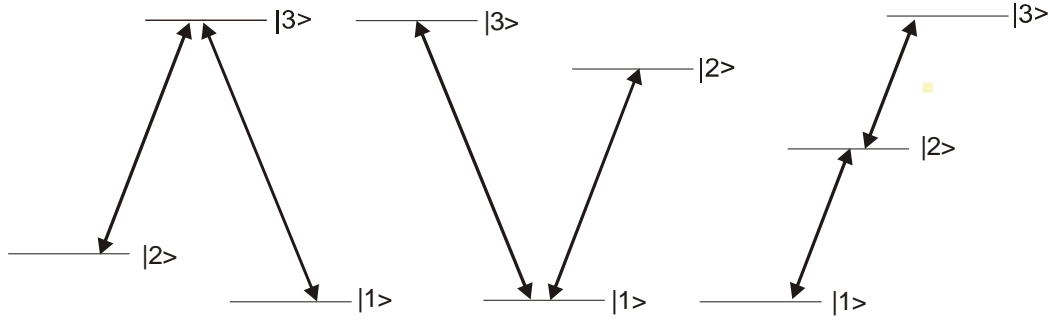
Figure 1-3: *(from left to right) Λ, V and ladder configurations applicable to a 3-level interacting system.*

quantum treatment, it is probability amplitudes and not probabilities which are summed to find the total transition probability and these are considered to describe the interference effects that are observed [6].

The effects of coherence can be observed in a 2-level system (Figure 1-2(a)), driven by a laser field at frequency ω. In this system, the population from the ground state of the system can be completely transferred to the excited state provided decoherence effects, such as spontaneous emission, are minimised. Through repeated stimulated absorption and stimulated emission the population repeatedly oscillates between the two states in the system. This process is known as Rabi flopping and occurs at the generalised Rabi frequency,

$$\Omega_R = \sqrt{\Delta^2 + \Omega_0{}^2} \qquad (1\text{-}19)$$

where

$$\Omega_0 = \frac{\mu \cdot E_0}{\hbar} . \qquad (1\text{-}20)$$

E_0 is the amplitude of the electric field, μ is the transition dipole moment and $\Delta = \omega - \omega_0$, the laser detuning from resonance. Rabi oscillations for $\Delta = 0$, $0.5\Omega_0$ and Ω_0 are shown in Figure 1-2(b); as the detuning increases the Rabi frequency also increases but the amplitude of the oscillation reduces. The Rabi frequency is often used as it takes into account both the transition strength and the laser intensity. The Rabi flopping process contrasts with that of incoherent illumination, through which a maximum of 50% of the population can be transferred to the excited state, in accordance with the Einstein rate equations [7]. The understanding of coherent interactions in a simple 2-level system can often be extended to more complex multi-level systems.

Electromagnetically Induced Transparency (EIT) is a quantum optic effect whereby a narrow transmission window can be induced within a Doppler broadened absorption line by the application of two lasers to a 3-level system. Typically, EIT is observed in a 3-level
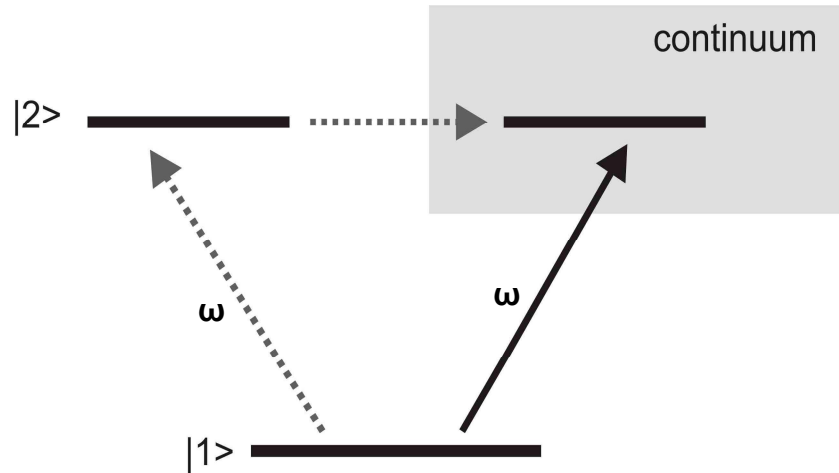
Figure 1-4: *Fano interference: the probability amplitudes of two different pathways to a continuum state can interfere constructively or destructively.*

system in a V, Λ, or ladder configuration (Figure 1-3). In these schemes, two of the transitions are typically dipole allowed while the third is forbidden (practically, this is an extremely long-lived state). The two lasers are tuned to be resonant with the dipole allowed transitions. This coherent technique is used extensively in this thesis.

Historically, EIT is related to Fano interference. In a multi-level system it is possible to have several excitation pathways to the same energy level which have different probability amplitudes. As probability amplitudes can be positive or negative this can lead to enhancement (constructive interference) or cancellation (destructive interference) of the total transition probability [6]. Fano [8] considered this in the system shown in Figure 1-4. In this simple demonstration of interference effects there are two different excitation pathways to a continuum level. One is direct excitation and the other is via a bound state (degenerate) within the continuum. Interference between these two pathways can be constructive or destructive to completely negate any absorption. This type of approach, which considers interference pathways, is the 'bare-atom' approach. An alternative, as explained below, is the dressed state approach.

1.3.2.   Coherent Population Trapping

As a precursor to the dressed state description of EIT it is useful to consider coherent population trapping (CPT) which is a similar coherent effect that is also observed in 3-level systems. CPT was first demonstrated by Alzetta *et al.* in 1976 [9]. Two lasers (here referred to as the probe and coupling lasers) with similar Rabi frequencies are coupled to the two dipole allowed transitions within the interacting system. When the detuning between the two lasers is equal to the detuning of the two states which form the non-dipole allowed transition, the fluorescence from the system decreases as a dark state is formed in which population can be trapped.
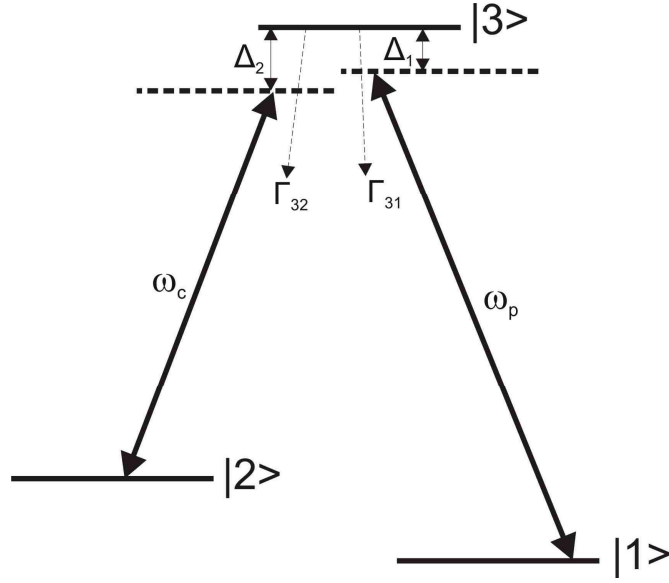
Figure 1-5: *Schematic of a Λ energy level system with relevant parameters labelled; ω_p and ω_c are the frequencies of the probe and coupling lasers respectively, Γ_{31} and Γ_{32} are decay terms from |3> to |1> and |3> to |2> respectively, Δ_1 and Δ_2 indicate laser detunings from the relevant atomic resonance frequencies.*

In the experimental conditions relevant to CPT, a very large number of atoms are present in the gas to be interrogated and therefore the analysis uses a Hamiltonian as an average representative of the ensemble and a density operator which corresponds to the ensemble average for the whole system [6]. In order to study the effect of the coupling laser on the bare atomic states, the Hamiltonian for the atom-laser system is calculated by assuming that it can be described by

$$H = H_0 + H_{\text{int}} , \tag{1-21}$$

where H_0 denotes the bare atom Hamiltonian and H_{int} is the interaction Hamiltonian. The interaction Hamiltonian for the Λ scheme where state |3> is common to both transitions is described in the rotating frame as [10],

$$H_{\text{int}} = -\frac{\hbar}{2} \begin{bmatrix} 0 & 0 & \Omega_p \\ 0 & -2(\Delta_1 - \Delta_2) & \Omega_c \\ \Omega_p & \Omega_c & -2\Delta_1 \end{bmatrix}, \tag{1-22}$$

where Ω_c and Ω_p are the Rabi frequencies of the coupling and probe laser transitions respectively and $\Delta_1 = \omega_{31} - \omega_p$ and $\Delta_2 = \omega_{32} - \omega_c$ are the detunings of the probe and coupling laser frequencies from their corresponding resonances. These labels are shown schematically in Figure 1-5. The off-diagonal components of the Hamiltonian relate to coherent interactions between two states while the on-diagonal components describe the state populations.

Through diagonalisation of the Hamiltonian, the eigenstates of the atom-laser system are found to be

$$\left|a^+\right\rangle = \sin\theta\sin\phi\left|1\right\rangle + \cos\phi\left|3\right\rangle + \cos\theta\sin\phi\left|2\right\rangle$$
$$\left|a^0\right\rangle = \cos\theta\left|1\right\rangle + \sin\theta\left|2\right\rangle \qquad\qquad , \qquad (1\text{-}23)$$
$$\left|a^-\right\rangle = \sin\theta\cos\phi\left|1\right\rangle + \sin\phi\left|3\right\rangle + \cos\theta\cos\phi\left|2\right\rangle$$

where θ and ϕ are referred to as 'mixing angles' which are defined by the expressions [6]

$$\tan\theta = \frac{\Omega_p}{\Omega_c} \qquad (1\text{-}24)$$

and

$$\tan 2\phi = \frac{\sqrt{\Omega_p^2 + \Omega_c^2}}{\Delta}. \qquad (1\text{-}25)$$

In this expression, $\Delta = \Delta_1$, the detuning of the probe laser. Equations (1-23) are referred to as the dressed states of this system and they indicate the formation of a dark state $|a_0>$ which is now completely decoupled from $|3>$. Any population which decays to the $|a_0>$ state becomes trapped there. Through this, population is effectively removed from the interacting system and a reduced fluorescence is experimentally observed.

1.3.3.   Electromagnetically Induced Transparency

EIT is a similar technique to CPT where absorption can be completely cancelled at the centre of a resonance with the key difference that the Rabi frequency of the probe laser is much smaller than that of the coupling laser ($\Omega_c >> \Omega_p$). The low power probe laser records the modified absorption and the high power coupling laser modifies the atomic states. EIT was theoretically predicted by both Harris [12] and Kocharovskaya [13] independently, as a means of achieving lasing without inversion. Results from the first
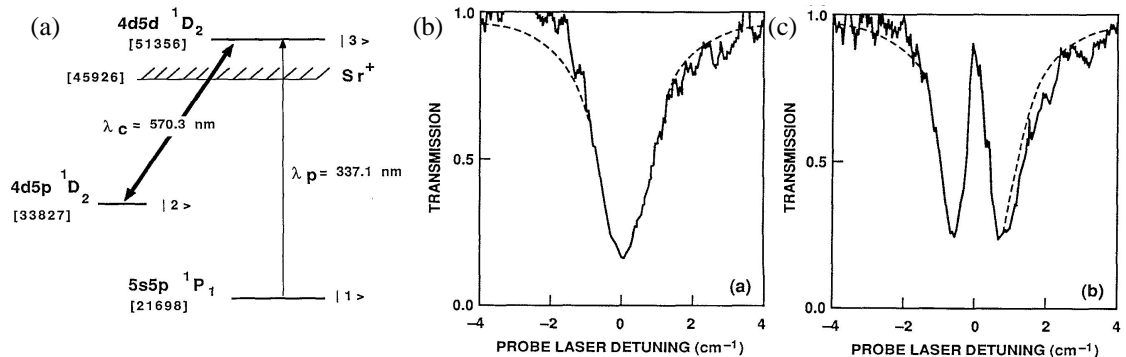
Figure 1-6: *From Boller et al. [11]. (a) Λ configuration used to observe EIT in strontium vapour, (b) absorption profile recorded using probe beam alone and (c) modified absorption line observed with co-propagating, higher power, coupling laser. Reprinted figure with permission from [11]. Copyright (1991) by the American Physical Society.*
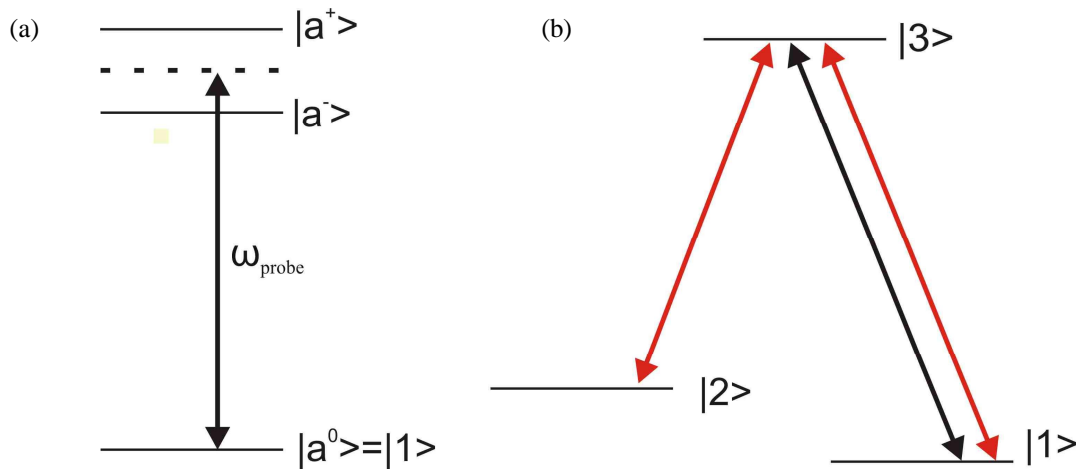
Figure 1-7: *(a) Dressed states of EIT (b) EIT can be understood through multipath interference; in this case path |1>-|3> (black line) interferes with the pathway |1>-|3>-|2>-|3> (red line).*

experimental demonstration of EIT by Boller *et al.* [11] in strontium vapour, are shown in Figure 1-6. Through the application of the coupling laser a medium which is initially nearly opaque to the probe beam on resonance (Figure 1-6(b)) is rendered almost transparent (Figure 1-6(c)); thus breaking the association of high refractive index with high absorption.

As mentioned above, a key practical difference in comparison to CPT is that one laser (the coupling laser) has much higher Rabi frequency than the other (the probe). There are also several differences in the dynamics of the two techniques; while in EIT only state |1> has any considerable population, in CPT the two lower states are typically hyperfine levels of an atomic ground state and therefore are both populated. Also, the time scale through which the coherence is generated is significantly shorter in EIT (~ps compared to ~ns for CPT [6]). Traditionally, the applications of the two techniques are also quite different which will be discussed in section 1.6.

As in the case for EIT, $\Omega_c >> \Omega_p$, equations (1-20) can be simplified to give:

$$\left|a^+\right\rangle = \frac{1}{\sqrt{2}}\left(\left|2\right\rangle + \left|3\right\rangle\right)$$
$$\left|a^0\right\rangle = \left|1\right\rangle \qquad . \qquad (1\text{-}26)$$
$$\left|a^-\right\rangle = \frac{1}{\sqrt{2}}\left(\left|2\right\rangle - \left|3\right\rangle\right)$$

The configuration of these dressed states is shown in Figure 1-7(a). From equations (1-26) we can see that the ground state is unmodified. If the probe laser is scanned across the bare states |2> and |3>, a modified absorption profile is recorded.

This 3-level system can also be understood using the bare atom approach and considering interference pathways (Figure 1-7(b)). There are different excitation pathways available to the excited state (|1>-|3> or |1>-|3>-|2>-|3>) (and higher order pathways). The coupling laser (which couples states |2> and |3>) has much higher Rabi frequency than the probe and therefore the probability amplitudes for these two pathways are actually quite similar and interference occurs, which on 2-photon resonance leads to cancellation of absorption [10].

Throughout the work presented in this thesis, spectral features created using EIT are characterised by their spectral width and height. The transparency height is defined as the ratio between the EIT feature height and the total height of the Doppler broadened absorption line (both measured from maximum to minimum absorption). The spectral linewidth is characterised by the FWHM of the EIT feature. The linewidth of an EIT feature is defined by the lifetime of the coherence between the uncoupled states |1> and|2>. Experimental conditions can be optimised to minimise this linewidth by reducing the decoherence rate; this is discussed further in section 1.7.1.

1.4.   Saturated Absorption Spectroscopy

An alternative means of obtaining a narrow spectroscopic feature is saturated absorption spectroscopy (SAS), which enables the creation of a Doppler-free dip in an absorption line through velocity-class selection. This sub-Doppler dip is sometimes referred to as a Bennett hole [15] or a Lamb dip [16] after two of the pioneers in this technique. SAS is unlike EIT in that it does not rely on coherence between atomic states; it is described using the population rate equations and can be realised using only a single laser source.
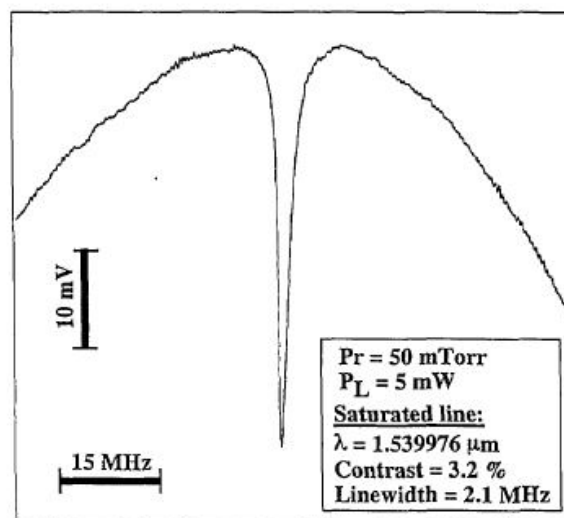
Figure 1-8: *Absorption dip created using saturable absorption technique with linewidth of 2 MHz [14].*

From this single source two beams are derived, a higher power pump and a weak probe beam, which counter-propagate through the gas medium.

In the case where the two fields are at the same frequency, an individual atom, at a velocity v, sees the two fields counter-propagating with opposing Doppler shifts and therefore cannot be resonant with both fields at the same time for a given transition. However, an atom with zero velocity in the plane perpendicular to the propagation of the laser fields sees two fields at the same frequency. On resonance, the pump beam can saturate the absorption of this velocity class by transferring the maximum population (50%) to the excited state so that the counter-propagating probe beam will not be absorbed for this zero velocity class specifically. If the probe laser frequency is scanned across the resonant transition a sub-Doppler dip will be recorded within the Doppler-broadened absorption line. This sub-Doppler feature is centred on the resonant frequency corresponding to the velocity class where the absorption of the probe is inhibited by the pump-induced saturation of the transition. If the pump and probe frequencies are not identical then the Lamb dip will not be in the centre of the absorption line.

SAS was first experimentally demonstrated in acetylene by de Labachelerie *et al.* [14] using a high finesse Fabry-Perot cavity in order to provide a sufficient interaction length for the gas-laser interaction. An example from this reference showing a sub-Doppler feature with a linewidth of around 2 MHz is shown in Figure 1-8. The feature linewidth can be as narrow as the homogeneous power broadened linewidth [2] and therefore sub-Doppler features generated using SAS have been extensively used in laser stabilisation schemes.

1.5.   Other Sources of Dephasing Effects

For coherent experiments the maintenance of the phase relationship is vital. Dephasing effects act to reduce or even completely extinguish coherence by perturbing the phase of the oscillations of individual atoms relative to the phase of the atomic ensemble. In SAS dephasing effects act to reduce the lifetime of the excited state and therefore the height of the sub-Doppler feature. Apart from the linewidth broadening mechanisms discussed in section 1.2.2, there are several other dephasing effects to consider. Two of the most prominent dephasing mechanisms which are relevant to the work in this thesis are additional decay channels out of an excited state which enable radiative coupling to energy levels outside of the interacting system and laser phase fluctuations which contribute to the laser linewidth. These factors can be controlled and minimised through the experimental conditions.

In particular, through the choice of atomic system; stable transitions with simple and understood decay pathways are favourable. The complex ro-vibrational structure of

molecules, which is discussed in the context of acetylene spectroscopy in the Appendix, can mean there are many different dipole-allowed transitions through which molecules in excited states can decay to levels outside of the interacting system and these can act to reduce the coherence.

1.6. Applications

As discussed earlier, the key to frequency stabilisation and metrology applications is a narrow spectral feature which is typically generated using one of the coherent techniques described in the previous section. This section presents a short introduction to these applications through which the need for a narrow spectral feature will become clear.

1.6.1. Slow Light

The potential of EIT as a technique for controlling the group velocity of light pulses was first discussed by Harris *et al.* in 1992 [17]. This potential arises from the steep dispersion in the region of the EIT resonance which is created by the rapid variation of the refractive index of the gas medium. Harris *et al.* predicted a reduction in the group velocity by a factor of 250 for a probe beam centred on resonance travelling through a 10 cm long lead vapour cell. This stimulated a huge amount of research into slow and superluminal propagation of light pulses using EIT.

The magnitude of the pulse delay increases with the dispersion slope on resonance and is therefore maximised for a narrow and large EIT feature. Benchmark experimental results include those of Hau *et al.* in 1999 [18] who recorded a group velocity as low as 17 ms^{-1} using ultra-cold sodium gas in Bose-Einstein condensate form. More recently, EIT has been used to stop and store light for over 1 ms, again using a sodium Bose-Einstein condensate [19]. In this state, thermal diffusion is completely suppressed to achieve localisation of the sodium atoms and therefore minimise decoherence effects, effectively minimising the resonance linewidth.

There are numerous practical applications of slow and stopped light which are driving intense research in this field. These include optical signal buffering and switching in signals processing systems, optical sensors with enhanced sensitivity [20] and quantum information storage [19, 21]. Furthermore, superluminal light propagation holds promise for enhancing sensitivity in interferometer systems [22]. An EIT-based slow and fast light system has desirable qualities, such as ease of delay tuning and large potential pulse delay and advance and is, therefore, a prominent candidate for these applications. This is discussed in more detail, along with an experimental demonstration of the first all-fibre EIT-based slow and fast light system, in chapter 3.

1.6.2.   Atomic Clocks

Coherent techniques have also been extensively used in atomic clock schemes. Atomic transitions provide the ultimate resonances for such schemes because the resonant frequency of the clock is set by the electronic structure of the atom concerned and, as each atomic oscillator should be identical, atomic clocks based on the same atomic transition can be unambiguously compared. It is this feature which renders atomic and molecular transitions as the sole candidates for primary frequency standards. Alkali vapours are particularly favoured due to their simple atomic structure and relatively stable transitions. Alternatives to atomic clocks, such as quartz crystals, have resonant frequencies which depend on the size and shape of the crystal and thus resonant frequencies vary from one artificial crystal to another.

Since the original atomic clock demonstrations, which already demonstrated fractional frequency deviations to the level of 1 part in 10^{10} [23], designs have continued to progress with fractional frequency deviations and long-term stability continuing to improve [24]. Current drives for further progression include improved synchronisation in optical telecommunications networks, astronomical measurements, satellite navigation systems and the desire to test physical laws that are currently considered as invariant with time [25].

The primary time standard at NIST is based on a caesium fountain clock. Caesium is chosen for several reasons, including its heavy mass, which leads to a slower average velocity and therefore longer interaction times with the exciting microwave radiation or laser beam, as well as the relatively high frequency of the transition between its hyperfine states, when compared to other atoms, of 9.2 GHz. The stability of this transition is also essential for the application of caesium as a high quality resonator. A narrow spectral linewidth is achieved through the Ramsey fringe technique [26] in the fountain clock design.

A current trend in the research field of atomic clocks is towards product miniaturisation; there are several applications including GPS systems and telecommunications where the accuracy provided by a primary standard is not necessary [27]. Instead compact, low cost devices with low power consumption and reasonable accuracy are required. Several compact packages based on both rubidium and caesium microwave resonances have been demonstrated with total device volumes of the order of 10 cm^3 [27-29]. Rubidium, like caesium, has been extensively used in atomic clocks throughout their evolution as it also provides stable resonances with suitably high resonant frequencies. The gas-laser interaction in these devices occurs in a gas cell with a volume of the order of a few mm^3. This interrogation of the gas is typically via CPT in order to generate the narrow linewidths required [30]. Miniature devices have demonstrated long term fractional instability of the order of 10^{-12} [27] but the SNR is limited by the nature of the light-atom

interaction volume; the interaction length is small, set by the dimensions of gas cell. This sets a minimum limit on the laser power required to generate a sub-Doppler feature which in turn limits the minimum linewidth of resonance and thus the accuracy of the clock. The possible enhancement of the SNR using an atomic vapour-filled HC-PCF as a miniature gas cell is discussed in more detail in section 1.7.1.

1.6.3. Frequency Stabilisation

Finally, sub-Doppler techniques, in particular SAS, have historically been extensively used for the frequency stabilisation of lasers. Using frequency modulation (FM) spectroscopy [31] a laser frequency can be unambiguously locked to a SAS resonance. Laser stabilisation is of paramount importance for the success of many experimental techniques.

Frequency stabilisation using an atomic or molecular resonance feature is preferable to alternative methods, such as interferometry and Fabry-Perot cavities due to the absolute nature of the resonance [32]. Fundamental vibrational absorption bands of molecular species are typically in the mid-IR region. Therefore to provide suitable resonant features in the optical region, overtone and combination vibrational bands can be used. For example, the $v_1 + v_3$ overtone band of acetylene has been extensively used as a frequency reference in the telecommunications spectral region between 1510 and 1540 nm. Additionally, atomic vapours such as rubidium and caesium provide electronic absorption bands in the near-IR; sub-Doppler features generated using the D-line resonances of rubidium vapour have been used to stabilise lasers operating at 780 and 795 nm.

Doppler-broadened absorption lines can be used in stabilisation schemes, however, the accuracy to which the laser can be stabilised is defined by the linewidth of the spectral resonance and therefore a narrow spectral feature is preferred. For example, in one of the earlier demonstrations of laser frequency stabilisation, Sato *et al.* [33] compared the relative stability achieved using the rubidium D1 Doppler-limited absorption line and a sub-Doppler feature created within the line; stabilisation using the sub-Doppler feature reduced frequency fluctuations by approximately an order of magnitude.

1.7. Quantum and Coherent Optics in HC-PCF

The gas-laser interaction for the coherent techniques discussed in the previous sections typically occurs in a macroscopic gas cell. The role of the macroscopic cell is to confine the gas medium, providing the means to have constant environmental conditions such as gas pressure and temperature and also enabling transport of the gas. Additionally the dimensions of the gas cell can be designed to maximise the gas-laser interaction length. As discussed in section 1.2.2, the dimensions of the gas cell can define the minimum

linewidth of spectral features observed in the cell due to collisions between the confined molecules and the inner cell walls.

Traditionally, the sub-Doppler generation techniques, discussed in sections 1.3 and 1.4, use gas cells with dimensions of the order of a few centimetres in diameter and up to several tens of centimetres in length and so have a reasonably large footprint. Techniques to counteract dephasing due to collisions between the confined molecules and the inner cell walls, such as anti-relaxation wall coatings and the use of a buffer gas have been successfully applied in a variety of macroscopic cells [34]. However, when using these cells, free space input and output coupling is required which can be very sensitive to any mechanical vibrations and easily misaligned, which limits the portability of such devices. Furthermore, in such arrangements the laser beam can only be focussed over a short distance at the beam waist, dependent on the optical components used. This interaction length can be extended by increasing the beam diameter in the waist region, but only at the expense of beam intensity. This compromise between interaction length of the beam with the gas sample and beam intensity limits the SNR of the spectral features observed.

Gas confinement in the core of a HC-PCF provides an alternative to macroscopic cells. Gas-filled HC-PCF has the potential to surpass the portability and compactness offered by macroscopic gas cells while its fibre form provides the means for integration with existing optical components. In this section the advantages and potential disadvantages of using HC-PCF as a gas host are discussed. Following this, some of the outstanding achievements which have been enabled using this interaction scheme are described.

1.7.1.   Advantages and Potential Disadvantages of using HC-PCF as a Host for Gas-Laser Interactions

HC-PCF is an optical waveguide where light is guided within the hollow core with extremely low attenuation, providing the possibility of kilometre-scale interaction lengths (see chapter 2). In the core mode the light is tightly confined to an area of the order of μm^2 and therefore high intensities can be generated even for very modest input laser powers. The remarkable advantage of a gas-laser interaction in such a scheme is elucidated by considering an appropriate figure of merit (FOM) [35],

$$f_{om} = \frac{L_{int} \lambda}{A_{eff}},$$ (1-27)

where L_{int} is the effective constant-intensity interaction length, λ is the vacuum wavelength and A_{eff} is the effective cross sectional area. In Figure 1-9, the FOM is compared for a free space beam, a capillary and two HC-PCFs with different attenuation. For a core diameter of 10 μm, a HC-PCF with an attenuation of 0.3 dB/m has an FOM which is ~10,000 times higher than that of a capillary tube, thus dramatically reducing the threshold power for the observation of non-linear effects such as EIT.
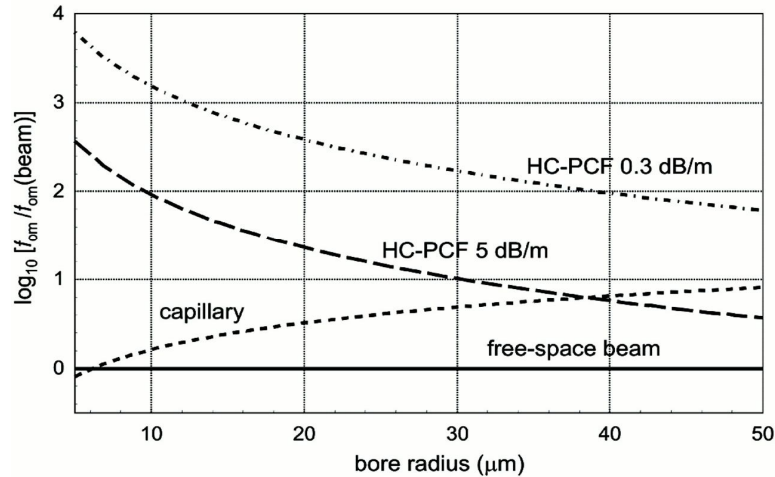
Figure 1-9: *Figure from [35]. Reprinted with permission from AAAS. Calculated using equation (1-27) for light with a wavelength of 532nm. FOM of HC-PCF with attenuation of 0.3 dB/m is four orders of magnitude higher than that of a capillary tube.*

Moreover, the ratio L_{int}/A_{eff} can be directly linked to the SNR of the gas-laser interaction. Therefore, by using a gas-filled HC-PCF, the SNR is dramatically increased, enabling the observation of resonances with extremely small transition dipole moments. For example, in chapter 4, hot band transitions of acetylene are recorded using acetylene-filled HC-PCF. This is remarkable since these transitions have dipole moments 100,000 times weaker than typical atomic vapour transitions [36].

Furthermore, a gas-filled HC-PCF can be integrated in to an all-fibre device known as a photonic microcell (PMC) (see chapter 3). In a PMC, gas is trapped in the core of HC-PCF by hermetic splices at each end of the hollow fibre to standard, all-solid single mode fibre (SMF), providing a compact and portable device which can be integrated into all-fibre systems with complete insertion losses as low as 1.8 dB [37]. The first PMCs were reported by Benabid *et al.* in 2005 [38]. In this paper the authors demonstrated the first all-fibre laser stabilisation scheme using an acetylene-filled PMC. The PMC fabrication technique has since been further expanded to enable the fabrication of extremely low pressure gas cells [37]. Prior to this demonstration, low pressure cells (<1 bar) were difficult to fabricate due to entry of contaminants from the atmosphere during the splicing process. In the advanced technique, helium is loaded into the fibre at a pressure of ~ 2 bars after filling the HC-PCF with the low pressure gas which is ultimately required and before the HC-PCF is removed from the vacuum system for splicing. Through this over pressurisation, contaminant entry during splicing is inhibited for a limited period of time (~30 s depending on core size) enabling a low loss splice to be formed. After the gas-filled PMC is sealed, the helium can permeate through the silica fibre cladding back into the atmosphere, over a typical time period of ~ 7 hours. EIT and SAS have been demonstrated using low pressure acetylene-filled PMCs [39].

The micron scale transverse confinement provided by HC-PCF does have some disadvantages which have to be addressed in order for this gas-laser interaction scheme to fulfil its potential. The most relevant for sub-Doppler feature generation is the increased confinement of the gas. As gas pressure in the fibre core is decreased, the mean free path of the gas becomes comparable and then larger than the core diameter. This means that dephasing effects due to collisions between the confined molecules and the inner core walls of the fibre are a significant and limiting contribution to the linewidth of sub-Doppler features generated in gas-filled HC-PCF.

Based on the hard-sphere model, this dephasing rate, γ_{walls}, can be calculated using the expression [40],

$$\gamma_{walls} = \frac{2.405^2 \, D}{R_c^2} \left(\frac{1}{1+cK} \right), \tag{1-28}$$

where c is 6.8 in the limit of the hard-sphere regime and R_c is the core radius. D is the self-diffusion co-efficient given by [41],

$$D = \frac{1.86 \times 10^{-22} \, T^{3/2}}{P\sigma^2 \sqrt{M_W}}, \tag{1-29}$$

where P is the gas pressure (Pa), M_W is the molecular weight, T is the temperature and σ is the collision cross section. Finally, K is the Knudsen number,

$$K = \frac{\lambda_{fp}}{R_c}, \tag{1-30}$$

where the mean free path, λ_{fp}, is given by the expression

$$\lambda_{fp} = \frac{k_B T}{\sqrt{2} \, \pi P \sigma^2}. \tag{1-31}$$

Using these expressions, the dephasing rate is plotted in Figure 1-10 for acetylene gas at room temperature confined in cylindrical gas cells with diameters of 10 μm, 3 mm and 1 cm. The pressure broadening rate is also included. This clearly identifies that the dephasing rate due to collisions between the confined molecules and the inner core walls of the fibre is the dominant broadening mechanism at low pressures. This effect limits the achievable Q-factor (equation (1-10)) of the gas-laser interaction in HC-PCF. However, as described by equation (1-11), the overall parameter which defines the quality of the gas-laser interaction is the product of the Q-factor and the SNR. Due to the extremely high SNR which is made possible by the extremely long interaction length offered by gas-filled HC-PCF, this overall product can still be large.
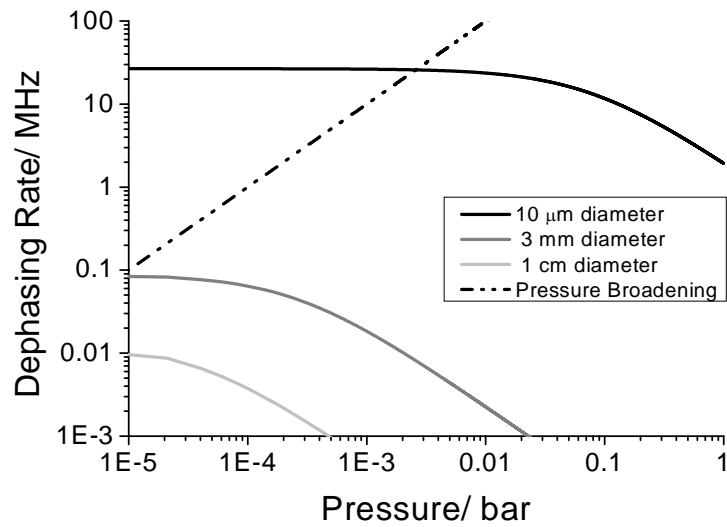
Figure 1-10: *Dephasing rates due to collisions between confined acetylene molecules and inner walls of cell for three different diameter gas cells. Dephasing due to pressure broadening is also plotted for comparison.*

From equations (1-28) and (1-30) it is clear that, at low pressures, the wall dephasing rate is $\sim \propto R_c^{-1}$. Therefore, in order to reduce the dephasing rate larger fibre cores are required. This desire has partially motivated the fabrication of large-pitch fibres. Details on the fabrication of large-pitch fibres can be found in chapter 2. Experimental results elucidating the effect of fibre diameter on sub-Doppler features are presented in chapter 4 and a technique for integrating large core fibres into PMC form is described in chapter 5.

A second consideration of using gas-filled HC-PCF is the large ratio between the core diameter (microns) and the fibre length (metres). This needs to be considered when loading the fibre with gas. In the experiments described in this thesis, the HC-PCF ends are mounted in vacuum chambers (brass or steel) attached to a vacuum system. This enables effective evacuation of the HC-PCF and subsequent loading with gas-phase material.

Equation (1-30) introduced the Knudsen number K; this can be used to qualify different gas flow regimes [41]. If the gas pressure is large, then λ_{fp} is much smaller than the core radius and therefore $K<<1$. In this regime, collisions between the molecules contribute to the flow dynamics; this is known as the hydrodynamic regime. $K\sim 1$ when $\lambda_{fp} \sim R_c$ which, in the case of acetylene-filled, 10 µm core diameter HC-PCF at room temperature, corresponds to a gas pressure of $\sim$ 17 mbar (using $\sigma = 3.3 \times 10^{-10}$ m [42] and equation (1-31)). Therefore, at pressures above 17 mbar, the acetylene gas dynamics enable loading of the HC-PCF through use of a differential pressure gradient at each end of the fibre as collisions between the gas molecules will cause diffusion into the fibre core. At pressures

below this value and for $K>>1$, the gas dynamics are described by the molecular flow regime. In this regime the gas is too rarefied for the loading technique described above; this is the case when loading atomic vapours such as rubidium and is described in chapter 7.

Finally as HC-PCF is an optical waveguide, the specific modes supported and guided by the fibre need to be considered. In particular, surface modes, which are localised in the glass core-surround can be supported by some HC-PCFs. The interaction of surface modes with the fundamental modes of the fibre can degrade the fibre transmission. This discussion is developed further in chapter 4. Also, HC-PCFs are rarely single mode; typically a fundamental mode (with two polarisation states) is strongly favoured and easily excited with appropriate coupling. However, the multimode nature of some HC-PCFs, in particular larger core fibres cannot be ignored when analysing their properties (see chapter 5).

1.7.2.   Progress in Quantum Optics in Gas-filled HC-PCF

In the previous section the advantages of HC-PCF as a host to a gas medium for highly efficient gas-laser interactions were discussed. The first experimental demonstration which exploited these exceptional qualities was published by Benabid *et al.* in 2002 [35]. These authors reported stimulated Raman scattering in hydrogen gas using pump pulses with energies two orders of magnitude lower than those used previously, enabled through use of a hydrogen-filled HC-PCF. This work elucidated the new paradigm of gas-laser interactions in HC-PCF and stimulated further work in this field.

In particular, using gas-filled HC-PCF has enabled observation of quantum optic effects such as EIT in acetylene [43, 44]. These were benchmark achievements as prior to these experiments EIT in a molecular gas had not been observed due to the extremely low transition dipole moment of molecules (~1000 times smaller than for an alkali vapour) and therefore the need for an extremely high intensity coupling beam to achieve a sufficiently high coupling Rabi frequency for EIT. Furthermore, Ghosh *et al.* [43] used EIT in an acetylene-filled HC-PCF to delay a pulse of probe light by up to 800 ns in only 1.3 metres of fibre. Development of an all-fibre slow and fast light system using EIT in acetylene-filled PMC is described in chapter 3.

In parallel to these endeavours, multi-octave frequency comb generation using stimulated Raman scattering was demonstrated in hydrogen-filled HC-PCF [45] and the mutual coherence of such a comb was extensively studied [46]. The demonstration of such a broadband frequency comb was enabled by developments in the fabrication of alternative HC-PCFs, in particular large-pitch Kagome lattice HC-PCF. Kagome HC-PCF provides a much larger transmission bandwidth than photonic bandgap (PBG) HC-

PCF enabling the guidance of comb lines over an octave span. Such a coherent frequency comb has potential applications in optical waveform synthesis [45].

Most recently, there has been significant interest in rubidium-filled HC-PCF [47, 48]. Several vapour loading techniques, such as light induced atomic desorption and light induced drift, have been demonstrated [47-49]. As explained in a section 1.6.2, rubidium atoms are used as oscillators in atomic clocks and a current trend in atomic clock development is towards more compact and portable designs. A rubidium-filled HC-PCF is an excellent candidate for such a requirement, in particular in PMC form. Progress towards the development of a rubidium-filled PMC is reported in chapter 7.

1.8.   Summary

This chapter has introduced the means to describe the resonant characteristics of an ideal oscillator. In particular, the linewidth of a resonant feature in a gas medium was highlighted as critically important for applications such as frequency stabilisation and metrology. Techniques for creating narrow sub-Doppler features within absorption lines were introduced which are used throughout this thesis.

Gas-filled HC-PCF, in particular in PMC form, was presented as a candidate for a compact, portable and easily integrated gas cell. In the next chapter, the key properties of HC-PCF are introduced and improved fibre designs which have applications as hosts for coherent gas-laser interactions are presented.

Chapter 2

Hollow Core-Photonic Crystal Fibres

This chapter introduces the key properties and guidance mechanisms of two of the most common types of HC-PCF. State-of-the-art HC-PCFs are presented, double photonic bandgap HC-PCF and large-pitch HC-PCF, where the author has made a significant contribution in the fabrication process. The work on the former is published in reference [50].

2.1. Introduction

Optical fibres are used for a variety of applications including telecommunications and interferometry. The most 'conventional' fibres are silica glass fibres, first developed in the 1960s, they confine light to a core at the centre of the fibre by total internal reflection; i.e., the fibre core has a higher refractive index than the surrounding cladding. The refractive index contrast is created through dopant addition to the core and/ or the cladding region. The extremely low attenuation of these fibres (0.1484 dB/km at 1550 nm [51]), combined with their relatively low cost, means they are now used extensively in the telecommunications industry.

Guidance in an air or vacuum core is not possible using total internal reflection because a cladding material with a lower refractive index than air is not available. There are many reasons why such a fibre is desirable. Conventional all-silica optical fibres have reached their minimum attenuation level which is set by a fundamental limit: Rayleigh scattering ($\propto \lambda^{-4}$) from the small refractive index variations which arise from density fluctuations in the glass. Guidance within an air core provides the potential to overcome this, provided there is a confinement process which can truly confine light in a core region. Furthermore, conventional fibre cores are formed from silica which is only optically transparent between approximately 0.4 and 3 μm [52], limiting their range of operation. Guidance within an air core can potentially increase the low loss window and enable guidance in the UV and the mid- to far-IR. Crucially, guidance in an air core increases the threshold intensity for the onset of heating and nonlinear effects which can occur at high powers in silica core fibres and therefore degrade transmission.

A further motivation for the fabrication of hollow core fibres is the possibility of loading the hollow core with gases or liquids and thus providing a novel regime for the simultaneous confinement of both light and fluid over distances of many metres or even kilometres; creating a new paradigm for gas-laser interactions with applications from quantum optics to gas sensing. Through this idea, guidance in a gas- or liquid-filled hollow core opens up the possibility of optical guidance in a whole new range of materials compared to the core materials dictated by total internal reflection.

There have been several demonstrations of air core fibres. Metallic and dielectric hollow tube waveguides were one of the earliest examples and losses down to 1.85 dB/km at 1.0 μm were predicted for a 1 mm core diameter, silica waveguide [53]. However, the bend loss in such fibres is too large to be implemented in practical applications and coupling into the lowest loss mode is challenging using such a large core fibre. Additionally, attenuation of these waveguides scales inversely to the cube of the radius and therefore low loss guidance and a micron scale core cannot be simultaneously achieved.

A later example is the Bragg fibre which was first proposed by Yariv and Yeh [54] who extended the concept of a one dimensional Bragg waveguide to cylindrical fibre form; coherent Bragg scattering from alternating layers of different refractive indices and thickness can confine light within an air core. Following this work, there have been several experimental examples of these fibres. Fink *et al.* [55] reported such a fibre, fabricated from alternating micron thick layers of polystyrene and tellurium, which operates over a wide range of wavelengths. The resulting cladding structure reflects incident radiation for any angle of incidence, leading to this fibre being called an 'OmniGuide' [55]. OmniGuide fibres have since been thoroughly theoretically investigated [56] and extremely low losses have been predicted. The best loss performance so far is 1 dB/m [57] for a fibre with a fundamental bandgap at 10.6 μm. This fibre has facilitated a breakthrough in CO_2 laser beam delivery for surgical applications [58]. However, the attenuation and bend loss is increased significantly at shorter wavelengths using this fibre design.

With the advent of HC-PCFs, low loss guidance within an air core with a micron-scale diameter was realised. A HC-PCF has a transverse cross-section formed by a periodic arrangement of air holes defined by a silica web which is invariant along the fibre length. The concept for these fibres was first proposed by Russell in 1991 [59] and stemmed from concepts of bandgap formation in photonic crystal structures; the fundamental idea was to design a fibre cladding structure based on a two dimensional photonic crystal which would exhibit a photonic bandgap (PBG). A PBG defines a range of frequencies for which modes of a certain longitudinal propagation constant, β, cannot propagate. Russell [59] postulated that the introduction of a defect (a core) into such a cladding
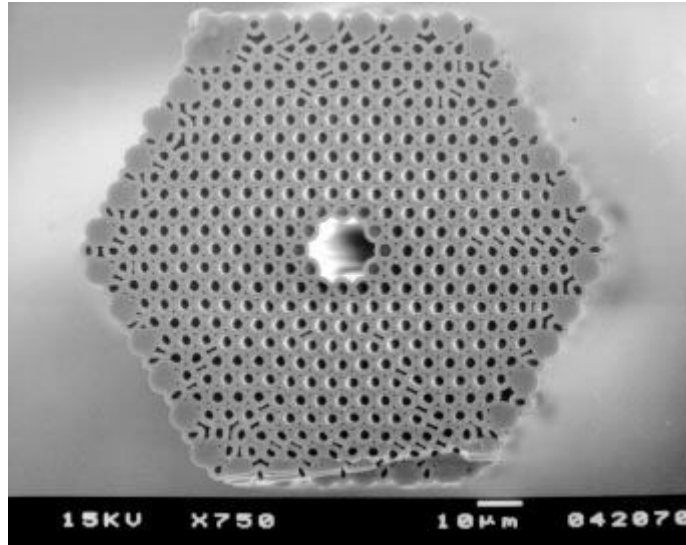
Figure 2-1: *Scanning electron micrograph (SEM) of the first HC-PCF, fabricated by Cregan et al. in 1999 [60]. Cladding pitch is 4.9 μm, core diameter is 14.8 μm and air filling fraction is 39%. From [60]. Reprinted with permission from AAAS.*

structure, which supports such modes at frequencies within the PBG, could lead to low loss guidance.

Before the demonstration of HC-PCF, several breakthroughs were reported in the fabrication of PCF. The first solid core PCF was fabricated in 1996 by Knight *et al.* [61] and guided via total internal reflection. This fibre was later shown to confine light in a single mode at all wavelengths for a well-defined range of structural parameters [62]. The first solid core PBG-guiding fibre was demonstrated by Knight *et al.* in 1998 [63] where the light was confined around the outside of a hole which formed an intentional defect in an otherwise periodic honeycomb lattice. The first HC-PCF, based on a triangular lattice cladding is shown in Figure 2-1 and was fabricated shortly after in 1999 [60].

These initial demonstrations stimulated significant research into the design of PCF structures and now we can distinguish two broad classes of HC-PCF which were first classified by their physical and optical properties, and later, by their guidance mechanism. The first group, similar to the early demonstrations of HC-PCF, guide through a full photonic band gap in the photonic modes of the cladding. The second group are classified, in this thesis, as 'large-pitch' HC-PCFs. The most notable example of this class is the Kagome lattice fibre which was first reported in 2002 by Benabid *et al.* [35] and whose guidance mechanism was elucidated by Couny *et al.* [45].

All the HC-PCFs used in this thesis are fabricated from pure silica glass alone (Heraeus-Tenevo F300) using the stack and draw technique and a fibre drawing tower. In the first stage of the fabrication process, a thin-walled silica tube with a diameter ~ 25 mm (inner diameter (ID)/outer diameter (OD) ~0.93) is drawn into ~ 1 mm diameter capillaries

which are cut to ~ 1 metre in length. These capillaries are placed by hand into the arrangement required. Typically this is a hexagonal structure. The core defect is formed by the omission of some capillaries from the structure and for some fibre designs the core shape can be supported by insertion of a core tube. This 'stack' is then inserted into a large silica cylindrical tube (the stack 'jacket'), both to increase the stack strength and to control the final fibre diameter and then fused and drawn down through the furnace to the intermediate cane stage. Canes are typically a few millimetres in diameter. The canes are then re-jacketed and drawn into fibre. During the fibre drawing stage it is usually necessary to pressurise the core, cladding and the interface between the cane and jacket separately to control surface tension effects. The furnace temperature and draw speed are also carefully controlled. The fibre is coated with a UV-cured polymer before collection to maintain the mechanical strength and integrity of the fibre. Through this process, many kilometres of fibre can be produced from a single stack.

In the two following sections the guidance mechanisms relevant to PBG and large-pitch HC-PCFs are described. State-of-the-art examples of both types of fibre are then presented in the final part of this chapter.

2.2. Photonic Bandgap Guidance

The first class of HC-PCFs use a PBG in the fibre cladding to confine light within an air core. The cladding structure is designed for an 'out-of-plane' PBG in the transverse plane, perpendicular to the axis of propagation. An out-of-plane PBG describes the existence of a PBG which, for a given propagation constant β ($\beta = kn_{eff}$, where n_{eff} is the effective index and k is the vacuum wave-vector) and frequency ω, supports no optical modes. This means that light entering such a cladding structure (within the given range of frequencies and effective indices) will be exponentially attenuated instead of guided. The most common cladding design for PBG HC-PCFs is the triangular-lattice arrangement (demonstrated by the cladding structure of the HC-PCF in Figure 2-1). Advances in the understanding of the PBG guidance mechanism, in particular the role of individual resonators in the cladding structure, have enabled the fabrication of extremely low loss fibres. The minimum attenuation achieved so far is 1.2 dB/km at 1550 nm [64] and the typical bandwidth of the low loss transmission window is ~30 % of the central transmission wavelength.

Several models have been used to explain the transmission characteristics and modal properties of hollow fibres. The work of Yariv and Yeh on Bragg fibres led to the development of the ARROW (Anti-Resonant Reflecting Optical Waveguide) model [65, 66]. This model considers a cladding material formed by a low index background material with high index inclusions. The key finding is that for values of pitch, $\Lambda > \lambda$, the spectral properties of such a material are mainly determined by the thickness of the high index

layers and the refractive index contrast; there is little sensitivity to the cladding pitch [66]. This model lead to the idea of considering the high index inclusions as optical resonators whose modal properties form the bandgap [67]. Birks *et al.* [68] advanced this with a semi-analytical description related to the cellular method in solid state physics and applicable to solid core PCF. In contrast to the ARROW model, their model considers the size of the low index regions which separate the high index inclusions and thus comprehends their effect on the width of cladding pass bands [68]. In parallel, several numerical solutions have also been developed [69].

The application of these models to HC-PCF is not straightforward as it is not simple to identify and single out the key resonators within the cladding structure of the fibre. Recently, Couny *et al.* [67] developed an intuitive model to explain the formation of photonic bandgaps, which is analogous to the tight binding model (TBM) that is used in solid state physics to explain the existence of allowed and forbidden electronic bands [70].

In the TBM, the amalgamation of the localised electron wavefunctions of isolated and identical atoms with distinct electronic structure is considered as the atoms are brought spatially closer. When the atomic orbitals of neighbouring atoms begin to overlap, each single atomic state splits to form a band of extended wavefunctions (Bloch modes) [71]. This results in the formation of allowed electronic bands and conversely, the existence of forbidden bands of the crystal structure. In each allowed band the highest energy mode (the bound mode) is anti-symmetric and the lowest energy mode (anti-bound) is symmetric; the latter corresponds to the case where adjacent wavefunctions have the same sign [71].

This concept can be transferred to the HC-PCF platform by identifying the key resonators of the cladding structure. In [67] the authors theoretically and experimentally highlight three key resonant features of the HC-PCF cladding structure which define the bandgap characteristics; 'strut' modes, 'apex' modes and 'airy' modes. The resonant features are used to develop a photonic analogy to the TBM, the photonic tight binding model (PTBM), which provides an intuitive and predictive tool for the description of PBG formation. The PTBM can be then be used to explain some of the salient features of HC-PCF.

For example, using the ideas of the TBM, the glass apexes in the cladding structure can be considered as analogous to the individual atoms in a crystal structure. When treated as isolated high index resonators each apex has a distinct set of modes in which light can be propagated through total internal reflection. This situation is illustrated in Figure 2-2(a) [70] where the dispersion of the fundamental and second order modes of an isolated silica glass rod (n_{glass} =1.45) are plotted. Considering an array of such rods which are brought spatially closer (equivalent to decreasing the fibre pitch), cladding photonic
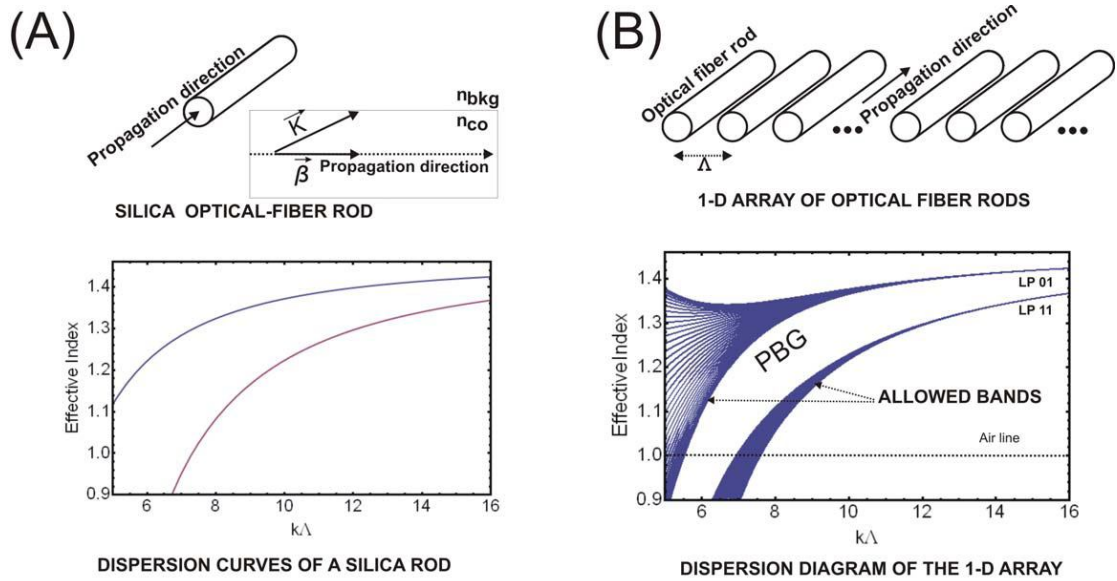
Figure 2-2: *(a) Dispersion of the fundamental and second order modes of an isolated silica rod and (b) dispersion diagram of an array of coupled silica rod. Modes below the air line are neglected for clarity [70].*

bands are formed due to the increased modal overlap between the equivalent modes assigned to the neighbouring apexes [67, 70]. These cladding bands are linear, superpositions of the modes of the individual apexes in the cladding structure. The resultant cladding bands, considering only nearest neighbour coupling between the glass rods, are plotted in Figure 2-2(b). It is clear that the formation of these cladding bands conversely leads to a formation of a forbidden band, the PBG.

Figure 2-3(a) shows a typical density of photonics states (DOPS), calculated for a triangular lattice cladding with an air filling fraction of 91.9 % (Figure 2-3(a) inset) [67]. The DOPS indicates the number of cladding modes present for a given effective index and normalised frequency. Black regions indicate zero density of states and the density of cladding modes is indicated in greyscale, where white indicates the maximum number of modes. The PBG is clearly defined between two cladding bands. The apex and strut resonators are highlighted in the simulated cladding structure shown in Figure 2-3(b). The calculated fields of the apex, strut and airy modes which define the upper and lower frequency edges of the PBG are displayed in Figure 2-3(c), (d) and (e) respectively and their trajectories are highlighted in colour on the DOPS.

The DOPS can be understood by application of the PTBM. Firstly, considering the cladding band which defines the lower frequency edge of the PBG; in [67] the source of this band is identified as the apex resonators. It is clear that as the cladding pitch is decreased, the increased spatial overlap of the apex modes leads to the hybridisation of the modes of the individual apexes into the allowed bands of the cladding. Furthermore,
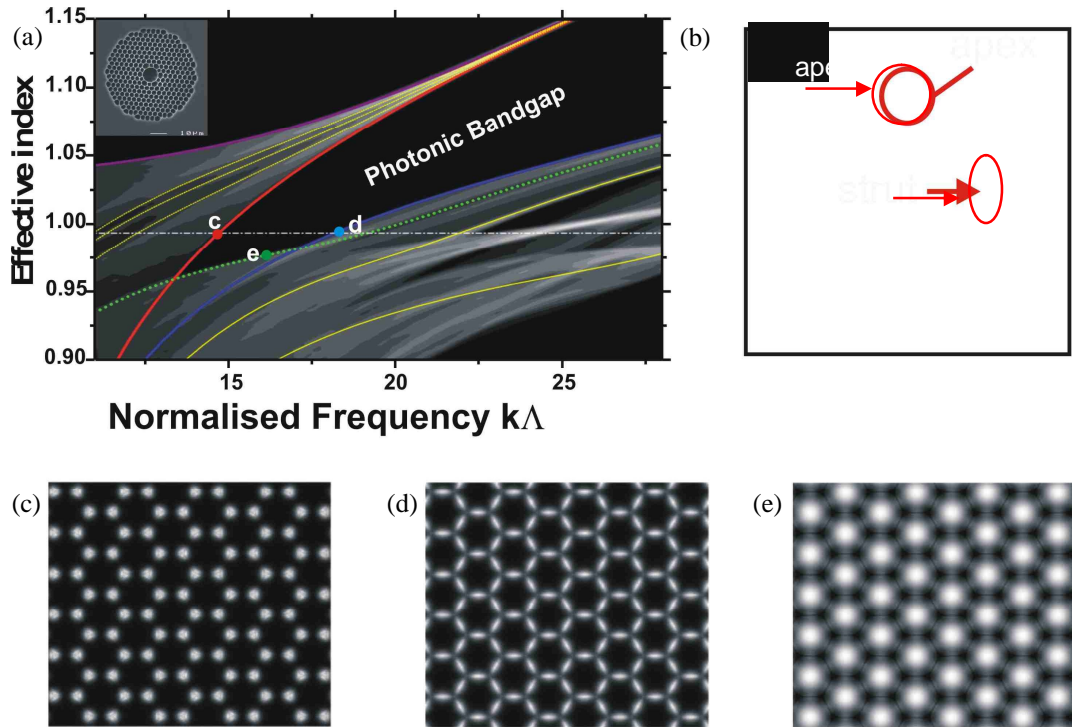
Figure 2-3: *Modified from [67]. (a) Density of photonic states (DOPS) calculated for a cladding structure with a 91.9% air-filling fraction (shown inset). Apex, strut and airy modes which define the bandgap are highlighted by red, blue and green dash lines respectively. (b) Simulated structure of fibre used to generate DOPS, strut and apex resonators are highlighted. Calculated mode profiles of apex, strut and airy modes are shown in (c), (d) and (e) respectively.*

this can explain the effect of changing the cladding pitch on the position of the band gap at the air line; as the pitch is decreased the overlap increases which increases the allowed cladding bandwidth, thus decreasing the PBG width and shifting it to shorter wavelengths with less spatial extent [67]. Alternatively, as the cladding pitch is increased, reducing the spatial overlap between modes, the cladding band dispersion tends towards the limit of an isolated apex resonator. Finally, this band is formed from anti-symmetric and symmetric modes and the highest effective index mode is a symmetric mode which is known as the fundamental space filling mode and indicated in purple in Figure 2-3(a). The highest energy anti-symmetric apex mode defines the lower frequency edge of the PBG.

The upper frequency edge of the PBG is more complex and is defined by the interplay between the strut and the airy modes (Figure 2-3(d) and (e)). It is clear that the dispersion of these modes defines the size and depth of the photonic bandgap. Understanding the origin of the modes which define the bandgap width and depth is paramount to the fabrication of HC-PCF with higher order bandgaps as discussed in the section 2.4.1.

2.3. Kagome Lattice HC-PCF

The second class of HC-PCFs considered in this thesis are large-pitch fibres, such as Kagome lattice HC-PCF. A typical triangular lattice PBG fibre has a ratio between the cladding pitch Λ and the central guided wavelength λ of ~2. In contrast this ratio can be between ~8 and ~30 for large pitch Kagome lattice fibres [72]. An SEM of a 1-cell Kagome fibre is shown in Figure 2-4: instead of a triangular lattice cladding, the silica matrix forms a Star of David structure. The first example of Kagome HC-PCF was reported in 2002 [35] and the design was extended to the truly large pitch regime in [73].

Kagome fibre does not guide via a photonic bandgap in the photonic modes of the cladding structure, instead regions of low loss guidance are associated with a low density of photonic states in the cladding. The Kagome fibre, therefore, provides low loss guidance through a different mechanism; one which enables cladding and core modes to be simultaneously be supported with extremely similar effective index and normalised frequency but without extremely leaky guidance.

Some insight into the guidance mechanism can be gained through an analogy to Bragg fibres; this is highlighted using Figure 2-4. In this figure, the cladding rings of a Kagome HC-PCF are highlighted in red and form an air-silica Bragg fibre (in the absence of the connecting silica bridges) under the assumption that each cladding ring has an identical thickness. From the transverse resonance condition [74], the low transmission losses can be predicted to be at wavelengths, λ, between,

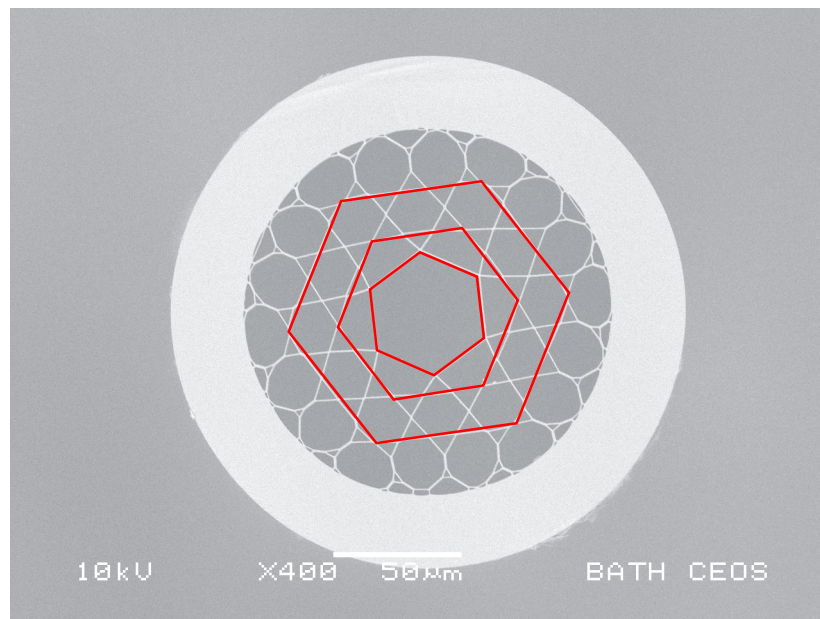$$\lambda = \frac{2t\left(n^2 - 1\right)^{\frac{1}{2}}}{m},$$

(2-1)

Figure 2-4: *An example of 1-cell Kagome lattice HC-PCF. Cladding rings are highlighted in red to elucidate the similarity between this fibre and Bragg fibre.*
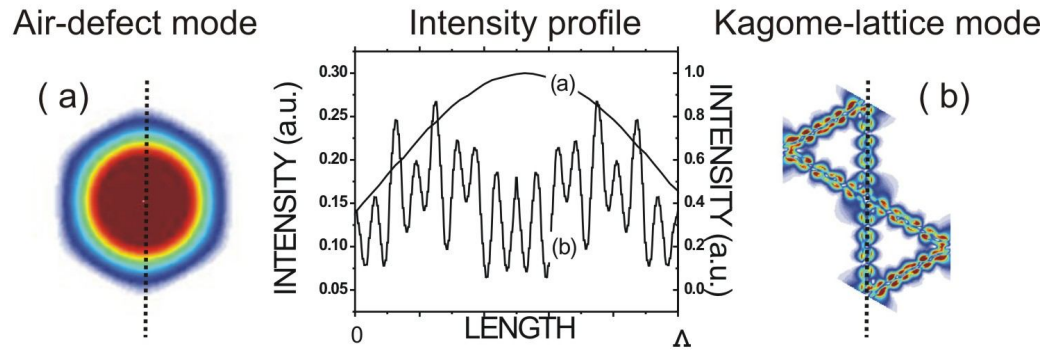
Figure 2-5: *(a) Core mode (b) silica cladding mode, from [45], reprinted with permission from AAAS. The negligible overlap between the transverse phase of the two modes is also shown. Middle segment highlights the phase mismatch between the fast oscillating cladding mode (b) and core confined mode (a) which contributes to the inhibited coupling and enables low loss guidance.*

where *m* is the mode order, *n* is the glass index (~1.45) and *t* is the strut thickness. This simple picture is, however, complicated by the need for mechanical support for the cladding rings in a realistic fibre design in the form of connecting struts. These struts can provide additional sources of loss.

Until recently the nature of the low loss guidance of Kagome HC-PCF was not well understood. The mechanism of the 'inhibited coupling' between core and cladding modes has now been explained by a mechanism analogous to Von-Neumann-Wigner quasi-bound or bound states (core modes) within a continuum (cladding modes). This mechanism enables the coexistence of the core and cladding modes with minimal interaction [45].

The coupling strength between two modes such as a core mode and a cladding mode depends on the spatial overlap of the modes as well as the phase mismatch between the modes. The physical nature of the inhibited coupling can, therefore, be explained by two factors. Firstly, very small spatial overlap between the core modes and cladding modes; the cladding modes in the Kagome lattice in the regions of low attenuation are constrained in the silica and decay evanescently into air. Secondly, large transverse phase mismatch between the fast oscillating cladding modes and the slowly oscillating core modes (highlighted in Figure 2-5). These two factors combine to diminish the overlap integral between the core and cladding modes, enabling low loss guidance over a broad bandwidth.

Large-pitch Kagome fibres have been fabricated with an extremely large, octave spanning bandwidth, but the current minimum attenuation is still higher than that of PBG fibres, especially in the near-IR. However, it is believed that the ultimate low loss that has been achieved in PBG fibres is limited by light scattering from surface capillary waves which are frozen into the silica surface during the fabrication process [64]. In Kagome HC-PCF, the fraction of the core mode which overlaps with the glass surround is extremely

small [72] so it may be possible to ultimately reach lower attenuations using this fibre structure due to a reduced sensitivity to surface roughness.

Furthermore, the large pitch of the Kagome cladding structure means that correspondingly large core diameters are feasible. So far, Kagome HC-PCFs with core diameters up to 80 µm have been fabricated. As described in chapter 1, the tight confinement of gas molecules in the core of a HC-PCF leads to a decoherence rate which scales inversely with core radius. Therefore, these large-pitch fibres provide the means to reduce decoherence effects in gas-laser interactions in HC-PCF. This is further discussed in chapters 4 to 7.

2.4. State-of-the-art HC-PCF

There are several drivers which are currently pushing fibre design and fabrication techniques forwards. These include the desire for low loss guidance over a broader transmission bandwidth [45, 72, 75], control over the modal characteristics of the fibre [76-78] (including extinction of surfaces modes and polarisation management) and quicker and simpler fabrication techniques [79]. In the following sections, developments in two examples of state-of-the-art fibres are described.

2.4.1. Double Photonic Bandgap Fibre

Through the development of large-pitch fibres such as the Kagome lattice fibre the desire for HC-PCF with broadband guidance has been partially satiated. However, even though the attenuation achieved in such fibres has recently been reduced (see section 2.4.2), the cost of the broadband guidance is still an increase in attenuation of up to 2 orders of magnitude at 1550 nm. In the work described in the present section, the triangular lattice PBG cladding design was modified, using insight from the PTBM, to enable low loss guidance in a higher order bandgap.

The possibility of guidance in a higher order bandgap is indicated in Figure 2-3(a) where, at a normalised frequency $k\Lambda \sim 22$, a second bandgap closes just above the air line. As explained in section 2.2, three resonators have been identified in the triangular lattice PBG cladding [67]; controlling the size of these cladding features alters the widths and the depths of the PBGs, indicating that, with correct parameters, the second bandgap can be opened up so that it extends below the air line [50].
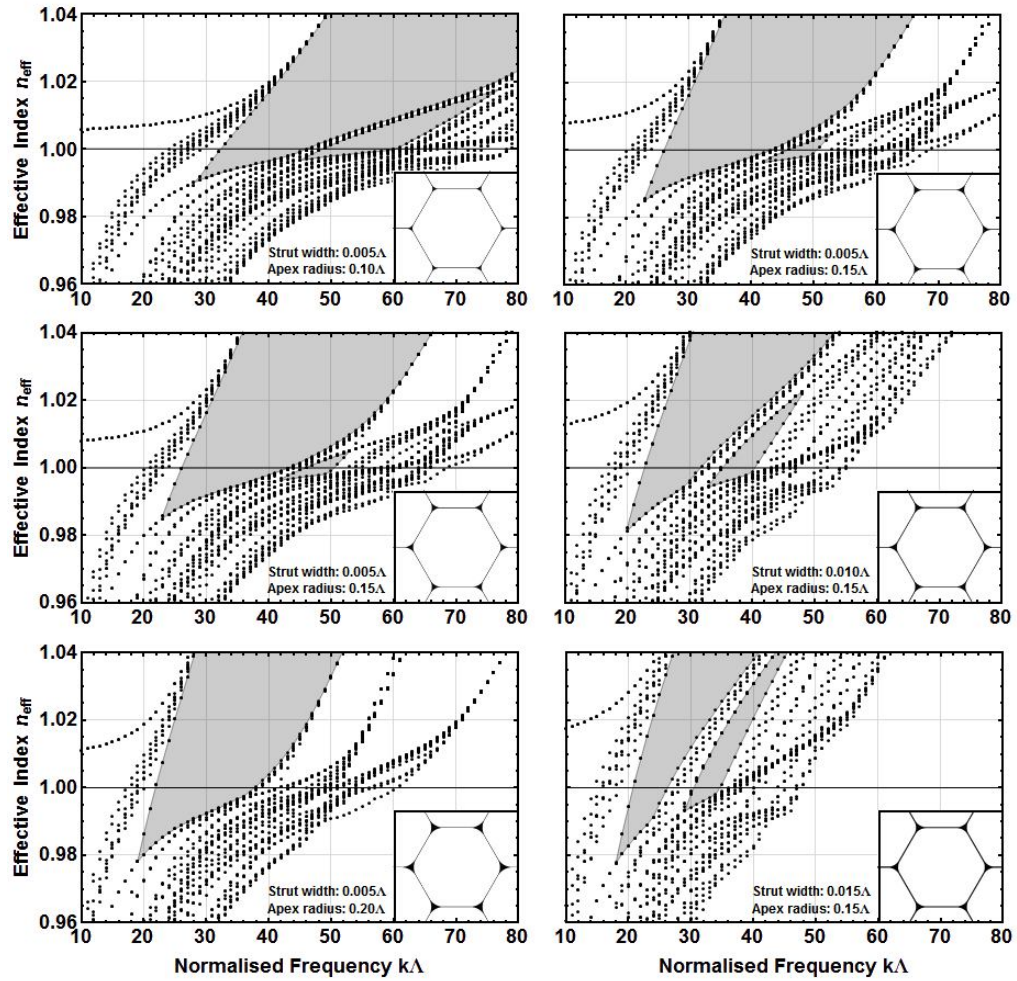
Figure 2-6: *Effective indices of cladding modes calculated at high symmetry points for six structures. Left: constant strut thickness 0.005Λ and varying apex curvature radius of (top) 0.10Λ, (middle) 0.15Λ and (bottom) 0.20Λ. Right: constant apex curvature 0.15Λ and varying strut thickness of (top) 0.005Λ, (middle) 0.010Λ and (bottom) 0.015Λ. The locations of bandgaps that cross the air-line are shaded; the horizontal line represents the air-line [50].*

During the fibre fabrication procedure the strut thickness and the apex size can be controlled approximately independently and therefore to find the parameters suitable for higher order bandgap guidance different cladding structures were generated by adjusting these values. Strut thicknesses t from 0.005Λ to 0.015Λ and apex curvatures r (defined as the radius of an arc which meets the struts tangentially to form the apex) from 0.1Λ to 0.15Λ were investigated using the finite element method for a cladding design with an air filling fraction of ~97%. The effective index of the cladding modes is plotted against normalised frequency for six different structures in Figure 2-6.

Figure 2-6 shows that the widest fundamental bandgap was achieved using a cladding structure with thin struts and large apexes. The width of the higher order bandgap was found to be largely insensitive to the strut thickness but favoured small apexes; therefore a compromise was required to gain optimum bandwidth in both bandgaps
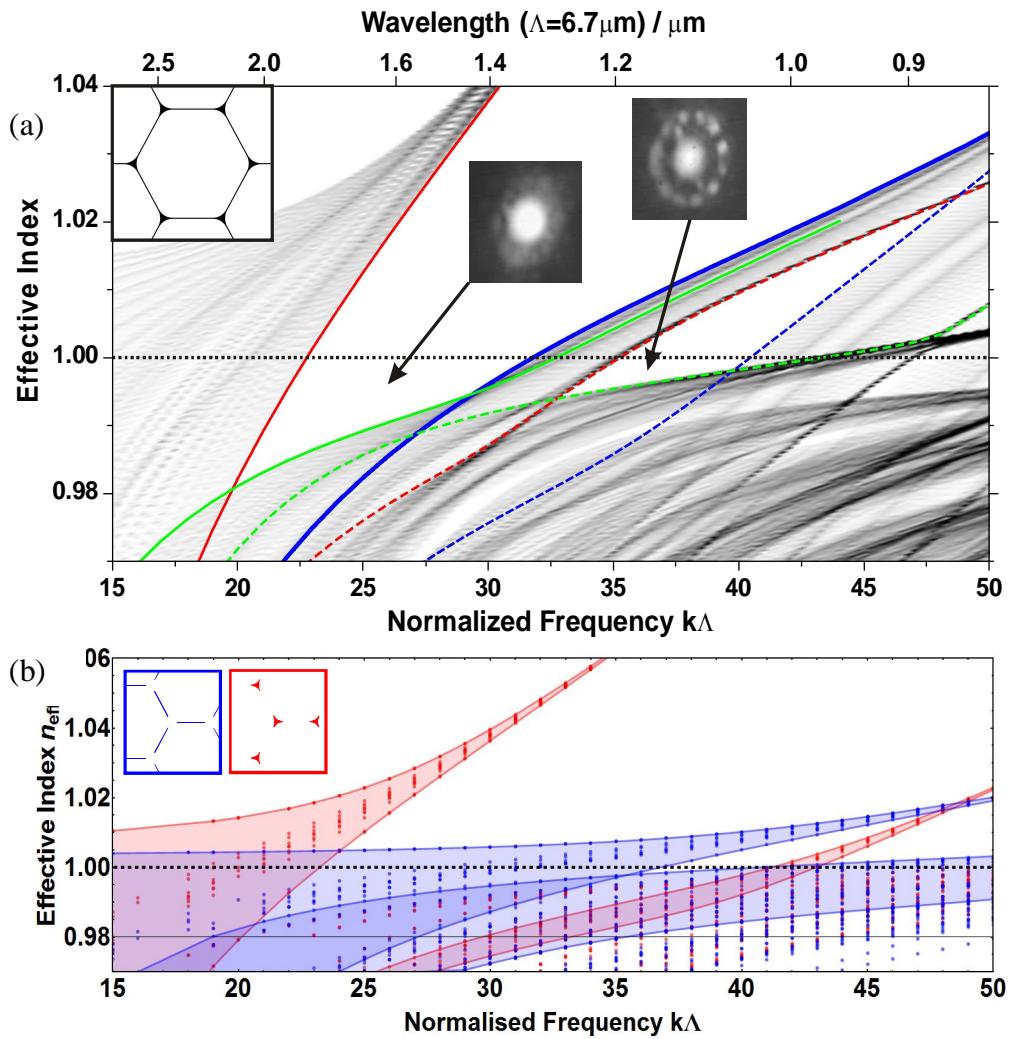
Figure 2-7: (*a) DOPS for optimised cladding structure with strut thickness equal to 0.01 Λ and apex curvature of 0.15Λ. Experimentally recorded near fields for each bandgap are shown inset, together with the modelled cladding structure. (b) DOPS with apex and strut bands distinguished in red and blue respectively.*

simultaneously. This compromise was achieved for a strut thickness equal to 0.01Λ and an apex curvature of 0.15Λ and a fibre with these parameters was chosen for fabrication. The calculated DOPS of this structure is shown in Figure 2-7(a). The cladding modes highlighted in colour indicate the modes which define the bandgap edges. To highlight the role of the key resonators in bandgap formation the apex and strut bands are distinguished in Figure 2-7(b). From this figure, the overlap between these bands is apparent and it is postulated that the repulsive interaction between the non-orthogonal modes opens up the photonic bandgap below the air line.
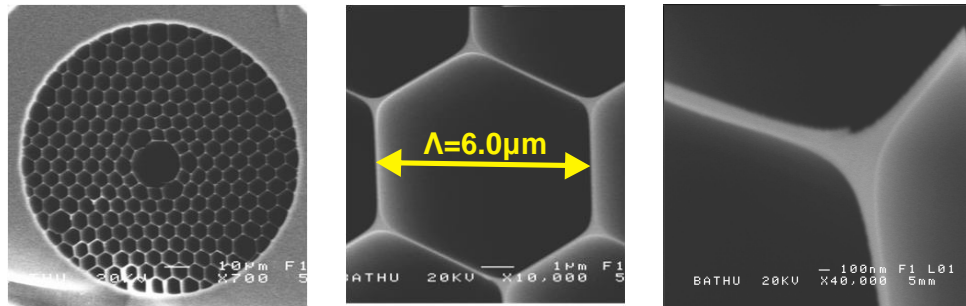
Figure 2-9: *(left to right) SEM of double PBG fibre cross section, cladding cell and apex.*
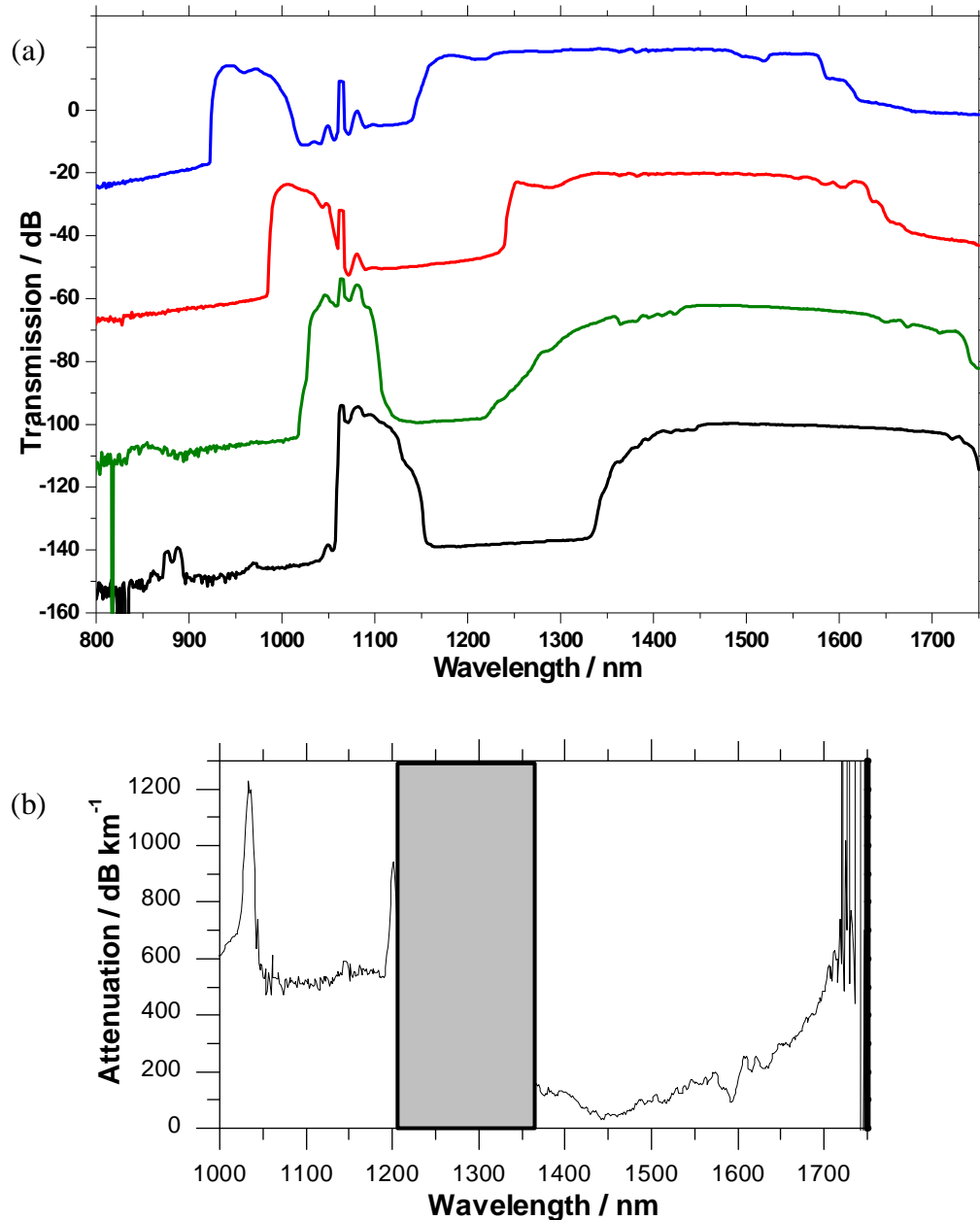
Figure 2-8: *(a) Transmission of four fabricated fibres with different cladding pitch: Λ = 6.0 µm (black line), Λ = 5.8 µm (green line), Λ = 5.6 µm (red line) and Λ = 5.3 µm (blue line). (b) Attenuation of fabricated fibre with Λ = 6.0 µm calculated from a cutback measurement of a 25 m length of fibre.*

In order to fabricate a final fibre with the optimised parameters, thick capillaries (ID/OD

= 0.76) were used in the initial stack. Pressurisation was then used during the fabrication process to reduce the strut thickness and increase the apex size. A core tube (ID/OD ~0.93) was used to create the core defect in the stack so that the final fibre would have a core wall thickness equal to ~60 % of the strut thickness. During the cane draw, vacuum was applied to collapse the interstitials between the capillaries to form the apexes. During the fibre draw, the cladding and core regions were pressurised independently using pressures of 29 and 22 kPa respectively.

An example SEM of a fabricated fibre, which has similar parameters to the optimum design found numerically, is shown in Figure 2-9. This fibre has an air filling fraction of 97% and an average pitch of 6.0 μm. The cladding structure is clearly slightly inhomogeneous and the pitch varies from 5.8 to 6.3 μm across the structure. The transmission of a 5 metre length of this fibre is shown in black in Figure 2-8(a). Two low attenuation regions, corresponding to the two expected bandgaps are clearly recorded. The fundamental bandgap spans between 1335 and 1750 nm (to the limit of the optical spectrum analyser) and the higher order bandgap extends from 1080 to 1140 nm. The attenuation of this fibre is shown in Figure 2-8(b). The minimum attenuation of the fundamental bandgap is 80 dB/km and the attenuation of the second bandgap is 500 dB/km. Although higher attenuation of the second bandgap is expected due to the increase in the effect of surface roughness at shorter wavelengths, it is believed that this attenuation figure can be reduced by improving the homogeneity of the cladding structure. The transmission spectra of three other fabricated fibres are also presented in Figure 2-8(a) and these show that, as expected, the bandgaps shift to shorter wavelengths as the cladding pitch is decreased.

These results show that this double PBG HC-PCF provides low loss guidance across an effectively broader bandwidth than conventional PBG HC-PCF. From the numerical simulations, it was found that the central wavelengths of the two bandgaps are fixed at a ratio of ~1.39. Fortunately, through tailoring of the cladding pitch this ratio is suitable for dual guidance of several key laser pairs including Nd:YAG/Ti:Sapph (1064nm and 800nm), and Ti:Sapph/HeNe (800nm and 633nm).

2.4.2. Low Loss Large-Pitch Kagome Fibre

Section 2.3 described Kagome HC-PCFs which can guide with low loss over a broad spectral bandwidth, but the current minimum attenuation is two orders of magnitude higher than PBG HC-PCF attenuation at 1550 nm. Intrinsically and irrespectively of any inhomogeneities in the photonic structure, the Kagome fibre design always exhibits optical power leakage; the level of this leakage depends on the residual overlap integral of the fast oscillating optical field of the silica cladding with that of the slowly oscillating core mode field. Additionally, due to the nanometre scale of the silica web which
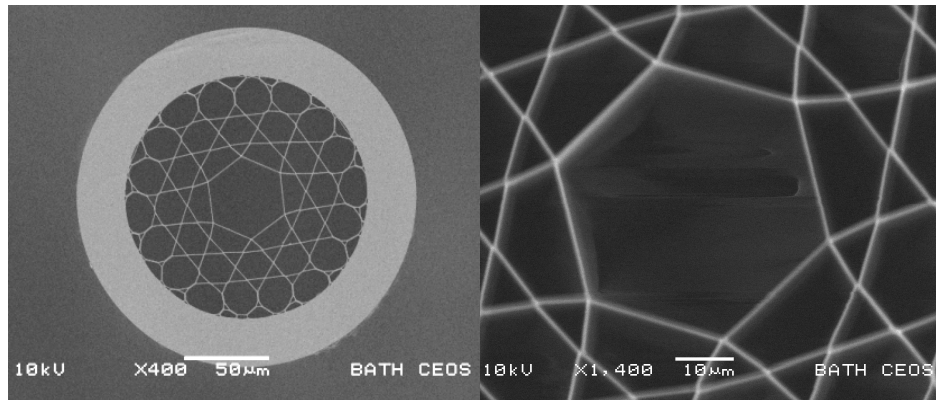
Figure 2-10: *SEMs of 1-cell Kagome HC-PCF; (left) fibre cross section and (right) fibre core detail. Fibre outer diameter is ~ 200 μm and core diameter is ~ 45 μm.*

supports the cladding structure, any small deviations from the structure design, such as variations in strut thickness and cladding pitch, act to further increase the fibre loss. This extreme sensitivity to the fine details in the cladding structure makes accurate numerical simulations of the fibre guidance very complex and also presents challenges for repeatability in fabricated fibres. Furthermore, the core-surround and first ring of the cladding structure are dominant in defining the loss of the fibre and therefore, optimisation of the core-surround is expected to reduce fibre attenuation.

In this section, the most recent advances in the fabrication of Kagome fibre, which have significantly reduced the fibre attenuation, are described. The structures here have only three cladding rings; this enables a fabrication process from stack to fibre that can be achieved in only 1 day. Few ring structures are suitable for the large-pitch Kagome fibre design as little reduction in attenuation is achieved by adding more rings to the structure; as there is no photonic bandgap in the cladding it follows that if, by some weak coupling, light from a core mode is lost to a cladding mode it can be immediately leaked away instead of being evanescent in the cladding as there will be cladding states with very similar propagation constants to that of the core modes. Currently, the optimum number of rings is not clear and will be certified in future work, but potentially a single cladding ring may be sufficient for some wavelength ranges.

Two examples of large-pitch Kagome fibre, fabricated by the author, are described in this section. The first, shown in Figure 2-10, is a 1-cell defect fibre; the core diameter is ~45 μm and the pitch is ~23 μm. The strut thickness is ~400 nm. This fibre was designed for experiments at 1520 nm. Following the usual stack and draw procedure, the stack was drawn first to cane and then to fibre. During the cane draw no pressurisation was used and during the fibre draw the core and cladding were both pressurised at 20 kPa.

The transmission through 20 m and 1.5 m lengths and the subsequent calculated loss are shown in Figure 2-12(a). The main guidance band starts at around 1200 nm and extends
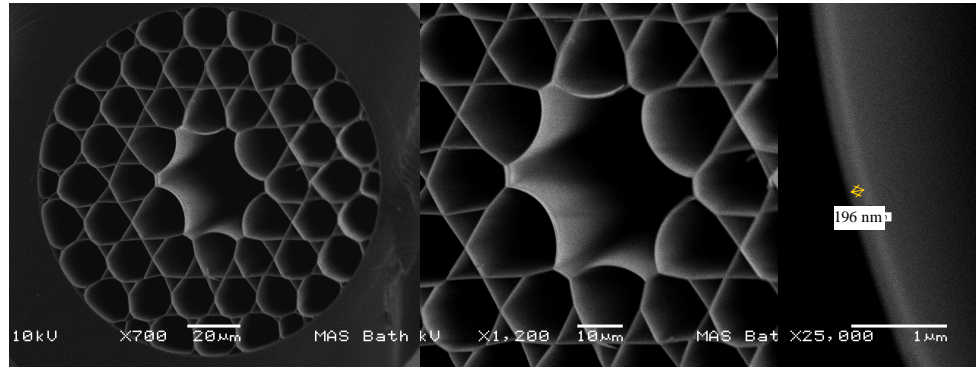
Figure 2-11: *7-cell defect Kagome (left to right); Fibre cross-section, core detail and core wall thickness.*

to 1750 nm (detection limit of the optical spectrum analyser (OSA)). There is also a smaller bandwidth low loss guidance band centred at 725 nm. The minimum attenuation is 0.34 dB/m at 1470 nm and a loss of ~0.5 dB/m is achieved at 1520 nm. There are clear peaks in the loss spectrum which arise from resonances in the cladding structure which have a thickness defined by equation (2-1).

The loss at 1520 nm is still considerably higher than that expected for state-of-the-art PBG fibre at this wavelength, however, such low loss guidance in a large diameter core is essential for experiments which are described in chapters 4 and 5. It is also noteworthy that the small guidance band at 725 nm has a loss of ~ 1dB/m; at shorter wavelengths the loss of PBG HC-PCF increases (scaling $\sim\lambda^{-3}$) while, in contrast, the attenuation of Kagome fibre is approximately independent of wavelength and therefore the difference between the attenuation of PBG and Kagome HC-PCFs decreases with wavelength.

Recent work [80] has shown that tailoring the core-surround shape can enhance the anti-resonance properties of the core and thus further reduce the fibre loss. The overlap between the core and cladding modes is highest at the core-surround and therefore both the shape and the thickness of the core-surround are paramount in determining the optical transmission properties of the fibre. The first ring of cladding holes is also the most dominant part of the remaining cladding structure in terms of defining the fibre loss. Introducing the core defect into the cladding structure can disrupt the periodicity of this first ring to an extent which is dependent on the core shape. For example, it is clear that the hexagonal core of the 1-cell Kagome fibre presented in Figure 2-10 slightly distorts the natural cladding structure. In [80], the authors report that a hypocycloid core shape significantly reduces the fibre attenuation because this shape is the most natural core shape and does not distort the surrounding cladding structure. Using this design Kagome fibres with attenuations as low as 0.2 dB/m at 1550 nm have been fabricated
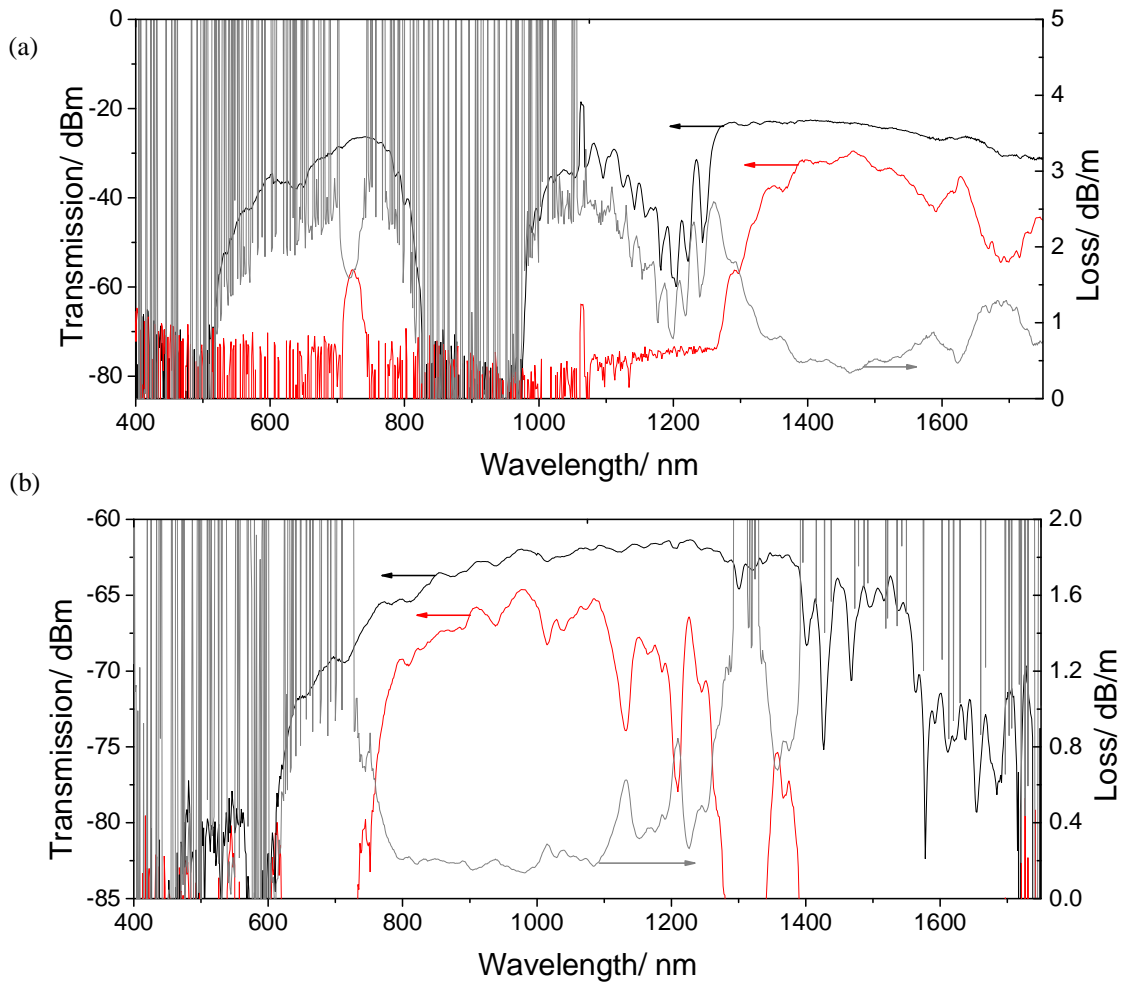
Figure 2-12: *(a) 1-cell Kagome transmission through 20 m (black line) and 1.5 m (red line). Calculated transmission loss is shown in grey. (b) 7-cell Kagome transmission through 20 m (black line) and 1.4 m (red line). Calculated transmission loss is shown in grey.*

[80]. The aim of the work described here was to tailor this fibre design to achieve equally low losses in the near-IR and visible regions.

The fabricated fibre is shown in Figure 2-11 and has a 7-cell core defect; the fibre core is elliptical and the diameter varies from 26 – 47 µm with a cladding pitch ~ 17 µm. This fibre was designed for guidance at 780 nm and therefore during the fibre draw high pressurisation was required in both the core (42.5 kPa) and cladding (65 kPa) regions to reduce the strut thickness. The difference between the core and cladding pressures was carefully controlled to achieve the optimised hypocycloid core-surround. The resultant core shape is slightly elliptical which lead to some small distortions in the first ring which may have increased the fibre attenuation. The core thickness is ~200 nm as indicated in Figure 2-11.

The transmission through 20.5 m and 1.4 m lengths and the subsequent calculated loss measurement are shown in Figure 2-12(b). There is only one guidance band recorded within the detection region of the OSA and it extends from 700 nm to 1400 nm. The

minimum loss of ~0.15 dB/m is recorded at 990 nm and a loss of ~0.3 dB/m is achieved at 780 nm. At these shorter wavelengths, Kagome fibres are now starting to compete with the attenuation provided by PBG fibres; state-of-the-art PBG HC-PCFs have a loss of ~0.1 dB/m at 990 nm and ~0.2 dB/m at 780 nm [64]. Furthermore, as mentioned above, the bandwidth of a PBG fibre decreases with the central wavelength and therefore for many applications (eg. Raman frequency comb generation), this low loss, broadband Kagome fibre is a truly competitive option. Using the core thickness of 200 nm indicated by the SEM in Figure 2-11 and equation (2-1), a high attenuation is expected at a wavelength of 420 nm. Figure 2-12 shows that the loss is this region is indeed high. However, this high loss region extends up to 600 nm. This is an indication of the variation in the strut thickness in the fabricated fibre. It is possible that the fibre attenuation may be reduced further by making the core-surround less elliptical through finer pressure control.

Following this success in the near-IR, Kagome fibres were drawn with smaller cladding pitches in order to try to shift the low loss guidance band to the visible region. As well as a reduction in pitch, a reduction in strut thickness is also necessary. This requires additional pressurisation during the fibre draw to thin the cladding struts and therefore is
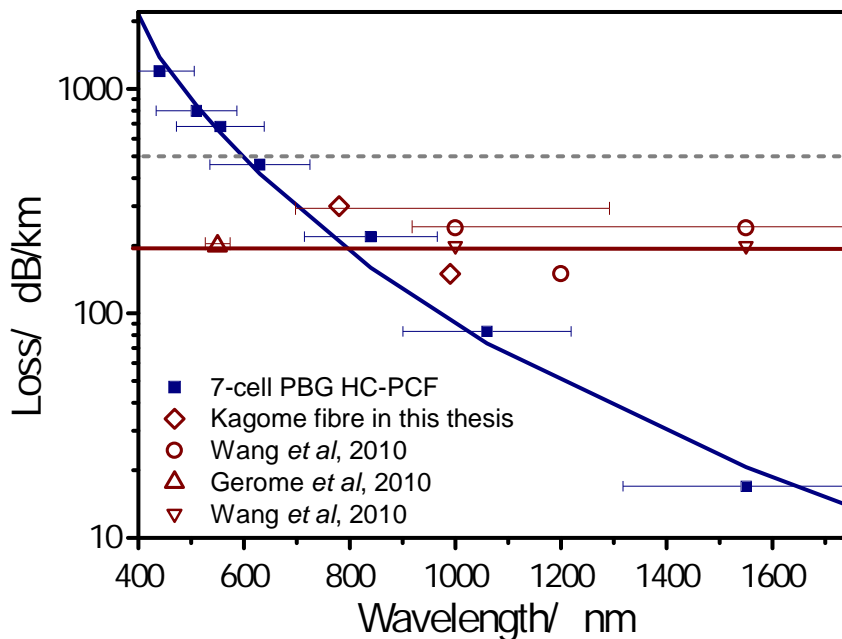
Figure 2-13: *Comparison of the attenuation of PBG HC-PCF (blue solid points) and Kagome HC-PCF (red hollow points). At wavelengths below ~900 nm the loss of the Kagome lattice fibre is competitive with the PBG HC-PCF. Attenuation of PBG HC-PCF scales approximately with λ^{-3} while attenuation of state-of-the-art large pitch Kagome HC-PCF is approximately independent of λ. The grey dashed line indicates the loss of previous state-of-the-art Kagome HC-PCF. The loss guidance of the Kagome HC-PCF across a broad bandwidth is also highlighted by the spectral range of the low loss values from each reference (each reference describes a single Kagome fibre only). Error bars highlight the transmission bandwidth of specific fibres. This contrasts to the PBG HC-PCF where each data point corresponds to a different cladding pitch.*

a demanding fabrication process; specifically due to the need to maintain the uniformity of the strut thickness, as indicated by the broad high attenuation region of the 7-cell Kagome HC-PCF presented in Figure 2-12(b). Initial work so far has demonstrated the need to adjust the initial fibre design as the maximum pressure of the current fabrication facility has been used without thinning the struts enough to shift the low loss guidance band into the visible region. This could be achieved by making the initial stack with thinner capillaries, using pressurisation during the cane drawing stage or alternatively, applying the hydrofluoric acid etching process reported in [76].

As mentioned above, the described reduction in attenuation of Kagome fibres means that this class of HC-PCF is beginning to compete with the attenuation of PBG HC-PCF at some wavelengths. This is highlighted in Figure 2-13 where benchmark losses [64, 79, 80] of each type of fibre are plotted for wavelengths between 400 and 1750 nm. The attenuation of the 7-cell Kagome reported in this thesis is included in this figure. The dependence of the loss of PBG HC-PCF on surface roughness is clear from the $\sim\lambda^{-3}$ variation of attenuation with wavelength [64]. In contrast, the Kagome attenuation is approximately independent of wavelength. This indicates that this fibre structure may be well suited for achieving lower loss hollow core guidance in the visible and UV regions. A further outstanding feature of Figure 2-13 is the broadband guidance offered by large-pitch Kagome fibre compared to the limited bandwidth of PBG HC-PCF.

2.5.   Summary

This chapter has introduced two of the most common types of HC-PCF. The guidance mechanisms relevant to these fibres have been explained and the stack and draw fabrication technique has been outlined. Developments in the fabrication of both types of HC-PCF, in which the author has made a significant contribution, have been described in the form of double PBG HC-PCF and low loss large-pitch Kagome fibre.

In chapter 3, PBG HC-PCF is used in an all-fibre slow and fast light scheme based on EIT. In chapters 4 – 7, Kagome lattice HC-PCF is used in several experiments which exploit the broadband guidance and large core diameter of this fibre.

Chapter 3

Slow and Superluminal Light Pulses via EIT in a 20 metre Acetylene-filled Photonic Microcell

This chapter describes an all-fibre slow and fast light system based on electromagnetically induced transparency. This system is realised by developing a record length, 20 metre acetylene-filled photonic microcell made from photonic bandgap HC-PCF. Experimental pulse delays and advances of 5 ns and 1 ns respectively are presented along with a simple analytical model which is used to provide insight into the experimental optimisation of pulse delay using this scheme. The content of this chapter is published in reference [81].

3.1.   Introduction

The terms slow and fast light refer to the ability to control the velocity of light pulse propagation through a material relative to the pulse velocity in a vacuum. Interest in this concept was stimulated in the early 1900s by the work of Sommerfield and Brillouin but experimental work was limited until the development of the laser and, some years later, the concept of EIT (introduced in chapter 1). Slow light pulses ($v_g << c/n_g$) or superluminal pulses ($v_g >> c/n_g$) (c: speed of light in vacuum, n_g: group index of the medium) can now be obtained through a variety of experimental techniques using diverse platforms such as photonic crystal waveguides [82], atomic vapours [18], rare earth doped fibres [83] and crystals. All these techniques have one key unifying property; the pulse velocity is controlled using the dispersion of a resonance feature. Possible applications of a slow or fast light system include all-optical signal processing and interferometry.

The development of slow and fast light systems is outlined in section 3.2 with a particular emphasis on fibre-based experimental techniques. In sections 3.3 and 3.4, the development of the first all-fibre slow and fast light system based on EIT in a 20-metre acetylene-filled photonic microcell (PMC) is described and experimental results are presented. This system combines the advantages of PMCs, such as ease of integration, with the ease of pulse delay tuning provided by EIT. The record length of the PMC increases the observed pulse delay and advance. In sections 3.6 and 3.7, the potential

optimisation of pulse delay using this system is then considered and limitations on the PMC length due to resonance dispersion and spectral reshaping are discussed.

3.2.   Slow and Superluminal Light

When discussing slow and fast light, an important distinction to make is that the velocity of the light pulse which is being controlled is the group velocity. The group velocity is expressed as

$$v_g = \frac{c}{n_g} = \frac{c}{n + \omega \dfrac{dn}{d\omega}},$$

(3-1)

where n is the refractive index and ω is the angular frequency. The time, T, that a light pulse takes to travel through a material of length L is

$$T = \frac{L}{v_g}.$$

(3-2)

From equation (3-1) it is apparent that in order to control the velocity of a pulse there are two factors which can be changed. Firstly, the refractive index n, this can only be increased up to a maximum of 10 in the optical region [84] due to the increase in oscillator decay rates with both transition strength and atomic density [85]. Secondly, the dispersion of the refractive index, $dn/d\omega$, which, in the vicinity of a spectrally narrow material resonance, can become extremely large. Slow light can be achieved for a large and positive (normal) dispersion and fast (superluminal) light can be accomplished for a large and negative (anomalous) dispersion. Through various techniques and material engineering or selection it is the dispersion which is experimentally controlled to enable group velocity control.

The centre of a gain resonance corresponds to the maximum normal dispersion. Early experimental slow light demonstrations exploited gain resonances in laser cavities. For example, in one of the first demonstrations of group velocity control, Carruthers *et al.* [86] recorded a reduction in pulse velocity of 6 parts in 10^4, compared to pulse velocity in vacuum, using a HeNe laser. Shortly after this, Casperson and Yariv recorded a reduction in group velocity by a factor of 2.5 using a gain resonance in a xenon discharge laser [87].

Although the centre of an absorption resonance corresponds to a maximum anomalous dispersion, and therefore leads to a superluminal group velocity, the wings of an absorption line demonstrate normal dispersion. The magnitude of this normal dispersion is much smaller than the magnitude of the anomalous dispersion in the resonance centre but has the additional advantage of corresponding to a reduced attenuation. For example, Grischkovsky [88] recorded a group velocity reduced by a factor of 14 using the wings of

a rubidium absorption resonance. This work highlighted a limitation of using resonance features; these features are typically associated with high absorption and therefore a superluminal group velocity could be achieved only at the cost of high pulse attenuation.

This restriction was overcome by the demonstration of EIT in an atomic vapour [11]. Through this technique a spectrally narrow resonance in a Doppler-broadened absorption line is created, which increases the transparency of the vapour and therefore reduces pulse attenuation. Subsequent experimental demonstrations of slow light using EIT stimulated intense research in this field. For example, in 1999, Hau *et al.* [18] demonstrated group velocities as low as 17 m/s using EIT in ultracold sodium vapour. Shortly afterwards, Kash *et al.* [89] reported group velocities as low as 90 m/s in hot rubidium vapour. These experiments showed that, through EIT, large, tuneable pulse delays could be achieved. Recent work in this field has expanded into the realm of stopped and stored light; in 2001, Liu *et al.* [90] stopped and stored a probe pulse for up to 1 ms using EIT in a cold cloud of sodium atoms. Very recently this storage time was extended to 1 s by carefully controlling the magnetic field applied to the ultracold sodium vapour cloud [19]. All of these demonstrations of group velocity control using EIT use macroscopic gas cells to confine the chosen atomic vapour in combination with very precisely engineered and controlled environmental conditions.

3.2.1.   Requirements of a Slow and Fast Light System

Before considering further the relative merits of different slow and fast light schemes, the possible practical applications are now considered. A major application of group velocity control is in all-optical signals processing; an all-optical router is in principle more efficient as the signal information remains in the optical domain. Possible signals processing devices include optical switches, all-optical memories and optical signal regenerators. More diverse applications include interferometry, quantum information storage, optical sensing with enhanced precision and slow light signal compression for enhanced light-matter interaction [21].

Considering these possible applications a key feature of a successful slow and fast light scheme is its ease of integration with existing systems. In view of the applications in all-optical signals processing, a fibre-based technique would be ideal; such a candidate would provide the possibility of low loss integration with existing systems combined with the compactness and portability which fibre systems can offer.

A further quality of a successful system is the maximum pulse delay achievable; this is primarily defined by the resonance dispersion as highlighted by equation (3-1). High dispersion corresponds to a narrow spectral resonance, yet a narrow spectral resonance has a small frequency bandwidth; this consequence highlights the trade off between

achieving large pulse delay or advance and the temporal duration of the input pulse. The pulse delay or advance is only effective over the spectral bandwidth of the resonance which implies that a pulse signal centred on the resonance feature must have a bandwidth less than the FWHM. Pulse bandwidth is further limited by the non-uniform transmission of the resonance shape. Resonance loss limits interaction length and storage time and therefore maximum achievable delay [21, 91]. An additional consideration is the ease with which the pulse delay or advance can be tuned; ideally the magnitude of the pulse delay should be tuned almost instantaneously by changing an experimental parameter. The tuning range of the pulse delay and the wavelength operating range are also important in defining the versatility of the system.

The operating conditions of a slow and fast light system are also of paramount importance when defining potential applications. For example, if cryogenic temperatures are required for the system to work effectively then the system size and portability are compromised.

To summarise; the key considerations for a practical slow and fast light scheme include pulse bandwidth, wavelength operating range, environmental conditions required, maximum pulse delay achievable and range of pulse delays, delay tuneability and ease of integration.

Currently, the different media which are being investigated in order to realise such a system include alkali vapours [18, 89, 92], rare-earth doped fibres [83], photonic crystal waveguides [82], microresonators and Brillouin [83, 93-95] and Raman optical amplifiers [96]. Each scheme has different advantages and disadvantages. Here, fibre-based schemes are highlighted for their ease of integration with existing systems. The leading fibre-based techniques use stimulated Raman scattering (SRS) and stimulated Brillouin scattering (SBS).

3.2.2.   Fibre-based Slow and Fast Light Systems

SBS is the most efficient parametric process in silica [91] due to the long lifetime of acoustic phonons. In this technique, counter-propagating pump and probe beams generate an acoustic wave which is stimulated by electrostriction and creates a dynamic Bragg grating that diffracts light from the pump to probe beams. In this way, the probe beam can see substantial gain. It is the dispersion of this gain feature which is suitable for group velocity control. The first slow light demonstrations using this scheme are reported in references [95] and [94]. In reference [95] a 20 ns delay is reported for an input pulse with 15 ns duration.

This SBS technique has the advantage that is a gain, not an absorption resonance which provides the steep dispersion required. Also the delay magnitude is tuneable by the pump

power and the system can be designed to delay pulses at any wavelength. Disadvantages include precise wavelength positioning of the probe signal with respect to the pump, long fibre lengths required (up to 2000 m depending on pump power) and that the pulse delays are subsequently only a minor fraction of the total propagation time [91]. By increasing the power of pump beam to 10 W reasonable delays have been reported for shorter fibres (~a few metres) [97]. However, this power requirement is very large and therefore current research is being directed into using exotic fibres (eg. chalcogenide fibres) with larger Brillouin gain. The Brillouin resonance also has the disadvantage of a narrow gain bandwidth (typically 30 MHz [98]). However, this can by circumvented by pumping multiple gain resonances simultaneously [94].

SRS is a similar candidate to SBS; the pump and probe (Stokes) beams co-propagate and energy is transferred, through the Raman resonance, from the pump to the Stokes beam. The SRS scheme has the advantage of a much larger bandwidth (up to 150 GHz [99]). However, the cost of this is a reduced dispersion over the resonance and the achievable delay per metre is again very small and again extremely long fibres are required. The large spectral bandwidth means that this technique is well suited to controlling the velocity of very short (sub ps) pulses [96].

Rare earth (eg. erbium) doped fibres provide an alternative to these two techniques. Schweinsberg *et al.* [83] demonstrated large pulse delays of up to 0.38 ms using 3.2 ms duration input pulses and coherent population oscillations in erbium doped fibre. Pulse advances of up to 0.32 ms were recorded. However, the gain resonance in this system has an extremely narrow bandwidth so this scheme is only suited for long pulses.

A final option has been made possible by the advent of HC-PCF. The Gaeta group at Cornell University used EIT in an acetylene-filled HC-PCF to delay an input pulse by 800 ps in only 1.3 m of fibre [43]. In this initial demonstration, the fibre was mounted in a vacuum system. This scheme combines the advantages of EIT, such as ease of delay and advance tuning and large maximum pulse delays, with the convenience of a fibre-based system. Moreover, acetylene gas provides a multitude of absorption resonances which coincide with the telecommunications bands. Now, with the development of the PMC, this technique can be extended to realise a compact, portable and truly all-fibre EIT-based slow and fast light system.

3.3. Photonic Microcell Fabrication

The PMC used in the following experimental work was fabricated using a 20 metre length of triangular lattice HC-PCF. The record length of this PMC extends the range of possible pulse delays and advances which can be recorded. An SEM of the fibre used is
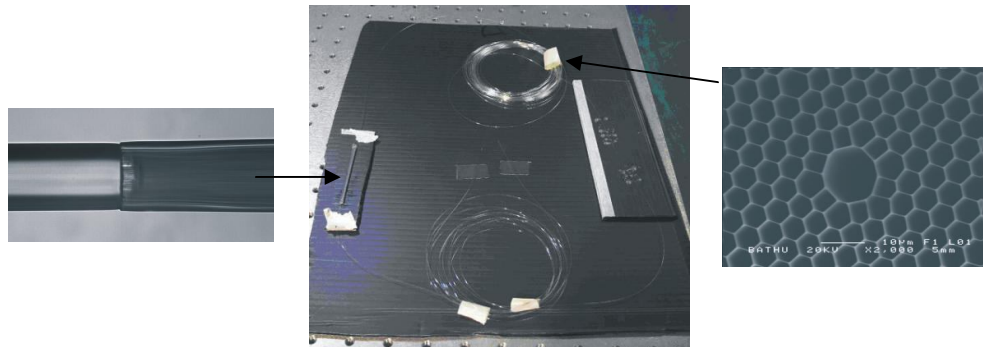
Figure 3-1: *Photograph of fabricated 20 metre acetylene-filled PMC. Insets: Image of a splice (left) between the HC-PCF and SMF and SEM (right) of HC-PCF used.*

shown inset to Figure 3-1; the core is a 7-cell defect with a diameter of 13 µm and the fibre attenuation is 150 dB/km at 1550 nm.

The PMC was fabricated using the technique described in [37] and summarised here. The key fabrication steps are shown schematically in Figure 3-2. Initially, the fibre is purged with argon gas and heated to remove any contaminants. One end of the HC-PCF is then spliced to SMF. An example splice is shown inset to Figure 3-1. The other end of the HC-PCF is then inserted into a vacuum chamber and through this the fibre is evacuated to a pressure below 10^{-4} mbar. Following this, the HC-PCF is filled with high pressure acetylene and re-evacuated until the required acetylene pressure (~100 µbar) is achieved. This pressure is monitored optically by scanning a weak probe external cavity diode laser (~100 µW) across an absorption line of acetylene and using the Beer-Lambert law (equation 1-2) to calculate the absorption co-efficient and subsequently the acetylene
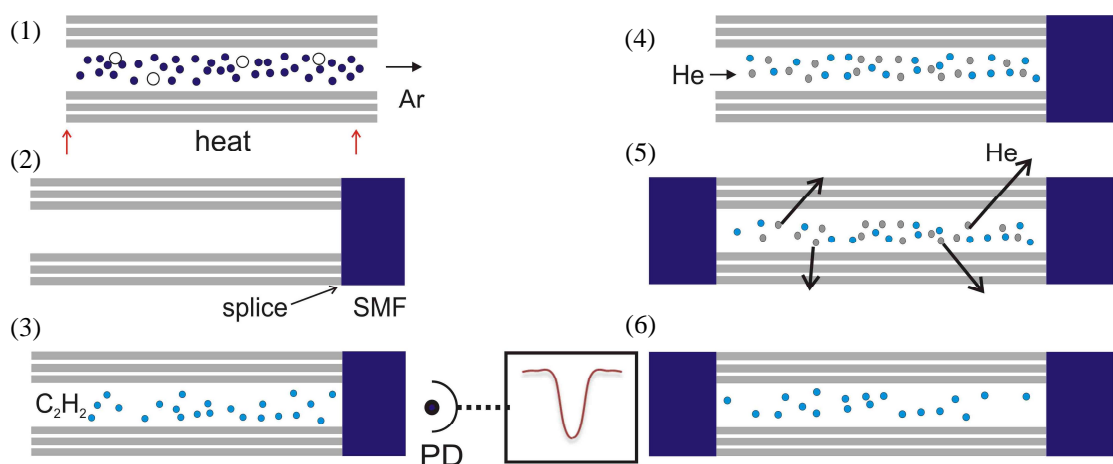
Figure 3-2: *Outline of PMC fabrication steps (1) – (6); (1) the fibre is heated and purged with argon to remove contaminants; (2) one end of the HC-PCF is spliced to SMF; (3) the HC-PCF is re-evacuated and then filled with acetylene and the gas pressure is monitored optically; (4) HC-PCF is over-pressurised with helium to stop contaminant entry on splicing; (5) helium permeates through silica cladding into atmosphere and (6) complete low pressure acetylene-filled PMC. PD: photodetector.*

pressure. At this point, in order to prevent contaminant entry upon splicing, the fibre is filled with helium to above atmospheric pressure. This step allows the second end of the HC-PCF to be spliced within a timeframe, set by the core diameter, without significant contamination. The second end of the HC-PCF is then removed from the vacuum system and spliced to SMF. The helium remaining in the PMC diffuses out of the HC-PCF core through the silica cladding over a timescale of a few hours, leaving a vacuum pressure acetylene-filled PMC. The complete 20-metre acetylene-filled PMC which was fabricated for the work presented in this chapter is shown in Figure 3-1.

Some of the experimental results presented in this chapter were recorded while the second end of the HC-PCF was still in the vacuum chamber. This was so that the optimum acetylene pressure for this particular experiment could be dynamically investigated and the importance of this is discussed further in the following sections.

3.4.   Experiment

The experimental set-up used to observe slow and superluminal pulses is shown in Figure 3-3. The probe and coupling beams required to create EIT are provided by two tuneable external cavity diode lasers which both have a linewidth of ~ 5 MHz. The probe beam (~150 µW) is fibre-coupled into an intensity modulator and the coupling beam (100 – 270 mW) is amplified using an erbium-doped fibre amplifier (EDFA) with a gain bandwidth spanning from 1540 nm to 1570 nm. The two beams are combined using a 50:50 fibre coupler. One of the coupler outputs is spliced to the 20 metre acetylene-filled PMC, whilst the second output is used to monitor the coupling power into the PMC. At the output of the PMC, a grating is used to separate the coupling and probe beams. For a truly all-fibre system this grating could be replaced with a tuneable fibre filter at the probe frequency.

The transmission trace of the scanning probe laser is recorded on a fast photodetector
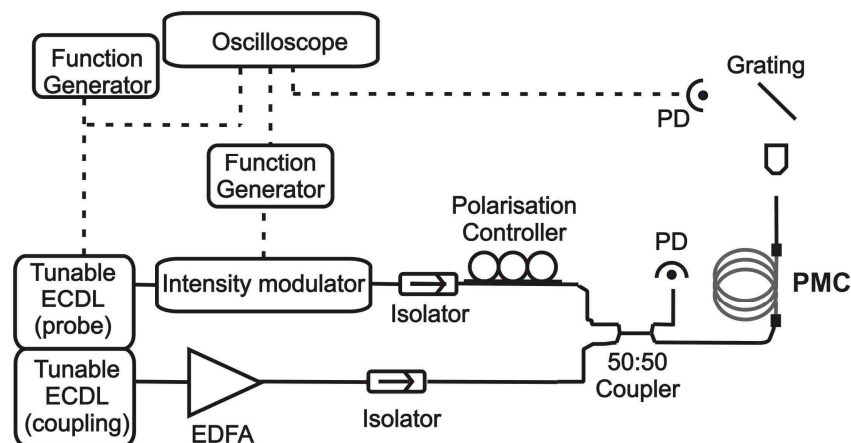
Figure 3-3: *Experimental set-up used to generate EIT in the acetylene-filled PMC and to delay/advance probe pulses. ECDL, external cavity diode laser; PD, photodetector; EDFA, erbium doped fibre amplifier.*
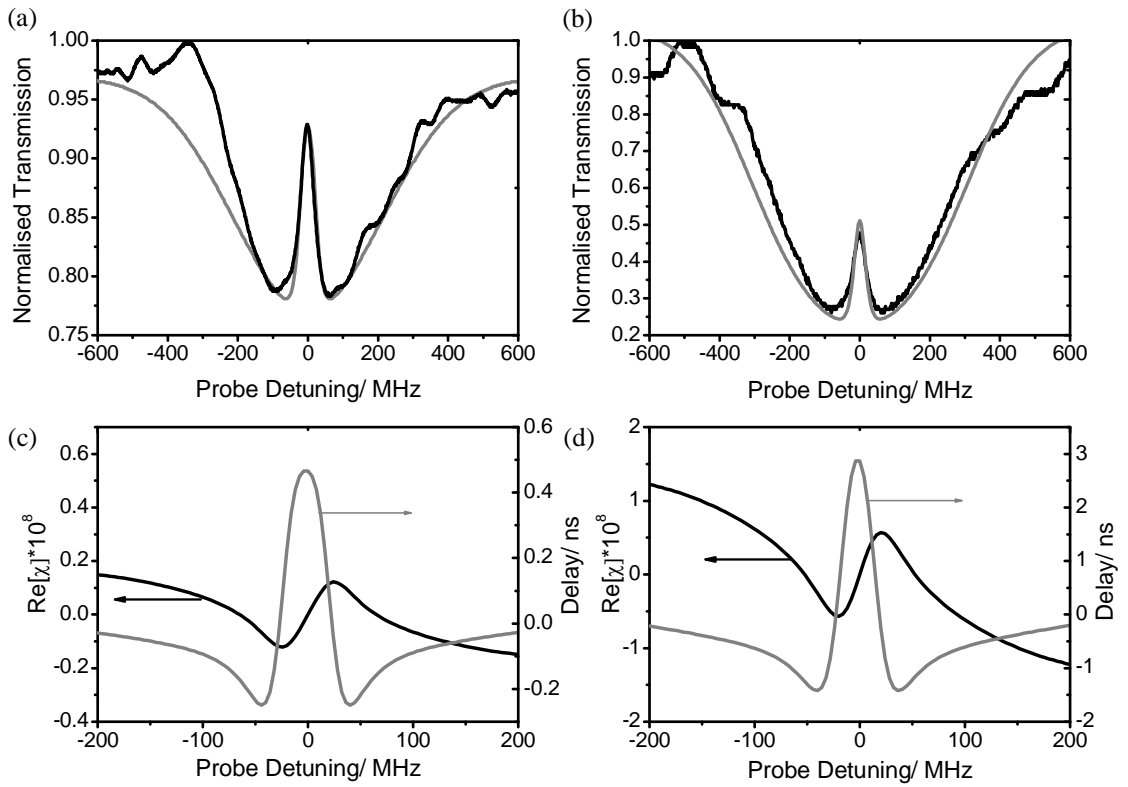
Figure 3-4: *(a) EIT trace produced with a coupling Rabi frequency of 200 MHz, at an acetylene pressure ~20 μbar (black line) and numerical fit (grey line). EIT height is ~86% and width is ~ 45 MHz. (b) EIT trace produced with a coupling Rabi frequency of 180 MHz, at an acetylene pressure ~140 μbar and numerical fit (grey line). EIT height is ~32% and width is ~41 MHz. (c) Real part of susceptibility calculated using fit from (a) (black line) and corresponding delay (grey line). (d) Real part of susceptibility calculated using fit from (b) (black line) and corresponding delay (grey line).*

(Thorlabs DET410) and viewed on an oscilloscope. Probe pulses with 30 ns FWHM duration were produced by intensity modulating the probe laser at a 50 MHz repetition rate. Initially, pulse delay and advance were investigated with the probe laser tuned around the absorption line R25 (1513.2 nm) from the $v_1 + v_3$ overtone band of acetylene (see Appendix for full details on the spectroscopy of acetylene). The coupling beam was tuned to the P25 transition (1540.8 nm) to form a V EIT configuration. The choice of these absorption lines was dictated by the limited gain bandwidth of the EDFA (1540 - 1570 nm).

As mentioned above, the optimum acetylene pressure in the fibre was investigated. The acetylene pressure is critical in defining the height and width (FWHM) of the EIT feature and the dispersion of this feature defines the achievable range of pulse delays and advances. This dependence is due to the contribution of pressure broadening to the decoherence rate and is discussed further in section 3.7. Experimental EIT traces for two acetylene pressures, 20 μbar and 140 μbar, are shown in Figure 3-4(a) and (b)
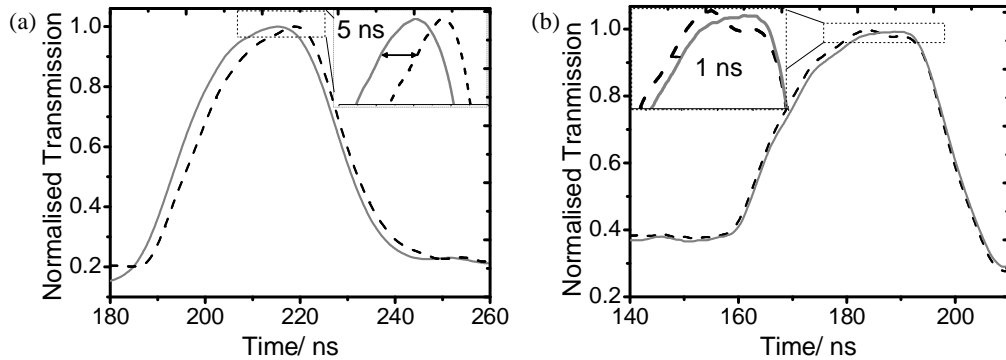
Figure 3-5: *(a) Probe pulse only (grey line) and delayed probe pulse in presence of coupling beam (black dash line), inset highlights pulse is delayed by up to 5 ns (b) Probe pulse only (grey line) and advanced probe pulse in presence of coupling beam (black dash line), inset highlights pulse is advanced by up to 1 ns.*

respectively. The gas pressure is deduced from the absorption line contrast and the absorption coefficient of the R25 line which is taken to be 0.005 $m^{-1}Pa^{-1}$ [100]. Figure 3-4(a) shows that at 20 µbar, a record transparency height of 86% was achieved with a linewidth of 45 MHz. This transparency height is especially large considering that here the coupling laser is tuned to the P25 line which is one of the weakest absorption lines from the $v_1 + v_3$ overtone band of acetylene. Figure 3-4(b) shows that at the higher acetylene pressure of 140 µbar and a coupling Rabi frequency of 180 MHz, the EIT width is 41 MHz but the height is only 32 %. Instinctively, larger delays were expected using the extremely large EIT feature shown in Figure 3-4(a). However, using this EIT resonance feature no significant pulse delays or advances were recorded. In contrast, significant delays were achieved using the EIT feature shown in Figure 3-4(b).

3.5. Numerical Model

To confirm this trend, a rigorous numerical model, which accounts for the open nature of the EIT system [101] was used and this corroborates these results. Based on the optical dipole strength [102], the thermal distribution for R25 [103] and the experimental output trace shown in Figure 3-4(a), the R25 susceptibility and group delay spectra were deduced. The results (see Figure 3-4(c)) show the typical S-shape for the susceptibility and a Lorentzian-like group delay with a maximum of 0.5 ns delay at zero-detuning and a maximum advance of ~ 0.2 ns for a detuning of ~40 MHz. These small values for pulse delay and advance help to explain why no substantial experimental delays were observed. In contrast, Figure 3-4(d) shows that for the experimental trace shown in Figure 3-4(b), the numerical model predicts a maximum delay of 3 ns for zero detuning and a maximum advance of 1.4 ns for a detuning of ~40 MHz.

In good agreement with the numerical model, a maximum delay of 5 ns at zero probe detuning (Figure 3-5(a)), and a maximum advance of 1 ns at ~40 MHz detuning (Figure 3-5(b)) were experimentally recorded. These maximum values were recorded near the peak of the pulse and it is worth mentioning that the delay and advance were not completely uniform across the pulse due to slight pulse distortion. This could be due to the limited bandwidth of the transparency feature relative to the laser linewidths combined with mode beating effects (see chapter 4 for more detail) in the fibre which lead to frequency dependent transmission.

In order to get a more physical insight into these results and to have a more intuitive and predictive tool in finding the optimum gas pressure, coupling laser power and fibre length, an approximate analytical expression was developed and this is described in detail in the next section.

3.6. Analytical Model

An analytical expression for the probe susceptibility can be deduced by considering a Lorentzian velocity distribution and a closed Λ system as shown in Figure 3-6. This leads to the following susceptibility expression near resonance of the probed transition [104]:

$$\chi(\delta) = \frac{ND^2}{\hbar\varepsilon_0} \frac{i\gamma_{coh} + \delta}{(\gamma_{coh} - i\delta)\left(\frac{\Gamma_{opt}}{2} + W_d - i\delta\right) + \frac{\Omega^2}{4}} \tag{3-3}$$

where γ_{coh} is the decoherence rate of the uncoupled states, Γ_{opt} is the total optical decay to the ground states, δ is the probe detuning, N is the molecular density, W_d is the Doppler
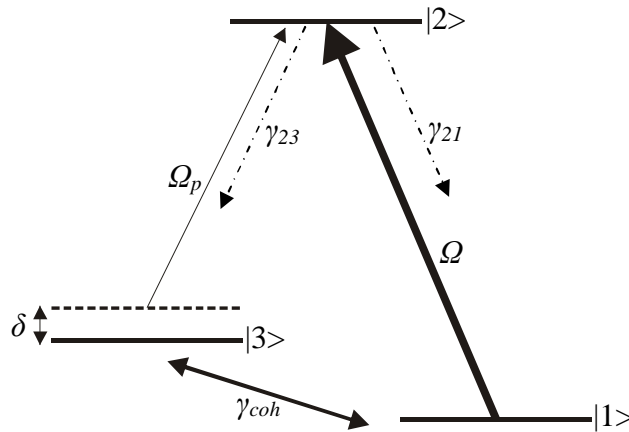
Figure 3-6: *EIT schematic for a Λ configuration. Ω_p, Ω: probe and coupling Rabi frequencies, δ: probe detuning, $γ_{coh}$: decoherence rate between the uncoupled states |1> and |3>, $γ_{21}$, $γ_{23}$: optical decay rates.*

half-width at half maximum of the absorption line, D is the dipole moment of the probe transition, Ω is the coupling Rabi frequency and ε_0 is the free space permittivity. The absorption coefficient and the group index are then readily deduced from the imaginary and real parts of the susceptibility respectively.

Adopting a convenient notation [105], one can write the expressions of the absorption coefficient $\alpha(\delta)$ and group index $n_g(\delta)$ as follows [106]:

$$\alpha(\delta) = \alpha_0 \left(1 - \frac{f}{1 + (\delta/\Delta v)^2} \right) \tag{3-4}$$

$$n_g(\delta) \approx f \left(\frac{\alpha_0}{2} \frac{c}{\Delta v} \right) \left(1 - 3(\delta/\Delta v)^2 \right) + n_0 \tag{3-5}$$

where the transparency factor is:

$$f = \frac{\Omega^2/4}{\left(\gamma_{coh} \left(W_d + \frac{\Gamma_{opt}}{2} \right) + \Omega^2/4 \right)} \tag{3-6}$$

and

$$\Delta v = \gamma_{coh} + \frac{\Omega^2/4}{W_d + \frac{\Gamma_{opt}}{2}} . \tag{3-7}$$

Here, α_0 is the absorption on resonance in the absence of a coupling laser, c is the speed of light in a vacuum, n_0 is the phase refractive index. f ranges from 0 for no transparency to 1 for complete transparency and Δv is the FWHM of the transparency feature.

Consequently, the expression of the delay, T_{del}, experienced by the probe beam is deduced from n_g through the relation $T_{del} = L(n_g - n_0)/c$ where L is the fibre length. The delay is largest on resonance ($\delta = 0$) and its expression is given by:

$$T_{del} = \frac{L\alpha_0}{8} \left(\frac{\Omega^2 \left(W_d + \frac{\Gamma_{opt}}{2} \right)}{\left(\gamma_{coh} \left(W_d + \frac{\Gamma_{opt}}{2} \right) + \Omega^2/4 \right)^2} \right) . \tag{3-8}$$
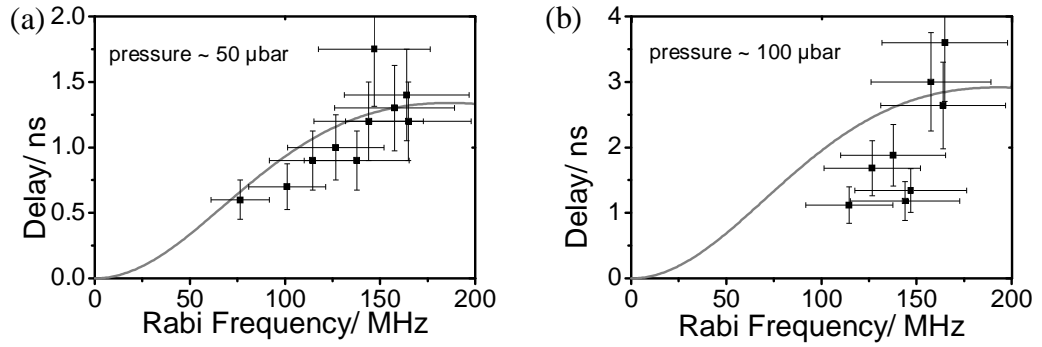
Figure 3-7: *(a) and (b): Probe pulse delay as a function of coupling laser Rabi frequency for acetylene pressure of 50 μbar and 100 μbar respectively.*

This simple analytical expression agrees reasonably well with the trends shown in the experimental data displayed in Figure 3-7(a) and (b) for the following fit parameters: $\gamma_{coh} = $ 34 MHz and $\alpha_0 = $ 0.02 and 0.04 m^{-1} respectively. The error bars are indicative of the uncertainty in splice loss at the input to the PMC and also the spread in pulse delay recorded across the pulse. The larger disagreement between the fit and the experimental data shown in Figure 3-7(b) could possibly be due to instabilities in the pressure in the fibre at the slightly higher pressure. For acetylene pressures less than 1 mbar, the decoherence rate is dominated by collisional broadening due to collisions between the acetylene molecules and the inner core walls rather than collisions between the acetylene molecules themselves. This was corroborated experimentally by the constancy of the transparency linewidth when the acetylene pressure was changed from 50 to 100 μbar. On the other hand, this corresponds to a doubling of α_0 and consequently, and according to equation 3-8, one would expect a doubling in T_{del}. For the experimentally available range of coupling laser powers (100 – 270 mW), the delay increased with coupling laser power and no saturation of the delay due to power broadening of the EIT was observed.

From equation (3-8), the pulse delay reaches a maximum for a particular Rabi frequency of the coupling laser given by $\Omega_{max} = 2\sqrt{\gamma_{coh}\left(W_d + \dfrac{\Gamma_{opt}}{2}\right)}$. This corresponds to a Rabi frequency where the transparency linewidth is doubled by power-broadening, i.e. $\Delta\nu = 2\gamma_{coh}$ (equation (3-7)) and $f = 0.5$ (equation (3-6)). Consequently this ratio reaches a maximum at a given limited value of Rabi frequency. At this Rabi frequency, the maximum delay takes the simple form

$$T_{del}^{(max)} = \frac{L\alpha_0}{8\gamma_{coh}}. \qquad (3\text{-}9)$$

Equation 3-9 indicates that the maximum delay per unit fibre length is solely determined by the ratio of the absorption coefficient, α_0, and the coherence dephasing rate, γ_{coh}. Consequently, the ratio α_0 / γ_{coh} represents the figure of merit of the achievable delay per unit length. It also explains the weak delay experimentally observed for ultra-low pressure despite a favourable strong transparency and narrow linewidth. Using this simple expression for the maximum pulse delay ideal experimental parameters such as length and pressure can be optimised and this is discussed in the following section.

3.7. Maximising Pulse Delay

The two parameters, α_0 and γ_{coh}, can be optimized through control of the experimental conditions. Firstly, the absorption coefficient α_0 increases linearly with the acetylene pressure in the fibre core. However, pressure broadening contributes to the decoherence rate γ_{coh} (see below) and so the pressure increase should be limited to a range where the pressure broadening of the transparency remains small. Secondly, a further increase in the absorption coefficient and hence larger pulse delay can be obtained by using different lines from the acetylene $v_1 + v_3$ band. For example, measurements taken in a macroscopic acetylene cell indicate that changing from the R25-P25 configuration to R11-P11 increases α_0 by a factor of 8. Using equation (3-8), the maximum delay per unit length obtained using the R11-P11 absorption line pair, a pressure of 375 µbar and $\gamma_{coh} \sim 26$ MHz is found to be 7 ns/m (Figure 3-8(a)), corresponding to a total delay of 140 ns with the present 20 metre long PMC. However, in the case of a strong absorption coefficient, care should be taken in choosing the fibre length so that the optical density remains sufficiently small for the probe pulse signal to be detected.

Figure 3-8(a) also shows how the transparency height (equation (3-6)) increases with the coupling Rabi frequency. As explained above, for maximum delay (i.e. at $\Omega = \Omega_{max}$), $f = 0.5$, corresponding to a transparency height of 50%. As the pulse attenuation affects the usable length of fibre, it also limits the overall achievable delay. A possible route to achieving maximum delay can therefore be to use an increased transparency height through increasing the coupling Rabi frequency. This leads to a lower delay per metre but decreases the pulse attenuation due to absorption, ultimately achieving a larger overall delay. For example, Figure 3-8(a) shows that at a coupling Rabi frequency of 500 MHz a transparency height of 95% should be achieved in the above experimental conditions. Using this transparency, a delay of 2.8 ns/m is expected. Although almost 3 times lower than the maximum delay of 7 ns/m, the pulse attenuation is much lower, enabling a larger overall delay to be achieved through using a longer length of HC-PCF.

Depending on system requirements (e.g. pulse bandwidth) it may be favourable to reduce the decoherence rate, γ_{coh}, instead of increasing the absorption coefficient. The decoherence rate can be expressed as,

$$\gamma_{coh} = \gamma_{pressure} + \gamma_{lasers} + \gamma_{walls} .$$ (3-10)

In the present experiment, the main contribution is γ_{walls} which arises from dephasing due to collisions between the acetylene molecules and the fibre's inner core walls. The core diameter of the HC-PCF used in our experiment was 13 μm which corresponds to a γ_{walls} contribution of ~20 MHz. This can be reduced by using a HC-PCF with a larger inner core diameter such as large-pitch Kagome fibre with which guidance at 1550 nm has been demonstrated with core diameters as large as 80 μm [72]. This corresponds to a γ_{walls} contribution of less than 3 MHz. The laser linewidths add an amount γ_{lasers} to the decoherence rate which can be reduced through the use of ultra narrow linewidth lasers. Finally the pressure broadening rate, $\gamma_{pressure}$, which originates from collisions between the
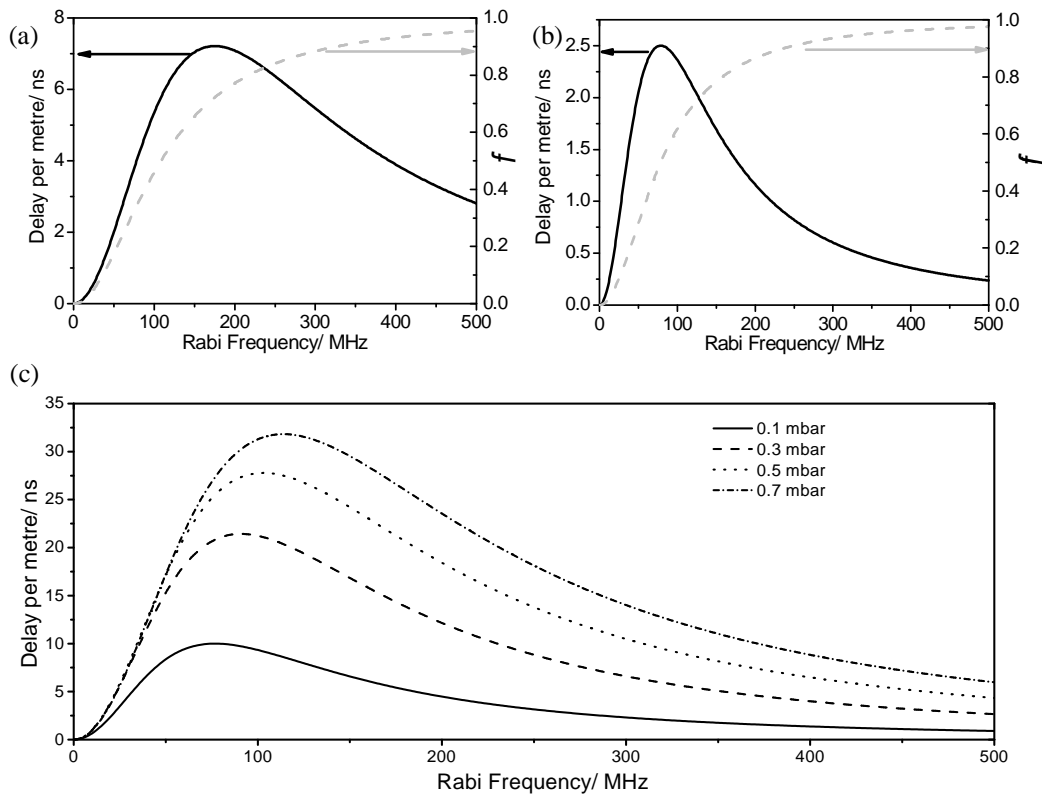
Figure 3-8: *Pulse delay per metre as a function of coupling Rabi frequency for experimental conditions: (a) R11-P11 absorption line pair, a pressure of 375 μbar and γ_{coh} ~ 26 MHz, (b) R11-P11 for γ_{coh} = 5 MHz and an acetylene pressure of 25 μbar and (c) R11-P11 absorption line pair for a series of acetylene pressures with decoherence contribution sum from laser linewidths and wall collision dephasing set to 4 MHz. In (a) and (b) the grey dashed line indicates the transparency factor, f, as a function of coupling Rabi frequency.*

gas molecules themselves, is ~10 MHz/ mbar in acetylene for the lines R11 and P11 and ~6 MHz/ mbar for R25 and P25 [4] and is hence reduced simply by decreasing the acetylene pressure. Figure 3-8(b) shows that a maximum delay per metre of 2.5 ns can be achieved using lines R11 and P11 for γ_{coh} = 5 MHz and an acetylene pressure of 25 μbar.

Realistically, a combination of reduction of decoherence rate and increase in absorption coefficient could be used depending on the total delay required, the pulse bandwidth and the detection scheme. As explained above, both γ_{coh} and α_0 are functions of acetylene pressure. Figure 3-8(c) shows the evolution of the maximum delay per metre as a function of acetylene pressure. This figure shows that a maximum delay of ~30 ns/m can be expected for a pressure of 0.7 mbar in a large core fibre using the strong absorption lines R11 and P11 and lasers with narrow linewidths. Yet, this corresponds to an absorption coefficient of 2.8 which would lead to very high pulse attenuation due to absorption, even at zero probe detuning and would severely limit the length of fibre used; after a propagation length of 2 metres the probe beam would be attenuated to ~6% of the original input power. This figure also shows that, as the pressure is increased the maximum delay per metre also increases but at a decreasing rate. Also, as the pressure is increased, the coupling laser power required to generate a 50% transparency increases.

In addition to the above limitations, the above deduced delays per unit length, as determined by the ratio of the absorption coefficient and the decoherence rate, are meaningful only if the total fibre length is not limited by the very same absorption coefficient or decoherence. Therefore, the last control parameter to consider in maximizing the delay is the fibre length. Several effects which can lead to pulse distortion need to be considered in order to find the optimum fibre length.

Firstly, the resonance group velocity dispersion (R-GVD) which arises from the spectral bandwidth of the input pulse. A transform-limited probe pulse of a duration T_0 exhibits a spectral bandwidth ~ $1/T_0$. As the pulse propagates through the fibre the spectral components contained in the pulse bandwidth experience slightly different delays, as indicated by the slope of the susceptibility in Figure 3-4(c). Following the treatments of Boyd *et al.* [105], the upper limit on the fibre length set by the R-GVD, L_{max}^{RGVD}, corresponds to a propagation length after which the initial probe pulse doubles in duration. At Ω_{max}, this is given by

$$L_{max}^{RGVD} = \frac{2}{3}\frac{T_0^3 \Delta v^3}{f\alpha_0} = \frac{32}{3}\frac{T_0^3 \gamma_{coh}^3}{\alpha_0} \qquad (3\text{-}11)$$

Applying this to our experimental set-up, with T_0 =30 ns, γ_{coh} = 28 MHz and α_0 = 0.04 m^{-1}, implies an R-GVD-limited maximum length of ~ 160 m.

Similarly to the resonance, the fibre waveguide exhibits a GVD. However, HC-PCF dispersion is typically ~ 50 ps/nm/km and the maximum fibre length before a pulse of 30 ns duration would double in extent is therefore ~ 10^7 m at a wavelength of 1550 nm. The 3 dB attenuation level for state-of-the-art HC-PCF at 1550 nm is ~ 2 km so the limitation this imparts on the maximum length can be disregarded.

A final factor to be considered when deciding the maximum PMC length is the spectral reshaping effect due to the different absorptions experienced by the different spectral components. For a Gaussian initial pulse, the maximum tolerable length at Ω_{max} is [105]:

$$L_{\max}^{sr} = \frac{3\Delta v^2 T_0^2}{\alpha_0 f} = \frac{24\gamma_{coh}^2 T_0^2}{\alpha_0} \tag{3-12}$$

Applying equation (3-12) in our experimental set-up leads to a spectral reshaping-limited maximum fibre length ~ 212 m. The importance of this effect compared to the R-GVD as described by equation (3-11) depends on the initial pulse duration. For pulse lengths < $9/4\gamma_{coh}$, the maximum fibre length is defined by the R-GVD and for pulse lengths > $9/4\gamma_{coh}$, spectral reshaping is dominant.

According to both equations (3-11) and (3-12), the maximum lengths set by the resonance GVD and spectral reshaping are inversely proportional to α_0/γ_{coh} , and hence to the delay per unit length. Consequently, for a fibre length larger than $L_{\max}^{RGVD}$, α_0/γ_{coh} is no longer the figure of merit for the maximum delay as the resonance GVD effect imposes a trade off. Thus, the total delay as expressed in equation (3-9) is valid only for a fibre length L that is smaller than the relevant maximum length. Figure 3-9(a) and (b) show the maximum lengths imposed by R-GVD and spectral reshaping, as expressed in equations (3-11) and (3-12), as a function of T_0 and acetylene pressure respectively for the same experimental conditions as Figure 3-8(b). It is clear that when considering the maximum fibre length to be used, the relevant limiting length is highly dependent on the experimental conditions.

Substituting the maximum lengths expressed in equations (3-11) and (3-12) into equation (3-9), the expected optimum fractional delay, $T_{del}^{(max)}/T_0$, is then

$$\frac{T_{del}^{(max)}}{T_0} = \frac{L_{\max}^{RGVD}\alpha_0}{8\gamma_{coh}} = \frac{4T_0^2\gamma_{coh}^2}{3}, \text{ for } \qquad T_0 < 9/4\gamma_{coh} \tag{3-13}$$

or

$$\frac{T_{del}^{(max)}}{T_0} = \frac{L_{\max}^{sr}\alpha_0}{8\gamma_{coh}} = 3T_0\gamma_{coh}, \text{ for } \qquad T_0 > 9/4\gamma_{coh} \quad . \tag{3-14}$$
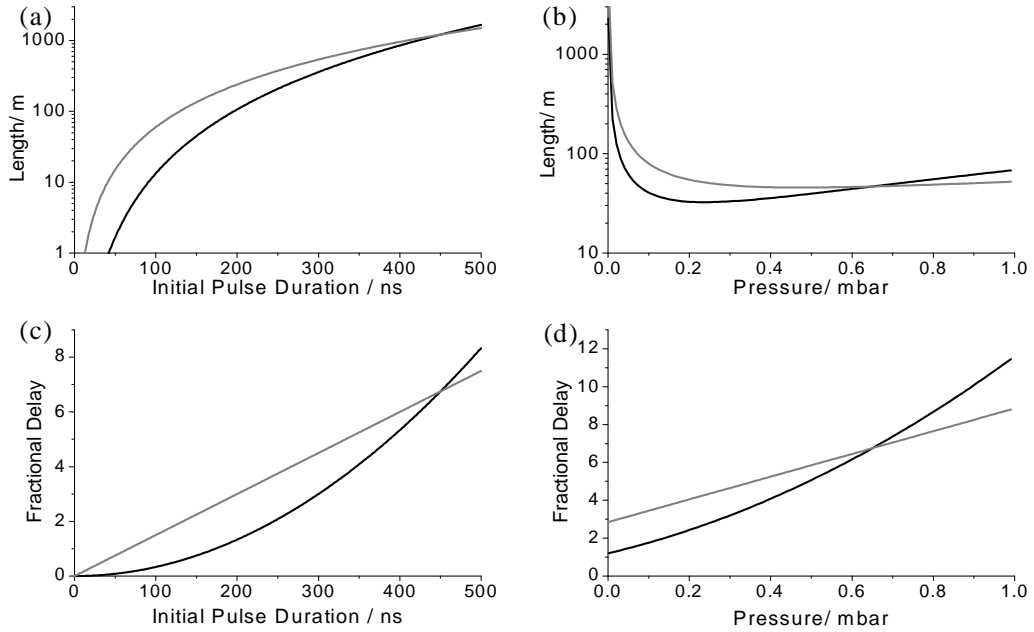
Figure 3-9: *(a) and (b) Maximum lengths as defined by R-GVD (black line) and spectral reshaping (grey line) as a function of initial pulse duration and acetylene pressure respectively. Calculated using equations (3-11) and (3-12). For (a) the experimental conditions are acetylene pressure = 25 μbar, γ_{coh} = 5 MHz and absorption lines are R11 and P11. (c) and (d) Achievable fraction pulse delay as defined by R-GVD (black line) and spectral reshaping (grey line) as a function of initial pulse duration and acetylene pressure respectively. Calculated using equations (3-13) and (3-14). Experimental conditions for (c) are as for (a).*

Equations (3-13) and (3-14) are plotted as a function of pulse duration in Figure 3-9(c). This figure shows that in these experimental conditions (same as in Figure 3-8(b)) the initial pulse duration must be greater than 200 ns to achieve a fractional pulse delay greater than 1. A probe pulse of 400 ns will be delayed by 5 pulse lengths (i.e. 2 μs). Figure 3-9(d) shows the fractional delay as a function of acetylene pressure for an initial pulse duration of 200 ns. This clearly shows that as the pressure is increased the fractional delay also increases. However, as the decoherence rate increases with the acetylene pressure, thus reducing the delay per metre. Therefore for high pressures longer fibre lengths are required. It is also important to remember that at high pressures the pulse attenuation will be increased. If higher fractional delays of shorter pulses are required, a higher coupling Rabi frequency could be used to increase the EIT linewidth through power broadening. However, by doing this the delay per metre will be reduced as explained above.

The simplified analytical model used in this chapter has enabled the key parameters which effect the magnitude of pulse delay to be identified; by increasing the absorption

coefficient while reducing the decoherence rate, large pulse delays of up to 30 ns/m are predicted. These factors are controlled experimentally using the acetylene gas pressure, the absorption line strength and the choice of HC-PCF. Increasing the length of the gas-filled fibre also increases the magnitude of the pulse delay within certain constraints defined by pulse distortion effects and pulse absorption.

Within the analytical model, the EIT feature is assumed to be Lorentzian and a Λ configuration is used to approximate the V configuration which was used in the experiment. Additionally, processes such as collision-induced energy transfer [107] and the possible role of acetylene adsorption to the inner fibre walls [108] are not explicitly accounted for. The role of these factors within the EIT system is discussed further in chapter 4.

3.8.   Example application: Gyroscope

Introduction of a slow light medium into the core of an HC-PCF could have applications in fibre optic sensing. The fibre-optic gyroscope (FOG) is an example whereby the fibre form brings several advantages [109] over a mechanical or free-space counter-part, such as enhancement of sensitivity, compactness and stability. Recent demonstrations by Kim *et al.* [110] have shown that HC-PCF has potential to improve upon the traditional FOG. The guidance of the light in an air core significantly reduces the noise imposed by Kerr, Faraday and thermal effects, which are inherently higher in a silica core [111]. It has been speculated that, with an optimised fibre design, the thermal noise of an air core gyroscope can be made 23 times lower than that of a conventional FOG [112] due to a combination of reduction in Shupe constant (relative change of propagation phase with temperature) and lower mode effective index [113]. A slow light medium in the hollow core, as demonstrated here, would add to the noise suppression due to an enhancement in the signal by a factor of the group index and thus has the potential to improve the relative rotation sensitivity of this device. Indeed, for a conventional FOG with a fibre coil radius R, the rotation induced phase-shift is

$$\Delta\phi = \frac{4\pi R^2 \Omega_{rot}\omega}{c^2}$$

(3-15)

where Ω_{rot} is the rotation rate. When slow light is implemented, this relative rotation induced phase shift is $\Delta\phi_s = n_g \Delta\phi$; the sensitivity is increased by a factor of the group index [22]. For the EIT-based system presented in this chapter, the value of the group index for a pressure of 125 µbar and γ_{coh} of 5 MHz can reach ~4. Combining this enhancement factor in the sensitivity with the aforementioned reduction in thermal noise due to use of a hollow core [112], an acetylene-filled PMC has the potential to increase the signal-to-noise ratio of a FOG by a factor of ~92.

3.9.   Further work

A key factor in the optimisations described in this chapter is the use of a larger core fibre such as 19-cell Kagome lattice HC-PCF. Fibres with core diameters of up to 80 μm have been fabricated but the attenuation of these fibres is ~ 1 dB/m at 1550 nm. Recent developments in the fabrication of extremely low loss 7-cell defect Kagome [80], as described in detail in chapter 2, have led to an increased understanding of the loss mechanisms in these fibres. Extending this work towards the fabrication of extremely low loss 19-cell defect Kagome fibres will be the next step forward and such fibres would be suitable for the optimisations discussed. Meanwhile, shorter lengths (eg. 5 metres) of current state-of-the-art 19-cell Kagome can be used to test some of the predictions made here. Techniques have now been developed, and are described in chapter 5, which enable these large dimension fibres to be integrated into PMC form.

Also, this chapter has mainly focussed on the demonstration and optimisation of pulse delay. Superluminal light also has a wide range of applications, particularly in interferometry [22] and a more detailed study into the optimisation of pulse advance in this system described is warranted.

Chapter 4

Gas Spectroscopy in Kagome Lattice HC-PCF

In this chapter, the optical properties of Kagome lattice and triangular lattice HC-PCF are compared in the specific context of gas-laser coherent interactions in gas-filled HC-PCF.

Three experiments are described which use acetylene-filled large-pitch Kagome HC-PCF to achieve new results in this field; the width and height of experimental electromagnetically induced transparency features recorded in 1-cell Kagome HC-PCF are compared to those in 7-cell PBG HC-PCF; narrow sub-Doppler features are generated in 19-cell defect Kagome fibre using saturated absorption and demonstrated as a 10 KHz accuracy optical frequency reference and the first optically pumped gas fibre-laser using 1-cell Kagome HC-PCF is demonstrated. The content of this chapter has been published in references [114-116].

4.1. Introduction

HC-PCF has been identified as an excellent candidate for gas-laser interactions as it offers tight modal confinement and low loss guidance combined with an extremely long interaction length. In chapter 2, two classes of HC-PCF were identified and distinguished by their guidance mechanism. Examples of these two classes are triangular lattice PBG HC-PCF and Kagome lattice HC-PCF. PBG HC-PCF provides extremely low loss guidance over a limited transmission bandwidth while large-pitch Kagome HC-PCF provides broadband guidance at a cost of an increased attenuation. Additionally, the physical properties of the fibres differ in that the large-pitch nature of the Kagome fibre enables low loss guidance in a core with a diameter of up to 80 μm.

In this chapter, the characteristics of these two classes of fibre are discussed with specific emphasis on gas-filled fibre applications. The smaller core, and thus higher intensity at a given power, offered by PBG HC-PCF has advantages in applications such as Raman generation where, for specific experiments, the limited transmission bandwidth of the fibre can be advantageous as it suppresses unwanted higher order Raman sidebands [117]. However, for applications such as frequency stabilisation and slow light, narrow spectral features are of paramount importance (see chapter 1). For these applications, the large-pitch Kagome fibre can be a preferable choice of gas-host, even at the cost of a slightly higher attenuation, as the large core diameter reduces decoherence due to

collisions between the confined molecules and the inner core walls of the fibre. In section 4.2, two attributes of HC-PCF are considered which are of direct relevance to gas-laser interactions in this host: firstly, the limited core diameter and secondly, surface mode guidance. The performance of both types of HC-PCF with respect to these two attributes is discussed in detail.

In the remainder of this chapter (sections 4.3 - 4.5), three experimental applications are demonstrated which emphasize regimes in which the Kagome HC-PCF has a superior performance compared to PBG HC-PCF. Firstly, the width and height of EIT features generated in acetylene-filled 7-cell PBG and 1-cell Kagome HC-PCFs are compared. Secondly, 19-cell Kagome HC-PCF is used to create the narrowest sub-Doppler feature observed so far in gas-filled HC-PCF and this feature is used as a sub-10 kHz accuracy optical frequency reference. Finally, the broadband guidance of Kagome HC-PCF is exploited in the first demonstration of an acetylene laser using population inversion. The Kagome HC-PCF used in this experiment is the first to demonstrate guidance in the mid-IR (at 3.2 μm). The latter two experiments were carried out in collaboration with co-workers from Kansas State University.

4.2.   Large-pitch Kagome vs. Triangular-lattice PBG HC-PCF

In this section, two key properties of HC-PCF which are crucial in defining the application of this fibre as a gas host for many coherent optical experiments are discussed.

4.2.1.   Decoherence Effects of Micron-scale Confinement in HC-PCF

As first discussed in chapter 1, tight gas confinement in a micron-scale hollow core, such as that offered by HC-PCF, leads to broadening of sub-Doppler features due to collisions between the confined molecules and the inner core walls of the fibre. This can be mitigated by increasing the core diameter as the dephasing rate due to wall collisions scales, for low gas pressure, as $\sim R_c^{-1}$, where R_c is the core radius.

The core diameter of PBG-guiding HC-PCF is intrinsically limited by the guidance mechanism; typically, for a central transmission wavelength of 1550 nm the cladding pitch required is ~3 μm and therefore the core diameters are ~10 μm and ~20 μm for 7-cell and 19-cell core designs respectively. It is possible to fabricate PBG-HC-PCF with a 37-cell core (with ~30 μm core diameter) but these fibres have so far posed a real challenge in terms of achieving low loss guidance. Additionally, 37-cell defect fibres are very multimode and support many surface modes (see section 4.2.2). In contrast, large-pitch fibres, such as Kagome lattice HC-PCF can be fabricated with core diameters up to 80 μm [72] and therefore present a medium for decreasing spectral linewidths of sub-Doppler features observed in gas-filled HC-PCF. This is highlighted in Figure 4-1 where
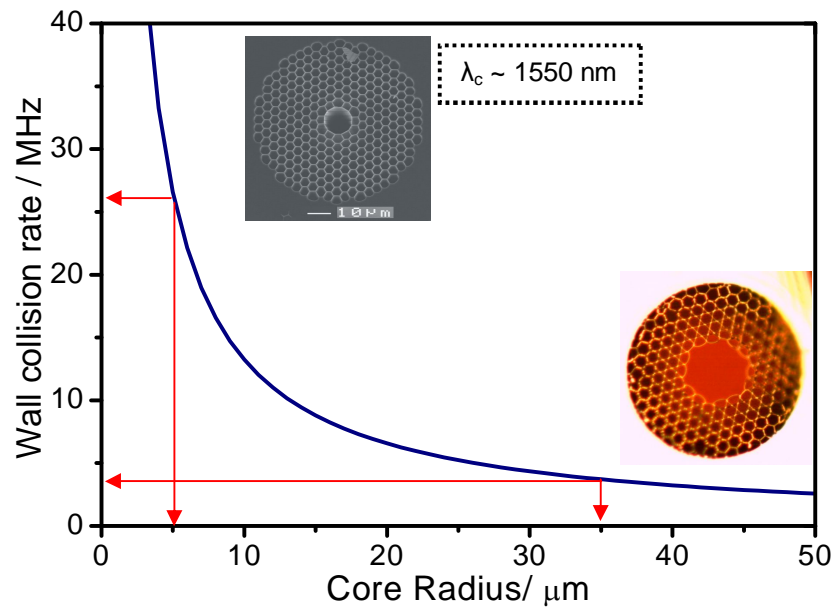
Figure 4-1: *Effects of dephasing due to wall collisions, calculated using equation (1-28) for acetylene gas at 1 mbar. Two fibre SEMs are shown inset representing 7-cell triangular and 19-cell Kagome HC-PCF. Using the latter, the dephasing rate is dramatically reduced. The central wavelength of the 7-cell PBG fibre's guidance band (λ_c) is 1550 nm.*

the dephasing rate, due to collisions between the confined molecules and the inner core walls of the fibre (equation 1-28), is plotted as a function of core radius for acetylene gas. Large core (19-cell defect) Kagome fibre has a dephasing rate of ~3 MHz while a 7-cell defect PBG fibre designed for guidance at 1550 nm has an expected dephasing rate contribution of ~26 MHz to the sub-Doppler linewidth. This large reduction in dephasing rate clearly highlights the potential of large core Kagome HC-PCF as a gas host for applications where narrow spectral features are required.

It is informative here to consider the mean free path (equation (1-31)) of acetylene molecules at the pressures used in the experiments described in this chapter, to confirm that in the larger core Kagome it is still collisions between the acetylene molecules and the inner core walls which limit the spectral linewidth, not collisions between the acetylene molecules themselves. From equation (1-31) the mean free path is ~ 170 μm for a gas pressure of 0.5 mbar and ~ 850 μm for a pressure of 100 μbar; these values confirm that the collisions between the confined molecules and the inner core walls are still the relevant limiting factor for the experimental conditions presented here.

Additionally, it is noteworthy to consider briefly current limitations on the maximum core diameters of HC-PCF. Physically, to maintain the ease of handling and integration that fibre-based devices provide, it is necessary to keep the outer diameter of the fibre below approximately 0.5 mm, due to considerations regarding the coiling of the fibre and

thus its compactness. Optically, as the core size increases, the number of guided modes also generally increases. For some applications a multimode fibre is not desirable.

4.2.2. Surface Modes in HC-PCF

The modal properties of HC-PCF are also an important factor in determining possible applications. PBG HC-PCF can support surface mode guidance which is an undesirable property for high resolution spectroscopy. Surface modes are localised in the glass core-surround and can hybridise with the core guided modes [118]. This hybridisation lifts the degeneracy of the two orthogonal polarisations of the fundamental core guided mode, thus enabling mode beating between these polarisations. This mode beating manifests itself as a noisy background on the fibre transmission spectrum which can masquerade as or obscure absorption features in the transmission spectrum. The end result is that the SNR of any absorption features is reduced due to surface mode guidance.

The spectral evolution of the two fundamental modes (HE_{11}) and two surface modes (SM), as calculated for a 10 μm core diameter, 7-cell defect PBG fibre is shown in Figure 4-2(a)[1]. In this figure three different points are highlighted; A, B and C. An anti-crossing between the SM and the HE_{11} modes at a wavelength of ~1.47 μm (point C); at this point the presence of the surface modes lifts the degeneracy of the two HE_{11} modes, indicated by the induced change in effective index. Figure 4-2(b) shows the electric field distribution calculated for the modes at points A, B and C and the corresponding modal profiles. These profiles clearly highlight that in the vicinity of an anti-crossing between the core modes and the surfaces modes, hybridisation between the two types of modes occurs. Mode rotation in the vicinity of anti-crossing events is studied further in [119].
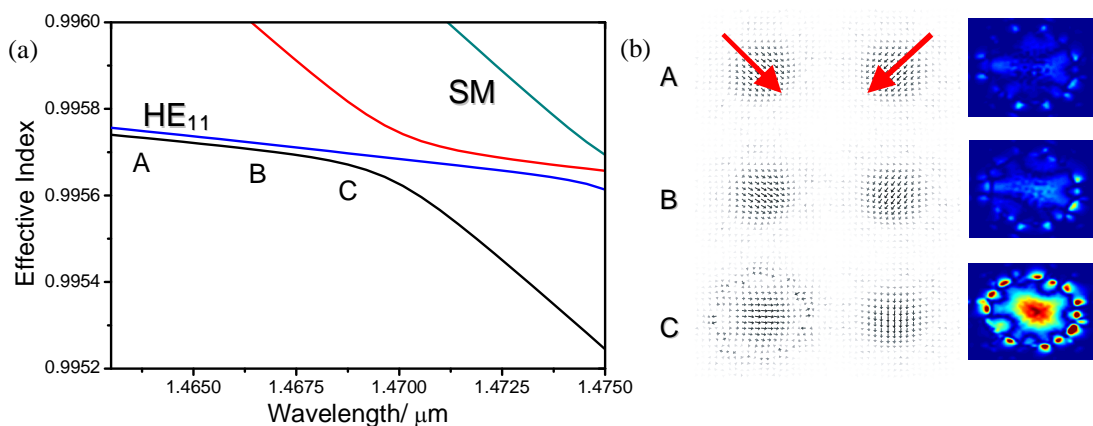

Figure 4-2: *(a) Effective index of HE_{11} core modes and surface modes (SM) supported in a 7-cell PBG HC-PCF as a function of wavelength. Hybridisation of these modes occurs in the region of the anti-crossing event.(b) Mode field profiles at points A, B and C elucidate this hybridisation.*

---

[1] All calculations of mode profiles and mode trajectories by P. J. Roberts.

To highlight the magnitude of the oscillations in transmission which this mode hybridisation induces, Figure 4-3(a) shows the transmission spectrum of 4 metres of 7-cell defect PBG fibre filled with acetylene at ~200 µbar. The background oscillations have a magnitude of up to 35% of the total absorption signal, masking any spectroscopic signals below this limit and severely reducing the SNR of the absorption feature present in the trace. This parasitic effect is further illustrated using a sub-Doppler spectroscopic signature in section 4.3. In PBG HC-PCFs which support surfaces modes, these oscillations can be controlled by the use of polarisation controllers before the input to the gas-filled fibre but cannot be completely removed.

These surface modes can be extinguished in PBG fibre by tailoring the core surround thickness or shape [76, 77, 118]. Alternatively, a large-pitch fibre such as Kagome HC-PCF can be used. Figure 4-3(b) shows the transmission through 1.5 m of 1-cell Kagome fibre filled with ~1 mbar of acetylene. In this figure, the extremely flat background transmission enables the observation of hot bands; these are absorption features due to transitions between excited states of the acetylene overtone bands which, therefore, have extremely small transition dipole moments (typically 10 to 100 times weaker than for an a transition in the $v_1 + v_3$ overtone band of acetylene [36]). This demonstration clearly highlights the potential to use Kagome HC-PCF for high precision spectroscopy applications as the SNR of the resonant features is greatly increased when compared to those observed in gas-filled PBG HC-PCF.

Initially, it was thought that the smooth background transmission of a Kagome HC-PCF could be explained by the multimode nature of this fibre which could cause the oscillations to average out. However, further studies have shown that, in most cases, this fibre has a very strongly favoured fundamental mode due to high mode field overlap
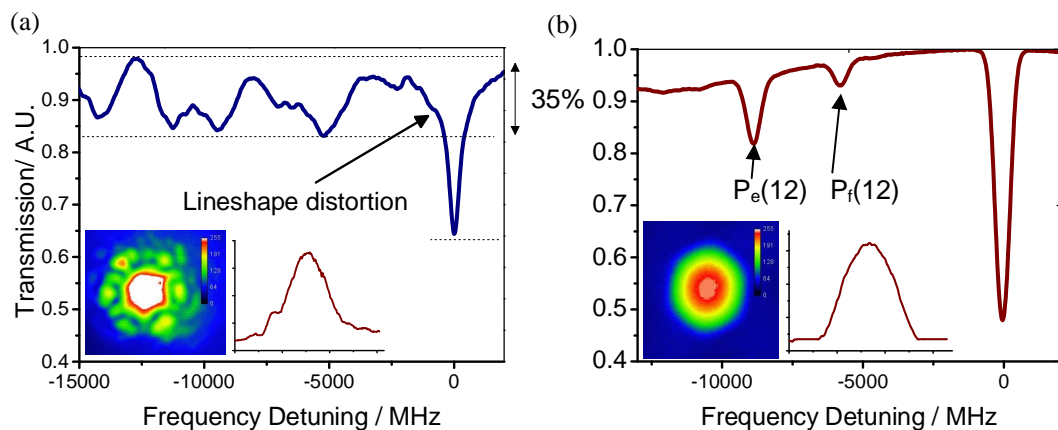

Figure 4-3: *Transmission through 4 m of acetylene-filled triangular lattice (left) and 1.5 m of acetylene-filled Kagome lattice HC-PCF (right).The main absorption line is the P(20) line from the $v_1 + v_3$ overtone band of acetylene. Experimental mode profiles and cross sections are shown inset to each figure.*

between this mode and a quasi-Gaussian input laser beam and therefore the fibre can exhibit almost single mode behaviour. This explanation does not fully explain the near-single mode behaviour of the fibre; it is also believed that the higher order core modes suffer a much larger transmission loss due to higher overlap with the cladding modes but further work is required to confirm such a speculation. In fact, the inhibited coupling guidance mechanism of Kagome HC-PCF can explain the flat background transmission. A key part of the inhibited coupling between core and cladding modes in Kagome fibre, as described in chapter 2, is the very small spatial overlap between the fundamental core mode and the cladding modes. In PBG fibres, 0.12-0.8% of the fundamental core guided mode overlaps with the glass surround compared with only 0.025% in Kagome-structured fibres [120]. This, along with the strong transverse phase mismatch due to the fast oscillating cladding modes means that the fundamental core modes do not hybridise with any of the modes supported in the glass and therefore no mode beating is evident on the transmission spectrum.

4.3. Sub-Doppler Spectroscopy in Kagome HC-PCF

In chapters 1 and 3, EIT was introduced as a coherent optical technique for creating a sub-Doppler feature within a Doppler-broadened absorption line. For many applications, such as the slow light scheme described in chapter 3, this sub-Doppler feature is ideally spectrally narrow. The use of large core HC-PCF, such as Kagome fibre, for the gas-laser interaction has the potential to reduce the linewidth of the EIT feature due to the dependence of the decoherence rate on the core diameter. For example, considering the two fibres presented in Figure 4-1 (19-cell Kagome and 7-cell PBG HC-PCF) the
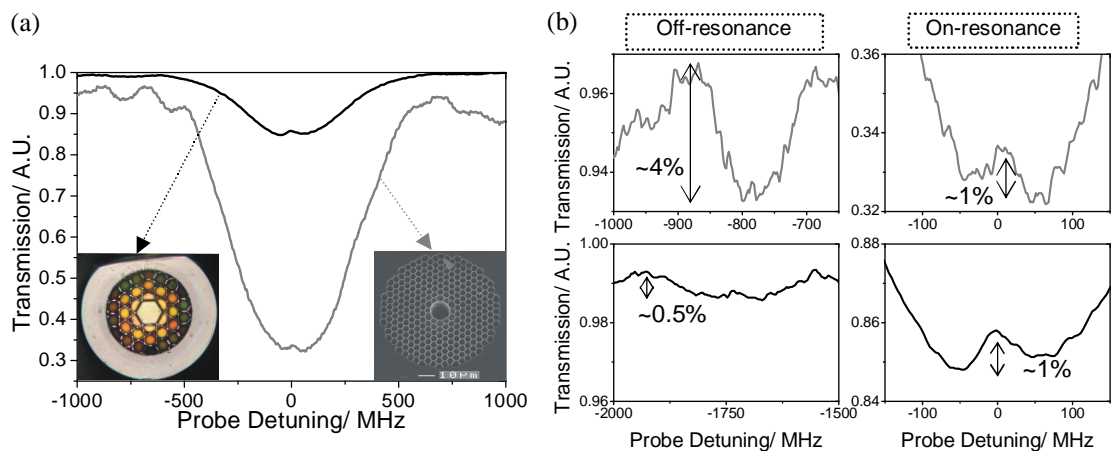
Figure 4-4: *Comparison between EIT in 1-cell Kagome HC-PCF (black line) and 7-cell PBG-HC-PCF [101] (grey line). Oscillatory background on trace from 7-cell PBG-HC-PCF degrades SNR of absorption features and is especially important when EIT feature is small (both EIT features <5% height).(a) Full EIT traces. An optical microscope image of the Kagome HC-PCF (left) and a SEM of the 7-cell PBG fibre (right) are also shown inset. (b) Magnified off-resonance and on-resonance signals, all to the same vertical scale, further highlight the degradation of the SNR in the PBG HC-PCF.*

decoherence rate due to collisions between the confined molecules and the inner core walls is reduced by more than a factor of 7.

All previously published demonstrations of EIT in acetylene-filled HC-PCF have used PBG HC-PCF as the gas host [43, 44]. EIT in rubidium-filled 1-cell defect Kagome HC-PCF was demonstrated in [47], however in this experiment the inner core walls were coated with a polymer solution which complicates the analysis of the EIT feature linewidth; more details on the anti-relaxation effects of polymer coatings are discussed in chapter 7. In this section, the first experimental results recorded in acetylene-filled Kagome HC-PCF are presented and compared and contrasted with previously published results achieved in 7-cell PBG HC-PCF [101].

Experiment

The experimental set-up used is described in chapter 3; one difference is that, for the set of results shown here using the Kagome HC-PCF, the second end of the HC-PCF was not spliced to SMF but mounted in a vacuum chamber. The 7-cell PBG HC-PCF has a core diameter of 10 μm and a length of ~4 metres. The 1-cell Kagome HC-PCF has a core diameter of 26 μm and a length of ~1.5 m. The acetylene pressure is approximately 100 μbar in both fibres.

Signal-to-noise Ratio of EIT features

Figure 4-4 compares EIT traces recorded in the 1-cell Kagome HC-PCF (black line) and the 7-cell PBG-HC-PCF (grey line). These two EIT traces were chosen for comparison because the absolute height of both of the EIT features (as a fraction of the total transmitted power) is approximately equal and also extremely small (~1%). For such small EIT features the SNR of the fibre transmission is extremely important. It is clear from the experimental traces shown in Figure 4-4 that the SNR of the 7-cell defect HC-PCF is reduced by the oscillatory background transmission attributed to the interaction between surface modes and the core-guided modes. In fact, as highlighted by Figure 4-4 (b), the EIT feature height in the PBG HC-PCF is much smaller than the amplitude of the oscillatory background; this sets a limit on the minimum acetylene pressure (or fibre length or absorption line strength) which can be used in this configuration, as an EIT feature within an absorption line with low signal contrast would be obscured by the noisy fibre transmission. In contrast, the near flat background transmission of the Kagome HC-PCF enables the absorption line and the EIT feature to be clearly distinct even though the fractional absorption is reduced for the absorption trace shown due to the shorter fibre length.
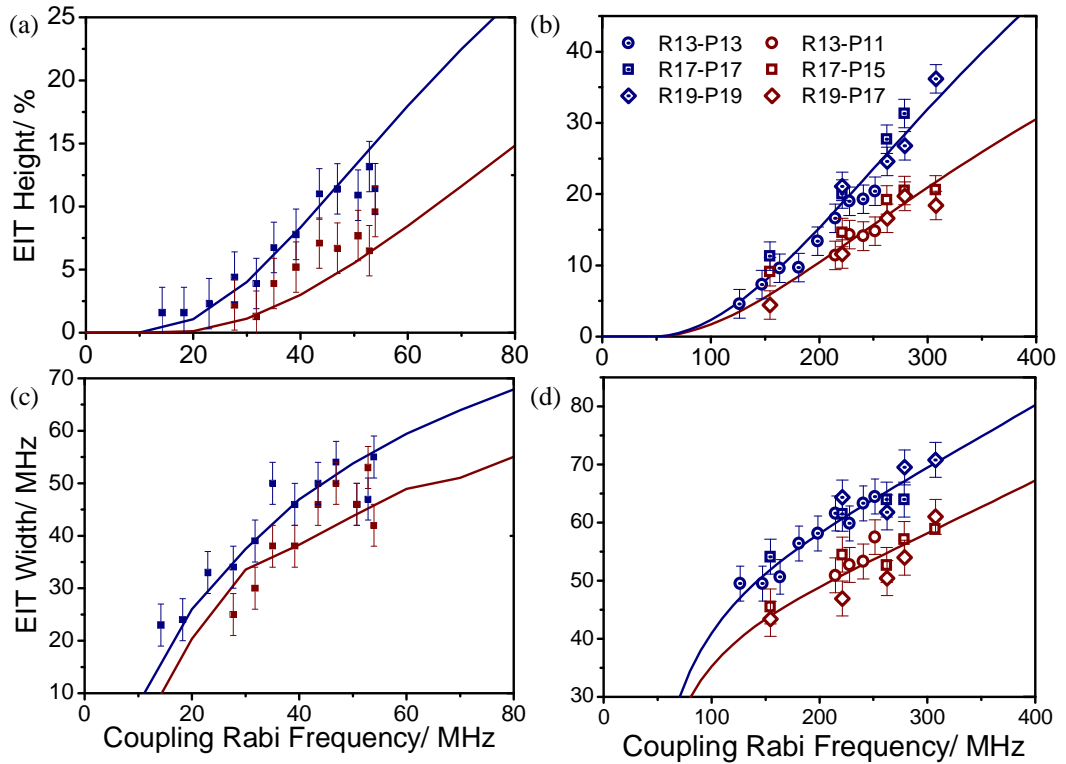
Figure 4-5: *EIT feature height and width evolution for 1-cell Kagome ((a) and (c) respectively) and 7-cell PBG ((b) and (d) respectively) HC-PCFs. Data from V configuration shown in blue and Λ configuration in red. For Kagome fibre data V configuration is R13P13 and Λ configuration is R13P15, configurations for 7-cell PBG data are indicated in legend. Theoretical fits (blue and red lines) were found using the numerical model developed in reference [101]. 7-cell data is taken from reference [101].*

EIT Feature Height and Width Comparison

Figure 4-5 shows the evolution of the height and width of the EIT features in the Kagome and PBG HC-PCFs, in both V and Λ configurations, as a function of coupling Rabi frequency. Comparing Figure 4-5(a) and (b) it is clear that the EIT feature height is larger in Kagome HC-PCF than in the PBG HC-PCF for a given coupling Rabi frequency. This increase in transparency height occurs even though the attenuation of the Kagome HC-PCF (~2 dB/m in this case) is significantly higher than the PBG HC-PCF (~150 dB/km).

By comparing Figure 4-5(c) and (d) it is apparent that the EIT feature width is reduced by almost a factor of 2, in the low coupling power limit, in the 1-cell Kagome HC-PCF compared to the 7-cell PBG HC-PCF. It is noteworthy that the EIT features in the Kagome HC-PCF are generated at much lower coupling laser Rabi frequencies which reduces the contribution to the linewidth from power broadening.

Figure 4-6: *V and Λ EIT configurations (left and right respectively). Parameters are highlighted which are included in the numerical model (from reference [101]). Ω_c and Ω_p are the coupling and probe laser Rabi frequencies respectively, Γ_{ij} des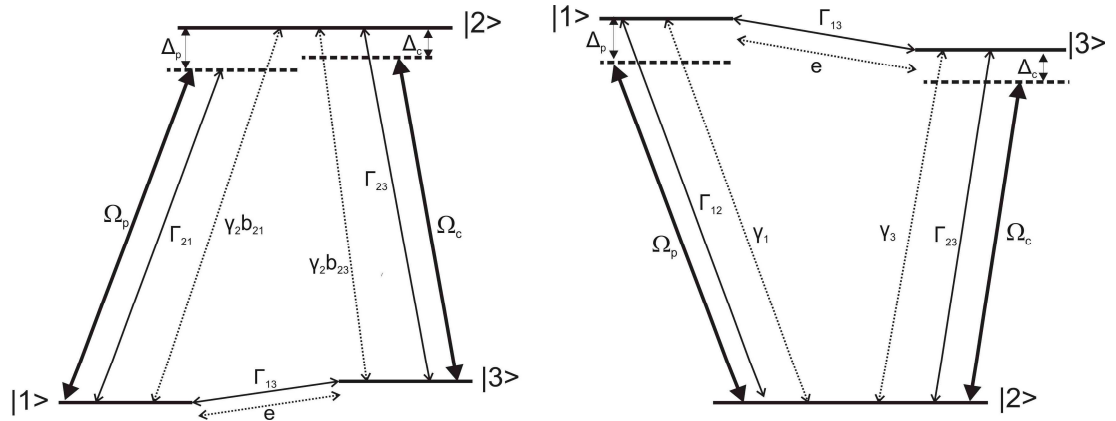cribes the total decoherence between levels i and j, γ_i describes the total population decay from level i, e is a non-radiative population exchange rate and Δ_c and Δ_p describe the detuning of the coupling and probe lasers from resonance respectively. For the work here, $\Delta_c = 0$. In the Λ configuration, the branching ratios b_{21} and b_{23} are both assumed to be 0.5.*

Furthermore, comparison between the EIT features observed in the V and Λ configurations shows that the same trend is observed in both fibres; the EIT features are larger and wider in the V configuration.

Numerical Model

The theoretical fitted lines presented in Figure 4-5 were calculated using a numerical model which is described in detail in [101]; the essential parameters included in this model are highlighted in the schematics shown in Figure 4-6. The simple analytical model presented in chapter 3 is not used here. Although its simplicity aids extraction of the scales of the experimental parameters required to optimise the pulse delays in the slow light system, this simplicity also limits its accuracy in describing the complex EIT system. This is especially significant in acetylene which has such a complicated absorption spectrum; the complex nature of the acetylene absorption spectrum is discussed in detail in the Appendix.

The numerical model assumes that the interacting system (describing the three levels of the V or Λ configuration) is closed; this means that the model does not allow population decay to other energy levels outside the interacting system. For acetylene this is not very realistic as there are many dipole allowed transition pathways between the excited and ground states of the system. To account for this inaccuracy, a non-radiative population exchange term, *e*, is introduced to the model. The numerical model also includes the fibre length, acetylene pressure and the dipole moment of acetylene and includes a scaling factor *c* which accounts for experimental uncertainties in the coupling laser Rabi frequency which arise from uncertainty in the input splice loss. This model is sufficient for the comparative study between different HC-PCF described here.

Table 4-1: *Comparison between the fitted parameters determined by the numerical model, found using experimental data recorded in acetylene-filled 10 µm core diameter PBG HC-PCF, 26 µm core diameter Kagome HC-PCF and 45 µm core diameter Kagome HC-PCF. The full experimental data from the 45 µm core Kagome HC-PCF is presented in chapter 5 but the numerical fit values are included here for comparison. The decoherence rate between the uncoupled levels in the V configuration,* Γ_{13}^V *,is highlighted and discussed in detail in the text.*

Scheme	Parameter	Definition	Fit: 7-cell PBG (10 µm core)	Fit: 1-cell Kagome (26 µm core)	Fit: 1-cell Kagome (45 µm core)
Both	c	Coupling Rabi frequency scaling	0.879	1.4	0.92
	$\gamma_2^V = \gamma_1^\Lambda = \gamma_2^\Lambda$	Excited State Optical Decay	110 MHz	14.2 MHz	15.4 MHz
V	$\Gamma_{12}^V = \Gamma_{32}^V$	Decoherence (coupled levels)	32.1 MHz	31.1 MHz	10.5 MHz
	Γ_{13}^V	**Decoherence (uncoupled levels)**	**44.4 MHz**	**16.5 MHz**	**7.4 MHz**
	e^V	Population exchange rate	33.2 MHz	5.5 MHz	0.04 MHz
Λ	$\Gamma_{21}^\Lambda = \Gamma_{23}^\Lambda$	Decoherence (coupled levels)	22.1 MHz	24.1 MHz	
	Γ_{32}^Λ	Decoherence (uncoupled levels)	55.7 MHz	36.0 MHz	
	e^Λ	Population exchange rate	18.2 MHz	5.5 MHz	

Table 4-1 summarises the fitted values produced by the numerical model using the experimental EIT height and width data. As well as data from the 7-cell PBG HC-PCF and the 26 µm core diameter 1-cell Kagome HC-PCF (which is shown in Figure 4-5), the parameters found using EIT data recorded using acetylene-filled 45 µm core diameter Kagome HC-PCF are included; the full experimental data recorded using this fibre is presented in chapter 5 but the key details are that the EIT was recorded in a V configuration using lines P25 and R25 from the $v_1 + v_3$ overtone band of acetylene and the acetylene pressure was 0.5 mbar. Inclusion of this extra data aids the identification of trends within the numerical fit values which are related to the core diameter of the HC-PCF.

The fitted values produced by the numerical model indicate that all of the decoherence and optical decay rates decrease as the fibre core diameter is increased. Specifically, the dependence of the fitted decoherence rate between the uncoupled levels in the V configuration on the fibre core radius is highlighted in Table 4-1 and plotted in Figure 4-7. The theoretical decoherence rate due to collisions between the confined acetylene molecules and the inner core walls of the fibre is also plotted in Figure 4-7 (equation 1-28). It is clear that there is good qualitative agreement between this theoretical contribution and the fitted decoherence values produced by the numerical model; both the theoretical decoherence and the fitted values scale approximately inversely with the

core radius. There is a vertical offset between the theoretical decoherence and the numerical fitted values which is expected due to contributions to the decoherence rate from the probe and coupling laser linewidths (5 MHz maximum for each laser) and the pressure broadening (~ 1 MHz for 0.1 mbar acetylene pressure [4]). These contributions are independent of the core radius and therefore cause a constant vertical offset. From Figure 4-7 it is clear that the vertical offset is not constant, in fact it decreases with core radius and this could be indicative of the accuracy limitations in the numerical model.

The population exchange rate, e, also decreases as the core radius is increased. As mentioned previously, this rate is included to account for the open nature of the realistic EIT system. The exchange rate is expected to be related to the collision rate of the confined molecules with the inner core walls because these collisions do not only cause decoherence but also act to thermalise the population distribution [101]. Collision-induced state-to-state energy transfer within the highly excited overtones of acetylene is studied in [107] using time-resolved optical double resonance spectroscopy. Through collision-induced energy transfer, an initially excited rovibrational state in the near-IR transfers population to a myriad of destination states; population can be transferred between rotational states within a single vibrational level and between vibrational states. This process of collision-induced energy transfer is a speculative explanation of the dependence of the population exchange rate, e, on the fibre core radius as it is dependent
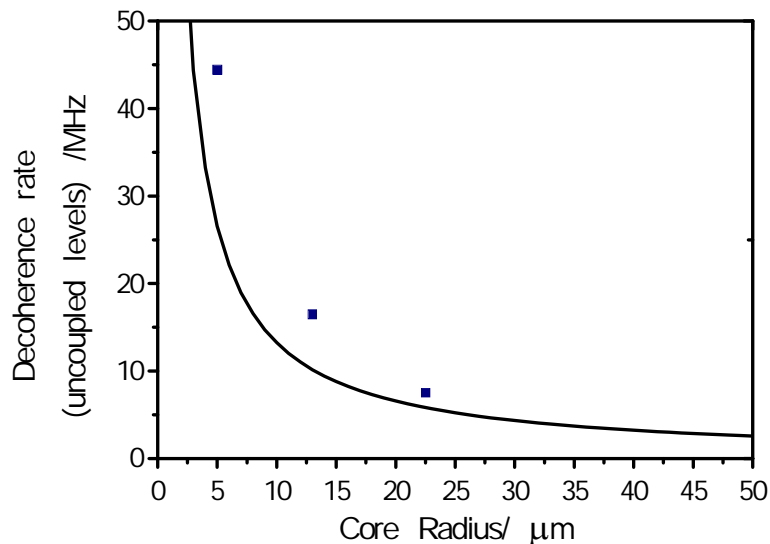
Figure 4-7: *Decoherence rate produced by the numerical fit to the experimental data (blue points) and theoretical contribution (black line) to the decoherence rate due to collisions between the confined acetylene molecules and the inner core walls of the fibre. It is clear that the values produced from the numerical model follow the same trend (approximately $\propto R_c^{-1}$) as the theoretical contribution from equation (1-28). Vertical offset can be attributed to other contributions to the decoherence rate which are independent of core radius, specifically due to the laser linewidths and pressure broadening.*

on the collision rate.

It is also noteworthy that the fitted value of excited state optical decay is significantly reduced in the larger core Kagome HC-PCF compared to the PBG HC-PCF. In [101] the large value (110 MHz) for this decay in the PBG HC-PCF is attributed to the fact that the numerical model treats the interacting system as closed and therefore the optical decay from the excited states to other states outside the interacting system is not included properly, even with the addition of the population exchange rate. The reduction in the optical decay for large core HC-PCF is a further indication of the role that collisions between the confined molecules and the inner core walls have in the process of collision-induced energy transfer between states as discussed above. Towards the limit of zero collisions, the authors in [107] observe a single resolved spectral peak instead of a multitude of peaks which are the signature of collision-induced energy transfer. In the acetylene EIT system, this limit of zero collisions could correspond to the interacting system actually being closed.

Limitations and Future Directions

The fitted values from the numerical model shown in Table 4-1 are not completely in line with the expected values. For instance, the decoherence rate between the coupled levels in the V configuration is higher than the decoherence rate between the uncoupled levels for the 26 µm core Kagome HC-PCF. Additionally, the excited state optical decay rate is higher in the larger core Kagome fibre than in the smaller core Kagome fibre. In order to increase the accuracy of these numerical values it will be necessary to record a larger number of experimental values over a larger range of coupling Rabi frequencies. Moreover, additional datasets taken in Kagome fibre cores with different core diameters would add weight and more quantitative value to the trends so far observed.

There are also some interesting features of EIT which are relevant to the work here but not accounted for by the numerical model. Firstly, the dependence of the EIT shape on the profiles of the coupling and probe beams. Taïchenachev *et al.* [121] considered the effect of Gaussian and step function beam profiles in the context of CPT and found that while the latter beam profile results in a Lorentzian CPT profile, a Gaussian beam profile results in a more complex feature shape. This is particularly interesting in the context of the large core Kagome fibres which can support several modes and may provide a direction for future work. In particular, the effect of modal overlap may be interesting if the coupling and probe beams were coupled into different modes of the fibre.

A related topic is the interplay between the linewidth broadening due to collisions between the confined molecules and the inner core walls and transit-time broadening. Transit-time broadening describes broadening of a spectral feature due to the finite time that a moving molecule spends interacting with a laser beam if the beam diameter is

smaller than the dimensions of the gas host. It is possible that this source of broadening may play a more dominant role in larger core fibres.

Finally, a study into the effect of the tight confinement provided by HC-PCF on the gas chemistry may provide interesting insight into the interaction between the confined molecules and the inner core walls. Specifically, the role of adsorption of acetylene onto the silica walls and subsequent re-release into the gas-phase would be of direct relevance.

To summarise the results presented here; EIT features observed in acetylene-filled Kagome lattice HC-PCF have been shown to be spectrally narrower than in acetylene-filled 7-cell PBG HC-PCF. This is attributed to the larger core diameter provided by Kagome HC-PCF. Additionally, the flat background transmission of the Kagome HC-PCF increases the SNR of absorption features observed in the gas-filled fibre.

4.4. Optical Frequency Reference based on Acetylene-filled Kagome Lattice HC-PCF [115] [2]

Saturated absorption spectroscopy (SAS) was introduced in chapter 1 as an alternative technique for creating a sub-Doppler feature within an absorption line. Here, SAS is used to create a narrow spectral feature in an acetylene-filled 19-cell Kagome lattice HC-PCF (shown inset in Figure 4-8). The hexagonal fibre core has dimensions of 68 × 48 µm which significantly reduce the contribution from wall dephasing effects to the feature linewidth. Using equation (1-28) the wall collision contribution to the linewidth is estimated to be between 3 and 5 MHz.

Experiment

The experimental set-up for SAS is shown in Figure 4-8. The laser source is an Orbits Lightwave CW fibre laser with a narrow linewidth (~500 Hz at 100 ms averaging time). Light from the laser is amplified using an EDFA and split into the pump (90%) and probe (10%) beams. A further tap on the probe arm is used for spectral calibration. The remaining probe beam is modulated by an acousto-optic modulator (AOM) so that any interference between the probe and pump beams occurs at the AOM modulation frequency of 55 MHz. Before the pump and probe beams are coupled into the HC-PCF, their polarisations are orthogonalised using polarisation optics, enabling beam separation at the fibre output. The probe beam trace is detected on a fast photodetector.

SAS and CW Laser Stabilisation

Using the set-up shown in Figure 4-8 with the 19-cell Kagome HC-PCF enabled the observation of the narrowest spectral features achieved so far in gas-filled HC-PCF. An example probe trace is shown in Figure 4-9. This trace is recorded by sweeping the

---

[2] Work carried out in collaboration with Kansas State University.

source laser frequency across the P(13) line from the $v_1 + v_3$ overtone band of acetylene. The FWHM of the sub-Doppler feature is 8 MHz. This compares with sub-Doppler linewidths of ~35 MHz and 22 MHz recorded in acetylene-filled 7-cell and 19-cell PBG HC-PCFs [122] respectively and thus represents a significant reduction in linewidth and therefore improvement in SNR. Further linewidth reduction could be achieved by employing the slow molecule selection technique described in [123].

The sub-Doppler feature shown in Figure 4-9 was used to stabilise the CW fibre laser source to the frequency of the P(13) absorption line by modifying the set-up shown in Figure 4-8. The modified experimental set-up incorporates a frequency modulation (FM) spectroscopy stabilisation scheme and is shown schematically in Figure 4-10(a). FM is necessary to create an asymmetric error signal which can be fed back to the source laser to correct fluctuations in frequency.

In Figure 4-10(a), the output from the CW fibre laser is split into three arms. Two of these arms are the pump and probe beams. The pump beam is amplitude modulated (AM) at f_{AM} = 900 kHz in order to provide a means to reduce the offset due to the Doppler-broadened background of the sub-Doppler feature. The probe beam is modulated using an electro-optic modulator to produce two sidebands at $\pm f_{FM}$ (f_{FM} = 22 MHz). This beam is then coupled into the gas-filled HC-PCF, again via polarisation optics and counter-propagating with the pump beam. The two modulation sidebands are 180º out of phase and therefore cancel completely if the laser frequency is exactly on resonance. However, if the laser frequency fluctuates, one sideband will be absorbed more than the other and therefore the frequency modulation is effectively transformed into amplitude modulation by the sub-Doppler feature. This amplitude modulation is detected by the high bandwidth photodetector at the output of the HC-PCF. The error
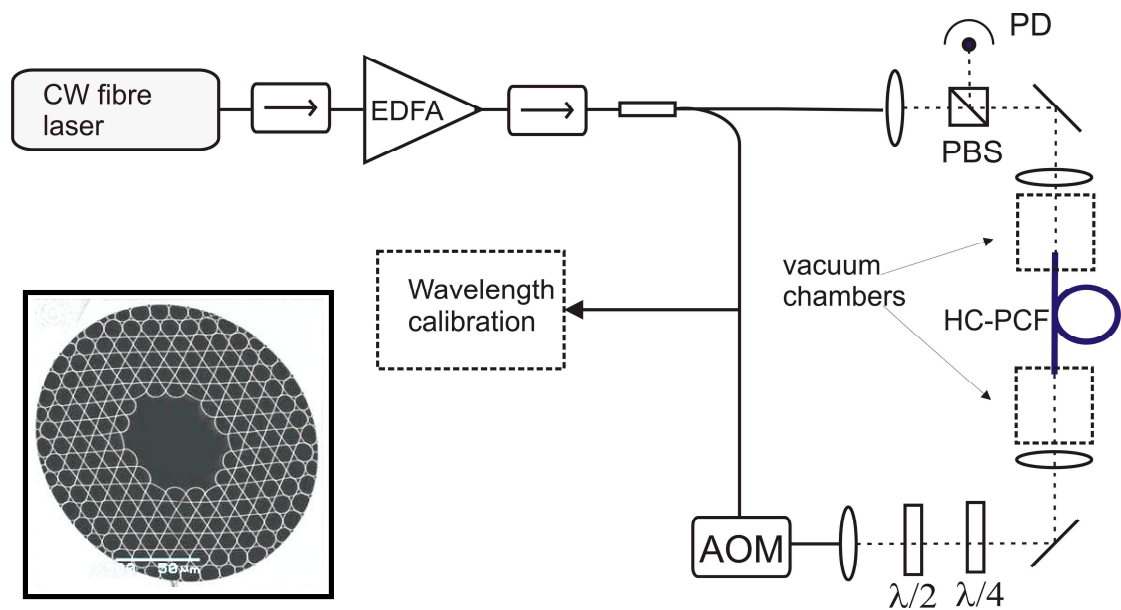

Figure 4-8: *Experimental set-up used for SAS. EDFA; Erbium-doped fibre amplifier, PD; photodetector, PBS; polarising beam splitter, AOM; acousto-optic modulator.*
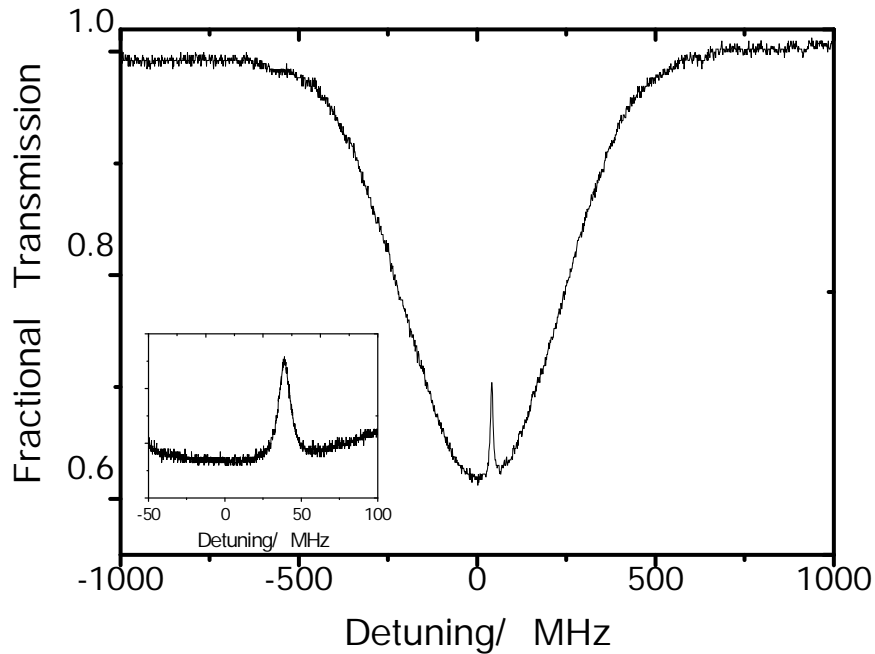
Figure 4-9: *Experimental SAS feature recorded in 4.1 m of acetylene-filled 19-cell defect Kagome HC-PCF for a pump power exiting the fibre of 32 mW. Inset shows the linewidth of the sub-Doppler feature is 8 MHz [115].*

signal is then isolated through filtering, amplifying and mixing the electronic signal from the photodetector at f_{FM} and f_{AM}. The resultant error signal (shown inset to Figure 4-10(a)) is then fed back to the source laser's piezoelectric transducer via a servo to correct the frequency fluctuation.

The frequency stability of the laser was characterised by heterodyning the stabilised laser output with a carbon nanotube fibre laser (CNFL) frequency comb. The comb repetition frequency, f_{rep}, is 167 MHz and the carrier envelope offset frequency, f_0, is 60 MHz. Further details of this frequency comb are described in [124]. A schematic of the experimental set-up used for this measurement is shown in Figure 4-10(b). The parameters of the frequency comb are stabilised using a GPS-disciplined rubidium (Rb) oscillator and are counted using 12 digit counters. The RF beat signal, f_{beat}, is counted using a 10-digit counter. From this measurement it was found that the relative frequency instability of the optical reference was $< 1.2 \times 10^{-11}$ (equivalent to 2.3 kHz) at a 1 s gate time and was limited by the Rb/GPS reference. This relative frequency instability is within an order of magnitude of acetylene frequency references in power build-up cavities and gas cells at 1 s averaging times [125-127]. The higher instability is attributed to the larger sub-Doppler width (8 MHz) achieved using the gas-filled fibre interaction scheme and therefore can be potentially reduced by using a HC-PCF with an even larger

core, lower acetylene pressure or the slow molecule selection scheme mentioned above [123].

Absolute Frequency of the Optical Reference

The absolute frequency of the optical reference was measured using a free-space prism
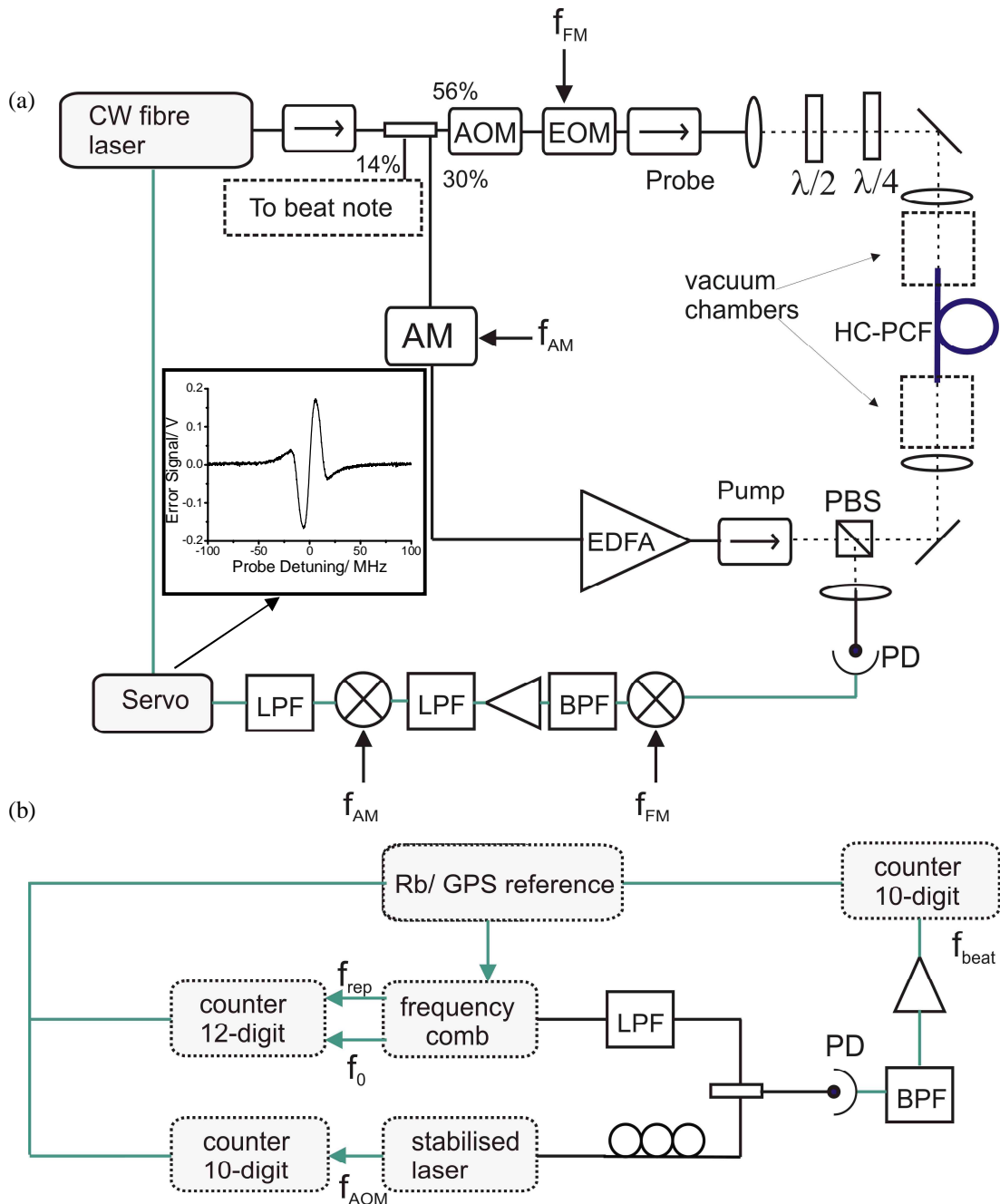
Figure 4-10: *(a) Laser stabilisation using FM spectroscopy. Probe beam is modulated using an electro-optic modulator (EOM) and pump beam is amplitude modulated (AM) to reduce offset due to Doppler-broadened background. Electronic signal from photodetector (PD) is filtered using a bandpass filter (BPF), amplified, filtered using low pass filters (LPF) and mixed at the frequency and amplitude modulation frequencies, f_{FM} and f_{AM} respectively to produce error signal (shown inset) (b) Set-up for heterodyne beat note measurement to determine stability of optical reference. Electrical signals are highlighted in green.*

based Cr:forsterite (Cr:f) frequency comb. The full measurement technique is described in [115]. Six separate measurements lead to a single value of the stabilised laser frequency which agreed with all measurements to within 100 kHz. However, a higher accuracy of ± 20 kHz was expected from the 8 MHz linewidth of the sub-Doppler feature (± 2 kHz is achieved using a ~1 MHz feature in references [127-129]). The source of this larger inaccuracy was found to be the laser alignment into the HC-PCF; the stabilised laser frequency was found to be very dependent on small changes in probe and pump beam alignment. This sensitivity was attributed to different spatial modes of the fibre experiencing different phase shifts. By cementing the input alignment it is thought that these shifts can either be eliminated or at least held to a constant value.

In order to measure the absolute frequency of the optical reference the input coupling to the Kagome fibre and the fibre connected to the photodetector was optimised which, while maintained, made the measurement of the laser frequency repeatable to ± 20 kHz. The absolute frequency of the P(13) line from the $v_1 + v_3$ band of acetylene was measured as 195,580,979,378.0 $\pm$ 9.3 kHz. The error budget includes contributions from pressure fluctuations, fibre alignment, pump power variations and fibre attenuation. This accuracy compares, to the same order of magnitude, with that currently achieved by bulky power build up cavities [130, 131] and thus presents gas-filled HC-PCF as a competitive standard for precision spectroscopy applications.

Future Work

The main drawback with the scheme presented in Figure 4-10 is that the HC-PCF is mounted in vacuum chambers. This leads to the issues with alignment of the probe and pump beams described above, as well as pressure fluctuations within the fibre. Additionally, this set-up severely limits the portability and thus the applications of this laser stabilisation scheme.

Therefore, the next step forward in this work will be to replace the fibre mounted in vacuum chambers with a Kagome HC-PCF PMC. The large dimensions of the fibre present challenges for integration into PMC form which have been overcome using techniques which are described in chapter 5.

4.5. First Demonstration of an Optically Pumped Acetylene Laser in Kagome HC-PCF [116] [3]

As well as the advantages described in previous sections, Kagome HC-PCF also provides extremely broadband guidance. Depending on the cladding pitch and the strut thickness and uniformity there can be several guidance bands within the optical region. In this section, a 1-cell Kagome fibre (Figure 4-11) is used which provides guidance in the near-

---

[3] All experimental work carried out by Kansas State University and University of New Mexico. Fibre used in this demonstration was fabricated by the author.
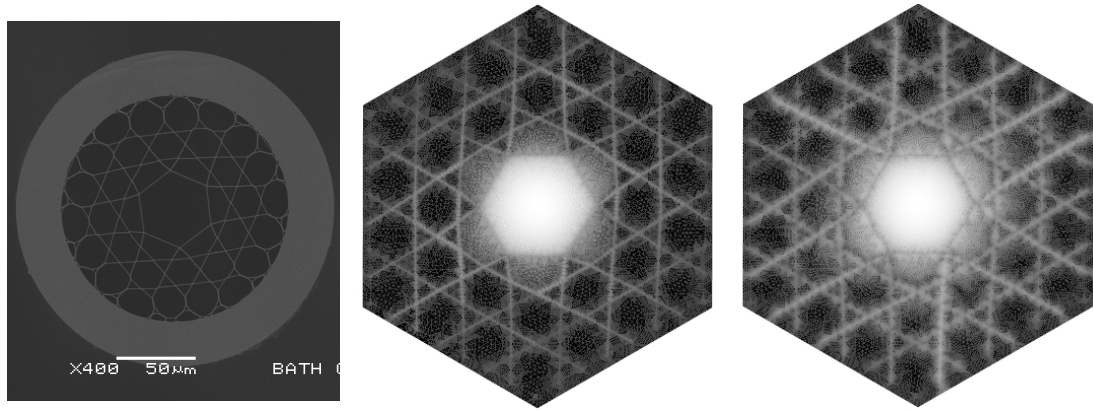
Figure 4-11: *(left to right) SEM of 1-cell Kagome fibre used in experiment, mode field profiles calculated at 1520 and 3120 nm respectively.*

IR (~1500 nm) and the mid-IR (~3 μm) simultaneously. Dual guidance in these regions has enabled the first demonstration of an optically pumped gas laser inside optical fibre based on population inversion [116]. This work was driven by a demand for portable and tuneable lasers in the mid-IR. Current solutions, such as quantum cascade lasers are working to answer this need but can become multimode at high powers and have heat management issues [132]. Optically pumped gas lasers are a possible solution here as they have several appealing qualities such as high damage threshold, the means for efficient heat dissipation and emissions from the near to the far-IR [133]. Using the Kagome HC-PCF as a host for the gas medium provides additional compactness and portability compared to existing solutions which can be bulky and alignment sensitive. In this first demonstration, the gas used was acetylene. In this section, the experimental results are briefly outlined to demonstrate the advantage of the broadband spectral guidance provided by Kagome HC-PCF.

Experiment

The experimental set up is shown in Figure 4-12. The acetylene-filled Kagome fibre
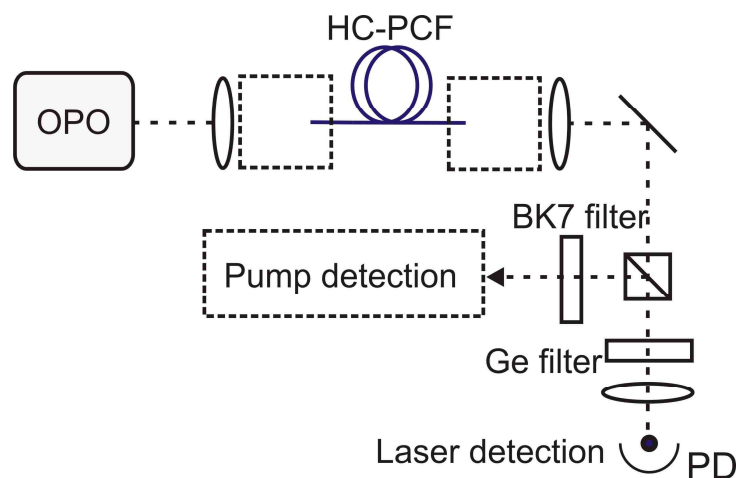

Figure 4-12: *Experimental set-up for acetylene laser. OPO; optical parametric oscillator, PD; photodetector.*

provides the laser cavity. Both ends of the fibre are mounted in vacuum chambers which enable evacuation of the fibre and subsequent pressurisation with acetylene to a pressure of a few mbar. Pump pulses of 5 ns duration and 3.5 GHz bandwidth are provided by an optical parametric oscillator (OPO) and the pump pulse energy is limited to <100 µJ to avoid damage to the fibre. The pump pulses are centred at 1521 nm, corresponding to the transition between J=7and J=8 in the $v_1 + v_3$ overtone band and are coupled into the HC-PCF using BK7 glass optics. From this excited state the molecules can then decay radiatively to the v_1 band with corresponding emissions around 3 µm.

At the fibre output CaF_2 optics are used and subsequently the pump and laser beams are separated using germanium wafers. A fast InGaAs detector records the pump pulse energy and a fast HgCdTe photodetector records the laser output in the mid-IR.

Kagome HC-PCF Properties

Due to the wide spacing of the pump and lasing wavelengths, the broad spectral guidance possible with Kagome lattice fibre is essential for this experiment. The guidance properties of the 1-cell fibre used are shown in Figure 4-13. As discussed in chapter 2, this fibre provides a low loss guidance band in the near-IR; specifically the fibre loss at the pump wavelength of 1521nm is 0.5 dB/m and the loss in the mid-IR at 3.2 µm, near the lasing wavelengths is 20 dB/m.

The calculated loss of the 1-cell Kagome fibre is also shown in Figure 4-13 and is in good
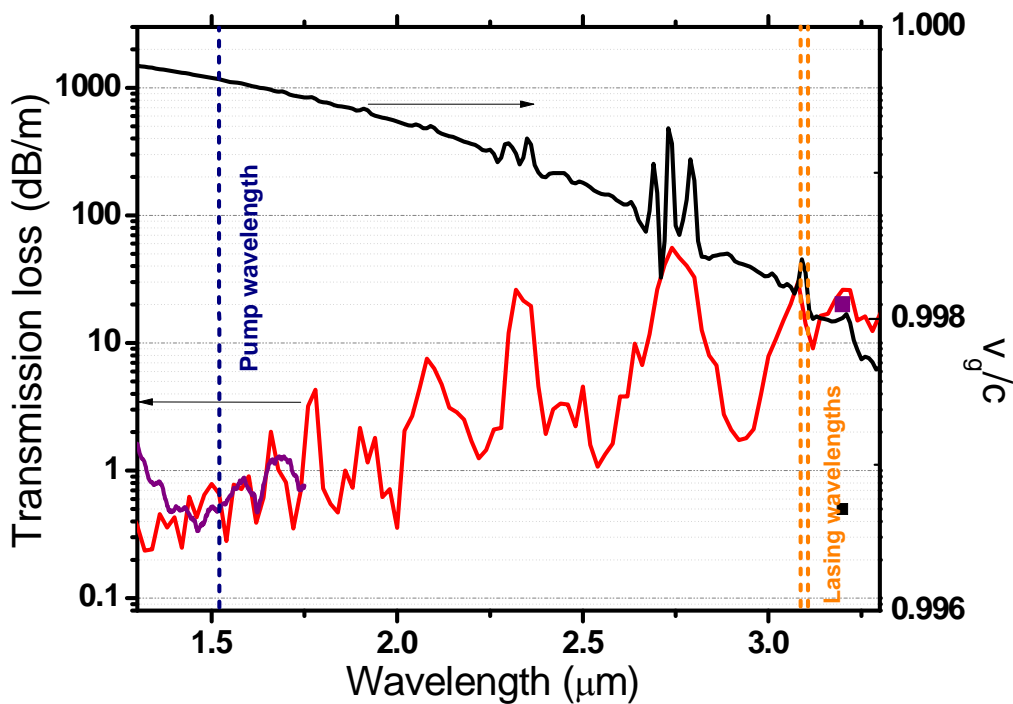

Figure 4-13: *Experimental and calculated transmission properties of Kagome fibre used in experiment (purple and red data respectively). Pump and lasing wavelengths are highlighted. Calculated fractional group velocity is shown in black.*

agreement with the measured transmission losses. Furthermore, the calculated mode field profiles near the pump and lasing wavelengths are shown in Figure 4-11. It is clear that the core mode is well confined in both spectral regions eliminating the possibility that the guidance measured at 3.2 μm is supported in cladding modes. This work represents the first experimental demonstration of guidance in the mid-IR using Kagome fibre. This fibre structure was optimised for low loss guidance in the near-IR and, with further work on design optimisation, it is expected that losses in the mid-IR can be significantly reduced.

Laser Output

Using this set-up shown in Figure 4-12, two laser emissions peaks were observed at ~3.12 μm and 3.16 μm as shown in Figure 4-14. The decay scheme corresponding to these two emission lines is also shown inset to Figure 4-14. The laser threshold was found to be ~200 nJ and the efficiency was estimated to be of the order of a few percent. It is thought that laser emission through alternative pathways is inhibited due to insufficient time for the molecules in the excited states to rotationally mix before the onset of lasing [116].

Future Work

Again this experimental result could be enhanced by removing the vacuum system and transforming the acetylene-filled Kagome HC-PCF into a PMC. However, due to the high absorption of silica at 3 μm [52] it would be necessary for the output of the HC-PCF to be spliced to specialty all solid fibre such as chalcogenide fibre (see application
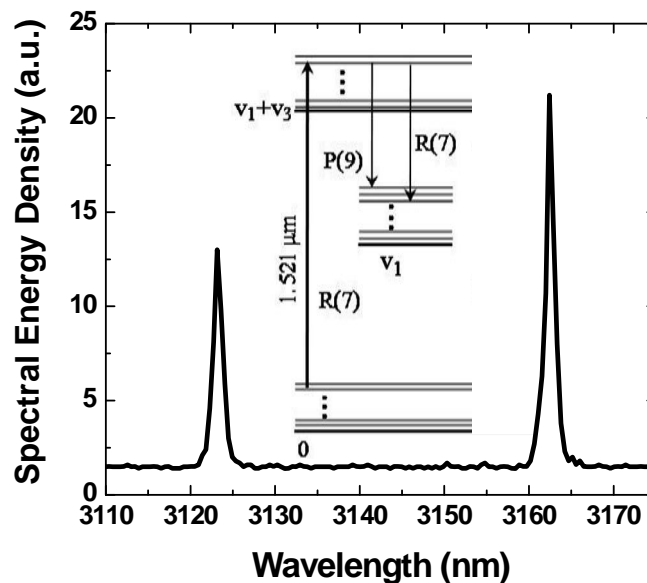
Figure 4-14: *Acetylene laser output. Two laser lines are observed corresponding to decays from the J=8 state from the $v_1 + v_3$ overtone band to the J=7 and J=9 states from the v_1 band.*

review [134]) instead of SMF, in order to provide both the hermetic seal and low loss guidance in the mid-IR.

4.6. Summary

This chapter has highlighted properties of PBG and Kagome HC-PCF which are of direct relevance to their application as hosts for gas-laser interactions. Three experiments were described which demonstrate breakthroughs achieved using the properties of Kagome HC-PCF. Specifically, the large core diameter, absence of surface mode guidance and the guidance mechanism lead to a reduction in the decoherence rate, flat optical transmission and broadband guidance. The reduction in the decoherence rate offered by 19-cell Kagome HC-PCF enabled the observation of the narrowest spectral feature achieved so far in gas-filled HC-PCF. This spectral feature was demonstrated as a sub-10 kHz absolute optical frequency reference. 1-cell Kagome HC-PCF was also used as a host for the first acetylene laser using population inversion.

These experiments demonstrate the need for a procedure for integration of large dimension fibres into PMC form; a low loss technique based on tapering is described in chapter 5.

Chapter 5

Large Core Photonic Microcells

In this chapter, a technique to integrate large dimension fibres, such as large-pitch Kagome fibre, into photonic microcell form is described. This technique is based on fibre tapering and enables low loss splicing between HC-PCF and single mode fibre. Electromagnetically induced transparency and saturated absorption spectroscopy are demonstrated in an acetylene-filled large core photonic microcell. This work is published in reference [135].

5.1.   Introduction

In chapter 4, the advantages of Kagome lattice HC-PCF for gas spectroscopy were presented. One key origin of these advantages is that, due to the nature of the guidance mechanism, Kagome fibres can be fabricated with very large core diameters. However, these same large dimensions provide an obstacle to low loss integration of gas-filled Kagome fibres into photonic microcell (PMC) form. The large diameter of the microstructured cladding region of a Kagome HC-PCF can exceed the outer diameter of SMF, inhibiting the fabrication of hermetic splices and integration of Kagome HC-PCF into standard fibre-based systems. Additionally, the large core diameter leads to large mode field mismatch and therefore high coupling losses with SMF. The origins and magnitudes of the main sources of splice loss are considered in section 5.2. Due to the difficulties presented by the large dimensions of Kagome HC-PCF, PMCs have mainly been fabricated using PBG HC-PCF and complete microcell insertion losses as low as 1.8 dB have been realised [37].

In the main body of this chapter, two techniques suitable for integrating any type (and size) of Kagome lattice HC-PCF into PMC form are demonstrated. These techniques are based on fibre tapering[4]. It is shown that these techniques significantly reduce the mode field mismatch between SMF and Kagome HC-PCF. Also, through tapering, the outer diameters of the two fibres can be matched to enable hermetic splice junctions. The fibre tapering process is outlined and the physical and optical properties of the tapers are discussed in section 5.3. Complete, acetylene-filled, Kagome lattice PMCs were fabricated

---

[4] Fibre tapering presented in this chapter was carried out by M. Grogan and Prof. T. A. Birks.

(section 5.4) and their advantages for coherent optics applications are demonstrated in section 5.5.

5.2. Origins of Splice Loss

Before considering how to integrate large dimension fibres into PMC form, it is useful to consider the relative magnitudes of the different loss mechanisms at a splice junction between two fibres. Here the losses at junctions between HC-PCF and SMF are considered. All the losses described referred to as 'splice' losses as we are interested in the overall product of a low loss hermetic splice, even though many of the mechanisms really describe coupling losses between two fibres.

Some simple assessments of loss magnitudes can be made by assuming that the HC-PCF is a single mode waveguide. This assumption is viable with good input coupling to the HC-PCF and for most HC-PCF designs. However, as the core diameter is increased, the number of modes supported also increases and therefore the viability of this assumption decreases. It is also assumed that the modes of both HC-PCF and SMF are well described using the Gaussian approximation so that the fundamental mode field distribution is described by a Gaussian profile,

$$\psi(r) = Ae^{\frac{-r^2}{w^2}},$$
(5-1)

where r is the distance from the centre of the core (radial co-ordinate) and w is known as the spot size. The fibre mode field diameter, d, is defined as $d = 2w$. It is noteworthy to recall that the modes in circular waveguides, such as SMF, are strictly described by Bessel functions and the Gaussian profile is an approximation which is valid in the limit $\varrho << 1$ where $\varrho = r/w$. Nevertheless, the Gaussian approximation is sufficiently accurate for HC-PCF, provided the light is coupled favourably into the fundamental mode of the HC-PCF.

The individual contributions to splice loss are well documented: (i) mode field mismatch, (ii) physical misalignment between the two fibres (transverse, longitudinal or angular), and (iii) Fresnel reflection, due to the discontinuity in refractive index at the splice junction. In addition to these conventional loss sources, a further loss source which is considered here arises from deformations introduced into the fibre structure by heating during the splicing process. In the following sections, these splice losses are outlined and discussed in the context of splicing large core Kagome HC-PCF to SMF.

Mode Field Mismatch

By considering the overlap integral between the Gaussian mode field distributions (equation 5-1) of two fibres with spot sizes w_1 and w_2, the splice loss at a junction between these fibres due to mode field mismatch can be expressed (in dB) as,
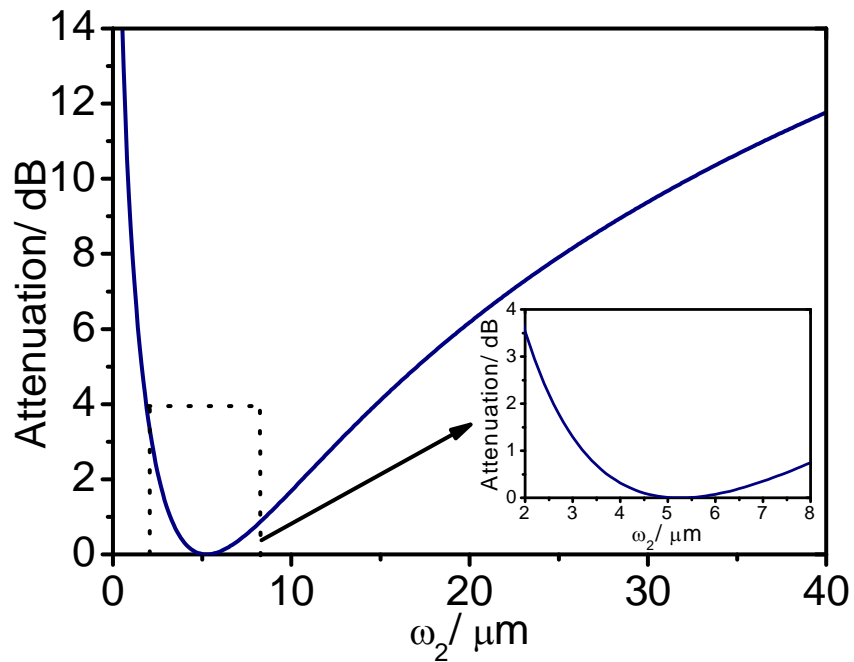
Figure 5-1: *Attenuation at a splice junction between SMF and HC-PCF due to mode field mismatch. Equation 5-2 is plotted as a function of w_2. w_1 is fixed at 5.2 µm (SMF-28 at 1550 nm).*

$$\alpha_m = -20 \log\left(\frac{2w_1 w_2}{w_1^2 + w_2^2}\right). \tag{5-2}$$

In all the estimates of loss magnitude in this chapter, the spot size w_1 is set to 5.2 µm which corresponds to the spot size for SMF-28 at 1550 nm [136]. In Figure 5-1, equation 5-2 is plotted as a function of the spot size of the HC-PCF (w_2). In order to keep the loss due to mode field mismatch below 0.5 dB, Figure 5-1 indicates that the difference in
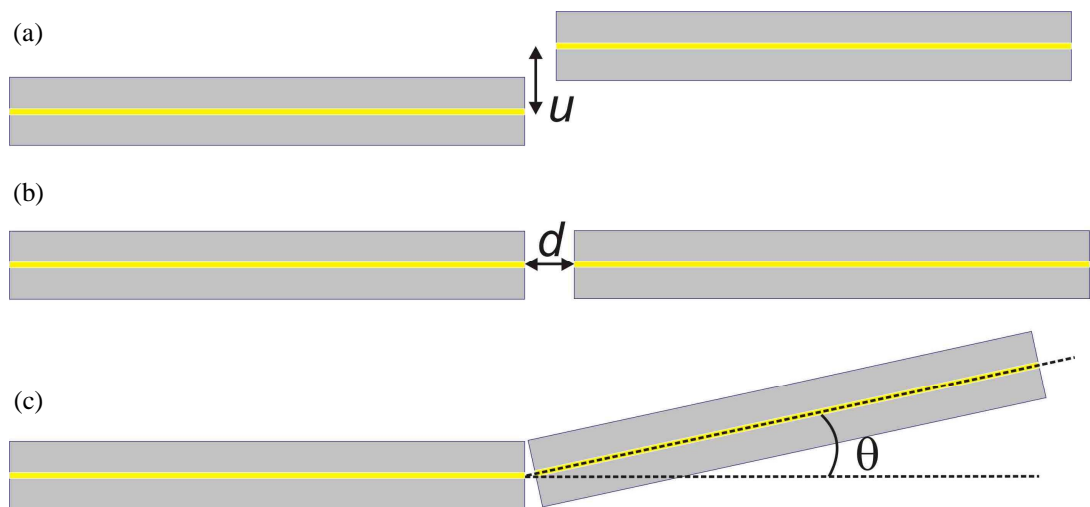
Figure 5-2: *Three possible sources of physical alignment between two fibres. (a) Transverse misalignment by a distance, u; (b) longitudinal misalignment by a distance d and (c) angular misalignment by an angle θ.*

86

mode field diameters can actually be up to 30% of w_1. However, the loss steeply increases as the difference in mode field diameters moves above 50% of w_2. A 19-cell Kagome lattice fibre with a 70 µm core diameter has a mode field diameter of approximately 46 µm using the Gaussian approximation. Using equation 5-2, the mode field mismatch between this fibre and SMF would lead to an attenuation of ~7 dB. This loss is extremely large and if these two fibres were spliced together, would severely limit the power handling capability of the splice due to heating effects.

For splices between SMF and large core HC-PCF, mode field match is likely to be the dominant source of loss. However, at a realistic splice junction, mode field mismatch must be considered in conjunction with additional losses to due fibre misalignment. Therefore, in the following section, each physical misalignment is considered individually, in combination with attenuation due to mode field diameter mismatch.

Physical Misalignment

Three possible physical misalignments are shown schematically in Figure 5-2. All losses due to fibre misalignment can be minimised during the splicing process by careful alignment.

Figure 5-2(a) highlights transverse misalignment between the two fibre cores by a distance u. By considering the modal overlap of two fibres and introducing a transverse misalignment by u, the attenuation (in dB) is
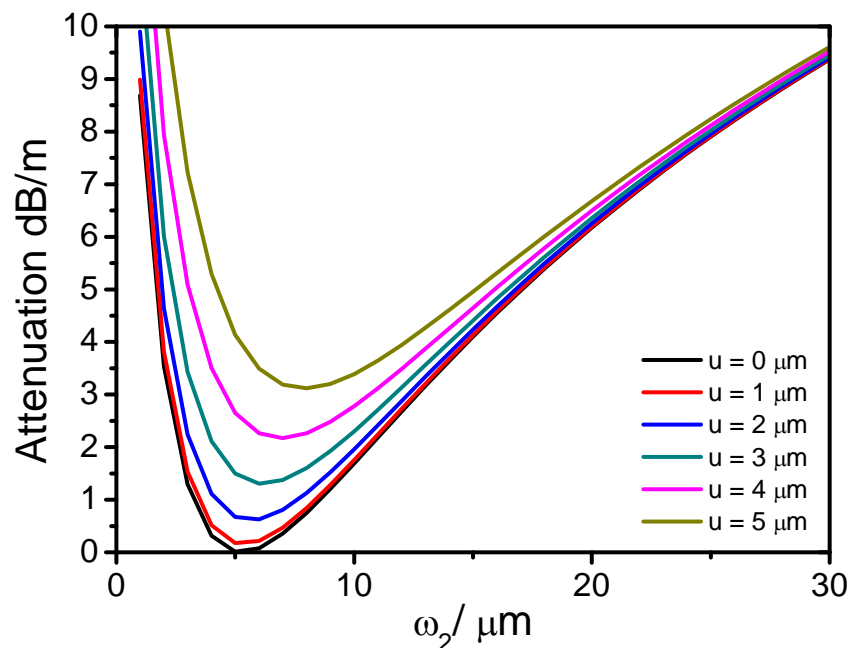

Figure 5-3: *Combined attenuation of transverse misalignment and mode field mismatch as a function of spot size w_2 for values of transverse misalignment, u, from 0 to 5 µm.*

$$\alpha_t = 4.34 \left\{ \frac{2u^2}{w_1^2 + w_2^2} - 2\ln\left(\frac{2w_1 w_2}{w_1^2 + w_2^2} \right) \right\}, \tag{5-3}$$

which simplifies for the case $w_1 = w_2 = w$ to:

$$\alpha_t = 4.34 \left(\frac{u}{w} \right)^2. \tag{5-4}$$

Equation 5-3 is plotted in Figure 5-3 as a function of w_2, for values of u ranging from 0 to 5 µm, whilst setting w_1 to 5.2 µm as previously. This figure shows that splice loss is extremely sensitive to transverse misalignment; even with identical mode field diameters it is necessary to keep $u<$ 1.7 µm to achieve junction losses <0.5 dB. It is noteworthy also, that Figure 5-3 indicates that as the difference in mode field mismatch increases, the effect of transverse misalignment is substantially inhibited. Considering 19-cell Kagome HC-PCF with an estimated mode field diameter of 46 µm, a transverse misalignment of 5 µm will induce an extra loss of 0.4 dB. This contrasts with an extra attenuation of 4 dB if the Kagome mode field diameter was identical to that of the SMF.

Longitudinal misalignment, by a distance d, is shown in Figure 5-2(b). It may not be readily apparent why this contribution is relevant when considering formation of hermetic splices as in this case the fibres must be touching. However, in [38] it was shown that a recess typically forms in the hollow core structure at the splice interface creating a small longitudinal misalignment between the two fibre cores. Considering two
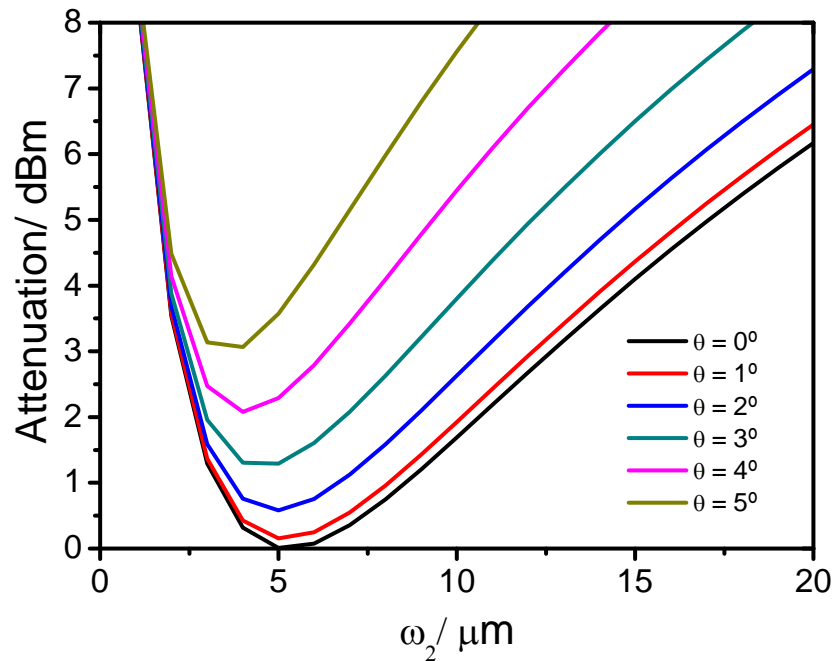

Figure 5-4: *Combined attenuation due to mode field mismatch and angular misalignment for values of θ between 0 and 5 degrees.*

fibres with identical spot sizes and by assessing the diffraction of the output field of the first fibre before incidence on the core of the second fibre, the attenuation due to longitudinal misalignment can be expressed as [137]

$$\alpha_l = 10 \log \left(1 + \left(\frac{d\lambda}{2\pi n w^2} \right)^2 \right), \tag{5-5}$$

where n is the refractive index of the medium between the two fibre tips (this medium is air for the splices described here) and λ is the free space wavelength. It is noteworthy, however, that in the case of PBG HC-PCF, the distance d is not simple to define. This is due to the nature of guided mode which, because of its spatial overlap with the cladding on one hand and the phase-coherence between the spatial field components of the mode on the other hand, exhibits diffraction effects which cause the output beam to focus before diverging. Interference occurs between the different spatial components from the beam, originating from both the HC-PCF cladding and core [138]. The attenuation due to longitudinal displacement for reasonable recess distances (~ 5 μm) is considerably smaller than the other contributions discussed in this section. Therefore, due to the combination of the difficulty in defining d and the expected small magnitude of this contribution, longitudinal misalignment is dismissed in subsequent discussions.

Angular misalignment is illustrated in Figure 5-2(c). This misalignment could arise from an angled fibre cleave or during the 'hot push' stage of the splicing technique. During the 'hot push' the two fibres are pushed together through a longitudinal distance between 10 and 25 μm in order to increase splice strength. If the hot push distance is too high angular misalignment can occur. The attenuation (in dB) for two fibres, misaligned by an angle θ, can be expressed as (see [137] for full derivation),

$$\alpha_a = 4.34 \left\{ \frac{2\pi^2 n^2 \theta^2 w_1^2 w_2^2}{\lambda^2 \left(w_1^2 + w_2^2 \right)} - 2 \ln \left(\frac{2 w_1 w_2}{\left(w_1^2 + w_2^2 \right)} \right) \right\}. \tag{5-6}$$

This expression simplifies for the case $w_1 = w_2 = w$ to

$$\alpha_a = 4.34 \left(\frac{\pi n w \theta}{\lambda} \right)^2. \tag{5-7}$$

Equation 5-6 is plotted in Figure 5-4 for values of θ between 0 and 5 degrees. From this figure, it is clear that in order to achieve splice losses <0.5 dB for fibres with identical mode field diameters it is necessary to restrain θ to 1 degree or less. It is also clear that, in contrast to transverse misalignment, attenuation due to angular displacement is not inhibited by a larger difference in mode field diameters.

Fresnel Reflection

A further loss mechanism at the splice interface arises due to the refractive index mismatch between the all-solid SMF and the hollow core Kagome fibre. By taking the index of the SMF core to be ~1.45, there is ~4% Fresnel reflection at a splice junction to a hollow core fibre. This back reflection can be mitigated through angle splicing [139] but the overall loss of an angle splice is typically much higher than that of a flat splice.

The aforementioned sources of splice loss highlight the difficultly in fabrication of low loss splices between SMF and Kagome lattice HC-PCF. An additional source to consider here is that Kagome lattice fibres are multimode; there is a dominant mode which has an approximately Gaussian distribution [72] which is favourably excited with appropriate input coupling but other higher order modes are also supported. These have different, non- Gaussian, modal distributions and will couple with a different efficiency to the SMF and therefore their guidance may increase or decrease the loss at the splice junction.

From equation 5-2, it is clear that a large mismatch in the spot sizes of the two fibres, which can stem from a large mismatch in core diameter, will lead to very large coupling losses. This high loss, combined with the physical impossibility of creating a hermetic splice when the microstructured region of the Kagome HC-PCF has a larger diameter of the SMF, means that a modified technique is required to integrate large dimension fibres into PMC form.

The solution presented here is to use fibre tapering; the outer diameter of the Kagome fibre can be reduced or the outer diameter of the SMF can be increased in order to improve modal overlap and provide the means to form a hermetic splice. In the following section, the fibre tapering technique is introduced and the coupling losses between tapered Kagome and SMF are analysed.

5.3. Fibre Tapering

5.3.1. Tapering Procedure

Kagome HC-PCFs were tapered using a moving flame-brush tapering rig as described in [140]. A schematic of this set-up is shown in Figure 5-5(a). The HC-PCF is heated, using an oxy-butane flame, and pulled simultaneously to create the taper profile required. A schematic of the taper profile used here is shown in Figure 5-5(b). The fibre outer diameter (OD) is reduced over a transition length (l_t) to the desired waist diameter (d_w). Typical transition lengths are of the order of 10 mm. In order to maximise the physical overlap of the Kagome fibre with the SMF and to minimise the mode field mismatch with the SMF, the fibre diameter was reduced to 125 μm in the waist section. The taper was then cleaved in this waist region ready for splicing to the SMF.
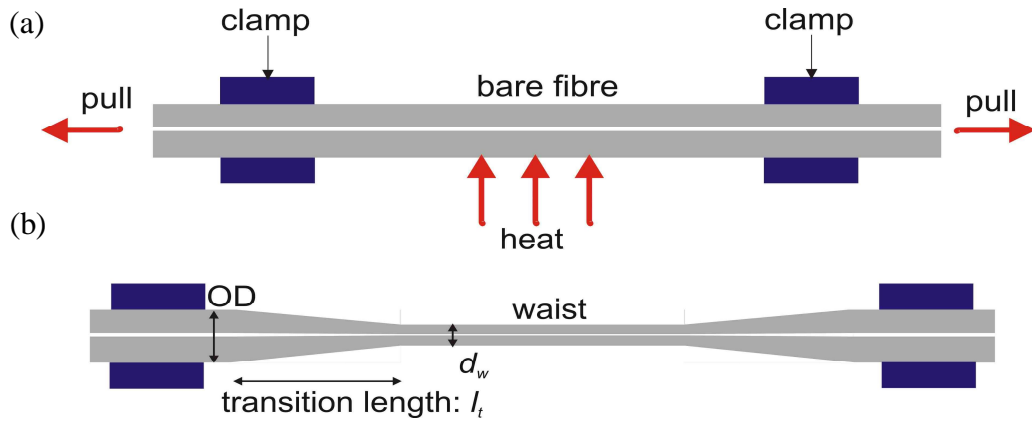
Figure 5-5: *(a) Schematic of moving flame-brush taper rig; fibre is clamped securely and then heated and pulled simultaneously to create the taper profile required. (b) Taper profile used in this work; the outer diameter (OD) of the Kagome HC-PCF is reduced, approximately linearly, over a taper transition length, l_t, to the waist diameter, d_w.*

This tapering approach was investigated for two different Kagome fibre structures; 19 cell Kagome (OD ~ 315 μm, maximum core diameter ~ 65 μm, attenuation ~1 dB/m at 1520 nm) which is shown in Figure 5-6(a) and 1-cell Kagome (OD ~ 200 μm, core diameter ~ 45 μm, attenuation ~0.5 dB/m at 1520 nm) as shown in Figure 5-6(b). The guidance mechanism of Kagome fibre enables the guidance bandwidth to be up to 20 times larger than that of PBG HC-PCF. This makes it amenable to tapering as some wavelength ranges can be guided at every point along the tapered structure as well as in the untapered fibre.

5.3.2. Taper Characterisation

Figure 5-6(c) and (d) show SEMs of the cross-sections of the 19-cell and 1-cell Kagome fibres in the taper waists. These correspond to approximately a 3× and a 2× reduction of the 19-cell and 1-cell fibre outer diameters respectively. From these figures it is clear that the fibre structure is generally well preserved during the tapering process. There are some deformations evident around the core interface in the 19-cell Kagome which can be attributed to surface tension effects around such a large core. These effects could be mitigated by introducing some pressurisation to the fibre cladding during the splicing process. However, for the work described here, such a development was not required.

To further characterise the tapers, the linearity of the taper transition region was studied using an optical microscope. A microscope image of an example taper of the 19-cell defect Kagome is shown inset in Figure 5-7. The variation in the HC-PCF outer diameter along the taper transition was extracted from this microscope image and is also shown in Figure 5-7. This figure shows that the reduction in fibre diameter is reasonably linear over the taper transition length (7 mm), indicating a smooth transition from maximum to minimum outer fibre diameter.
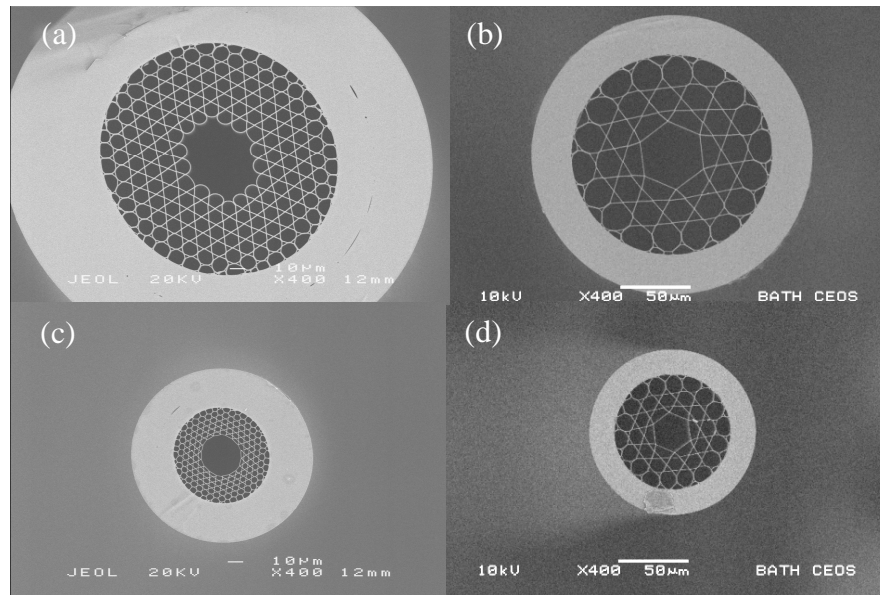
Figure 5-6: *(a) and (b) SEMs of full size 19-cell and 1-cell Kagome fibre respectively. (c) and (d) Corresponding SEMs of the fibres tapered to an outer diameter of 125 µm. To the same scale.*

Finally, the modal profile at the output of a tapered length of Kagome was characterised and compared to the modal profile of full size Kagome HC-PCF. The light source used to record the mode profiles was a supercontinuum fibre, filtered using a 10 nm bandpass filter centred at 1550 nm. Initially the mode profile through a ~1 m length of 1 cell Kagome HC-PCF with a 15 mm length taper transition at the output end was recorded
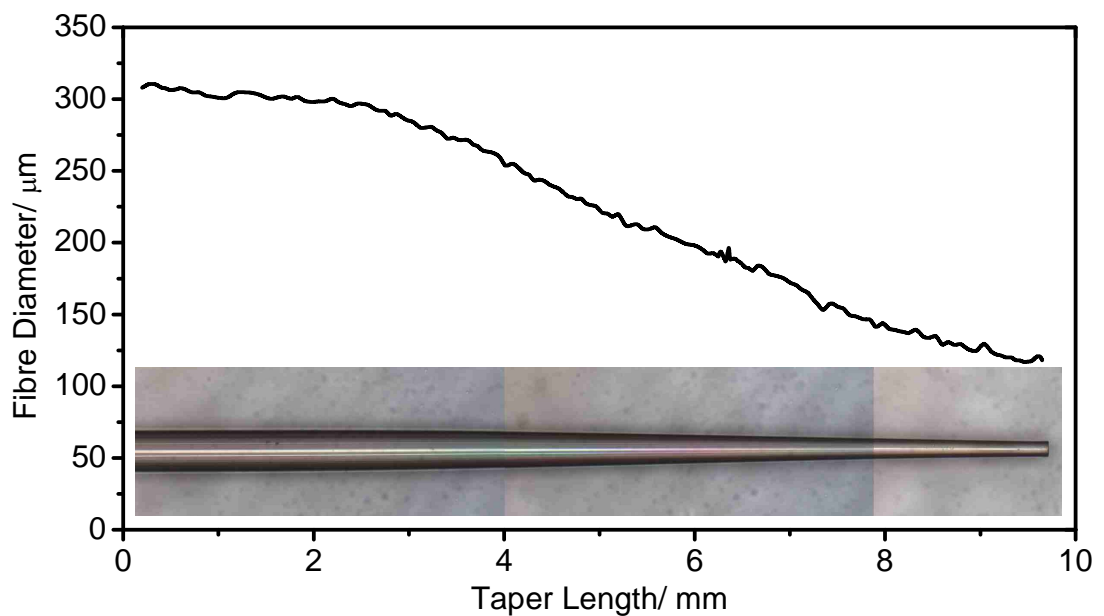
Figure 5-7: *Extracted fibre diameter profile along a 7mm taper transition. (inset) Optical microscope image of a tapered 19-cell Kagome fibre.*
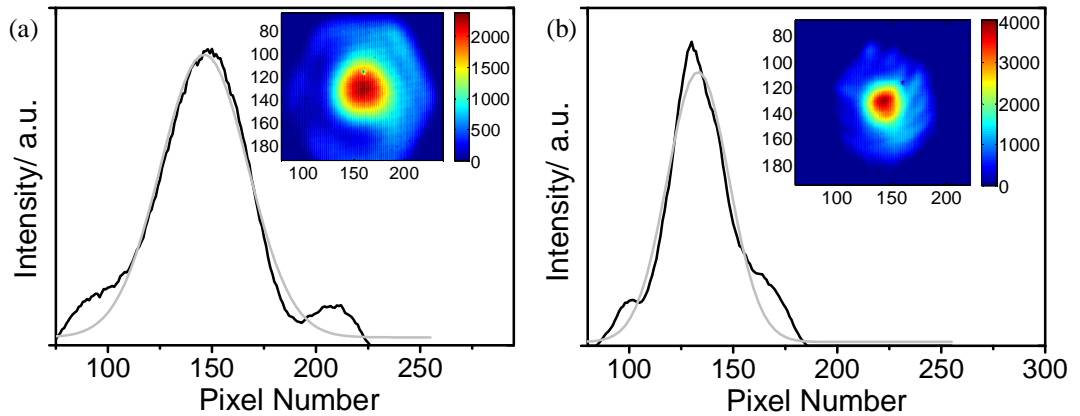
Figure 5-8: *(a) and (b) show experimental modal profiles (black line) for full size and tapered 1-cell Kagome (with 15 mm transition length). Gaussian fits to each profile are also shown (grey line) and full mode images are shown inset.*

(Figure 5-8(b)). Subsequently, without changing the input coupling to the fibre, the taper transition was cleaved from the output end of the fibre and the mode profile of the full size HC-PCF was recorded (Figure 5-8(a)). From the mode profiles shown in Figure 5-8 it is clear that both mode profiles can be approximated by a Gaussian profile and therefore the equations describing splice loss in section 5.2 should be applicable. Furthermore, these modal images confirm that guidance in a core confined mode is maintained through the taper transition.

5.3.3.   Splice Characterisation

Figure 5-9 shows the butt-coupling loss between SMF and the 1-cell and 19-cell Kagome fibres as function of l_t. The dashed lines indicate typical butt-coupling losses to the
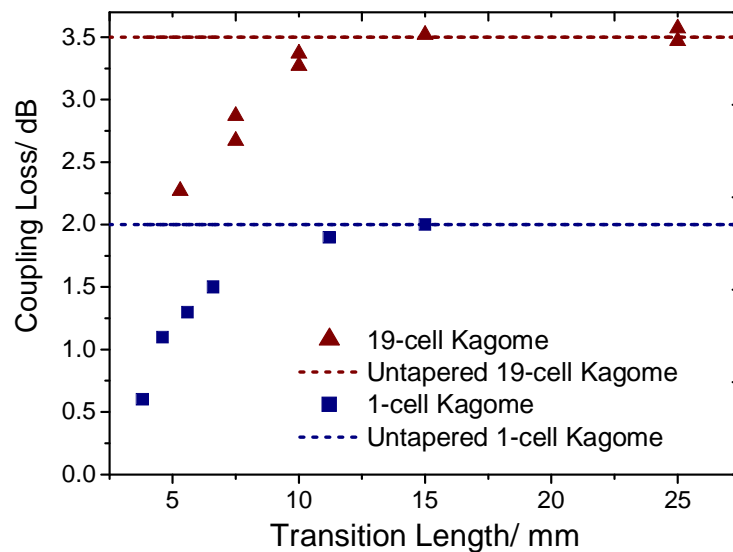
Figure 5-9: *Butt-coupling loss between SMF and tapered Kagome as a function of transition length. Dashed lines indicate coupling loss between SMF and untapered Kagome HC-PCF.*
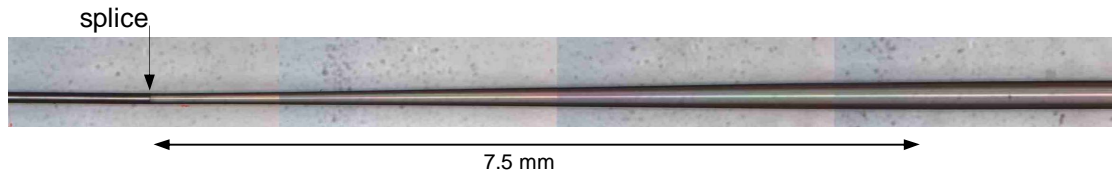
Figure 5-10: *Composite optical microscope image of splice between SMF (left) and tapered19-cell Kagome (right).*

untapered Kagome fibre. Figure 5-9 shows that, through tapering, the butt-coupling loss between SMF and Kagome fibre can be reduced by more than a factor of 3 as the mode field overlap between the fibres is increased. The loss increases approximately linearly with transition length for both fibres but starts to plateau for $l_t > 10$ mm. This trend is surprising because the loss of an index-guiding, tapered fibre (like SMF) decreases as the taper transition length is increased. This loss reduction is because, for longer transition lengths, the taper becomes more adiabatic. However, adiabaticity arguments can be misleading when describing HC-PCF because the strictly fundamental mode of the fibre is not an air-guided mode, but a cladding mode which propagates mainly in glass.

In fact, several factors related to the characteristics of the transmission spectrum of Kagome-lattice HC-PCF support the attenuation trend indicated in Figure 5-9 [45]. Firstly, the attenuation of the fibre is not constant as a function of wavelength and as the outer diameter of the HC-PCF is reduced (and subsequently the pitch is reduced) the low loss transmission bands are shifted to shorter wavelengths. For longer taper transitions, the outer diameter decreases more slowly and so the light is guided for a longer length in any higher-loss regions and this may act to increase the total loss. Secondly, small deformations in the structure of the HC-PCF across the transition region will raise the attenuation, thus favouring short transitions. The transmission spectrum of Kagome HC-PCF is highly sensitive to the thickness of the silica web forming the cladding (see chapter 2). Consequently, any change of thickness in the silica which results from heating during the tapering process would alter the loss figure at a given wavelength. The shortest transitions achievable were ~4 mm as variations in taper diameter were incurred for shorter transitions. As l_t tends to zero the loss should rise to the untapered value, so the transition lengths achieved could already be very close to the optimum.

The additional loss during the splicing process is typically 0.2 dB and is due to deformations in the cladding structure which arise as the fibres are heated. Figure 5-10 is a composite image of the SMF, splice and transition to the full-size 19-cell Kagome fibre. Splice losses from SMF as low as 0.6 dB to 1-cell Kagome fibre ($l_t = 3.8$ mm), and 2 dB to 19-cell fibre ($l_t = 6$ mm) were achieved. These compare with the lowest-reported loss of 0.9 dB for a splice between SMF-28 and bandgap-guiding HC-PCF [37]. For

completeness, it is worth noting here that a loss of 0.79 dB between SMF with a mode field diameter optimised to match 7-cell PBG HC-PCF is reported in [141].

5.3.4. Loss Analysis

The coupling losses described above can be analysed by considering the splice loss contributions described in section 5.2. Firstly the minimum attainable loss of a splice between SMF and HC-PCF is ~ 4% due to Fresnel reflection, which equates to 0.18 dB.

In the case of the 1-cell Kagome, the core diameter is decreased from ~45 μm to ~25 μm by the taper transition. Subtracting the loss originating from Fresnel reflection, the coupling measurements show that the taper transition reduces the coupling loss from 1.8 dB to a minimum of 0.4 dB (l_t = 3.8 mm); therefore reducing the coupling loss by a factor of 4.5. Using equation 5-2, and assuming mode field diameters of 30 μm and 16 μm for the untapered and tapered Kagome HC-PCF respectively, the expected attenuation should be reduced by a factor of 5 which is in good qualitative agreement with the experimental value. However the absolute attenuation values predicted by equation 5-2 are much higher.

In the case of the 19-cell Kagome, the core diameter is reduced from a maximum of ~65 μm to ~ 30 μm by the taper transition. Using mode field diameter estimates of 32 μm and 20 μm for the full size and tapered fibres respectively, equation 5-2 predicts a reduction in attenuation by a factor of ~3. Experimentally, the attenuation was reduced by a factor of 1.7 which is lower than the predicted value. This could be due to the larger structural deformations which arise when tapering the larger core, 19-cell fibre which may act to increase the guidance loss in the taper transition region.

The reduction in attenuation at the splice junction can be attributed to reduction in mode field mismatch between the SMF and HC-PCF. Further reduction in loss could be achieved by optimising the taper structure in the transition (especially for the 19-cell fibres) and minimising the coupling loss due to mode field mismatch through further core diameter reduction. Both of these could be attempted through differential pressurisation of the core and cladding regions of the fibre during the tapering process.

5.3.5. Uptapers

An alternative to decreasing the outer diameter of the Kagome fibre is to increase the diameter of the SMF by uptapering [142]. This can be done using the same tapering rig (Figure 5-5(a)), by using a sequence of pushes and heating to fatten the fibre in the waist region. This technique has been successfully used to significantly reduce the mode coupling losse between different all-solid fibres [143]. Furthermore, the authors in [144] managed to increase the diameter of SMF to 240 μm with adiabatic transitions so that the single mode output was effectively retained.
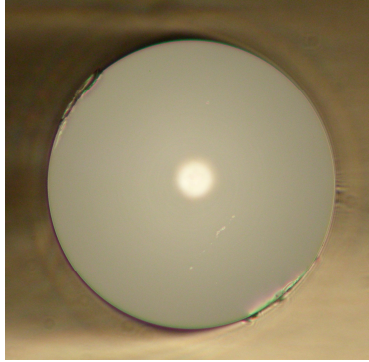
Figure 5-11: *Uptapered SMF optical microscope image, OD~ 210 μm, core diameter ~ 34 μm.*

An example cross section from the waist of an uptaper is shown in Figure 5-11; the outer diameter is increased to 210 μm and the core diameter is ~34 μm. Initial splice losses between this uptapered SMF and the 1-cell Kagome used in the previous sections have been recorded to be as low as 0.75 dB. This attenuation figure includes the uptaper transition loss (0.1 dB or less typical) and the 0.18 dB which arises from Fresnel reflection, thus indicating extremely low coupling losses of ~0.5 dB. These low losses are very promising for achieving lower loss splices.

The reduction in loss may be due to increased mode field matching between the fibres. This reduction is enhanced because the core diameter of the SMF increases at a faster rate than the outer diameter of the fibre because of dopant diffusion [145]. As well as increasing the mode field overlap, dopant diffusion also enables some extra control of the final SMF core size through control of the heating process during uptaper fabrication. A further possible advantage of uptapering the SMF, compared to down-tapering the Kagome fibre, is that the splices can be stronger due to a larger glass area overlap between the uptapered SMF and the microstructured fibre.

One possible disadvantage of uptapering is that the Kagome fibre core diameter is not reduced and therefore the diffusion of contaminants into the core during the PMC fabrication process is very fast, severely limiting the splice time when fabricating low pressure cells. Furthermore, initial tests have shown that the recorded splice loss is sensitive to the radius of curvature of bends in the Kagome fibre. This is an indication of the guidance of higher order modes and needs to be investigated further.

5.4.   PMC Fabrication

In order to make a low pressure acetylene-filled PMC using large core Kagome HC-PCF the input splice to the HC-PCF was prepared using the Kagome fibre tapering technique described in section 5.3.2. Subsequently, the HC-PCF was evacuated from the remaining open fibre end and then filled with acetylene gas to the required pressure. The helium

technique described in [37] and outlined in chapter 1 was then used to splice the second end of the PMC. This end was also tapered, so contamination by diffusion of air was minimized; the conductance of the fibre core scales with R_c^2, where R_c is the core radius and therefore a smaller core minimises contaminant entry during the splicing process, thus aiding the fabrication of low pressure gas cells. The splice losses were non-reciprocal (attributed to multimode propagation in the Kagome fibre) and lowest total PMC losses were achieved by splicing the output end of the Kagome fibre to multimode fibre (MMF) with a ~60 μm core diameter.

A complete acetylene-filled PMC made using 1-cell defect Kagome fibre length was fabricated. The Kagome fibre length was 6.5 m and the acetylene pressure was ~0.5 mbar. The total PMC insertion loss was 6 dB (3.25 dB fibre attenuation and 1.5 dB and 1.25 dB from the input and output splices respectively). In the following section, this PMC is used to demonstrate EIT and SAS.

5.5.   Applications

5.5.1.   EIT

The experimental set-up used to demonstrate EIT is shown in Figure 5-12(a). Two tuneable ECDLs provide the probe and coupling beams. The coupling beam is amplified using an EDFA. The beams are then combined using a 50/50 coupler, one output of which is spliced to the PMC. At the output of the PMC the coupling light is removed using interference filters. The probe and coupling beams were tuned to the R25 and P25 absorption lines from the acetylene $\nu_1 + \nu_3$ overtone band to create a V EIT configuration.

A typical probe trace is shown in Figure 5-12(b) for a coupling laser power of 250 mW. The EIT feature has a height of 16% and FWHM ~ 25 MHz. Figure 5-13(a) and (b) show the evolution of the EIT feature height and width with coupling laser Rabi
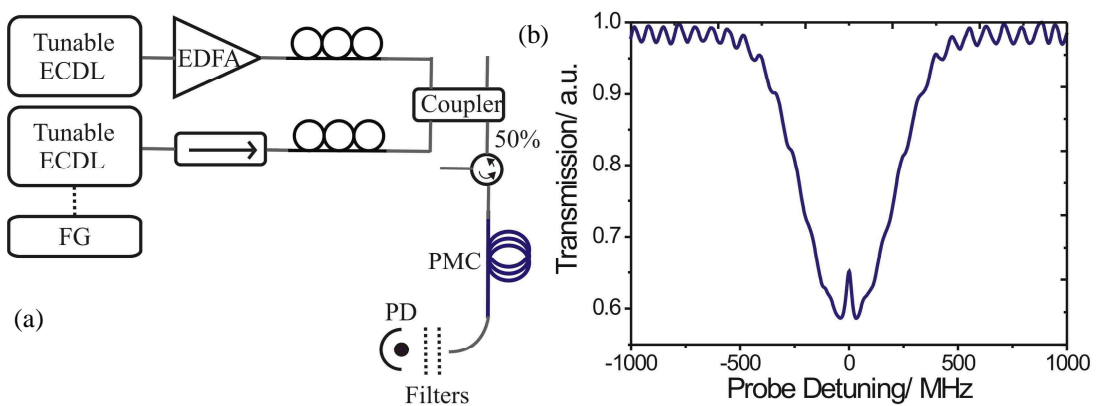
Figure 5-12: *(a) Experimental set-up used to observe EIT and (b) Example EIT trace for a coupling laser power of 250 mW. Feature height is ~16 % and linewidth is ~25 MHz.*
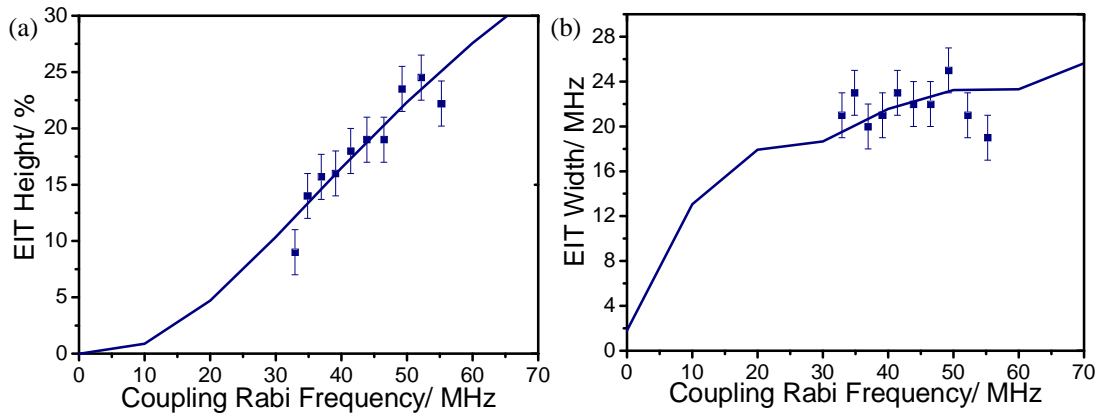
Figure 5-13: *(a) and (b) EIT feature width and height respectively as a function of coupling laser Rabi frequency. Data recorded in acetylene-filled PMC fabricated using tapering technique. Experimental 1-cell Kagome data (blue point) is compared to numerical model (blue line) used in chapter 4 and from reference [101].*

frequency using the acetylene-filled large-core PMC. The theoretical fits presented in this figure use the numerical model [101] outlined in chapter 4.

The full summary of the fitted values from the numerical model is presented in chapter 4 and contrasted with two other experimental EIT datasets recorded in different HC-PCFs. Using the larger core Kagome HC-PCF it is clear that considerably narrower EIT features and larger EIT feature heights are achieved and this is attributed to the decrease in the collision rate between the confined acetylene molecules and the inner core walls of the HC-PCF. From the fitted values given by the numerical model, this reduction in collision rate decreases the decoherence rate in qualitative agreement with the reduction expected using equation (1-28). Furthermore, reductions in the population exchange rate and excited state optical decay indicate the role of these collisions in collision-induced energy transfer.

5.5.2. SAS

SAS was demonstrated using the set-up shown in Figure 5-14(a). The pump beam is provided by a tuneable ECDL, amplified using an EDFA, and coupled via polarization controllers and a circulator to the PMC input. The reflected pump technique [146], where the probe beam is formed from Fresnel reflection at the PMC output splice, was used to create the sub-Doppler feature. This dramatically reduces the number of optical components and the alignment required.

An example of a saturable absorption feature with a linewidth of ~110 MHz is shown in Figure 5-14(b). This trace is time-averaged to reduce the etalon effects due to interference between the pump and probe beams (discussed below). Such a large linewidth compared to ~20 MHz linewidth expected for this core diameter and gas
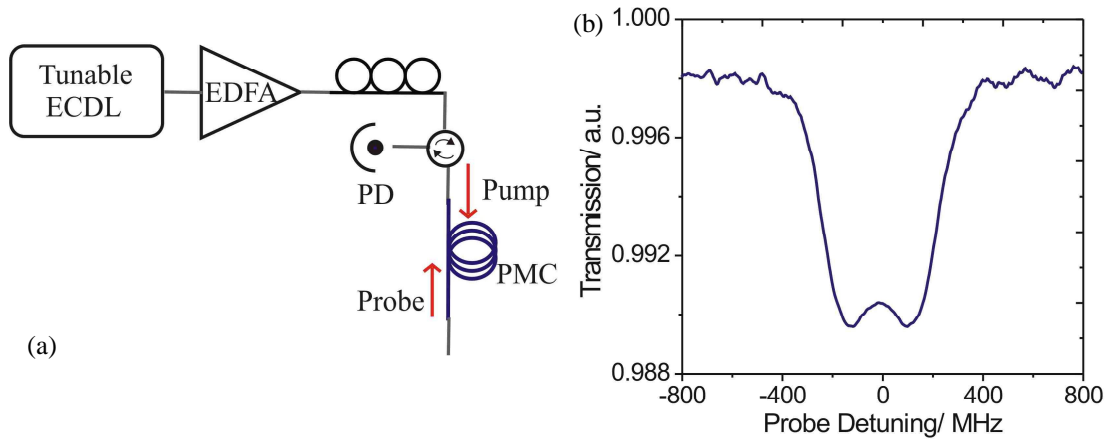
Figure 5-14: *(a) Experimental set-up used to create and observe SA in large core PMC in line P25 of the acetylene $v_1 + v_3$ spectrum. Probe beam is created through reflection from the second Kagome-fibre-to-MMF splice. (b) Experimental EIT trace for coupling laser power of 250 mW.*

pressure is attributed to power broadening, which is induced by the use of extremely high pump power of 250 mW. This power level was required to have a measurable probe signal because of the very small contrast (1%) of the probed acetylene absorption line on one hand and the strong etalon effect on the other hand. This contrast can be improved using the coated micromirrors described in chapter 6. The etalon effect could be reduced by an angled splice at the input [139] or alternatively, by dithering the fibre cavity length. The SAS generation indicates that, with these improvements, this large core PMC will have applications in frequency stabilisation.

5.6.   Summary

In this chapter, two techniques based on fibre tapering which enable low loss splices between large-core Kagome HC-PCF and SMF have been presented. By reducing the outer diameter of the Kagome to match the outer diameter of the SMF, strong hermetic and low loss splices were formed and used to fabricate a complete acetylene-filled PMC. EIT and SAS were recorded using this PMC.

In chapter 4, a 10 kHz accuracy optical reference based on acetylene-filled Kagome fibre was presented. One of the limitations of the set-up used for this high accuracy demonstration was that the HC-PCF was mounted in a vacuum system which reduced portability and robustness of the optical alignment into and out of the fibre and thus the reference frequency stability. Currently, stability measurements using the acetylene-filled PMC presented in this chapter are being carried out to investigate the change in the stability of the reference with the fixed alignment and acetylene pressure that the PMC provides.

Chapter 6

Multi-pass Photonic Microcell using Micromirrors

In this chapter, novel micromirrors are introduced. A micromirror is formed from the end face of a single mode fibre taper which has been cleaved in the taper waist. These micromirrors can be inserted into the core of a HC-PCF to provide confinement in the longitudinal dimension and ultimately provide the means to fabricate multi-pass photonic microcells.

Using two micromirrors, a microcavity is formed inside a Kagome HC-PCF and also a silver-coated micromirror is used to demonstrate saturable absorption in a compact configuration using the reflected pump technique.

6.1. Introduction

In previous chapters, the gas-laser interaction was achieved using a single beam pass through the HC-PCF. In fact, for nearly all reported experiments using gas-filled HC-PCF this is the case. Considering the exceptional attributes of HC-PCF in tightly confining light in the tranverse plane in micron-scale modal areas and over large length-scales with low loss attenuation, it is desirable to introduce to the fibre a means to control light in the propagation direction. This requires the introduction of an integrated reflective optical component within the fibre. If such a solution to confine the light in the longitudinal dimension is found it would render HC-PCF an excellent candidate for a number of applications. For example, an optical microcavity with a high Q-factor could be formed by introducing two highly reflective mirrors into the hollow core. Alternatively, a single integrated mirror could be used in counter-propagating pump-probe spectroscopy such as saturable absorption.

A HC-PCF microcavity could have diverse applications from gas or strain sensing to cavity quantum electrodynamics (CQED). In gas-sensing, whilst the long interaction length offered by a HC-PCF is an obvious advantage in enhancing the signal, it is also a limiting factor because the gas loading time required to fill the entirety of the fibre-length is also proportional to the square of this length. A microcavity introduced into the HC-PCF could enable a long interaction length for a short piece of fibre which would greatly reduce the loading time while maintaining the sensitivity that a long interaction length provides. Additionally, a HC-PCF based microcavity would be a promising alternative to
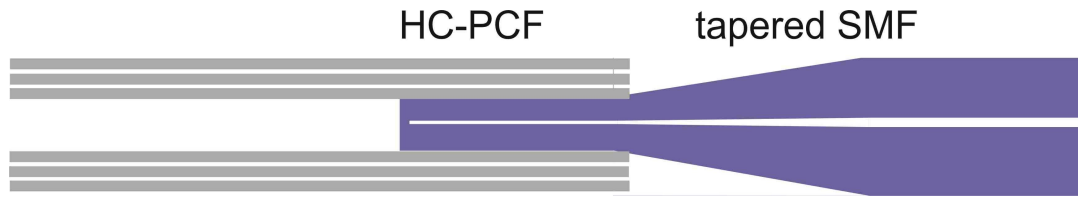
Figure 6-1: *Schematic of micromirror concept; a cleaved SMF taper can be inserted into the core of a HC-PCF to provide a reflective surface and light confinement in the longitudinal direction.*

Fabry-Perot based CQED by providing the compactness and the ease of coupling which are associated with optical fibre solutions, while also increasing the cavity robustness and versatility.

In this chapter, a novel micromirror design based on tapered SMF[5] and suitable for insertion into the core of a HC-PCF is described (Figure 6-1). Section 6.2 is a review of the requirements of optical microcavities and current outstanding candidates with a particular focus on fibre-based Fabry-Perot cavities. In section 6.3 the micromirror fabrication procedure is outlined. In section 6.4, a low finesse optical microcavity is developed as a proof of principle that the present configuration exhibits near ideal conditions for coupling light into the cavity with perfect mode matching conditons. The results show that the present low-finesse cavity exhibits higher performance than any previously reported HC-PCF-based cavities.

The introduction of only one micromirror into HC-PCF also has several possible applications. In section 6.4.2, a saturated absorption signal is generated using a micromirror which had been surface-coated with silver to increase the mirror reflectivity above the 4% expected at a silica/air junction.

6.2. Microcavities

The key requirements of optical microcavities vary depending on application. Microcavities are typically characterized using the cavity finesse (F), which is defined as the free spectral range (FSR) divided by the FWHM of the cavity resonances ($\delta\nu$). Finesse is related to the Q-factor of the cavity using the expression,

$$Q = \frac{F \nu_0}{FSR},$$
(6-1)

where ν_0 is the resonance frequency. For applications in CQED, strong atom-cavity coupling is only achieved for high Q-factor cavities, as the Q-factor is proportional to the

---

[5] SMF tapering by M. Grogan

confinement time [147]. Current candidates for this high specification application include microtoroid resonators [148], photonic crystals [149] and Fabry-Perot cavities [150]. In a Fabry-Perot cavity, the finesse, and thus the Q-factor, can be increased by increasing the reflectivities of the cavity mirrors into the cavity modes. This requires minimization of loss, due to scattering, absorption and mode-field mismatch, at the mirror interfaces.

Fibre-based Fabry-Perot cavities have been fabricated to study CQED of Bose-Einstein condensates on a chip [151]. The reflective mirrors are formed by laser machining the tip of a conventional optical fibre to produce a concave surface and subsequently applying a dielectric coating to increase the reflectivity [152]. Two such mirrors are carefully aligned to produce an open Fabry-Perot cavity, to which light is coupled through the fibre mirrors. Using this technique, cavity finesse values of ~ 37,000 have been achieved [153]. This fibre-based Fabry-Perot cavity implements all the advantages of optical fibres such as immunity to electromagnetic interference, low loss input and output coupling to the device, ease of integration and resistance to harsh environments. However, this scheme still relies on free space alignment and sensitive procedures for cavity mode-matching, which raises concerns about its robustness.

The formation of a fibre coupled Fabry-Perot cavity within a HC-PCF has the potential to relieve these practicality issues. Additionally, the waveguiding nature of the fibre would lift the strict constraints on cavity mode field matching at the mirror interfaces due to diffraction effects. Formation of such a cavity requires a suitable reflective component to be integrated with the HC-PCF.

One of the early efforts towards forming a HC-PCF based optical cavity, reported by Couny *et al.* [154], consisted of splicing conventional fibre Bragg gratings to a hydrogen-filled PMC to enhance the generation of SRS. However, the relatively high loss of intra-cavity splices limited the impact of this solution as the finesse was less than 10. Alternative approaches have exploited the otherwise parasitic effect [155] of the ~4% Fresnel reflection at the splice interface between HC-PCF and SMF to form a low reflection mirror. For example, this approach was used for a simplified SAS scheme [146], where the counter-propagating probe-beam was formed from the reflection of the pump beam at the HC-PCF and SMF interface. A further example was a low finesse, HC-PCF based extrinsic Fabry-Perot interferometer [156]. This was formed by splicing each end of a short length of HC-PCF to a face-coated and face-uncoated SMF respectively. Such low finesse cavities have been demonstrated for a variety of sensing applications including strain, pressure and temperature sensing [156].

In the schemes described above the reflections take place at the spliced interfaces. This poses two limiting factors on the maximum reflectivity achievable and therefore the maximum finesse of the cavity. Firstly, because the reflections are formed at an abrupt splice junction, this induces an optical loss due to the unavoidable mode field mismatch
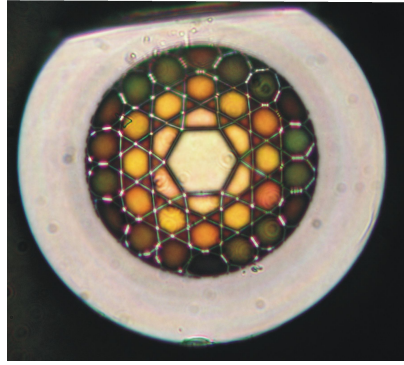
Figure 6-2: *Optical microscope image of 1-cell Kagome HC-PCF used throughout this work. Outer diameter is 136 µm and maximum core diameter is 26 µm.*

between two different fibres such as HC-PCF and SMF. Secondly, the high temperature (~1900ºC) required during the splicing procedure degrades any coating material deposited on the SMF tip [157]. Recently, Marty *et al.* [158] successfully overcame this through use of a gas-tight adaptor to hold the fibres in place as an alternative to splicing. However, this adaptor increases the complexity of the system.

In this chapter, a technique is proposed for addressing both these issues; micromirrors are formed using a section of tapered SMF which is cleaved in the waist region and designed to fit into the core of the HC-PCF. This cleaved face can be coated with a reflective film to increase the reflectivity of the micromirror. Once inserted, the taper can be hermetically fused in place, away from the mirror surface, hence avoiding damage to the mirror coating and providing a controllable reflectivity within an all-fibre system. The SMF taper also provides adiabatic coupling to the HC-PCF core and enables precise mode field match. The micromirror fabrication technique is described in detail in the following section.

6.3.   Micromirror Fabrication

A micromirror is fabricated from a piece of tapered SMF by cleaving the taper in the waist region to form a small, flat, reflective surface. The SMF is tapered using the moving flame-brush technique [140] which is outlined in chapter 5. The reflective surface is made by cleaving ~1 mm into the waist region. In order to optimise the reflection from the micromirror into the fundamental mode of the HC-PCF, it is essential that the cleaved surface is flat. Therefore, each cleaved taper is inspected using an optical microscope and any angled faces are rejected.

In order to achieve optimal coupling from the micromirror into the fundamental mode of the HC-PCF is it necessary to tailor the mode field diameter of the dominant output mode of tapered SMF to match that of the fundamental mode of the Kagome fibre. The evolution of the mode field diameter of an SMF taper in air as a function of outer fibre
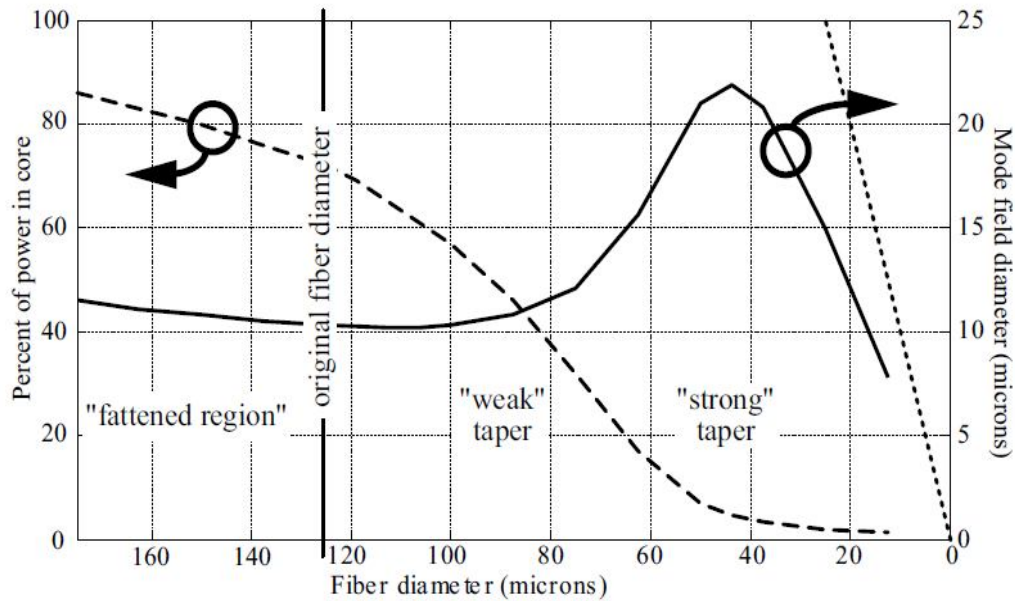
Figure 6-3: *The evolution of the mode field diameter (black line) and percentage of power confined in the core (dashed line) for SMF as a function of fibre outer diameter. Cladding outer diameter is shown by dotted line. As the taper diameter is decreased the mode field diameter starts to increase as the confinement effects of the fibre core are reduced and the light remains confinement by total internal reflection at the glass-air interface. Figure from [159] with kind permission from Springer Science+Business Media: Optical Fiber Fusion Splicing, chapter 8, 2005, page 223, A. D. Yablon, figure 8.7.*

diameter is shown in Figure 6-3 [159]. For this calculation, the original (untapered) fibre outer diameter is 125 μm and the original core diameter is 8.3 μm [159]. The behaviour of the mode field diameter is split into two categories; the 'weak' and 'strong' taper regions. In the weak taper region, the mode field diameter is largely unaffected by the reduction in fibre outer diameter. This applies for outer fibre diameters between 80 and 125 μm. As the fibre diameter is reduced further, below 80 μm, the mode field diameter is described in the strong taper regime; the core diameter becomes so small that the variation in refractive index between this area and the fibre cladding has a negligible effect on the tapered fibre guidance. Therefore, the fibre guides due to the refractive index difference between the cladding and the surrounding air and the mode field diameter expands accordingly. As the fibre diameter continues to be reduced below ~45 μm a turning point in mode field diameter occurs due to the physical restriction of the cladding diameter (indicated by the dotted line in Figure 6-3 [159]).

For all the work described in this chapter, the HC-PCF has a Kagome-lattice cladding and the minimum (maximum) diameter of the hollow core is 23 (26) μm (Figure 6-2). Therefore, the tapered fibre has a diameter of ~20 μm and is therefore described in the strong taper regime outlined in Figure 6-3. The loss of a complete adiabatic taper of this size was measured to be ~0.05 dB at 1550 nm. In the work described here, the taper transition length is 10.4 mm in order to ensure adiabatic transitions.
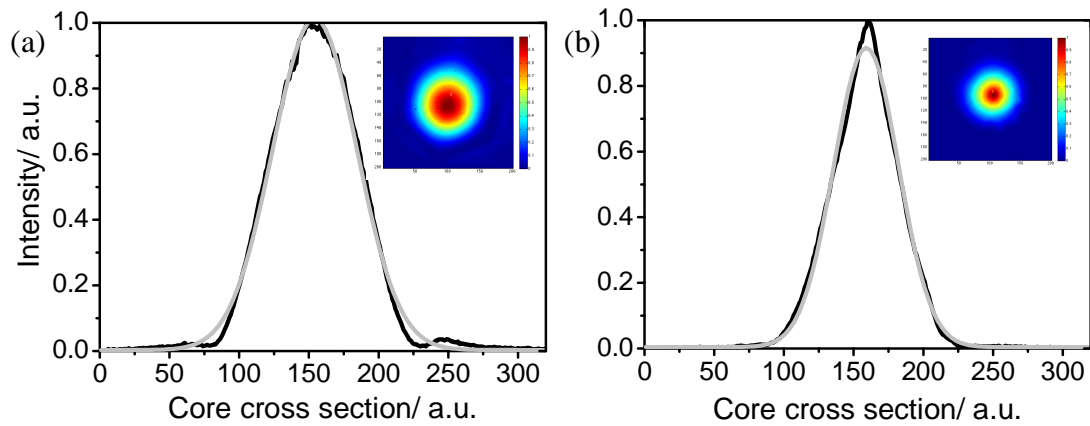
Figure 6-4: *(a) and (b) show experimental mode profiles (black line) of Kagome 1-cell HC-PCF and tapered SMF respectively. Gaussian fits are shown for comparison (grey line). Mode images are shown inset.*

From Figure 6-3, a SMF taper with a diameter of 20 μm is expected to have a mode field diameter of ~12 μm. Assuming a Gaussian profile for the fundamental mode of the Kagome fibre, which is well confined in the hollow core, the mode field diameter of the HC-PCF is expected to be ~15 μm. Using these values, equation (5-2) estimates an attenuation of ~0.2 dB due to mode field mismatch between these fibres. In contrast, the measured loss at a splice junction between untapered SMF and the Kagome fibre used here is typically 2 dB. This highlights the potential of the micromirrors to provide extremely low loss coupling to the HC-PCF. This coupling could be improved even further using a micromirror with a 22 μm diameter. However, a note of caution is prudent here, as in the strong taper regime the light can be coupled out of the taper if it is coated with any material with an equal or higher refractive index than silica. Additionally, perturbations in the output mode of the micromirror can arise through bending the taper.

To support this loss estimate experimentally, the mode field profiles of the Kagome fibre and a micromirror were recorded on a XenICs InGaAs camera and are shown in Figure 6-4. The input light source was a supercontinuum fibre filtered using a 10 nm band pass filter centred at 1550 nm. Figure 6-4(a) shows that the mode field profile of the 1-cell Kagome fibre is well described by a Gaussian profile. The micromirror modal profile (Figure 6-4(b)), although approximated by a Gaussian profile, displays significant deviations from Gaussian behaviour near the centre of the mode. This deviation indicates that even with a diameter of 20 μm, which is well into the strong taper regime, the core of the fibre is still providing some confinement. It is not possible using this experimental technique to accurately scale the mode field diameter for these modal profiles due to the different numerical apertures of the fibres. However, a rough estimate can be made using the un-scaled mode field diameters from this data which were found
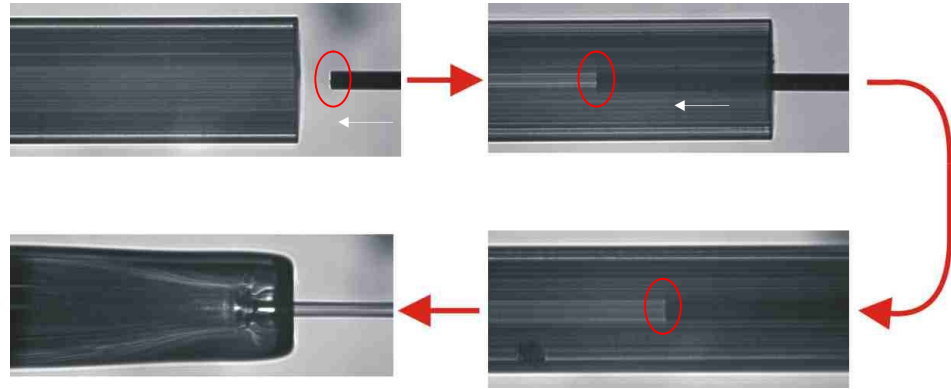
Figure 6-5: *Photographic sequence portraying the insertion of a micromirror (right) into the core of the Kagome fibre (left) and its subsequent fusion in place. The micromirror position is circled in red.*

to be 117 and 96 for the Kagome and micromirror fibres respectively. Using equation (5-2) this indicates a coupling loss of 0.17 dB which is in very good agreement with the estimate performed above.

The insertion of the micromirror into the HC-PCF follows a series of steps which are shown in Figure 6-5. The micromirror is inserted ~1 mm into the core of the HC-PCF using the alignment stages of a Vytran filament splicer. The micromirror can be permanently held in place by fusing and collapsing the end of the Kagome fibre onto the tapered SMF using the splicer. This collapse does provide a means for light to be coupled out of the micromirror into the PCF cladding and therefore is not an optimal method of holding the micromirror in place. An alternative low loss solution would be to use an adhesive with a suitably low refractive index ($n < 1.45$).

6.3.1. Micromirror Coating Investigation

In order to increase the reflection from the micromirror tip above the 4% reflection expected at an air/silica interface, a reflective coating can be applied. Here a silver coating was applied using a simple thermal evaporation method. The thickness was monitored and controlled by the deposition time.

Figure 6-6(a) shows the experimental set-up used to calibrate the reflectivity of the silver coating; light from an ECDL (λ ~1540 nm) is launched, via a fibre circulator, into the input of the Kagome fibre which is angle-spliced beforehand to untapered SMF to reduce Fresnel reflection at this junction [139]. The reference reflected power, $P_{uncoated}$, is measured at the third port of the circulator when an uncoated, untapered piece of SMF is butt-coupled to the output of the Kagome fibre. The uncoated SMF is then replaced by silver-coated untapered and tapered SMF samples, the reflectivities of which are quantified by the reflectivity ratio $R = P_{coated}/P_{uncoated}$. Figure 6-6(b)-(e) show data recorded using coated, untapered SMF samples as a function of coating time. Figure 6-6(b) shows

that *R* increases with coating evaporation time until a plateau occurs at a time of ~80 s which, from calibration of the thermal evaporator, corresponds to a film thickness of ~16 nm. This plateau occurs for an increase in reflectivity by a factor of 28.

By evaluating the losses in the measurement system, the butt-coupled untapered and uncoated SMF reflected an estimated 3.4% of the HC-PCF output power back into the core. Using this estimate as a reference it was deduced that a maximum reflectivity of 95% was achieved using untapered silver-coated SMF, butt-coupled to Kagome HC-PCF. This is indicated in Figure 6-6(c). The corresponding transmission measurements are shown in Figure 6-6(d) and indicate significant scattering loss (Figure 6-6(e)) due to the coating application. This can be attributed to the very basic coating procedure and could be overcome by using existing fibre-tip coating procedures (eg. [153]). Upon splicing, the reflection from the coated, untapered fibre dramatically decreased to ~2%, well *below* the reflection achieved with an *uncoated* fibre. This is due to degradation of the silver coating during the splicing process.

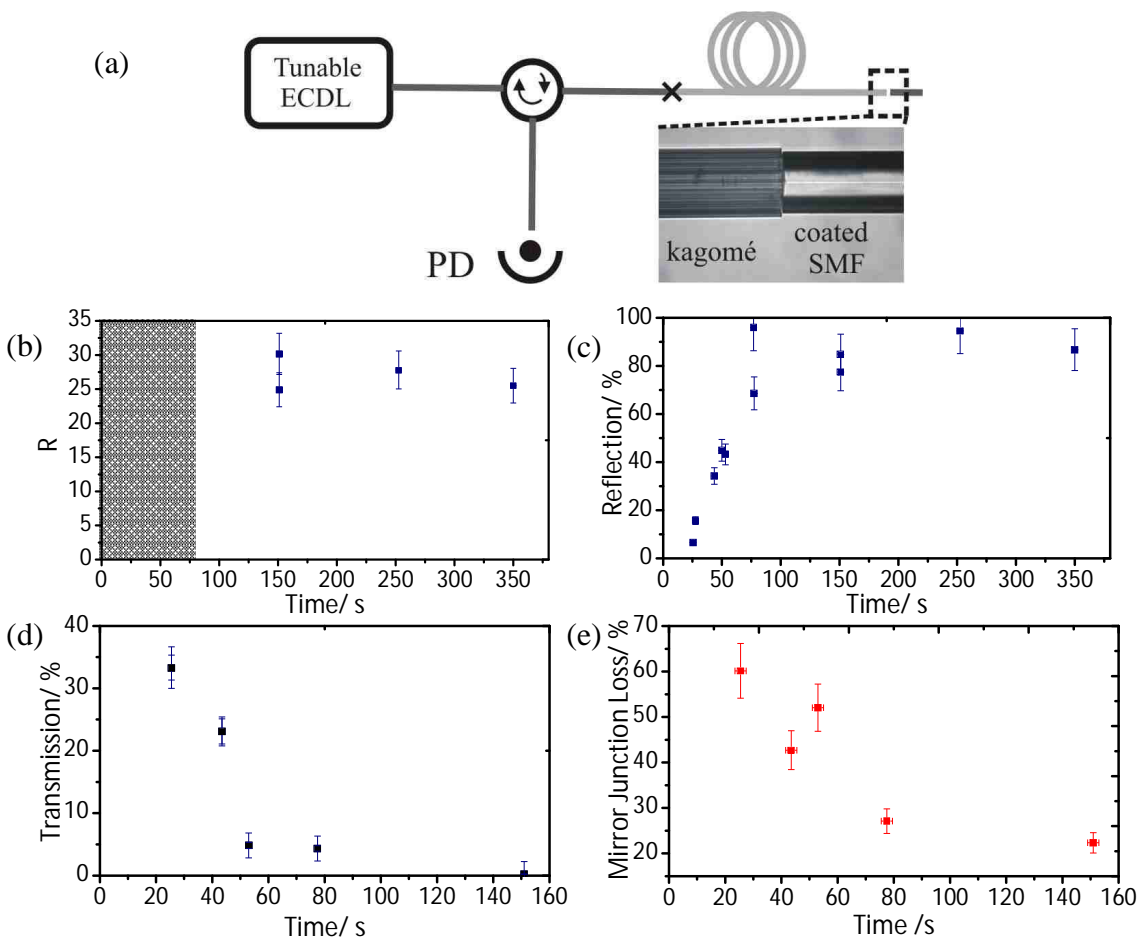**Figure 6-6:** *(a) Experimental set-up for coating calibration. (b) Reflectivity ratio R ($P_{coated}/P_{uncoated}$) as a function of coating deposition time. (c) Calculated reflectivity of micromirror coated assuming uncoated untapered SMF reflects 3.4% of incident light. (d) Corresponding transmission through SMF and (e) Mirror junction loss calculated using reflection and transmission data.*

A maximum reflectivity of 85% was recorded using a silver-coated micromirror, inserted ~1 mm into the Kagome fibre core. There are several possible reasons for the reduction in reflectivity of a micromirror compared to the untapered fibres. Firstly, an untapered fibre reflects all the light coming out of the Kagome fibre, including higher order cladding modes, whereas the micromirror will favourably reflect the fundamental core mode. Secondly, the surface roughness of the cleaved taper is likely to be higher than that of the untapered fibre due to water penetration during the taper process and accentuated further by the basic coating application. Water penetration during the taper process can be inhibited by using a carbon monoxide environment [160].

Upon fusion, the reflection from the micromirror remained unchanged; in this configuration there is no degradation to the silver coating when the micromirror is fused in place. These results show that using a micromirror the range of possible reflective coatings can be expanded in order to maximize the reflectivity from the end face of the micromirror.

However, the maximum reflectivity of 85% is not sufficient for development of a high Q-cavity. This maximum value was limited by the simplicity of the coating technique used here and much higher reflectivities should be possible using the advanced fibre tip preparation and coating techniques described in [153]. Yet, for the purpose of applications where only a single mirror is required, or for moderate finesse cavities, such a basic and economical coating method is sufficient.

Using the techniques described in this section, micromirrors were fabricated and used to demonstrate two different applications. These applications are described in the following sections.

6.4. Micromirror Applications

6.4.1. Low Finesse Microcavity

As a first demonstration of the potential applications of micromirrors, two uncoated micromirrors were used to form a microcavity within a 3 mm length section of Kagome lattice HC-PCF. The micromirrors were inserted from each end of the Kagome core and the cavity length was adjusted using the alignment features of the Vytran splicer. The back mirror was fixed by collapsing the HC-PCF end as described in section 6.3, whilst the front mirror was kept free running so that the low loss input coupling to the HC-PCF was maintained. Additionally, the position of this front micromirror could be tuned within the alignment range of the splicer to adjust the cavity length.

An optical image of a microcavity with a cavity length of 340 μm is shown in Figure 6-7(a). The tapered SMF end faces which form the micromirrors are clearly visible. The cavity spectral characteristics were measured in reflection and recorded on an OSA with

(a)

(b)

(c)
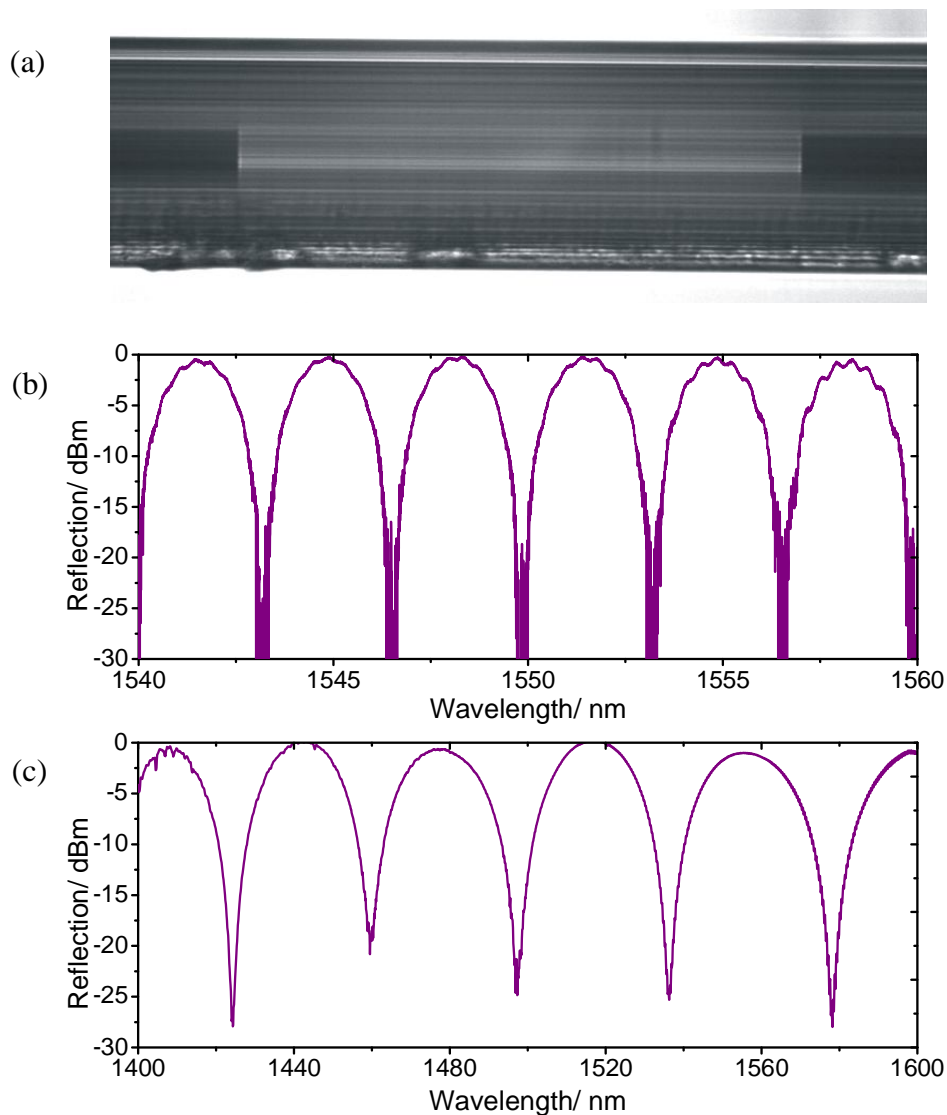
Figure 6-7: *(a) Example cavity formed from two uncoated micromirrors inserted into the core of a HC-PCF. L= 340 µm. (b) Reflection from cavity shown in (a). (c) Reflection from cavity with L ~ 30 µm. Traces recorded on OSA and normalised using spectrum of white light source.*

a resolution of 0.02 nm. The reflection spectrum for this cavity is shown in Figure 6-7(b). This was obtained by recording the optical output from a fibre circulator, which was spliced to the end of the non-tapered section of the micromirror. Small oscillations visible on the reflected signal are thought to arise from a weak reflection from the region where the back mirror is held in place through cladding collapse. Figure 6-7(c) shows the reflection spectrum from a cavity with a length of only 30 µm recorded at a resolution of 0.5 nm. Cavity lengths were initially determined through measurements taken with an optical microscope and subsequently corroborated using the cavity free spectral range.

The finesse for these microcavities is ~2.1. This is very low and is due to the low reflectivity of the uncoated micromirrors. Yet, the spectrum in Figure 6-7(c) shows

experimental fringe contrasts as high as 28 dB, which is the best performance reported so far for a cavity formed using reflections at a silica-air interface [161] and is the highest contrast demonstrated in a HC-PCF cavity to the best of the author's knowledge. This extremely high fringe visibility is indicative of the excellent mode field matching at the cavity interfaces.

In order to assess this quantitatively, the theoretical expression of the contrast for such a cavity is derived here, considering the cavity schematic shown in Figure 6-8. Due to the low cavity finesse, two passes through the cavity are considered only. The field amplitudes, as defined in Figure 6-8, E_1 - E_4 and E_r are expressed as,

$$
\begin{aligned}
E_1 &= t_1 E_{in} + i r_1 E_4 \\
E_2 &= e^{i\tilde{\beta}L} E_1 \\
E_3 &= i r_2 E_2 \\
E_4 &= e^{i\tilde{\beta}L} E_3 \\
E_r &= t_1 E_4 + i r_1 E_{in}
\end{aligned}
\tag{6-2}
$$

where $\tilde{\beta} = \beta + i\alpha_f$ and β is the propagation constant and α_f is the fibre attenuation. r_1 and r_2 are the amplitude reflectivities of the front and end cavity-mirrors respectively. Using equations (6-2) the power reflectivity, R_{cav}, is given by,

$$
R_{cav} = \frac{(r_1 - B)^2 + 4Br_1 \sin^2\left(\delta\beta L_f\right)}{(1 - A)^2 + 4A \sin^2\left(\delta\beta L_f\right)},
\tag{6-3}
$$

where

$$
A = r_1 r_2 \left(1 - 2\alpha_f L_f\right)
\tag{6-4}
$$

and

$$
B = r_2 \left(1 - L_1\right)\left(1 - 2\alpha_f L_f\right).
\tag{6-5}
$$
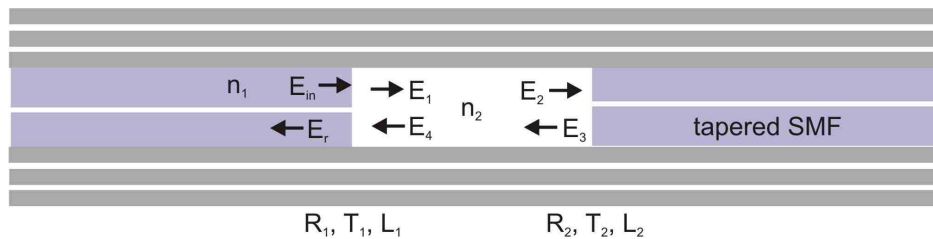
Figure 6-8: *Schematic microcavity formed inside the core of a Kagome HC-PCF using two micromirrors.*
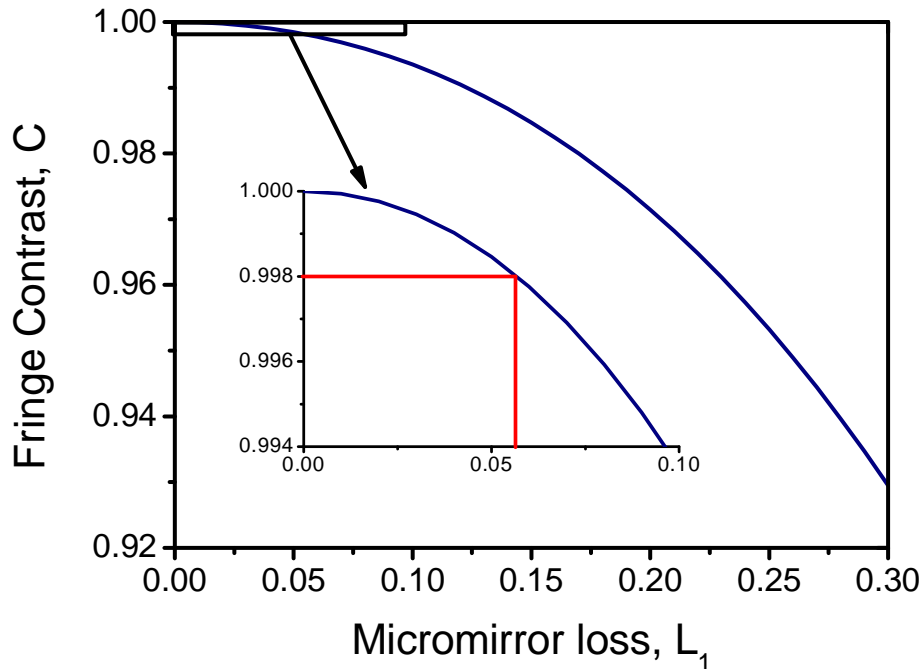
Figure 6-9: *Fringe contrast (calculated using equation 6-6) as a function of loss of input micromirror.*

Here, L_f is the length of the fibre section between the two micromirrors, $\delta\beta$ is the propagation detuning from the cavity resonance and L_1 is the power loss coefficient at the front interface. Consequently and given the reflectivity of the air-silica boundary and the fibre loss, the coupling loss at the front mirror L_1 can be deduced from the fringe contrast, which is given by:

$$C = \frac{R_{max} - R_{min}}{R_{max} + R_{min}} = \left(2\left(\frac{Br_1}{(r_1 - B)^2} - \frac{A}{(1 - A)^2} \right) \right)\left(1 + 2\left(\frac{Br_1}{(r_1 - B)^2} - \frac{A}{(1 - A)^2} \right) \right)^{-1} \quad .(6\text{-}6)$$

This fringe contrast is plotted in Figure 6-9 as a function of L_1. It is evident that to achieve high fringe visibility, very low loss at the input micromirror is required. Applying equation (6-6) and using the measured fringe extinction value of 28 dB, which corresponds to $C = 0.998$, 4% to the intensity reflection for each micromirror and neglecting the fibre transmission loss, gives a loss L_1 due to the front mirror of 0.25 dB.

This loss encompasses attenuation due to mode field mismatch, taper transition loss (~0.025 dB) and scattering due to surface roughness. Also, if cleave in the taper waist is not perfectly flat this will contribute to this loss figure. As explained in the previous section, the expected attenuation due to mode field mismatch between the micromirror and the HC-PCF is ~0.2 dB, which is in good agreement with the loss value calculated

using this simple model. Further improvement of the loss figure could be achieved with better surface treatment and core shape and taper size matching.

The formation of a similar microcavity with silver-coated micromirrors was attempted but the observed fringe contrast was reduced. This was attributed to the increase in L_1 due to surface roughness induced scattering at the micromirror interface.

6.4.2. SAS

A further application of micromirrors is in gas spectroscopy. Here, the SAS reflected pump technique, reported in [146], is reproduced using acetylene-filled Kagome HC-PCF and a silver-coated micromirror to create the reflected probe beam.

This work contrasts with the experiment reported in [146] where the probe beam is created from the reflection of the pump beam at a splice between the HC-PCF and SMF. Additionally, the fibre in [146] was a PBG HC-PCF, guiding with extremely low attenuation in a limited core diameter. Here, Kagome fibre is used as it offers a larger core diameter, hence providing a reduction of the wall-collision component of the acetylene line broadening. Yet, the Kagome fibre used here has a significantly higher attenuation (1.5 dB/m) than the PBG HC-PCF and consequently, the SAS experiment requires an increased reflection of the pump beam. Therefore, the micromirror is coated with a thin silver film (as described in section 6.3.1) to increase the power of the back reflected probe light.

Even though the coatings used here are very basic they are suitable for the purpose of increasing the probe back-reflection for the SAS application. The experimental set-up is shown in Figure 6-10(a). Light from an ECDL tuned to the P25 transition from the acetylene $\nu_1 + \nu_3$ overtone band passes through an EDFA and a circulator. The (SMF) output of the circulator is angle-spliced to the input of 3 metres of Kagome fibre. Even with the angle splice, the reflection at this junction is not completely extinguished; this
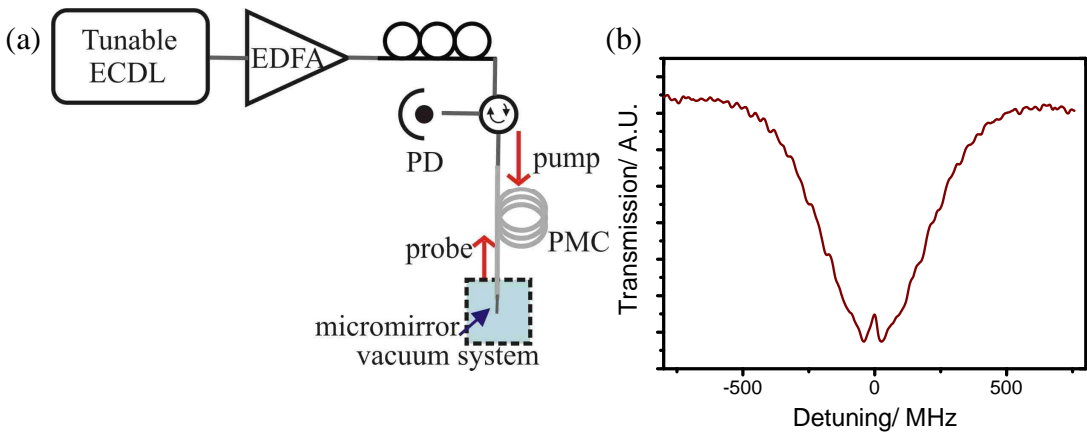

Figure 6-10: *(a) Experimental set-up for reflected pump SAS and (b) SAS trace recorded. Linewidth of sub-Doppler feature is 25 MHz.*

increases the motivation for a higher power probe beam in order to increase the SNR of the recorded SAS trace compared to etalon effects. A micromirror with a reflectivity of ~25% (tailored through coating time) was inserted into the other end of the Kagome fibre which was then loaded into the vacuum system. The fibre collapse around the micromirror was sufficient to hold the mirror in place but was left incomplete to allow evacuation of and acetylene-loading into the Kagome core.

Figure 6-10(b) shows a SAS feature recorded at the third port of the circulator for a pump power of 97 mW and acetylene pressure ~0.5 mbar. This trace is time-averaged to remove background oscillations due to interference effects. The sub-Doppler feature width is ~25 MHz which is similar to previously published results [122] for a fibre of similar core size indicating there is little increase in power broadening despite the higher power probe beam. This compactness of this SAS device could be further enhanced by using the helium loading technique reported in [37] to remove the Kagome fibre from the vacuum system followed by fully collapsing the fibre core around the micromirror. However, as explained in chapter 5, etalon effects which can degrade the SAS signal need to be reduced for this scheme to maximise its potential.

6.5.   Summary and Outlook

In this chapter, micromirrors have been introduced which, when inserted into the core of HC-PCF, provide a means for confinement in the longitudinal dimension. The micromirrors are formed using tapered SMF which is cleaved in the waist region to produce the reflective surface. It has been shown that the adiabatic coupling into the core mode of the HC-PCF is very low loss by the record fringe visibility observed when two micromirrors were used to create a microcavity in HC-PCF. Additionally, an application in gas spectroscopy was demonstrated using a silver-coated micromirror.

The coatings used in this work were very basic and therefore did not provide the means for creating a high finesse cavity in the HC-PCF. The micromirror reflectivity could be increased using commercially available dielectric stacks (as used in [152]), especially if the fibre is cleaned and polished pre-coating to reduce the surface roughness. Additionally, further work is required to develop a means to hold the micromirrors in place without inducing additional optical loss.

Chapter 7

Rubidium Loading in HC-PCF

In this chapter, preliminary work towards fabrication of a rubidium-filled photonic microcell is described. Rubidium vapour loading into a 19-cell Kagome HC-PCF is analysed and future modifications to the vapour loading system are outlined.

7.1.   Introduction

In previous chapters the work presented has revolved around the use of molecular gases, specifically acetylene. The complex rovibrational absorption structure of these gases provides a multitude of absorption lines which can be used as a reference grid in the frequency domain. However there are cases where a simpler atomic structure is desirable.

Simple, stable and well calibrated states are provided by alkali vapours such as rubidium and caesium; the energy structure of these atoms is analogous to that of the hydrogen atom as there is a single electron in the outer shell. In particular, the hyperfine structure of their energy levels has been extensively used to provide an oscillator signal for atomic clocks. In fact the transition between the hyperfine levels of the ground state of caesium-133 (at 9.2 GHz) has been used in the definition of the second since 1967 [162]. The transition dipole strengths of atomic vapours are approximately 1000 times larger than those for molecules, enabling gas-laser interactions at accordingly lower intensities and pressures. This enables generation of narrower spectroscopic features due to reduced power and pressure broadening. Additionally, this strong optical strength makes alkali vapours excellent candidates for single photon interactions [163].

Spectral features generated in alkali vapour have diverse applications including frequency stabilisation (using SAS) [164], atomic clocks as mentioned above (using CPT [165] or Ramsey fringes [26]), magnetometry and interferometry [20]. The gas host for such applications is typically a macroscopic, Pyrex cell with dimensions on the centimetre scale. However, recent trends have been towards the development of miniature, on-chip scale devices. The gas-laser interaction in these devices occurs in a gas cell with a volume of the order of a few mm^3 [28]. The SNR of these compact devices is limited by the dimensions of the light-atom interaction volume; the short interaction length available in

these devices sets an upper limit on the laser power level required which in turn directly affects the resonance linewidth through power broadening.

A rubidium-filled PMC would provide a very competitive alternative to these chip-based devices; as discussed in previous chapters the tight light confinement over a long interaction length would enable interrogation of the atomic vapour using ultralow powers and the achievement of a superior SNR, enabling observation of quantum optic effects such as EIT at extremely low light levels. In this few-photon scheme there is potential for single atom interactions with extremely well defined and extremely narrow spectral resonances.

Several groups have already shown this potential through using rubidium-filled HC-PCFs for demonstrations such as passive slow light, SAS [166] and EIT with extremely low power lasers [47, 48], efficient all-optical switching [163, 167] and ultralow threshold four wave mixing [168].

In this chapter, rubidium loading into HC-PCF is investigated towards the development of a rubidium-filled PMC. There are significant challenges in loading a HC-PCF with rubidium vapour, most notably due to the extremely reactive nature of rubidium vapour, which are explained in section 7.2 along with possible solutions. Previous loading schemes [101] have used vacuum systems fabricated using only stainless steel due to its compatibility with ultra-high vacuum (UHV) components. In the experimental scheme described in section 7.3, a PDMS-coated glass cylinder is inserted in the rubidium loading chamber in order to try to reduce the loss of rubidium vapour through adsorption to the stainless steel chamber. The preliminary results presented in sections 7.4 and 7.5 indicate that the coated glass cylinder inserted in the rubidium source chamber increases the effective lifetime of the rubidium vapour.

7.2. Rubidium Loading Techniques

Rubidium is a soft, silvery metal which is solid at room temperature. Natural rubidium is 73% rubidium-85 (the only stable isotope of rubidium) and 27% rubidium-87 (radioactive but with an extremely long half life). The melting point of rubidium is 39 °C and the boiling point is 688 °C [5]. For the work presented in this chapter, the D2 spectral lines ($\lambda \sim 780$ nm) are studied; the relevant energy level configuration is shown schematically in Figure 7-1 for rubidium-85.

The vapour pressure of rubidium is ~10^{-7} mbar at room temperature [5] which presents the first challenge to loading rubidium vapour into HC-PCF; in contrast to molecular gases such as acetylene it is very difficult to generate a large enough density of rubidium to load a fibre through a pressure gradient.
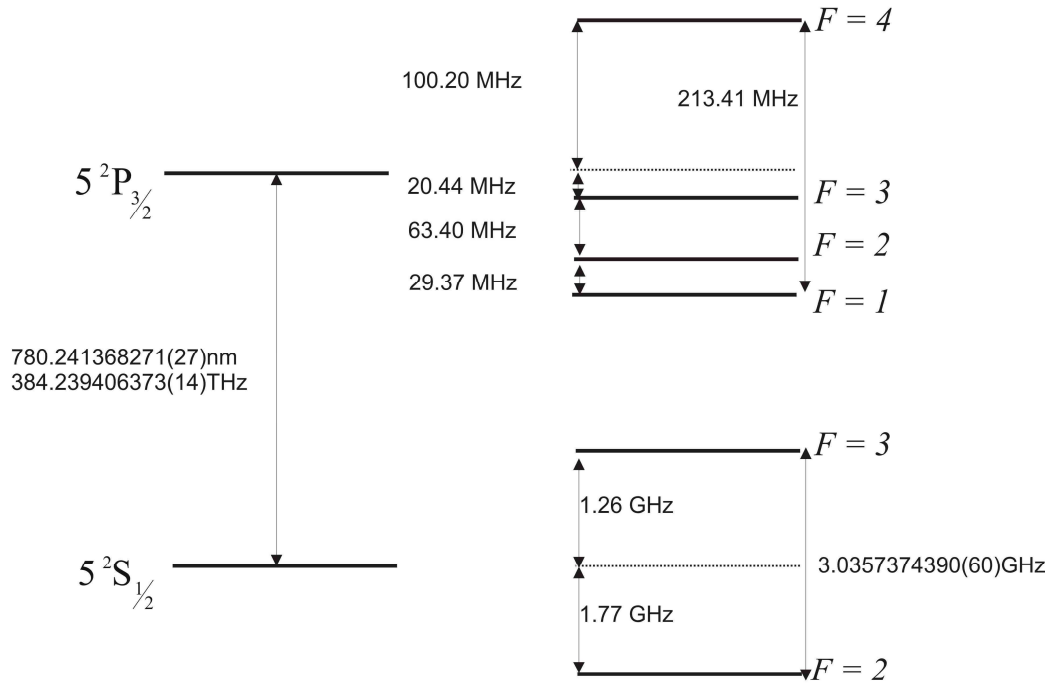
Figure 7-1: *Energy level scheme for the D2 absorption lines of rubidium-85 (frequencies taken from [5]). The hyperfine splitting of the $5\,^2S_{1/2}$ ground state at the microwave frequency of 3.036 GHz is used as the reference oscillator in many atomic clocks.*

The second, and most problematic, challenge arises from the extremely reactive nature of rubidium; it spontaneously reacts with oxygen in the air and is explosive on contact with water. In the fibre geometry, this means that the rubidium atoms tend to stick to the inner core walls of the fibre rather than stay in the vapour phase. The interaction between a rubidium atom and the silica core wall can occur via two different mechanisms; physisorption and chemisorption. The interaction via chemisorption involves a chemical reaction between the rubidium atom and the silica surface or molecules that are adsorbed to the silica surface. Through this process the rubidium atom becomes permanently bonded to the core wall. The interaction via physisorption is temporary; the atom sticks to the silica wall for a finite sticking time τ_s before being released back into the rubidium vapour [169]. In both cases, the rubidium atom is attracted to the silica walls by an image charge which forms in the surface.

Over recent years there have been several steps forward in loading HC-PCF with rubidium which have used a variety of techniques, largely adapted from macroscopic vapour cell fabrication, to overcome these challenges.

The first of these is to apply a coating to the silica surface, in the case of HC-PCF to the inner core walls, to reduce rubidium interaction with the surface. The first wall-coating for an alkali vapour cell was demonstrated by Robinson *et al.* in 1958 [170]. Since then numerous coatings have been investigated, including siloxane coatings. An example of

such a coating is the polymer polydimethylsiloxane (PDMS), which has the repeating unit [$SiO(CH_3)_2$]. Physical properties which make it an excellent coating candidate are very high mechanical, thermal and chemical stabilities which originate from the high energy of the siloxane (Si-O) bond. It is a viscous, transparent fluid at room temperature [171].

The most important property of the polymer coating is that it reduces the reaction rate of the rubidium vapour with the coating substrate, usually silica. After a ripening period, which varies depending on cell geometry and rubidium density, an ambient rubidium vapour is established in the vapour cell, indicating a reduction in the amount of rubidium being adsorbed [172]. Siloxane coatings are successful because they are terminated by methyl groups. These groups have a low dielectric constant and therefore act to reduce the van der Waals attraction between the surface and the alkali vapour. The low dielectric constant is due to the fact the methyl groups are sufficiently polarisable to react with their neighbours, in order to present a smooth surface to the rubidium vapour but not so polarisable that an image charge is formed in the surface [173]. It has also been shown that the longer the polymer chain, the lower the reaction rate between the surface and the rubidium vapour. This has been attributed to better shielding of the oxygen in the coating from the alkali vapour [173]. These coatings have also been applied to stainless steel and have been shown to reduce the rubidium reaction rate but not as effectively as on a glass substrate. It is believed that the polymer coating has a tendency to form incorrectly on the stainless steel surface due to a lack of available OH radicals for the polymer to bond with [169, 173]. Further evidence of the dramatic effect of the reduced interaction between the alkali vapour and coated cell walls is the extremely narrow linewidth spectral features which have been recorded in wall coated cells [34, 174]. This 'anti-relaxation' effect of the coating is becoming even more critical as cell volume reduces.

Siloxane coatings have been applied to the inner core walls of HC-PCF by Ghosh *et al.* [48] and Light *et al.* [47] to reduce the interaction between rubidium and silica. Additionally, Light *et al.* [47] observed a reduction in the linewidth of their EIT features due to the anti-relaxation effect of the coating.

A further advantage of using coatings such as PDMS is that they have been shown to demonstrate light induced atomic desorption (LIAD) [175]. When non-resonant light is incident on the coating, previously adsorbed rubidium atoms are rereleased into the vapour phase as the incident light increases the mobility of the atoms inside the coating and the desorption rate from the surface [176]. The dependence of LIAD on the desorbing light intensity and wavelength has been extensively studied [176-178] and it has been proven to be a non thermal effect.

LIAD has been very successfully used by Gaeta's group at Cornell University to create an on-demand rubidium vapour density in the core of a HC-PCF [48]. This group reported

that it is very difficult to sustain a rubidium vapour in the core in the absence of LIAD due to rubidium adsorption to the inner core walls but by means of LIAD they achieve large optical depths (up to 1200 [179]) on-demand, using desorption beam powers from ~10 – 90 mW. Typically, fibres are exposed to rubidium vapour for ~ 3 weeks before reproducible LIAD is observed and fibre lengths are of the order of a few centimetres. This group have also investigated the effects of the LIAD beam on resonance signals, in particular ac stark shifts have been recorded [166].

It is also very noteworthy that recently LIAD has been demonstrated from uncoated stainless steel (with a higher intensity threshold) [180], as well as very recently from uncoated porous silica [181] and most intriguingly bare HC-PCF [179]. The use of bare HC-PCF is interesting as it has been reported that coating the fibre core walls can degrade the fibre transmission properties [49]. Furthermore, in both the porous and HC-PCF geometry the nature of the rubidium adsorption to the surface is believed to differ from that in macroscopic cells. The extreme nano-scale confinement in porous silica enhances the recycling of desorbed rubidium; instead of moving away from the silica surface the confinement ensures that the rubidium atoms continue to have a strong interaction with the surface even after being desorbed. This leads to the formation of nanoclusters which can be probed optically as they exhibit surface plasmon based resonance effects which relate to their size [181]. This differs from LIAD in macroscopic cells which so far has always been considered a non-resonant effect. The formation of such nanoclusters has important consequences in the HC-PCF geometry as they also act to reduce the transmission of the fibre [49]. This reduction in transmission partially counteracts the advantages that a vapour-filled HC-PCF can provide.

An alternative atomic vapour loading technique is light induced drift (LID) through which the drift velocity of atoms can be increased in a specific direction either co- or counter-propagating with a resonance-detuned laser. In the context of vapour loading into HC-PCF, LID can be used to push atoms into the core of the fibre. LID was first theoretically predicted by Gel'mukharov [182] and is based on velocity class selection from the Maxwell distribution of atomic velocities by a laser which is red detuned from resonance. Atoms from this velocity class are selectively excited and acquire a drift velocity in the direction of the laser beam. Due to this perturbation in the velocity distribution, ground state atoms acquire an equal and opposite drift velocity in the absence of any further perturbations. Addition of a buffer gas provides such a perturbation via collisions; an excited state generally has a higher collision cross section than a ground state and this leads to a difference in the diffusion rates of the excited and unexcited atomic species [183]. Through this technique velocities of the order of 14 m/s have been generated. The drift velocity is dependent on the intensity of the detuned laser, the buffer gas pressure and the buffer gas species used [40]. Addition of a coating is also

advantageous when using this loading scheme as the reduction in rubidium adsorption reduces the frictional coefficient felt by the atomic species and thus enables higher drift velocities to be achieved [183]. This technique was used by Light *et al.* [47] to load a PDMS-coated HC-PCF with rubidium vapour. Using a red detuned laser, coupled into the core of the HC-PCF, they observed a twofold increase in the rubidium absorption signal from the fibre.

Further techniques which have been used to load HC-PCF include radiation pressure [47], MOT [163] and atom guiding [184]. The latter two techniques require complex experimental schemes.

The aforementioned vapour loading techniques have typically been applied to short fibres (a few centimetres) and the loading takes place over a timescale of a few weeks. In the following sections, possible experimental conditions to reduce this timescale and increase the length of HC-PCF loaded with rubidium are described, followed by preliminary experimental results, with the ultimate goal being a reproducible rubidium loading technique for PMC fabrication.

7.3. Experiment Design

The physical properties of rubidium described in section 7.2 help to define the system required for rubidium loading (Figure 7-2). The choice of rubidium source is a key parameter; for this experiment a source containing rubidium in an inter-metallic compound is used. Rubidium vapour sublimes from this compound at a temperature of ~ 450 °C (achieved by applying an external current source). This temperature is suitable as it is above the typical temperatures required to bake out the vacuum system (150 °C) and yet still low enough to be reached using a reasonable current magnitude. Rubidium sources are mounted in two vacuum chambers which also contain the open ends of the HC-PCF.

Due to the extremely reactive nature of the rubidium vapour and the desire for narrow spectral features, an UHV environment is required. To this end, the vacuum system incorporates a turbo pumping system, which can achieve ~10^{-6} mbar, combined with an ion pump which can further reduce the system pressure to <10^{-8} mbar. Additionally, the vacuum system is designed using UHV stainless steel vacuum chambers and connectors which are cleaned (using an ultrasonic bath followed by rinsing in acetone and methanol [185]) and then baked for 4 hours at 400 °C before being installed into the vacuum system. This preparation is necessary to reduce the outgassing rate from the stainless steel surface which can act to limit the minimum system pressure and is also a means through which contaminants can enter the system.

Due to the low vapour density of rubidium at room temperature, the entire vacuum system is heated to ~150 °C (limited by the vacuum valves) and the HC-PCF is heated to
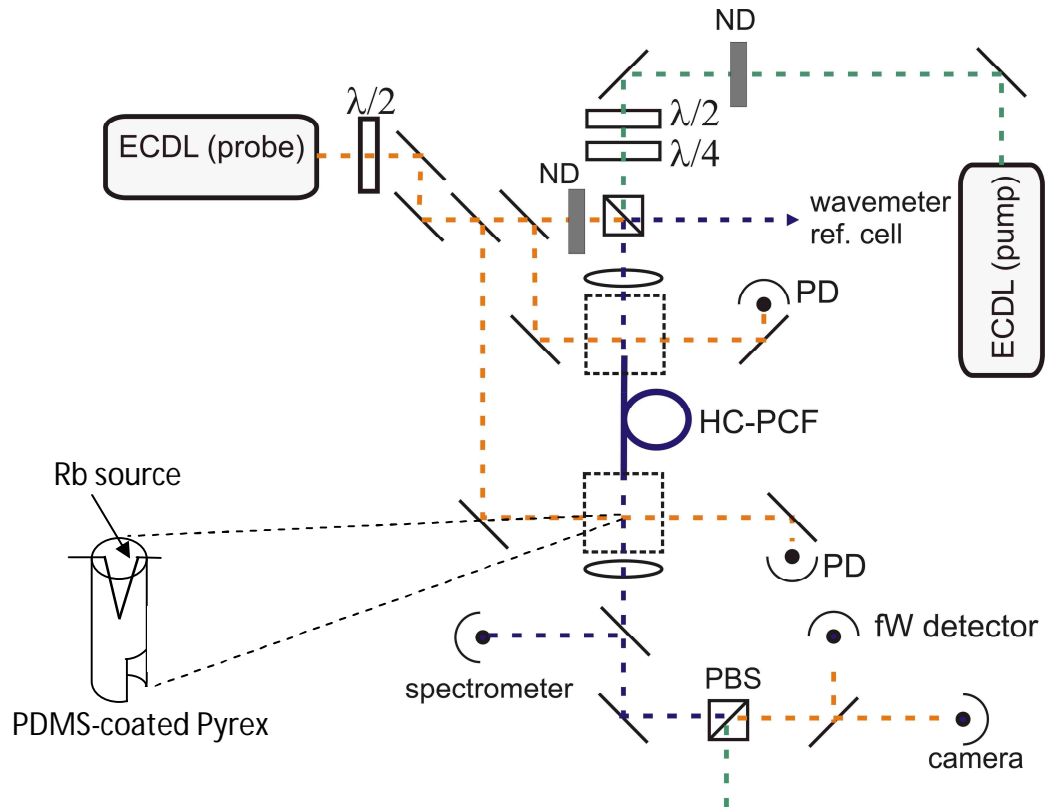
Figure 7-2: *Experimental set-up for rubidium loading into HC-PCF. ECDL, external cavity diode laser, PBS, polarising beam splitter; ND, neutral density filte; fW, femtowatt detector; PD, photodetector.*

100 °C (limited by the polymer coating). Due to the high temperature sensitivity of the vapour pressure [5] this temperature increase of 120 °C leads to a 3000-fold increase in the rubidium pressure in the source chamber. A 19-cell Kagome HC-PCF is chosen to be the rubidium vapour host as the larger diameter core greatly increases the conductance of the fibre (proportional to the square of the core radius) and therefore should increase the efficiency of the loading process. This choice of fibre is also motivated by the need to minimise the linewidth broadening induced by collisions between the rubidium atoms and the fibre core wall. For this experiment, the inner core walls of the fibre were not coated with polymer in order to keep the transmission properties of the fibre unmodified.

In section 7.2, LIAD from coated Pyrex was introduced as a means for generating a large on-demand rubidium vapour density [175]. The desorption rate is much higher from a glass substrate compared to the rate from a stainless steel substrate [180]. After the coating has ripened it is expected that the rubidium adsorption rate onto a coated surface will decrease; this behaviour has not been reported from a coated stainless steel surface. Therefore, in this experiment, PDMS-coated glass cylinders are inserted into the vacuum chambers where the rubidium vapour is loaded into the HC-PCF. These coated cylinders act to isolate the rubidium source and the open end of the HC-PCF from the stainless steel chamber walls with the dual purpose of providing a source of rubidium through

LIAD and also decreasing the loss of rubidium vapour through adsorption to the stainless steel chamber walls. The PDMS coating is applied to the glass from a few percent polymer solution diluted in ether. In order to ensure a complete layer of coating the PDMS concentration can be increased, at the expense of increased surface roughness [186].

The complete experimental set-up used for rubidium loading is shown in Figure 7-2. Two ECDLs are used; the first is a probe which continually scans across the D2 rubidium absorption lines (~780 nm). It is necessary to reduce the power of this laser beam to the order of a few nano-watts to interrogate the vapour density within the fibre due to the low saturation intensity of these absorptions lines (~1.6 mWcm^{-2} [5]). The second ECDL is operated at a fixed frequency and can provide powers up to 100 mW. This laser is used to investigate LIAD (at 776 nm) and to attempt EIT. These two laser beams are combined using a beam splitter. One output from the beam splitter is coupled into the fibre and the fibre mode profile is monitored at the fibre output using a camera. The second output of the beam splitter is used for wavelength calibration. Through use of polarisation optics the two input beams can be separated at the fibre output using a polarising beam splitter. The probe beam trace is recorded on a femto-watt detector.

This probe beam has a small interaction length with the vapour density in the chamber (both before and after coupling into the fibre). Therefore, it is necessary, for calibration purposes, to monitor the rubidium vapour in the stainless steel chamber from which the rubidium is being released. To this end, a 4% tap on the probe beam is directed through the windows in the vacuum chambers and simultaneously detected with the probe fibre trace. Subsequently, using the Beer-Lambert law (equation (1-2)) the interaction length of the probe beam with the rubidium vapour can be deduced and used to monitor the fibre loading rate. Other possible ways of demonstrating that the rubidium vapour, as detected by the probe beam coupled to the fibre, is definitely in the fibre core include observation of LIAD from the fibre, comparison of the FWHM of the absorption features and observation of quantum optic effects such as EIT at ultralow coupling powers.

7.4.   Preliminary Results

The rubidium vapour density in the vacuum chamber and the HC-PCF was monitored periodically using the probe laser while the rubidium vapour was being continuously released into the vacuum system. Typical probe traces for the fibre and chamber are shown in Figure 7-3. Four absorption lines are observed; the two strongest lines originate from rubidium-85 atoms and two weakest are from the less abundant rubidium-87 atoms. The hyperfine splitting of the excited state ($5^2P_{3/2}$) is not observed due to Doppler broadening.
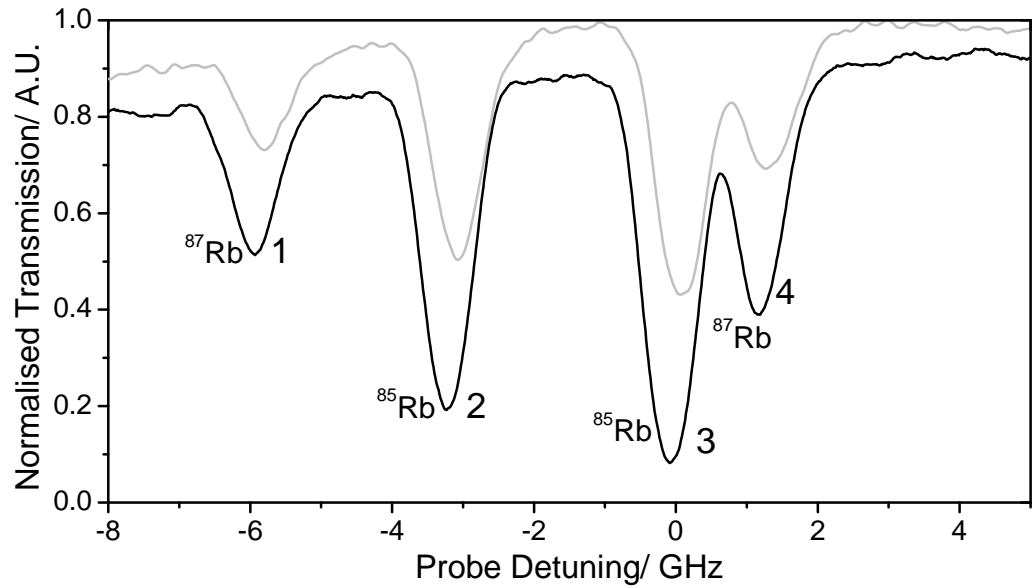
Figure 7-3: *Probe beam absorption through chamber (black line) and fibre (grey line). Four Rb D2 absorption lines are observed; hyperfine splitting is obscured by Doppler broadening.*

The rubidium vapour loads into the HC-PCF slowly over many days. The evolution of the loading distance (L_l) is calculated by comparing the absorption contrast on the chamber and fibre probe beams using the Beer-Lambert law. Due to the presence of the coated glass cylinder it is difficult to ascertain the definite interaction length of the chamber probe beam; a larger rubidium density may be present inside the cylinder
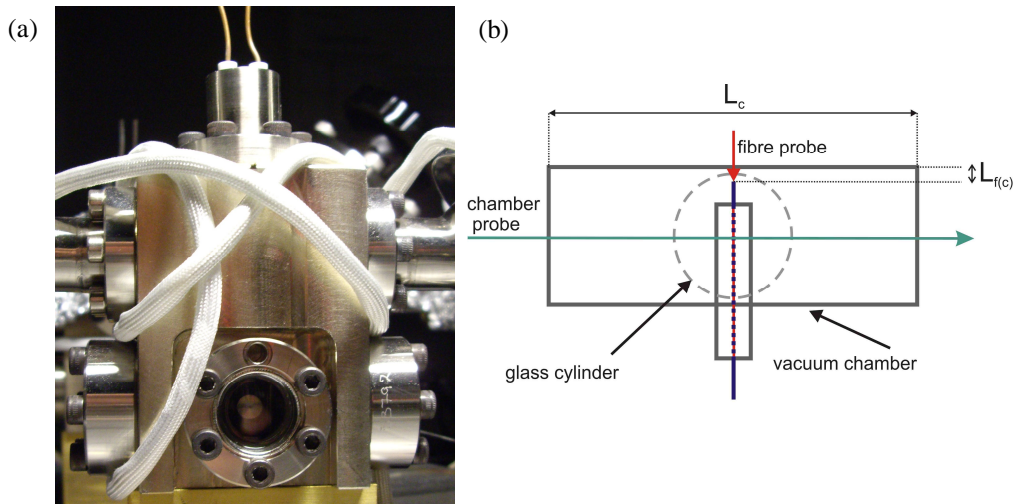
Figure 7-4: *(a) photo of stainless steel vacuum chamber which contains rubidium source. Fibre holder is clearly seen through front window. White cord is heating tape which is used to maintain the chamber temperature. During experiment, chamber is covered with foil to encourage even heat distribution, (b) schematic of vacuum chamber from top view showing interaction of probe beam with rubidium vapour in chamber and HC-PCF.*

Figure 7-5: *Ratio between interaction length in chamber (L_c) and interaction length of fibre probe beam ($L_{f(total)}$) (black) as a function of time and deduced distance that rubidium is loaded into HC-PCF (grey) assuming L_c=60 mm. After ~ 14 days, increase in loading distance ceases. Note that time axis starts on day 6 after rubidi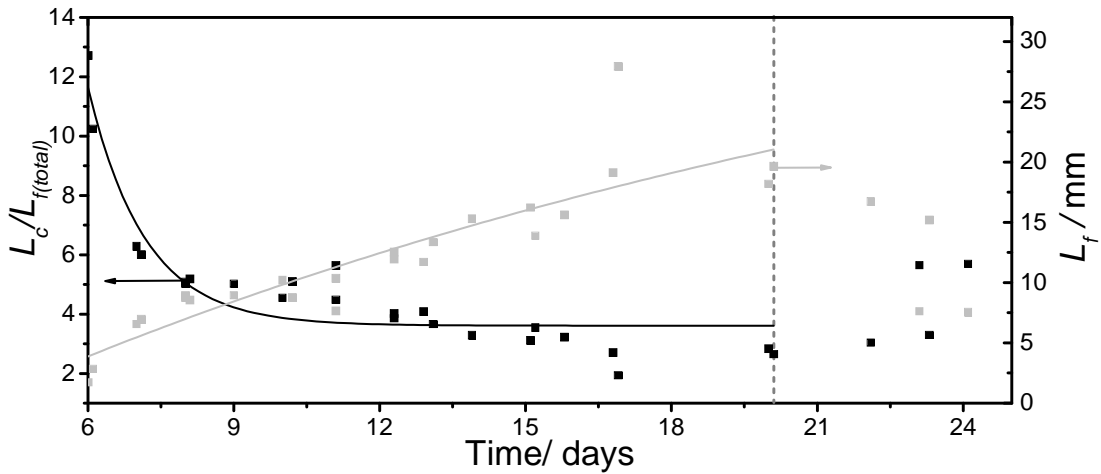um source turned on as data before this point was unreliable. For the duration of the experiment the rubidium density is kept approximately constant in the vacuum chamber by adjusting the current to the rubidium source.*

compared to the chamber as a whole. Due to the physical configuration of the stainless steel chamber (Figure 7-4(a)) it is not possible to take any measurements of the rubidium vapour distribution and therefore for the following estimations of the fibre loading length, the rubidium vapour distribution in the vacuum chamber is considered uniform.

Figure 7-4 (b) shows the alignment of the chamber and fibre probe beams schematically and highlights the important length scales, L_c and $L_{f(c)}$, which must be considered when calculating L_f. L_c is the interaction length of the chamber probe beam with the rubidium vapour in the vacuum chamber and $L_{f(c)}$ is the interaction length of the fibre probe beam with the rubidium vapour in the chamber before it is coupled into the fibre. The total fibre probe interaction length is then defined as $L_{f(total)} = L_{f(c)} + L_f$.

Assuming constant rubidium density over the entire vacuum chamber, the interaction length of the chamber probe beam is 60 mm. The fibre probe beam interaction length in the chamber, pre-coupling to the fibre, $L_{f(c)}$, is 3 ± 1 mm. Therefore if the fibre is not loaded, then the expected ratio between L_c and $L_{f(total)}$ is 20.

Chamber and fibre probe absorption traces such as those shown in Figure 7-3, were recorded every few hours and using these traces the ratio between L_c and $L_{f(total)}$ was calculated. For the first 6 days after the rubidium source was turned on, the data recorded was unreliable due to fluctuations in the vapour pressure in the chamber and outgassing from the rubidium source. Figure 7-5 shows that the ratio between L_c and $L_{f(total)}$ from day 6 onwards, decreases with time which indicates that L_f is increasing. L_f is
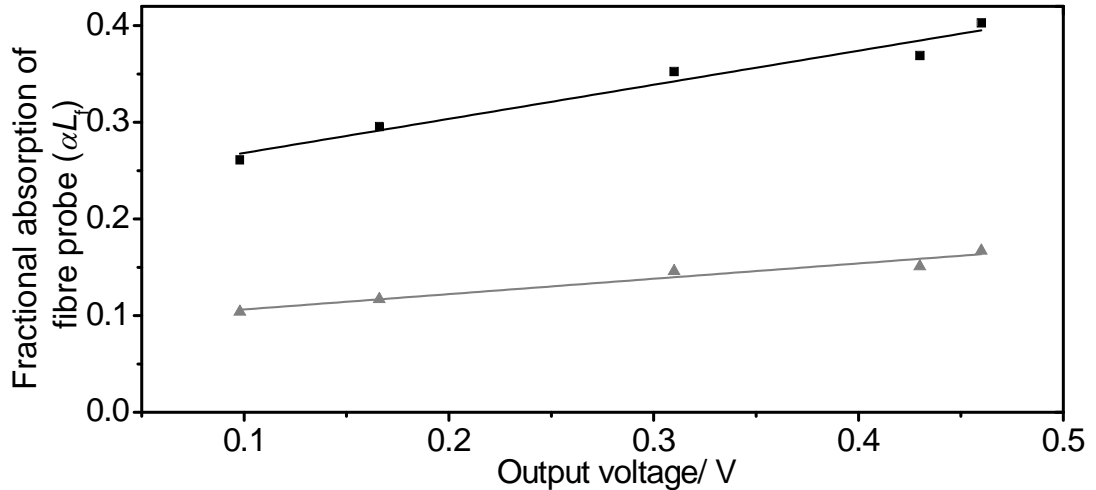
Figure 7-6: *When the fibre probe beam is misaligned (recorded by reduction in output voltage on photodetector), the amount of light guided in the core is reduced and the amount guided in the cladding nodes increases. This corresponds to a reduction in the fractional absorption of the fibre probe beam and therefore indicates that rubidium vapour is loaded into the fibre core. Data in black corresponds to absorption line 3 and data in grey corresponds to line 4 (lines as identified in* Figure 7-3*).*

then calculated by assuming that L_c is 60 mm and is also plotted in Figure 7-5 as a function of time. The maximum calculated loading distance of ~ 20 mm is recorded after 20 days.

After 20 days the loading distance stops increasing, flattens and then starts to decrease. A possible explanation of this is that over the extended time period, some 'ripening' of the stainless steel chamber occurs and therefore the rubidium density distribution in the system starts to change. In fact the rubidium density distribution may evolve continuously over the loading time. These uncertainties in L_f are a limit of this detection method and it is expected that they will be substantially reduced using the modified set-up described in section 7.7. Additionally, after day 24 the rubidium source was completely depleted so fluctuations in rubidium vapour pressure in the chamber may have introduced errors in the data recorded on the days just prior to this. Also, it is noteworthy that the trend observed in Figure 7-5 may also be affected by chemisorption and physisorption dynamics within the chamber due to the large surface to volume ratio. These adsorption effects are hard to quantify in the current scheme and therefore are not accounted for in the calculation of the fibre loading length.

An alternative technique for estimating L_f is available due to the nature of the Kagome fibre cladding; the apexes in the cladding are low loss waveguides and therefore the fibre probe beam can be aligned into these silica nodes and the fractional absorption compared with the absorption when the light is optimally aligned into the Kagome core, to provide evidence that the rubidium vapour is loaded into the core of the HC-PCF.

Figure 7-6 shows the fractional absorption ($\alpha L_{f(total)}$) of absorption lines 3 and 4 (as highlighted in Figure 7-3) as a function of fibre output power (recorded on the photodetector in volts). This figure clearly shows that the fractional absorption decreases when the fraction of light coupled into the HC-PCF core is reduced. In fact, by comparing the minimum and maximum fibre output values, the fractional absorption increases by ~60%; indicative of an increase in $L_{f(total)}$ by 60 %. When the fibre is misaligned some light is still guided in the core so it is difficult to use this method to find an absolute value of the loading distance. However, it can be used to put a minimum value on the distance if, as above, $L_{f(c)}$ is 3 mm, then L_f is ~2 mm. This data was recorded 15 days after the rubidium source was turned on.

7.5. Glass Cylinder Performance

The effect of the coated glass cylinder on the rubidium vapour loading was quantitatively assessed by two means. Firstly, the decay of the rubidium absorption signal in the vacuum system when the rubidium source was turned off was recorded daily. The signal decays recorded over a 12 day period are shown in Figure 7-7(a). This figure clearly shows that the coating ripens over this time period as the decay constant (Figure 7-7(b)) increases over time. This shows that the coated cylinder is prolonging the effective lifetime of the rubidium vapour in the chamber. This lifetime is limited by both the continuous pumping by the ion pump and chemisorption to the chamber walls; for the decay measurements the valve to the ion pump was closed so that the only effective pumping mechanism to consider was chemisorption. The fractional absorption of the chamber probe signal 1000 seconds after the rubidium source is turned off is shown in Figure 7-7(c) and also indicates that the coating ripens as the fractional absorption at this time increases each day.

Secondly, LIAD was demonstrated from the coated cylinder surface. Desorption using lasers at both 776 nm and 532 nm was observed. The LIAD at the shorter wavelength was much stronger as expected considering the wavelength dependence observed in [175, 176, 178]. Figure 7-8 shows that the fractional absorption was approximately doubled using a 100 mWcm^{-2} desorption beam at 532 nm. These results indicate that the coated cylinder insert is a suitable means for controlling the rubidium vapour pressure in the source chamber.
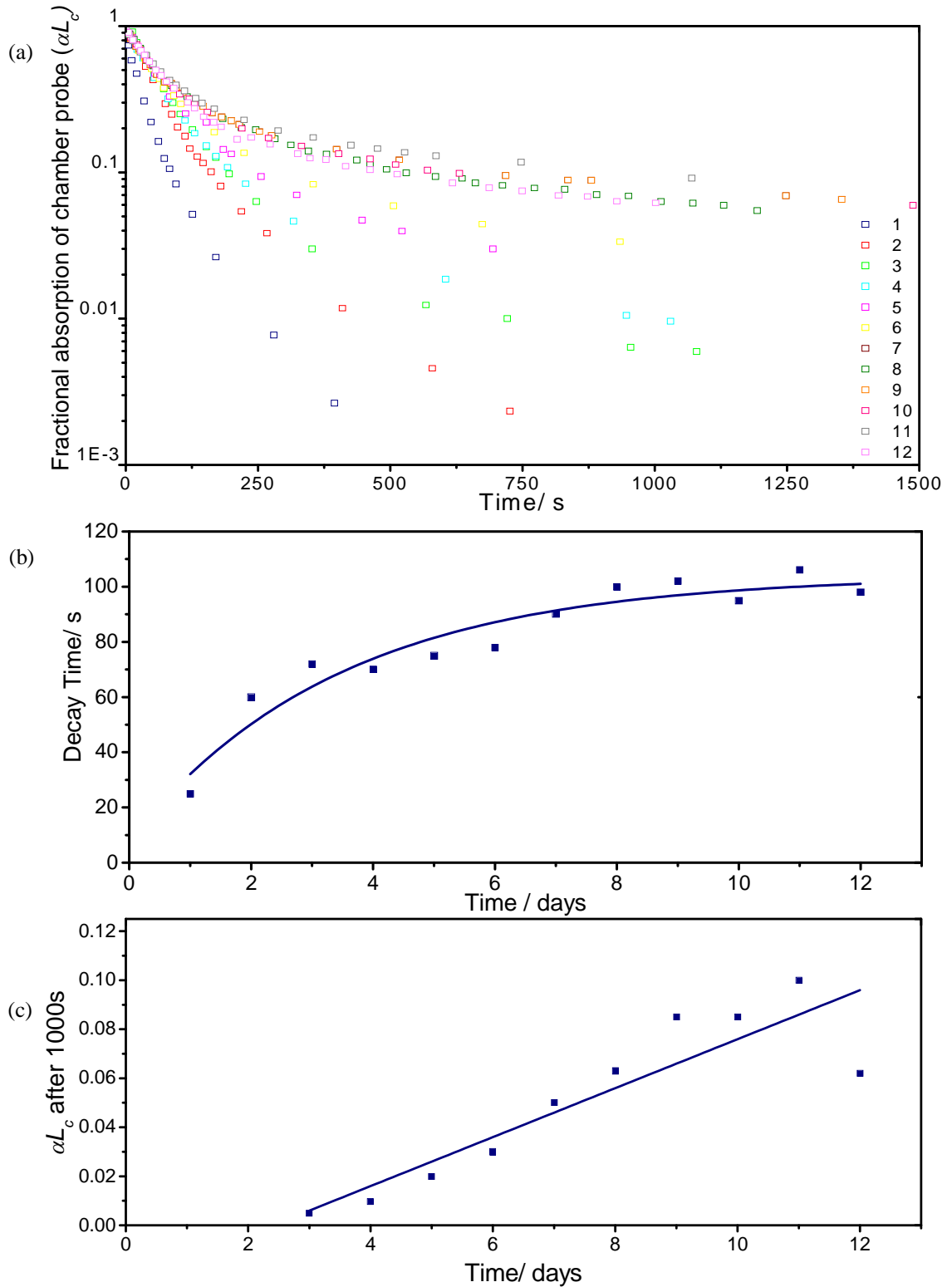
Figure 7-7: *(a) Decay of rubidium fractional absorption of rubidium lines as a function of time (after rubidium source is turned off) (b) Decay constants extracted from (a) (c) Fractional absorption of chamber, αL$_c$, 1000 s after rubidium source is turned off. Extracted from (a).*
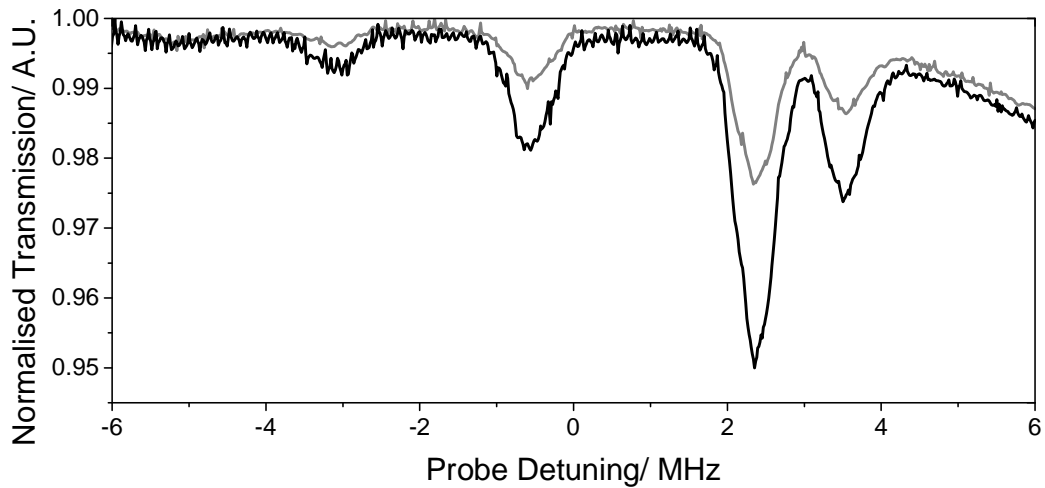
Figure 7-8: *Chamber probe trace in absence of LIAD beam (grey line) and in presence of 100 mWcm^{-2} desorbing beam at 532 nm (black line). Through LIAD fractional absorption of beam is doubled indicating a similar increase in rubidium vapour in the chamber.*

7.6.   Discussion

From the preliminary results presented here it is clear that the rubidium vapour loading distance into the HC-PCF using this experimental configuration is small. By assuming that the chamber interaction length L_c is 60 mm, the maximum loading distance L_f is calculated to be 20 mm. Moreover, this maximum distance occurred after the rubidium source had been running for 20 days. Therefore, only a short loading distance was achieved and over a relatively long time period. To fully exploit the long interaction length provided by HC-PCF a longer loading length is required.

Furthermore, using this interaction scheme, it is not trivial to determine the rubidium vapour loading distance as there is some uncertainty in the origin of the rubidium absorption on the fibre probe beam; this is due to the finite interaction length of the fibre probe beam with the rubidium vapour in the chamber, $L_{f(c)}$, before it is coupled into the fibre. In the following section, a modified set-up is outlined which removes all uncertainty in L_f and will hopefully enable faster and more evenly distributed loading along a section of HC-PCF.

7.7.   Future Work

The preliminary results presented here indicate that the coated glass cylinder inserted in the rubidium source chamber, increases the effective lifetime of the rubidium vapour. Therefore, a modified rubidium loading chamber formed predominantly from glass should act to increase the rubidium loading efficiency. Additionally, the LIAD observed
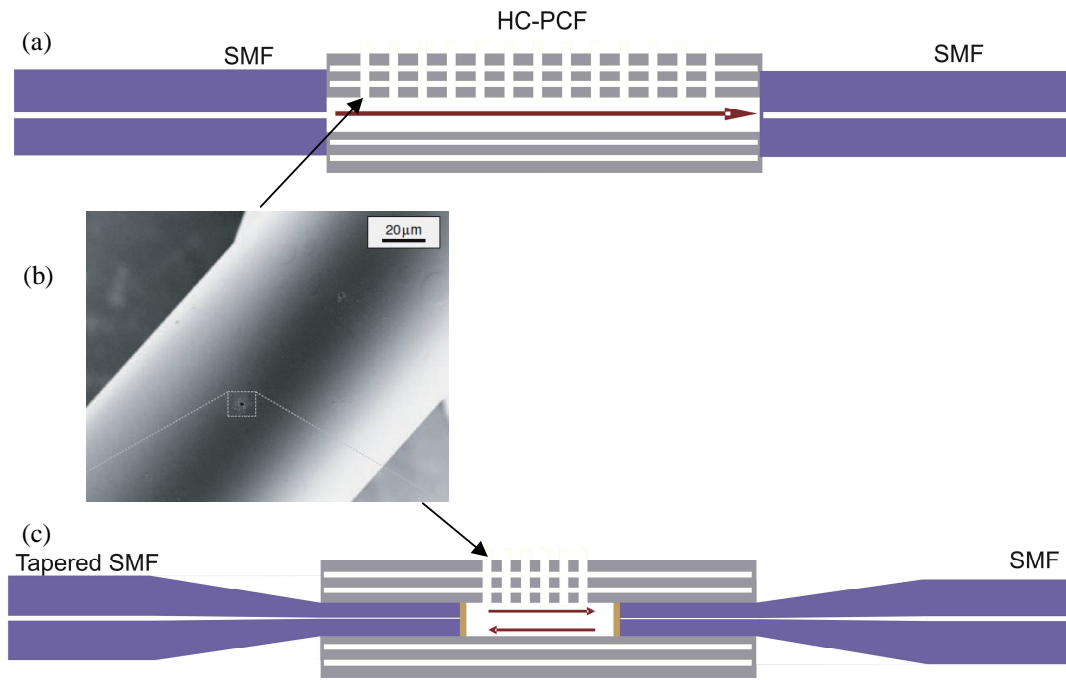
Figure 7-9: *Modified schemes for rubidium loading in HC-PCF. (a) HC-PCF spliced at both ends to SMF and (b) HC-PCF microcavity similar to that presented in chapter 6; micromirrors can be coated to increase reflectivity. In both cases, nanoscale holes drilled into the HC-PCF enable rubidium vapour loading into the core of the fibre as shown in (b) which is taken from [187].*

from the glass cylinder shows that such a glass loading system could act as a controllable source of rubidium vapour.

Two possible schemes for rubidium PMCs which would eliminate any confusion over the location of the rubidium vapour are presented in Figure 7-9. In Figure 7-9(a) the HC-PCF is spliced at both ends to SMF and the rubidium vapour is loaded into the core of the HC-PCF via channels (Figure 7-9(b)), machined through the HC-PCF cladding using a femtosecond laser. This technique was first reported by Hensley *et al.* [187] who reported losses as low as 0.35 dB per channel. By distributing these loading channels along the length of the HC-PCF a more even rubidium vapour density could be achieved in the hollow core and the fibre loading distance L_f increased. A similar scheme is presented in Figure 7-9(c), the key difference being that instead of splicing to SMF at each end, micromirrors are used to couple the light in and out of the HC-PCF. This scheme has the potential advantage that, by coating the micromirrors to produce a multi-pass PMC, the length of the HC-PCF to be loaded with rubidium vapour can be reduced while still maintaining a long overall interaction length.

Chapter 8

Summary and Outlook

This thesis reported developments in the fabrication and applications of photonic microcells. In this chapter the key developments are summarised and future work in this field based on the results presented here is outlined.

8.1.   Summary

In chapter 2, two classes of HC-PCF were defined; PBG and large pitch HC-PCF. The key properties of the fibres were introduced and the guidance mechanisms described. State-of-the-art examples of each class were fabricated, namely double PBG and large-pitch Kagome HC-PCF.

Dual PBG guidance was achieved by optimising the fibre cladding structure, specifically the apex size and strut thickness. Dual PBG guidance increases the low loss guidance bandwidth of the fibre and importantly enables simultaneous guidance of key laser pairs, for example an EDFA at 1550 nm and Nd:Yag and Yb lasers at 1 µm.

Large-pitch Kagome HC-PCFs were fabricated with record low loss (0.15 dB/m at 990 nm and 0.3 dB/m at 800 nm). The reduced loss is attributed to an improved anti-resonant core surround. The large core diameters of these fibres, combined with their lack of surface mode guidance and their guidance mechanism makes them excellent candidates for gas-laser interactions in HC-PCF. The results of these excellent properties, specifically reduced decoherence, spectrally flat transmission and broadband guidance were highlighted in three experiments which were described in chapter 4. These experiments all demonstrate advances in this field and emphasize the potential of gas-laser interactions in Kagome fibres.

These state-of-the-art fibres are used to fabricate acetylene-filled PMCs. In chapter 3, a record length 20 metre acetylene-filled PMC formed from PBG HC-PCF is used in the first demonstration of an all-fibre slow and superluminal light pulse system based on EIT. This system is easily integrated with existing optical components and the pulse delay and advance can be tuned using the coupling laser power. Pulse delays and advances of up to 5 ns and 1 ns were recorded respectively. A simple analytical model was used to

extract optimised experimental parameters; using large core HC-PCF, ultranarrow linewidth lasers, the strongest absorption lines from the acetylene $v_1 + v_3$ overtone band pulse and an acetylene pressure of 0.7 mbar delays of up to 30 ns per metre were predicted. However, it was noted that high acetylene pressures will limit the interaction length possible due to probe beam absorption, to an extent dependent on the detection scheme. Moreover, effects such as resonance group velocity dispersion and spectral reshaping which distort the pulse shape must be considered when defining the PMC length.

In chapters 5 and 6, two advances in PMC fabrication techniques were reported. In chapter 5, a technique for integration of large core Kagome HC-PCF into PMC form was described. Hermetic and low loss splices between the HC-PCF and SMF were achieved using fibre tapering; the outer diameter of the Kagome fibre can be reduced to match that of the SMF or alternatively the outer diameter of the SMF can be increased through uptapering. Both these techniques reduce the coupling loss between the two fibres by increasing the mode field overlap. A complete, acetylene-filled large core PMC was used to demonstrate EIT and SAS.

In chapter 6, a novel micromirror technique was introduced which enables the fabrication of multi-pass PMCs. The micromirrors are formed from tapered SMF, with a waist diameter which is designed to match the inner core diameter of a HC-PCF. The SMF taper is then cleaved in the waist and each half of the taper forms a micromirror which can then be inserted into the core of the HC-PCF. Two uncoated micromirrors were inserted into each end of a 1-cell Kagome HC-PCF to form a low finesse microcavity with record fringe extinction and a silver-coated micromirror was used in a compact SAS scheme.

In chapter 7, rubidium loading into HC-PCF was explored. Preliminary results indicate that the maximum loading distance into the fibre core was ~20 mm. LIAD was demonstrated from a PDMS-coated glass cylinder inserted into the rubidium release chamber. Additionally, the ripening of the coating of this cylinder was observed through the increase in the lifetime of the rubidium vapour in the chamber over a period of several days. The accuracy in determining the rubidium loading distance was limited by the experimental set-up and therefore a modified loading scheme was presented.

8.2. Future Work

8.2.1. Fibre Fabrication

The reduced attenuation of the Kagome HC-PCF presented in chapter 2 means that this fibre is starting to compete with the loss of PBG HC-PCF at wavelengths below ~900 nm. Initial attempts to reduce the loss of Kagome HC-PCF in the visible region while maintaining broadband guidance have so far been unsuccessful; this is attributed to the

strut thickness variation across the cladding structure. Future work towards this goal is planned and will include modifying the original stack design as well as careful control of the relative pressures of the core and cladding regions.

Additionally, in chapter 4, the first Kagome HC-PCF which has demonstrated guidance in the mid-IR (with a loss 20 dB/m at 3 µm) was used in the first demonstration of an optically pumped gas laser in a gas-filled HC-PCF. This fibre was initially designed for low loss guidance at 1520 nm and therefore it is thought that, through optimisation of the fibre structure, the attenuation in the mid-IR should be reduced and therefore the laser efficiency increased.

8.2.2.   Multi-pass PMCs

In order to improve the results achieved using the micromirrors, two key advances are required. Firstly, the coating technique needs to be improved; in the literature there are many examples of application of highly reflective coatings to fibre tips and therefore this should be achievable. Secondly, a means for holding the micromirror in place without inducing optical loss will be necessary if sealed gas-filled multi-pass PMCs are to be fabricated. A possible solution is to use low index and low outgassing adhesive to fuse the micromirror to the HC-PCF.

8.2.3.   Rubidium-filled PMC

The ultimate aim of this work is to fabricate a rubidium-filled PMC suitable for frequency standard applications which would rival 'on-chip' designs. This PMC would have all the advantages of the acetylene-filled PMCs used throughout this thesis combined with additional benefits such as the strong dipole moment provided by an atomic vapour and the potential to reduce the linewidth of resonant features recorded in the vapour by coating the inner core wall of the fibre.

The extremely reactive nature of the rubidium vapour is the major challenge in achieving this goal and the preliminary results which highlight the success of the glass insert indicate that a complete glass system would improve the loading efficiency. Furthermore, it may prove extremely difficult to splice a rubidium-filled fibre due to this reactivity and therefore a modified PMC fabrication procedure may be required.

Appendix

A. Introduction to Molecular Spectroscopy

Molecular spectroscopy is more complex than atomic spectroscopy; as well as electronic transitions, vibrational and rotational transitions are allowed (Figure A- 1) due to the additional degrees of freedom in a molecular species. This means that the absorption spectra of molecules contain bands of regularly spaced absorption features, spread throughout the electromagnetic spectrum, which can be used as frequency standards. Molecular candidates for frequency metrology include acetylene (at 1.5 µm [14]), water (at 0.8 µm [188]), ammonia (at 1.4 µm [189]), and methane (at 3.3 and 7.7 µm [190, 191]). Since the introduction of semiconductor diode lasers, which have low noise and are easily tuneable, studies into the complex rovibrational spectra of these molecules has advanced rapidly. In the work presented in this thesis, acetylene (C_2H_2) is used extensively and therefore the relevant absorption characteristics of acetylene are described in this appendix.
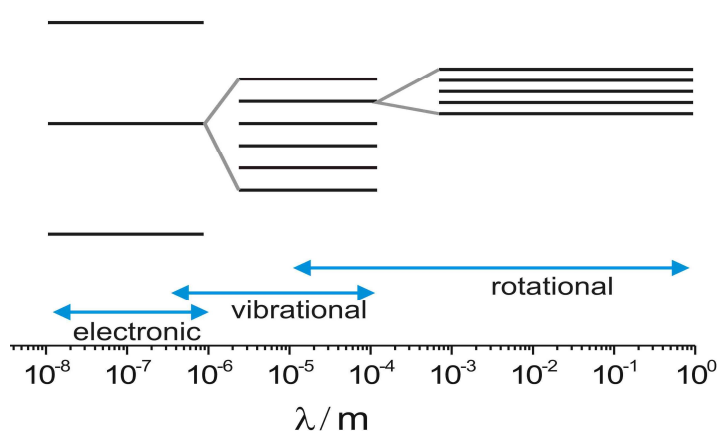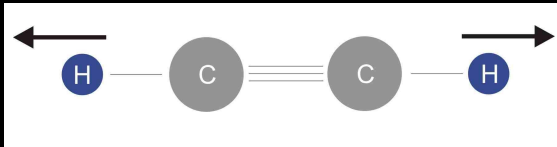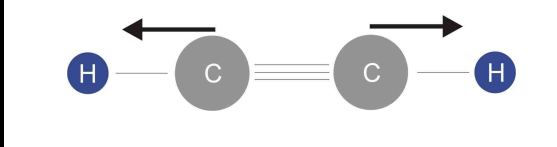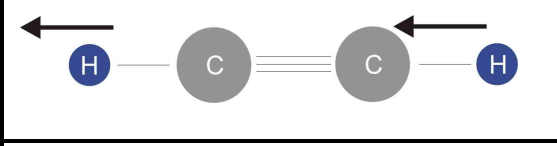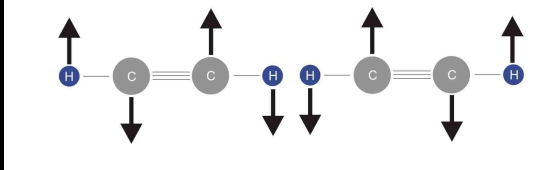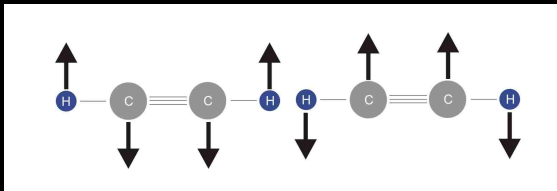
Figure A- 1: *The absorption spectrum of a molecular species, such as acetylene, is complex to due the additional vibrational and rotational transitions allowed in molecules. The relevant energies required for each type of transition are shown (values from [192]).*

Acetylene is a linear, symmetric molecule and its $v_1 + v_3$ combination band (see definitions below) provides an array of absorption lines between 1510 and 1540 nm. It has no permanent dipole and is therefore unaffected by external fields and it is gaseous at room temperature. These qualities combine to make it an excellent candidate for a frequency standard; in 2003 the Consultative Committee for Length added lasers stabilised to the P(16) line from the $v_1 + v_3$ combination band of $^{13}C_2H_2$ to the register of atomic and molecular transitions used for the SI definition of the metre [193].

Table A- 1: *The five normal modes of acetylene. Wavenumbers from [192].*

Normal Mode	Vibration	Wavenumber	Schematic
v_1	*symmetric C-H stretch*	3374 cm^{-1}	
v_2	*symmetric C≡C stretch*	1974 cm^{-1}	
v_3	*asymmetric C-H stretch*	3287 cm^{-1}	
v_4	*symmetric bend*	612 cm^{-1}	
v_5	*asymmetric bend*	729 cm^{-1}	

The relative energies of types of transitions applicable to the acetylene molecule are shown in Figure A- 1. A vibrational transition refers to a variation in the inter-nuclear separation and a change in the orientation of the molecule in laboratory-fixed space is referred to as a rotational transition [103]. Separation between vibrational levels is much larger than that between rotational levels and therefore vibrational transitions occur at a higher frequency. Figure A- 1 also highlights how many rotational transitions can be centred on a single vibrational transition.

Linear molecules have (3N -5) normal modes of vibration where N is the number of atoms in the molecule. The 5 distinct normal modes of acetylene are shown in Table A-1(vibrations v_4 and v_5 are both doubly degenerate) [192]. Normal modes v_1, v_2 and v_3 describe stretching vibrations and modes v_4 and v_5 describe bending vibrational modes.

The vibrational potential energy curve for the normal modes which describe a stretching vibration (v_1, v_2 and v_3) can be approximated using the Morse potential function which describes the vibrational potential energy curve for a diatomic molecule [194]. The Morse potential function can be expressed as [192],
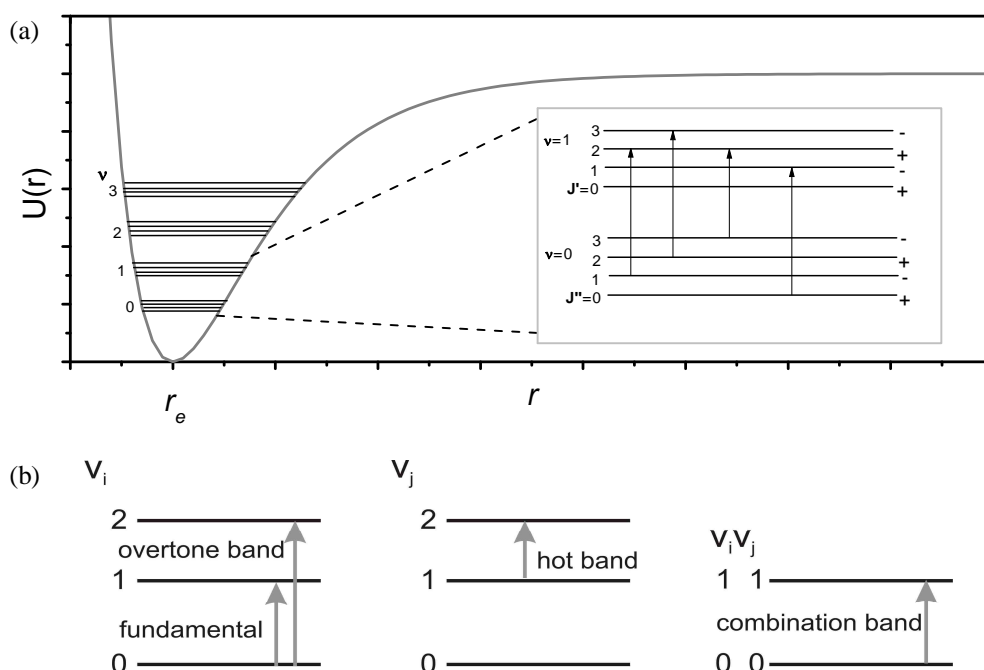
Figure A- 2: *(a) Potential energy curve for a stretch vibrational mode in a linear molecule. Potential energy curve is anharmonic but can be approximated as a harmonic oscillator for small deviations from the equilibrium bond length, r_e. (b) (adapted from [192]) Possible vibrational transitions; fundamental absorption band corresponds to transition from v=0 to v=1; weaker overtone bands occur at multiples of the fundamental absorption frequency; hot bands arise from transitions from an excited state to higher levels and combination bands, such as the $v_1 + v_3$ band of acetylene arise at the sum of two or more fundamental transition frequencies.*

$$U(r) = D_e \left(1 - e^{-Aq}\right)^2 , \qquad\qquad (A-1)$$

where D_e is the stretching bond's dissociation energy (the energy at which the bond breaks), q is the displacement of the bond length, r, from its equilibrium length, r_e, and A is a constant characteristic of a particular electronic state of the molecule. The Morse potential is plotted in Figure A- 2(a); as r is reduced from the equilibrium bond length the potential energy sharply increases and as r increases beyond the equilibrium length the potential energy initial rises before reaching a plateau at an approximately constant value which corresponds to the bond dissociation energy [103]. For small deviations from the equilibrium length, the potential curve can be approximated by a harmonic oscillator, which simplifies the task of defining the allowed vibrational energy levels.

Considering a simple harmonic oscillator, the energies of the vibrational levels, E_{vib}, in a molecule such as acetylene are given by,

$$E_{vib} = \left(\upsilon + \frac{1}{2}\right)h\nu , \qquad\qquad (A-2)$$

where υ is the vibrational quantum number, *h* is Planck's constant and *v* is the transition frequency [103]. From this model, the selection rule,

$$\Delta\upsilon = \pm 1, \tag{A-3}$$

is derived. The fundamental band of a normal mode (υ=0 to υ=1) is the strongest band because, at room temperature and for transitions in the IR spectral region, the υ=0 has the highest population. When the anharmonic nature of the vibrational potential is fully accounted for, it is found that the selection rule shown in equation (A-3) is modified to read,

$$\Delta\upsilon = \pm 1, \pm 2, \pm 3,... \tag{A-4}$$

The transitions which correspond to higher changes in the vibrational quantum number are known as overtone bands if they involve just one vibrational mode and combination bands if they involve more than one vibrational mode. These possible transitions are shown schematically in Figure A- 2(b). This figure also highlights 'hot band' transitions; these describe transitions from an excited vibrational state to a higher state. Due to the low population of the excited vibrational levels in the IR spectral region at room temperature, the relative intensity of these transitions is very small compared to the fundamental and overtone bands. The relative intensity can be increased by increasing the ambient temperature, hence the name hot band. Most fundamental vibrational frequencies of molecules are in the mid-IR (~3 - 8 μm) and therefore absorption lines observed in the near-IR belong to combination bands.

As previously mentioned, many rotational levels are centred on each vibrational level; this is highlighted in the inset to Figure A- 2(a). The quantised rotational energy levels, E_{rot}(Hz), of acetylene, derived using the rigid rotor model [103], are expressed as

$$E_{rot} = BhJ(J+1) \qquad \text{where } J = 0,1,2,... \tag{A-5}$$

J is the rotational angular quantum number and *B* is the rotational constant (Hz), given by:

$$B = \frac{h}{4\pi I}, \tag{A-6}$$

where *I* is the moment of inertia of the rigid molecule. The rotational constant defines the spacing between adjacent rotational levels.

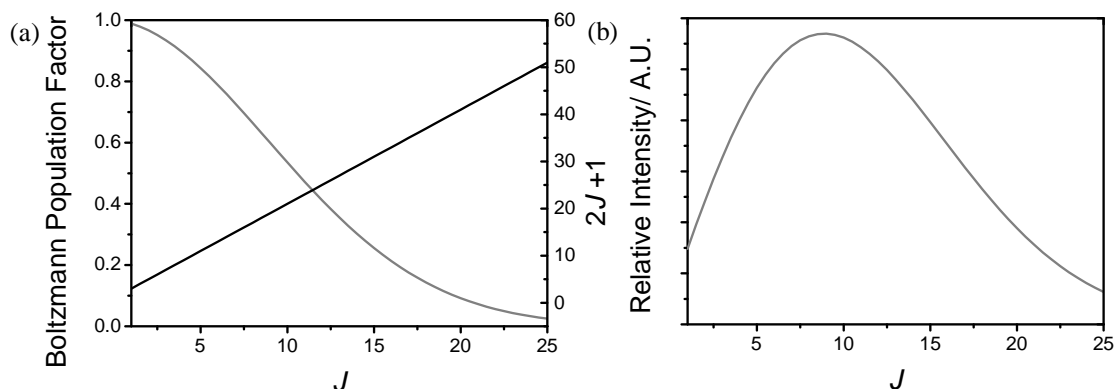The selection rule imposed on the angular quantum number *J* is,

Figure A- 3: *(a) Individual contributions to the energy level populations as a function of angular quantum number J; Boltzmann distribution (grey line) and level degeneracy in the absence of a magnetic field (black line). (b) Combined population factors control the relative intensity across the absorption band branch.*

$$\Delta J = 0, \pm 1 . \qquad\qquad\qquad (A\text{-}7)$$

This rule combines with the selection rule on the vibrational quantum number (equation (A-3)) and state symmetry considerations to define the rovibrational absorption spectrum acetylene. The three different possible changes in the angular momentum quantum number define different branches of the spectrum. For the $v_1 + v_3$ combination band of acetylene, the relevant branches are the P and R branches corresponding to changes in *J* of -1 and +1 respectively. Examples of allowed transitions are highlighted in Figure A-2(a).

The shape and intensity of an absorption band branch, as a function of *J*, is defined by the level populations and the transition dipole moment. This dipole moment is largely independent of *J* across a band, rendering the population difference as the key feature [103]. The population of an individual rotational level can be defined using the Boltzmann distribution ($\propto e^{-(hcBJ(J+1)/kT)}$) and the level degeneracy ($2J + 1$). These two contributions are plotted in Figure A- 3(a) as a function of *J* and the relative intensity of the absorption band branch found through combining these two factors is plotted in Figure A- 3(b). This calculated shape is in good agreement with the observed spectrum of the $v_1 + v_3$ combination band of acetylene which is shown in Figure A- 4. The spectrum shown in this figure was recorded using ~ 1 metre of acetylene-filled PBG-HC-PCF at a pressure of ~ 1 mbar [101]. Low acetylene pressure is required to minimise pressure broadening and therefore enable observation of the distinct rotational transitions. One distinct difference between the calculated band shape and the experimentally observed absorption band is the difference in the relative intensities of levels with odd and even values of *J*. This is explained by the statistical weight of the levels induced by the nuclear spin of the hydrogen atoms in the acetylene molecule and
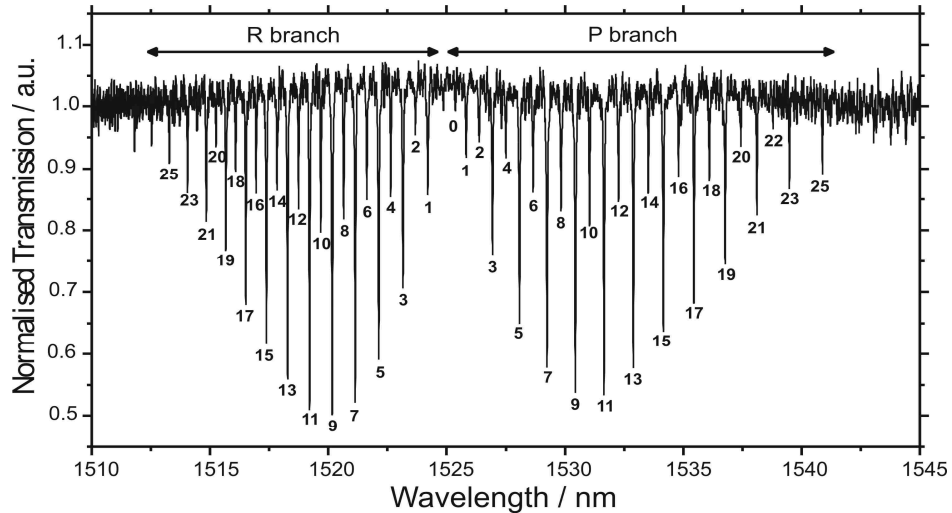
Figure A- 4: $v_1 + v_3$ *combination band of acetylene recorded using ~ 1 metre of acetylene-filled PBG HC-PCF. From ref. [101].*

results in the odd *J* levels having a relative intensity three times higher than the even *J* levels [103].

The transition dipole strengths for this combination band are approximately 0.01 Debye, approximately three orders of magnitude smaller than that of an atomic vapour. This low strength requires high intensity laser sources and long interaction lengths in order for coherent optics effects, such as electromagnetically-induced transparency, to be observed in acetylene. The use of HC-PCF in this field has enabled this [43, 44] due to the tight confinement of the light and gas in the small fibre core over several metres. This provides both the required high intensity and an extremely long interaction length.

The complex nature of the rovibrational spectrum of molecules, such as acetylene, means that there are multitudes of dipole allowed transitions from any given excited state. The rate of collision induced state-to-state energy transfer is studied in [107]. Through this process population can be transferred within a single vibrational level, between rotational levels and between vibrational levels. The pressure dependence of this process is important in the context of gas-filled HC-PCF where collisions between the confined molecules and the inner core walls dominate collisional broadening effects due to the tight confinement in HC-PCF and the large mean free path of molecules at low pressures. This spectral complexity is also highlighted by the success of the acetylene laser presented in chapter 4 where lasing at 3 µm results from pumping at 1.5 µm.

References

1.   A. E. Siegman, *Lasers* (University Science Books, California, 1986).

2.   F. Riehle, *Frequency Standards: Basics and Applications* (Wiley-vch Verlag GmbH & Co. KGaA, Weinhiem, 2004).

3.   J. Steinfeld, *Molecules and Radiation: An Introduction to Modern Spectroscopy* (MIT Press, Cambridge, England, 1978).

4.   W. C. Swann, and S. L. Gilbert, "Pressure-induced shift and broadening of 1510-1540-nm acetylene wavelength calibration lines," Journal of the Optical Society of America B-Optical Physics **17**, 1263-1270 (2000).

5.   D. A. Steck, "Rubidium 85 D line Data," (2010), http://www.steck.us/alkalidata Accessed 16th September 2010, 2010.

6.   J. P. Marangos, "Topical Review: Electromagnetically Induced Transparency," Journal of Modern Optics **45**, 471- 503 (1998).

7.   D. Suter, *The Physics of Laser-Atom Interactions* (Cambridge University Press, USA, 1997).

8.   U. Fano, "Effects of Configuration Interaction on Intensities and Phase-shifts," Physical Review **124** (1961).

9.   G. Alzetta, A. Gozzini, L. Moi, and G. Orriols, "An experimental method for the observation of R.F. transitions and laser beam resonances in orientated Na vapour," Nuovo Cim. B **36**, 5- 20 (1976).

10.   M. Fleischhauer, A. Imamoglu, and J. P. Marangos, "Electromagnetically Induced Transparency: Optics in Coherent Media," Reviews of Modern Physics **77**, 633- 673 (2005).

11.   K. J. Boller, A. Imamoglu, and S. E. Harris, "Observation of Electromagnetically Induced Transparency," Physical Review Letters **66**, 2593-2596 (1991).

12.   S. E. Harris, "Lasers without Inversion - Interference of Lifetime-Broadened Resonances," Physical Review Letters **62**, 1033-1036 (1989).

13.   O. A. Kocharovskaya, and Y. I. Khanin, "Coherent Amplification of an Ultrashort Pulse in a Three-Level Medium without a Population Inversion," Journal of Experimental and Theoretical Physics **48**, 630- 634 (1988).

14.   M. Delabachelerie, K. Nakagawa, and M. Ohtsu, "Ultranarrow (C2h2)-C-13 Saturated-Absorption Lines at 1.5 Mu-M," Optics Letters **19**, 840-842 (1994).

15.   W. R. Bennett, "Hole Burning Effects in a He-Ne Optical Maser," Physical Review **126**, 580-593 (1962).

16.   W. E. Lamb, and R. C. Retherford, "Fine Structure of the Hydrogen Atom .1.," Physical Review **79**, 549-572 (1950).

17.   S. E. Harris, J. E. Field, and A. Kasapi, "Dispersive Properties of Electromagnetically Induced Transparency," Physical Review A **46**, R29-R32 (1992).

18.   L. V. Hau, S. E. Harris, Z. Dutton, and C. H. Behroozi, "Light speed reduction to 17 metres per second in an ultracold atomic gas," Nature **397**, 594-598 (1999).

19.   R. Zhang, S. R. Garner, and L. V. Hau, "Creation of Long-Term Coherent Optical Memory via Controlled Nonlinear Interactions in Bose-Einstein Condensates," Physical Review Letters **103**, 233602 (2009).

20.   M. O. Scully, and M. Fleischhauer, "High-Sensitivity Magnetometer Based on Index-Enhanced Media," Physical Review Letters **69**, 1360-1363 (1992).

21.   T. F. Krauss, "Why do we need slow light?," Nat Photon **2**, 448-450 (2008).

22.   M. S. Shahriar, G. S. Pati, R. Tripathi, V. Gopal, M. Messall, and K. Salit, "Ultrahigh enhancement in absolute and relative rotation sensing using fast and slow light," Physical Review A **75**, 053807 (2007).

23.   J. L. Hall, "Nobel Lecture: Defining and measuring optical frequencies," Reviews of Modern Physics **78**, 1279-1295 (2006).

24.   D. Kleppner, "Physics - A milestone in time keeping," Science **319**, 1768-1769 (2008).

25.   T. W. Hansch, "Nobel Lecture: Passion for precision," Reviews of Modern Physics **78**, 1297-1309 (2006).

26.   N. F. Ramsey, "A Molecular Beam Resonance Method with Separated Oscillating Fields," Physical Review **78**, 695 (1950).

27.   S. Knappe, P. D. D. Schwindt, V. Gerginov, V. Shah, H. G. Robinson, L. Hollberg, and J. Kitching, "Microfabricated atomic clocks and magnetometers," Laser Spectroscopy, 337-345 (2005).

28.   S. Knappe, P. D. D. Schwindt, V. Gerginov, V. Shah, L. Liew, J. Moreland, H. G. Robinson, L. Hollberg, and J. Kitching, "Microfabricated atomic clocks and magnetometers," Journal of Optics a-Pure and Applied Optics **8**, S318-S322 (2006).

29.   S. Knappe, "Miniature atomic clock uses MEMS fabrication techniques," Laser Focus World **40**, 11-11 (2004).

30.   S. Knappe, R. Wynands, J. Kitching, H. G. Robinson, and L. Hollberg, "Characterization of coherent population-trapping resonances as atomic frequency references," Journal of the Optical Society of America B-Optical Physics **18**, 1545-1553 (2001).

31.   G. C. Bjorklund, M. D. Levenson, W. Lenth, and C. Ortiz, "Frequency-Modulation (Fm) Spectroscopy - Theory of Lineshapes and Signal-to-Noise Analysis," Applied Physics B-Photophysics and Laser Chemistry **32**, 145-152 (1983).

32.   M. Ohtsu, *Frequency Stabilization of Semiconductor Laser Diodes* (John Wiley & Sons, United States of America, 1996).

33.   T. Sato, M. Niikuni, S. Sato, and M. Shimba, "Frequency Stabilization of a Semiconductor-Laser Using Rb-D1 and D-2 Absorption-Lines," Electronics Letters **24**, 429-431 (1988).

34.   H. G. Robinson, and C. E. Johnson, "Narrow Rb-87 Hyperfine-Structure Resonances in an Evacuated Wall-Coated Cell," Applied Physics Letters **40**, 771-773 (1982).

35.   F. Benabid, J. C. Knight, G. Antonopoulos, and P. S. J. Russell, "Stimulated Raman scattering in hydrogen-filled hollow-core photonic crystal fiber," Science **298**, 399-402 (2002).

36.   R. E. Hachtouki, and J. Vander Auwera, "Absolute Line Intensities in Acetylene: The 1.5 um Region," J. Mol. Spect. **216**, 355-362 (2002).

37.   P. S. Light, F. Couny, and F. Benabid, "Low optical insertion-loss and vacuum-pressure all-fiber acetylene cell based on hollow-core photonic crystal fiber," Optics Letters **31**, 2538-2540 (2006).

38.   F. Benabid, F. Couny, J. C. Knight, T. A. Birks, and P. S. Russell, "Compact, stable and efficient all-fibre gas cells using hollow-core photonic crystal fibres," Nature **434**, 488-491 (2005).

39.   F. Couny, P. S. Light, F. Benabid, and P. S. Russell, "Electromagnetically induced transparency and saturable absorption in all-fiber devices based on (C_2H_2)-^{12}C filled hollow-core photonic crystal fiber," Optics Communications **263**, 28-31 (2006).

40.   J. E. M. Haverkort, H. G. C. Werij, and J. P. Woerdman, "Numerical Study of Light-Induced Drift of Na in Noble-Gases," Physical Review A **38**, 4054-4063 (1988).

41.   E. Cussler, *Diffusion: Mass Transfer in Fluid Systems* (Cambridge University Press, Cambridge, 1984).

42.   J. Henningsen, and J. Hald, "Dynamics of gas flow in hollow core photonic bandgap fibers," Applied Optics **47**, 2790-2797 (2008).

43.   S. Ghosh, J. E. Sharping, D. G. Ouzounov, and A. L. Gaeta, "Resonant optical interactions with molecules confined in photonic band-gap fibers," Physical Review Letters **94**, 093902 (2005).

44.   F. Benabid, P. S. Light, F. Couny, and P. S. Russell, "Electromagnetically-induced transparency grid in acetylene-filled hollow-core PCF," Optics Express **13**, 5694-5703 (2005).

45.   F. Couny, F. Benabid, P. J. Roberts, P. S. Light, and M. G. Raymer, "Generation and photonic guidance of multi-octave optical-frequency combs," Science **318**, 1118-1121 (2007).

46.   Y. Y. Wang, F. Couny, P. S. Light, and F. Benabid, "Coherence Properties of Optical Frequency Comb Generated in Large Pitch HC-PCF Filled with H-2," 2009 Conference on Lasers and Electro-Optics and Quantum Electronics and Laser Science Conference (Cleo/Qels 2009), Vols 1-5, 1271-1272 (2009).

47.   P. S. Light, F. Benabid, F. Couny, M. Maric, and A. N. Luiten, "Electromagnetically induced transparency in Rb-filled coated hollow-core photonic crystal fiber," Optics Letters **32**, 1323-1325 (2007).

48.   S. Ghosh, A. R. Bhagwat, C. K. Renshaw, S. Goh, A. L. Gaeta, and B. J. Kirby, "Low-Light-Level Optical Interactions with Rubidium Vapor in a Photonic Band-Gap Fiber," Physical Review Letters **97**, 023603 (2006).

49.   A. R. Bhagwat, A. D. Slepkov, V. Venkataraman, P. Londero, and A. L. Gaeta, "On-demand all-optical generation of controlled Rb-vapor densities in photonic-band-gap fibers," Physical Review A **79**, 063809 (2009).

50.   P. S. Light, F. Couny, Y. Y. Wang, N. V. Wheeler, P. J. Roberts, and F. Benabid, "Double photonic bandgap hollow-core photonic crystal fiber," Optics Express **17**, 16238-16243 (2009).

51.   K. Nagayama, M. Kakui, M. Matsui, T. Saitoh, and Y. Chigusa, "Ultra-low-loss (0.1484 dB/km) pure silica core fibre and extension of transmission distance," Electronics Letters **38**, 1168-1169 (2002).

52.   O. Humbach, H. Fabian, U. Grzesik, U. Haken, and W. Heitmann, "Analysis of OH absorption bands in synthetic silica," Journal of Non-Crystalline Solids **203**, 19-26 (1996).

53.   E. A. J. Marcatili, and R. A. Schmetzer, "Hollow Metallic and Dielectric Waveguides for Long Distance Optical Transmission and Lasers," Bell. Syst. Tech. J. **43**, 1783 (1964).

54.   P. Yeh, A. Yariv, and E. Marom, "Theory of Bragg Fiber," Journal of the Optical Society of America **68**, 1196-1201 (1978).

55.   Y. Fink, J. N. Winn, S. H. Fan, C. P. Chen, J. Michel, J. D. Joannopoulos, and E. L. Thomas, "A dielectric omnidirectional reflector," Science **282**, 1679-1682 (1998).

56.   S. G. Johnson, M. Ibanescu, M. Skorobogatiy, O. Weisberg, T. D. Engeness, M. Soljacic, S. A. Jacobs, J. D. Joannopoulos, and Y. Fink, "Low-loss Asymptotically Single-Mode Propagation in Large Core OmniGuide Fibers," Optics Express **9**, 748- 779 (2001).

57.   B. Temelkuran, S. D. Hart, G. Benoit, J. D. Joannopoulos, and Y. Fink, "Wavelength-scalable hollow optical fibres with large photonic bandgaps for CO2 laser transmission," Nature **420**, 650-653 (2002).

58.   D. Torres, O. Weisberg, G. Shapira, C. Anastassiou, B. Temelkuran, M. Shurgalin, S. A. Jacobs, R. U. Ahmad, T. Wang, U. Kolodny, S. M. Shapshay, Z. Wang, A. K. Devaiah, U. D. Upadhyay, and J. A. Koufman, "OmniGuide photonic bandgap fibers for flexible delivery of CO2 laser energy for laryngeal and airway surgery," Photonic Therapeutics and Diagnostics **5686**, 310-321 (2005).

59.   P. Russell, "Photonic crystal fibers," Science **299**, 358-362 (2003).

60.   R. F. Cregan, B. J. Mangan, J. C. Knight, T. A. Birks, P. S. Russell, P. J. Roberts, and D. C. Allan, "Single-mode photonic band gap guidance of light in air," Science **285**, 1537-1539 (1999).

61.   T. A. Birks, P. J. Roberts, P. S. J. Russell, D. M. Atkin, and T. J. Shepherd, "Full 2-D Photonic Bandgaps in Silica/Air Structures," Electronics Letters **31**, 1941-1943 (1995).

62.   T. A. Birks, J. C. Knight, and P. S. Russell, "Endlessly single-mode photonic crystal fiber," Optics Letters **22**, 961-963 (1997).

63.   J. C. Knight, J. Broeng, T. A. Birks, and P. S. J. Russell, "Photonic band gap guidance in optical fibers," Science **282**, 1476-1478 (1998).

64.   P. J. Roberts, F. Couny, H. Sabert, B. J. Mangan, D. P. Williams, L. Farr, M. W. Mason, A. Tomlinson, T. A. Birks, J. C. Knight, and P. S. J. Russell, "Ultimate low loss of hollow-core photonic crystal fibres," Optics Express **13**, 236-244 (2005).

65.   M. A. Duguay, Y. Kokubun, T. L. Koch, and L. Pfeiffer, "Antiresonant Reflecting Optical Waveguides in SiO2-Si Multilayer Structures," Applied Physics Letters **49**, 13-15 (1986).

66.   N. M. Litchinitser, A. K. Abeeluk, C. Headley, and B. J. Eggleton, "Antiresonant Reflecting Photonic Crystal Optical Waveguides," Optics Letters **27**, 1592- 1594 (2002).

67.   F. Couny, F. Benabid, P. J. Roberts, M. T. Burnett, and S. A. Maier, "Identification of Bloch-modes in hollow-core photonic crystal fiber cladding," Optics Express **15**, 325-338 (2007).

68.   T. A. Birks, G. J. Pearce, and D. M. Bird, "Approximate band structure calculation for photonic bandgap fibres," Optics Express **14**, 9483-9490 (2006).

69.   T. P. White, R. C. McPhedran, C. M. de Sterke, N. M. Litchinitser, and B. J. Eggleton, "Resonance and scattering in microstructured optical fibers," Optics Letters **27**, 1977-1979 (2002).

70.   F. Benabid, and P. J. Roberts, "Guidance mechanisms in hollow-core photonic crystal fiber - art. no. 69010U," Photonic Crystal Materials and Devices Vii **6901**, U9010-U9010 (2008).

71.   J. R. Hook, and H. E. Hall, *Solid State Physics* (John Wiley & Sons, Norfolk, Great Britain, 2004).

72.   F. Couny, F. Benabid, and P. S. Light, "Large-pitch kagome-structured hollow-core photonic crystal fiber," Optics Letters **31**, 3574-3576 (2006).

73.   B. Beaudou, F. Couny, F. Benabid, and P. J. Roberts, "Large Pitch Hollow Core Honeycomb Fiber," 2008 Conference on Lasers and Electro-Optics & Quantum Electronics and Laser Science Conference, Vols 1-9, 1981-1982 (2008).

74.   G. J. Pearce, G. S. Wiederhecker, C. G. Poulton, S. Burger, and P. S. J. Russell, "Models for guidance in kagome-structured hollow-core photonic crystal fibres," Optics Express **15**, 12680-12685 (2007).

75.   F. Couny, P. J. Roberts, T. A. Birks, and F. Benabid, "Square-lattice large-pitch hollow-core photonic crystal fiber," Optics Express **16**, 20626-20636 (2008).

76.   Y. Y. Wang, P. S. Light, and F. Benabid, "Core-surround shaping of hollow-core photonic crystal fiber via HF etching," Ieee Photonics Technology Letters **20**, 1018-1020 (2008).

77.   R. Amezcua-Correa, F. Gerome, S. G. Leon-Saval, N. G. R. Broderick, T. A. Birks, and J. C. Knight, "Control of surface modes in low loss hollow-core photonic bandgap fibers," Optics Express **16**, 1142-1149 (2008).

78.   B. J. Mangan, J. K. Lyngso, and P. J. Roberts, "Realization of low loss and polarization maintaining hollow core photonic crystal fibers," 2008 Conference on Lasers and Electro-Optics & Quantum Electronics and Laser Science Conference, Vols 1-9, 2016-2017 (2008).

79.   F. Gerome, R. Jamier, J. L. Auguste, G. Humbert, and J. M. Blondy, "Simplified hollow-core photonic crystal fiber," Optics Letters **35**, 1157-1159 (2010).

80.   Y. Y. Wang, F. Couny, P. J. Roberts, and F. Benabid, "Low Loss Broadband Transmission in Optimised Core-shape Kagome Hollow Core PCF," in *CLEO/ QELS* (San Jose, USA, 2010).

81.   N. V. Wheeler, P. S. Light, F. Couny, and F. Benabid, "Slow and Superluminal Light Pulses Via EIT in a 20-m Acetylene-Filled Photonic Microcell," Journal of Lightwave Technology **28**, 870-875 (2010).

82.   T. F. Krauss, "Slow Light in Photonic Crystal Waveguides," J. Phys. D: Appl. Phys. **40** (2007).

83.   A. Schweinsberg, N. N. Lepeshkin, M. S. Bigelow, R. W. Boyd, and S. Jarabo, "Observation of superluminal and slow light propagation in erbium-doped optical fiber," Europhysics Letters **73**, 218-224 (2006).

84.   R. W. Boyd, and D. J. Gauthier, ""Slow" and "Fast" Light," in *Frontiers in Optics*, E. Wolf, ed. (Elsevier, 2001), pp. 497-530.

85.   J. B. Khurgin, "Slow light in various media: a tutorial," Adv. Opt. Photon. **2**, 287-318 (2010).

86.   J. Carruthers, and T. Bieber, "Pulse Velocity in a Self-Locked He-Ne Laser," Journal of Applied Physics **40**, 426-& (1969).

87.   Casperso.L, and A. Yariv, "Pulse Propagation in a High-Gain Medium," Physical Review Letters **26**, 293-& (1971).

88.   D. Grischkowsky, "Adiabatic Following and Slow Optical Pulse Propagation in Rubidium Vapor," Physical Review A **7**, 2096-2102 (1973).

89.   M. M. Kash, V. A. Sautenkov, A. S. Zibrov, L. Hollberg, G. R. Welch, M. D. Lukin, Y. Rostovtsev, E. S. Fry, and M. O. Scully, "Ultraslow group velocity and enhanced nonlinear optical effects in a coherently driven hot atomic gas," Physical Review Letters **82**, 5229-5232 (1999).

90.   C. Liu, Z. Dutton, C. H. Behroozi, and L. V. Hau, "Observation of coherent optical information storage in an atomic medium using halted light pulses," Nature **409**, 490-493 (2001).

91.   L. Thevenaz, "Slow and fast light in optical fibres," Nat Photon **2**, 474-481 (2008).

92.   R. M. Camacho, M. V. Pack, J. C. Howell, A. Schweinsberg, and R. W. Boyd, "Wide-bandwidth, tunable, multiple-pulse-width optical delays using slow light in cesium vapor," Physical Review Letters **98**, - (2007).

93.   K. Y. Song, M. G. Herraez, and L. Thevenaz, "Observation of pulse delaying and advancement in optical fibers using stimulated Brillouin scattering," Optics Express **13**, 82-88 (2005).

94.   Z. M. Zhu, D. J. Gauthier, and R. W. Boyd, "Stored light in an optical fiber via stimulated Brillouin scattering," Science **318**, 1748-1750 (2007).

95.   Y. Okawachi, M. S. Bigelow, J. E. Sharping, Z. M. Zhu, A. Schweinsberg, D. J. Gauthier, R. W. Boyd, and A. L. Gaeta, "Tunable all-optical delays via Brillouin slow light in an optical fiber," Physical Review Letters **94**, - (2005).

96.   J. E. Sharping, Y. Okawachi, and A. L. Gaeta, "Wide bandwidth slow light using a Raman fiber amplifier," Optics Express **13**, 6092-6098 (2005).

97.   M. Gonzalez-Herraez, K. Y. Song, and L. Thevenaz, "Optically controlled slow and fast light in optical fibers using stimulated Brillouin scattering," Applied Physics Letters **87**, - (2005).

98.   M. Nikles, L. Thevenaz, and P. A. Robert, "Brillouin gain spectrum characterization in single-mode optical fibers," Journal of Lightwave Technology **15**, 1842-1851 (1997).

99.   D. Dahan, and G. Eisenstein, "Tunable all optical delay via slow and fast light propagation in a Raman assisted fiber optical parametric amplifier: a route to all optical buffering," Optics Express **13**, 6234-6249 (2005).

100.   R. Okazawa, H. Kuze, H. Masusaki, and N. Takeuchi, "Sensitivity Enhancement for Acetylene Detection at 1.5 micron by Use of a High-Finesse Optical Cavity " Jpn. J. Appl. Phys. **38**, 4946 - 4949 (1999).

101.   P. S. Light, "Photonic Microcells for Quantum Optic Applications." Thesis (PhD) in *Dept. of Physics* (University of Bath, Bath, 2008). Available from: www.opus.bath.ac.uk.

102.   C. P. Rinsland, A. Baldacci, and K. N. Rao, "Acetylene bands observed in carbon stars: a laboratory study and an illustrative example of its application," Astrophys. J. Suppl. Ser. **49**, 487-513 (1982).

103.   J. M. Brown, *Molecular Spectroscopy* (Oxford University Press, United States of America, 1998).

104.   P. W. Milonni, *Fast Light, Slow Light and Left-handed Light* (Taylor & Francis Group, United States of America, 2005).

105.   R. W. Boyd, D. J. Gauthier, A. L. Gaeta, and A. E. Willner, "Maximum time delay achievable on propagation through a slow-light medium (vol 71, pg 023801, 2005)," Physical Review A **72**, 059903 (2005).

106.   E. Figueroa, F. Vewinger, J. Appel, and A. I. Lvovsky, "Decoherence of electromagnetically induced transparency in atomic vapor," Optics Letters **31**, 2625-2627 (2006).

107.   M. A. Payne, A. P. Milce, M. J. Frost, and B. J. Orr, "Rovibrational energy transfer in the 4vCH manifold of acetylene, viewed by IR-UV double-resonance spectroscopy. 4. Collision-induced quasi-continuous background effects," Journal of Physical Chemistry A **110**, 3307-3319 (2006).

108.   D. H. Bangham, and F. P. Burt, "The Behaviour of Gases in Contact with Glass Surfaces," Proceedings of the Royal Society of London: Series A. **105**, 481- 488 (1924).

109.   E. Udd, *Fiber Optic Sensors: An Introduction for Scientists and Engineers* (John Wiley & Sons, New York, 2006).

110.   H. K. Kim, M. J. F. Digonnet, and G. S. Kino, "Air-core photonic-bandgap fiber-optic gyroscope," Journal of Lightwave Technology **24**, 3169-3174 (2006).

111.   S. Blin, M. J. F. Digonnet, and G. S. Kino, "Noise analysis of an air-core fiber optic gyroscope," Ieee Photonics Technology Letters **19**, 1520-1522 (2007).

112.   S. Blin, H. K. Kim, M. J. F. Digonnet, and G. S. Kino, "Reduced thermal sensitivity of a fiber-optic gyroscope using an air-core photonic-bandgap fiber," Journal of Lightwave Technology **25**, 861-865 (2007).

113.   V. Dangui, H. Kim, M. J. F. Digonnet, and G. S. Kino, "Phase sensitivity to temperature of the fundamental mode in air-guiding photonic bandgap fibers," Optics Express **13**, 6669 -6684 (2005).

114.   N. V. Wilding, P. S. Light, F. Couny, and F. Benabid, "Experimental Comparison of Electromagnetically Induced Transparency in Acetylene-Filled Kagome and Triangular Lattice Hollow Core Photonic Crystal Fiber," 2008 Conference on Lasers and Electro-Optics & Quantum Electronics and Laser Science Conference, Vols 1-9, 1953-1954 (2008).

115.   K. Knabe, S. Wu, J. K. Lim, K. A. Tillman, P. S. Light, F. Couny, N. Wheeler, R. Thapa, A. M. Jones, J. W. Nicholson, B. R. Washburn, F. Benabid, and K. L. Corwin, "10 kHz accuracy of an optical frequency reference based on (C2H2)-filled large-core kagome photonic crystal fibers," Optics Express **17**, 16017-16026 (2009).

116.   A. M. Jones, V. V. Nampoothiri, A. Ratanavis, R. Kadel, N. V. Wheeler, F. Couny, F. Benabid, W. Rudolph, B. R. Washburn, and K. L. Corwin, "C_2H_2 Gas Laser Inside Hollow-Core Photonic Crystal Fiber Based on Population Inversion," in *Conference of Lasers and Electro-optics (CLEO)*(San Jose, CA, 2010).

117.   B. Beaudou, F. Couny, Y. Y. Wang, P. S. Light, N. V. Wheeler, F. Gerome, and F. Benabid, "Matched cascade of bandgap-shift and frequency-conversion using stimulated Raman scattering in a tapered hollow-core photonic crystal fibre," Optics Express **18**, 12381-12390 (2010).

118.   J. A. West, C. M. Smith, N. F. Borrelli, D. C. Allan, and K. W. Koch, "Surface modes in air-core photonic band-gap fibers," Optics Express **12**, 1485-1496 (2004).

119.   P. S. Light, P. J. Roberts, P. Mirault, and F. Benabid, "Observation of anti-crossing events via mode-pattern rotation in HC-PCF," 2008 Conference on Lasers and Electro-Optics & Quantum Electronics and Laser Science Conference, Vols 1-9, 905-906 (2008).

120.   A. Argyros, and J. Pla, "Hollow-core polymer fibres with a kagome lattice: potential for transmission in the infrared," Optics Express **15**, 7713-7719 (2007).

121.   A. V. Taichenachev, A. M. Tumaikin, V. I. Yudin, M. Stahler, R. Wynands, J. Kitching, and L. Hollberg, "Nonlinear-resonance line shapes: Dependence on the transverse intensity distribution of a light beam," Physical Review A **69**, - (2004).

122.   R. Thapa, K. Knabe, M. Faheem, A. Naweed, O. L. Weaver, and K. L. Corwin, "Saturated absorption spectroscopy of acetylene gas inside large-core photonic bandgap fiber," Optics Letters **31**, 2489-2491 (2006).

123.   J. Hald, J. C. Petersen, and J. Henningsen, "Saturated optical absorption by slow molecules in hollow-core photonic band-gap fibers," Physical Review Letters **98**, 213902 (2007).

124.   J. K. Lim, K. Knabe, K. A. Tillman, W. Neely, Y. S. Wang, R. Amezcua-Correa, F. Couny, P. S. Light, F. Benabid, J. C. Knight, K. L. Corwin, J. W. Nicholson, and B. R. Washburn, "A phase-stabilized carbon nanotube fiber laser frequency comb," Optics Express **17**, 14115-14120 (2009).

125.   A. A. Madej, J. E. Bernard, A. J. Alcock, A. Czajkowski, and S. Chepurov, "Accurate absolute frequencies of the nu(1) + nu(3) band of (C2H2)-C-13 determined using an infrared inode-locked Cr : YAG laser frequency comb," Journal of the Optical Society of America B-Optical Physics **23**, 741-749 (2006).

126.   H. S. Moon, W. K. Lee, and H. S. Suh, "Absolute-frequency measurement of an acetylene-stabilized laser locked to the P(16) transition of (C2H2)-C-13 using an optical-

frequency comb," Ieee Transactions on Instrumentation and Measurement **56**, 509-512 (2007).

127.	P. Balling, M. Fischer, P. Kubina, and R. Holzwarth, "Absolute frequency measurement of wavelength standard at 1542nm: acetylene stabilized DFB laser," Optics Express **13**, 9196-9201 (2005).

128.	A. A. Madej, A. J. Alcock, A. Czajkowski, J. E. Bernard, and S. Chepurov, "Accurate Absolute Reference Frequencies from 1511 to 1545 nm of the $v_1 + v_3$ band of $^{12}C_2H_2$ determined with laser frequency comb interval measurements," J. Opt. Soc. Am. B **23**, 2200 - 2208 (2006).

129.	C. S. Edwards, G. P. Barwood, H. S. Margolis, P. Gill, and W. R. C. Rowley, "High-precision frequency measurements of the v(1) + v(3) combination band of (C_2H_2)-C^{12} in the 1.5 ʋm region," Journal of Molecular Spectroscopy **234**, 143-148 (2005).

130.	C. S. Edwards, H. S. Margolis, G. P. Barwood, S. N. Lea, P. Gill, and W. R. C. Rowley, "Absolute frequency measurements of 1.55 mu m diode laser acetylene standards," 2005 Digest of the LEOS Summer Topical Meetings, 137-138 (2005).

131.	A. A. Madej, J. E. Bernard, A. J. Alcock, A. Czajkowski, and S. Chepurov, "Accurate absolute frequencies of the nu(1) + nu(3) band of (C2H2)-C-13 determined using an infrared mode-locked Cr : YAG laser frequency comb," Journal of the Optical Society of America B-Optical Physics **23**, 741-749 (2006).

132.	R. F. Curl, F. Capasso, C. Gmachl, A. A. Kosterev, B. McManus, R. Lewicki, M. Pusharsky, G. Wysocki, and F. K. Tittel, "Quantum cascade lasers in chemical physics," Chemical Physics Letters **487**, 1-18 (2010).

133.	A. V. V. Nampoothiri, A. Ratanavis, N. Campbell, and W. Rudolph, "Molecular C2H2 and HCN lasers pumped by an optical parametric oscillator in the 1.5-mu m band," Optics Express **18**, 1946-1951 (2010).

134.	J. S. Sanghera, L. B. Shaw, and I. D. Aggarwal, "Chalcogenide Glass-Fiber-Based Mid-IR Sources and Applications," Ieee Journal of Selected Topics in Quantum Electronics **15**, 114-119 (2009).

135.	N. V. Wheeler, M. D. W. Grogan, P. S. Light, F. Couny, T. A. Birks, and F. Benabid, "Large-core acetylene-filled photonic microcells made by tapering a hollow-core photonic crystal fiber," Optics Letters **35**, 1875-1877 (2010).

136.	Corning, "Corning SMF28e Optical Fiber," (Corning Incorporated, 2007), Accessed 22nd October, 2010.

137.	A. Ghatak, and K. Thyagarajan, *Introduction to Fibre Optics* (Cambridge University Press, Cambridge, 1998).

138.	F. Benabid, Department of Physics, University of Bath, Claverton Down, Bath, BA2 6PZ (Personal communication 2010).

139.	F. Couny, F. Benabid, and P. S. Light, "Reduction of fresnel back-reflection at splice interface between hollow core PCF and single-mode fiber," IEEE Photonics Technology Letters **19**, 1020-1022 (2007).

140.	T. A. Birks, and Y. W. Li, "The Shape of Fiber Tapers," Journal of Lightwave Technology **10**, 432-438 (1992).

141.   K. Z. Aghaie, M. J. F. Digonnet, and S. H. Fan, "Optimization of the splice loss between photonic-bandgap fibers and conventional single-mode fibers," Optics Letters **35**, 1938-1940 (2010).

142.   N. Amitay, H. M. Presby, F. V. Dimarcello, and K. T. Nelson, "Optical Fiber Tapers - a Novel-Approach to Self-Aligned Beam Expansion and Single-Mode Hardware," Journal of Lightwave Technology **5**, 70-76 (1987).

143.   E. M. O' Brien, and C. D. Hussey, "Low-loss fattened fusion splices between different fibres," Electronics Letters **35**, 168- 169 (1999).

144.   G. Kakarantzas, L. Prill-Sempere, and P. S. J. Russell, "Up-tapering of Optical Fibers using a Conventional Flame Tapering Rig," in *CLEO*(Baltimore, 2007).

145.   K. Shiraishi, Y. Aizawa, and S. Kawakami, "Beam Expanding Fiber Using Thermal-Diffusion of the Dopant," Journal of Lightwave Technology **8**, 1151-1161 (1990).

146.   K. Knabe, R. Thapa, B. R. Washburn, and K. L. Corwin, "Reflected Pump Technique for Saturated Absorption Spectroscopy Inside Photonic Bandgap Fibers," 2007 Conference on Lasers & Electro-Optics/Quantum Electronics and Laser Science Conference (CLEO/QELS 2007), Vols 1-5, 2508-2509 (2007).

147.   K. J. Vahala, "Optical microcavities," Nature **424**, 839-846 (2003).

148.   D. K. Armani, T. J. Kippenberg, S. M. Spillane, and K. J. Vahala, "Ultra-high-Q toroid microcavity on a chip," Nature **421**, 925-928 (2003).

149.   K. Srinivasan, P. E. Barclay, O. Painter, J. X. Chen, A. Y. Cho, and C. Gmachl, "Experimental demonstration of a high quality factor photonic crystal microcavity," Applied Physics Letters **83**, 1915-1917 (2003).

150.   Y. Colombe, T. Steinmetz, G. Dubois, F. Linke, D. Hunger, and J. Reichel, "Strong atom-field coupling for Bose-Einstein condensates in an optical cavity on a chip," Nature **450**, 272-U279 (2007).

151.   Y. Colombe, T. Steinmetz, G. Dubois, F. Linke, D. Hunger, and J. Reichel, "Strong atom-field coupling for Bose-Einstein condensates in an optical cavity on a chip," Nature **450**, 272-276 (2007).

152.   T. Steinmetz, Y. Colombe, D. Hunger, T. W. Hansch, A. Balocchi, R. J. Warburton, and J. Reichel, "Stable fiber-based Fabry-Perot cavity," Applied Physics Letters **89**, - (2006).

153.   D. Hunger, T. Steinmetz, Y. Colombe, C. Deutsch, T. W. Hansch, and J. Reichel, "A fiber Fabry-Perot cavity with high finesse," New Journal of Physics **12**, - (2010).

154.   F. Couny, F. Benabid, and O. Carraz, "Enhanced SRS in H2 filled Hollow Core Photonic Crystal Fibre by use of Fibre Bragg Grating," J. Opt. A-Pure Appl. Opt. **9**, 156-159 (2007).

155.   P. S. Light, F. Couny, and F. Benabid, "Low optical insertion-loss and vacuum-pressure all-fiber acetylene cell based on Hollow Core PCF," Optics Letters **31**, 2538-2540 (2006).

156.   Y. J. Rao, T. Zhu, X. C. Yang, and D. W. Duan, "In-line fiber-optic etalon formed by hollow-core photonic crystal fiber," Optics Letters **32**, 2662-2664 (2007).

157.   C. E. Lee, R. A. Atkins, and H. F. Taylor, "Reflectively Tapped Optical Fiber Transversal Filters," Electronics Letters **23**, 596-598 (1987).

158.   P. T. Marty, J. Morel, and T. Feurer, "All-Fiber Multi-Purpose Gas Cells and Their Applications in Spectroscopy," Journal of Lightwave Technology **28**, 1236-1240 (2010).

159.   A. D. Yablon, *Optical Fiber Fusion Splicing* (Springer-Verlag Berlin Heidelberg, Berlin, 2005).

160.   T. A. Birks, R. P. Kenny, K. P. Oakley, and C. V. Cryan, "Elimination of Water Peak in Optical Fiber Taper Components," Electronics Letters **26**, 1761-1762 (1990).

161.   Y. J. Rao, M. Deng, D. W. Duan, X. C. Yang, T. Zhu, and G. H. Cheng, "Micro Fabry-Perot interferometers in silica fibers machined by femtosecond laser," Optics Express **15**, 14123-14128 (2007).

162.   E. Gobel, I. M. Mills, and A. J. Wallard, "The International System of Units," (Bureau International des Poids et Mesures, 2006), p. 180.

163.   M. Bajcsy, S. Hofferberth, V. Balic, T. Peyronel, M. Hafezi, A. S. Zibrov, V. Vuletic, and M. D. Lukin, "Efficient All-Optical Switching Using Slow Light within a Hollow Fiber," Physical Review Letters **102**, 203902 (2009).

164.   T. Tako, M. Ohtsu, and H. Tsuchida, "Frequency Stabilization of A1gaas Lasers Based on the H2o and Rb-D2 Lines," Journal De Physique **42**, 83-88 (1981).

165.   J. Kitching, L. Hollberg, S. Knappe, and R. Wynands, "Compact atomic clock based on coherent population trapping," Electronics Letters **37**, 1449-1451 (2001).

166.   A. D. Slepkov, A. R. Bhagwat, V. Venkataraman, P. Londero, and A. L. Gaeta, "Spectroscopy of Rb atoms in hollow-core fibers," Physical Review A **81**, - (2010).

167.   V. Venkataraman, P. Londero, A. R. Bhagwat, A. D. Slepkov, and A. L. Gaeta, "All-optical modulation of four-wave mixing in an Rb-filled photonic bandgap fiber," Optics Letters **35**, 2287-2289 (2010).

168.   P. Londero, V. Venkataraman, A. R. Bhagwat, A. D. Slepkov, and A. L. Gaeta, "All-Optical Modulation of Four Wave Mixing in a Rb-Filled Hollow-Core Photonic Band-Gap Fiber," 2009 Conference on Lasers and Electro-Optics and Quantum Electronics and Laser Science Conference (Cleo/Qels 2009), Vols 1-5, 1875-1876 (2009).

169.   M. Stephens, and C. Wieman, "High Collection Efficiency in a Laser Trap," Physical Review Letters **72**, 3787- 3798 (1993).

170.   H. G. Robinson, E. S. Ensberg, and H. G. Dehmelt, Bull. Am. Phys. Soc. **3** (1958).

171.   M. T. Ghannam, and M. N. Esmail, "Rheological properties of poly(dimethylsiloxane)," Industrial & Engineering Chemistry Research **37**, 1335-1340 (1998).

172.   J. C. Camparo, R. P. Frueholz, and B. Jaduszliwer, "Alkali Reactions with Wall Coating Materials Used in Atomic Resonance Cells," Journal of Applied Physics **62**, 676-681 (1987).

173.   M. Stephens, R. Rhodes, and C. Wieman, "Study of Wall Coatings for Vapor-Cell Laser Traps," J. App. Phys. **76**, 3479- 3488 (1994).

174.   M. A. Bouchiat, and J. Brossel, "Relaxation of Optically Pumped Rb Atoms on Paraffin-Coated Walls," Physical Review **147**, 41-& (1966).

175.   A. Gozzini, F. Mango, J. H. Xu, G. Alzetta, F. Maccarrone, and R. A. Bernheim, "Light-Induced Ejection of Alkali Atoms in Polysiloxane Coated Cells," Nuovo Cimento Della Societa Italiana Di Fisica D-Condensed Matter Atomic Molecular and Chemical Physics Fluids Plasmas Biophysics **15**, 709-722 (1993).

176.   S. N. Atutov, V. Biancalana, P. Bicchi, C. Marinelli, E. Mariotti, M. Meucci, A. Nagel, K. A. Nasyrov, S. Rachini, and L. Moi, "Light-induced diffusion and desorption of alkali metals in a siloxane film: Theory and experiment," Physical Review A **60**, 4693-4700 (1999).

177.   M. Meucci, E. Mariotti, P. Bicchi, C. Marinelli, and L. Moi, "Light-Induced Atom Desorption," Europhysics Letters **25**, 639-643 (1994).

178.   E. B. Alexandrov, M. V. Balabas, D. Budker, D. English, D. F. Kimball, C. H. Li, and V. V. Yashchuk, "Light-induced desorption of alkali-metal atoms from paraffin coating," Physical Review A **66**, 042903 (2002).

179.   A. D. Slepkov, A. R. Bhagwat, V. Venkataraman, P. Londero, and A. L. Gaeta, "Generation of large alkali vapor densities inside bare hollow-core photonic band-gap fibers," Optics Express **16**, 18976-18983 (2008).

180.   B. P. Anderson, and M. A. Kasevich, "Loading a vapor-cell magneto-optic trap using light-induced atom desorption," Physical Review A **6302**, - (2001).

181.   A. Burchianti, A. Bogi, C. Marinelli, C. Maibohm, E. Mariotti, and L. Moi, "Reversible light-controlled formation and evaporation of rubidium clusters in nanoporous silica," Physical Review Letters **97**, - (2006).

182.   F. K. Gelmukhanov, and A. M. Shalagin, "Diffusion Pulling in and Pushing out of Atoms by a Light-Field," Zhurnal Eksperimentalnoi I Teoreticheskoi Fiziki **77**, 461-470 (1979).

183.   E. Mariotti, J. H. Xu, M. Allegrini, G. Alzetta, S. Gozzini, and L. Moi, "Light-Induced-Drift Stationary States," Physical Review A **38**, 1327-1334 (1988).

184.   T. Takekoshi, and R. J. Knize, "Optical guiding of atoms through a hollow-core photonic band-gap fiber," Physical Review Letters **98**, - (2007).

185.   H. J. Lewandowski, D. M. Harber, D. L. Whitaker, and E. A. Cornell, "Simplified system for creating a Bose-Einstein condensate," Journal of Low Temperature Physics **132**, 309-367 (2003).

186.   J. Brewer, A. Burchianti, C. Marinelli, E. Mariotti, L. Moi, K. Rubahn, and H. G. Rubahn, "Pulsed laser desorption of alkali atoms from PDMS thin films," Applied Surface Science **228**, 40-47 (2004).

187.   C. J. Hensley, D. H. Broaddus, C. B. Schaffer, and A. L. Gaeta, "Photonic band-gap fiber gas cell fabricated using femtosecond micromachining," Optics Express **15**, 6690-6695 (2007).

188.   H. Tsuchida, M. Ohtsu, and T. Tako, "Frequency Stabilization of Algaas Semiconductor-Laser to the Absorption-Line of Water-Vapor," Japanese Journal of Applied Physics Part 2-Letters **21**, L1-L3 (1982).

189.   T. Yanagawa, S. Saito, and Y. Yamamoto, "Frequency Stabilization of 1.5-Mu-M Ingaasp Distributed Feedback Laser to Nh3 Absorption-Lines," Applied Physics Letters **45**, 826-828 (1984).

190.   M. Ohi, "Frequency Stabilization of a Pbsnte Laser on a Methane Line in the Nu-4 Band," Japanese Journal of Applied Physics **19**, L541-L543 (1980).

191.   M. A. Gubin, D. A. Tyurikov, A. S. Shelkovnikov, E. V. Kovalchuk, G. Kramer, and B. Lipphardt, "Transportable He-Ne/Ch4 Optical Frequency Standard and Absolute Measurements of Its Frequency," Ieee Journal of Quantum Electronics **31**, 2177-2182 (1995).

192.   J. M. Hollas, *Basic Atomic and Molecular Spectroscopy* (The Royal Society of Chemistry, Cambridge, UK, 2002).

193.   R. Felder, "Practical realization of the definition of the metre, including recommended radiations of other optical frequency standards (2003)," Metrologia **42**, 323-325 (2005).

194.   P. M. Morse, "Diatomic Molecules According to the Wave Mechanics. II. Vibrational Levels," Physical Review **34**, 57 (1929).